1-1-1995

The evolution of dust in the terrestrial planet region of circumstellar disks around young stars.

Diane Dutkevitch
University of Massachusetts Amherst

THE EVOLUTION OF DUST IN THE TERRESTRIAL PLANET REGION OF CIRCUMSTELLAR DISKS AROUND YOUNG STARS

A Dissertation Presented

by

DIANE DUTKEVITCH

Submitted to the Graduate School of the
University of Massachusetts Amherst in partial fulfillment
of the requirements for the degree of

DOCTOR OF PHILOSOPHY

May 1995

Department of Physics and Astronomy

THE EVOLUTION OF DUST IN THE TERRESTRIAL PLANET REGION OF CIRCUMSTELLAR DISKS AROUND YOUNG STARS

A Dissertation Presented

by

DIANE DUTKEVITCH

Approved as to style and content by:

Michael F. Skrutskie, Chair

Stephen E. Strom, Member

Suzan Edwards, Member

James F. Walker, Outside Member

John F. Dubach, Department Head
Department of Physics and Astronomy

To my Lord, Jesus, and those who showed me His love.

Acknowledgments

If you take long enough to finish your degree, the list of people who contribute to your success grows rather large. My list of acknowledgments will be appropriately lengthy. I started working real jobs before I defended, and you know how that goes. Well into my second job, the list of folks who have been and are a major part of my life keeps increasing. Many of those mentioned here are not scientists, but wonderful people who gave me a lot of love, joy, fun, friendship, and support, particularly during a long and difficult illness. I would not have had the courage or strength to continue working at my degree without their support.

First of all, I would like to thank Steve Rae of Wells College, whose teaching turned my interest in physics into a real love of physics. Steve also gave me my first view through a telescope: a tiny Saturn in a 4″ telescope Steve purchased for the college. I credit my classmate Chip Wendell at the University of Rochester for inspiring me to take a seminar on galaxies, which led to my eventual decision to specialize in astronomy. Bill Forrest introduced me to enough infrared instrumentation to clinch my decision.

And then there's UMASS. I've worked for and/or with almost everybody in the department. Thanks first to Mike Skrutskie, for giving me the opportunity to do some instrumentation in his lab, and teaching me how to do single-channel photometry. It's delightful to see how marriage and daddyhood have put a sparkle in his eyes (credits to Anne and Emily). The original idea for this doctoral research was the brainchild of Steve Strom; Steve also funded a large fraction of the research presented here. Suzan Edwards was my advisor for my "second-year

project," in addition to serving as a dissertation committee member. I've always appreciated Suzan's ability to work me hard, while maintaining a personal warmth. Tony Morse was originally the fourth member of my committee. I could not manage to get all four committee members in the same room at the same time before he left for a sabbatical in Cambridge, England, so I was forced to find a substitute at the last minute. Enter Jim Walker, the program director for physics and astronomy. Jim is amazing. While I was sweating it 1000 miles away, Jim e-mailed me at 10 PM, 3 AM, whenever, to tell me he made arrangements for extensions, payments of fees, room reservations, whatever. I think we grad students should let him get more sleep. In the end, Jim became my fourth committee member.

Several undergrads who worked in Mike's lab were real characters, and we had a lot of fun together. Most noteworthy were Eugene Hertz, Peter Shread, Catrina Hamilton, and later, Dave Whalen. I won't say who fried the most electronics. Ashley Webb, superb machinist, is an adopted member of the lab; his enthusiasm is contagious.

I am deeply indebted to the Five College Radio Astronomy Observatory for allowing me to work as a technician for two years. Thanks to Paul Goldsmith, Neal Erickson and Read Predmore for hiring me. I learned one heck of a lot working with Neal and Ronna Erickson, Ron Grosslein and John Karakla. There were many others with whom I worked less directly, especially Bob Dragon, Marianne Laukaitis, Barry Stone, "T.C." Li, Paul Luippold, and the machinists in Draper, including Tom Scott. They're a great crew, and it was a real pleasure to work with all of them.

Special thanks to Ronna, who went well beyond the call of duty to teach me things that will be of value to me later in my career. Thanks also for the

encouragement and wisdom when times were rough, and even when they weren't so rough. Ronna is a precious jewel.

A few faculty require special mention. Dave Van Blerkom helped me move into my apartment when I first came to the Amherst area, and has been a friend ever since. Dave can recite quite a bit of Dr. Seuss from memory, which shows he recognizes the important things in life. Graduate students gravitate towards his office just to chat. John Kwan taught a superb course in astrophysics, for which he is so well known. I have a lot of respect for John as a person, not just as a scientist. And then there's Ron Snell. Ron is a riot. He should also have a water balloon thrown at him.

The astronomy department and radio observatory would fall apart without the staff. They're terrific people, and I will miss them. I am grateful to Terri Grzybowski, Sandy Ostrowski, Ann Cairl, Denise Parent, Barb Keyworth, Sally Rule, Jackie Golonka, and Pam Barlow. They have been of immeasurable help to me.

Over the (many) years, graduate students and postdocs have come and gone. Students in our department are quite social, and we get to know each other pretty well. I can't list all of them, but they all made life in the "Death Tower" a little more bearable. (Will they ever give us ventilation after 7 PM again?) Alan Welty was about the best classmate anyone could want, and a dear friend. His wife Emily is a treasure. Hiking the Bright Angel Trail in the Grand Canyon with Alan after PPIII was one of the highlights of my life. Late-night badminton with Shuding Xie and Sandor Molnar provided a welcome relief from a hard day's work. Shuding has been a blessing ever since I arrived at UMASS; behind that shy and unassuming exterior lurks a very talented astronomer. Georgina Beristain and David Kendall never cease to amaze me with their warmth and generosity. Gina is more a sister than a friend. Someday, David, the three of us may yet hike Mount Greylock.

Gene Lauria was the best biking partner I ever had, with Nancy Eaton a close second. "C tower" was definitely enlivened by Mike Meyer, Gary Kleiman, Will Pughe, Lori Allen, and Meg Lysaght. Will still bails me out of computer problems, and Meg has been kind enough to print out copies of my dissertation at UMASS while I'm 1000 miles away. Denise Barberet, currently a grad student in Spanish, ran up to the 10th floor of the tower to attend my defense talk. Now that's a friend!

Others who have enhanced life at UMASS over the years include Paul Viscuso, Kevin and Vicki Long, Mike Rudenko, Bev Smith, Doug McGonagle, David and Milena Hiriart, Amy Lovell, David Smith (and Eron), Pat Knezek, Louma Ghandour, Taoling Xie, Gerald Moriarty-Schieven, Luis Salas-Casales, Darek Lis, Mike Wentz, Wayne Kinzel, Daryl Swade, Ted Bergin, German Cortez, Lisa Prato, Hector Aceves, Chigurupati Murali, John Spitzak, John Carpenter, and many others.

My life in Amherst was much more than graduate school; I had a family in my housemates and the Amherst Area New Testament Church. They were faithful in prayer and service, and I am a much healthier, joyous, and better-adjusted person for their efforts. They showed me the meaning of "unconditional love." My deepest thanks to Laura, Charlie and Simon Henze, Laura Noddin, Tina and Andrew Power, Marjanneke Wright, Lisa Nadeau Graves, Nancy and Jim Fenstermacher, Kathleen and Matt Schwab, Kathy and Stan Urbanowicz, Mary Bartels, Linda Preston, Silvana Gravini Downey, Caron Bowen, Dave and Ingrid Hill, Phil, Nancy, Joseph, Benjamin, Nathan, Natalie and Lydia Arant, Steve, Diane and Nathan Johnson, Kathleen and Gary Aller, Jack and Tammy Gravell, Peter and Julie Castillo, Chib and Selina Mbubaegbu, Daniel, Evelyn and Amara Okorafor, Barb and Rob Schulze, Sue and Jamie O'Connell, Tony and Ellen Curd, Mike and Shelly Warren, Rusty and Ann Denton, Mark and Karry Orelup, Scott

Dunn, Doug Selkirk, Greg Bishop, Pat Rusk, Terri Kay, Josephine Aggor Boyington, Lila Bonnell, and many others whose names will not come to me now.

Teaching last year at Franklin and Marshall College was my first job as a proto-doctor. Dana Backman maintains a sense of humor (although not necessarily his sanity) in the face of absurdity, and Bruce reminded us all of the simple pleasures in life. I could not have asked for a finer colleague than Dana. Mike Seeds has a wit that never quits, and worked an awful lot for someone on sabbatical. Mary Jane Jasin keeps the department running smoothly, and has a smile that brightens even the toughest day. Linda Fritz challenged me to think about teaching in new ways; my future students will benefit from her counsel. Thanks to the skill of Arlan Mantz, I can now get an inflated balloon through the tiny neck of a soda bottle. I had been trying unsuccessfully for years. Greg Adkins, Calvin Stubbins, Ned Dixon, Phil Sutter and Al Burns completed the friendly department. Many thanks to Annalisa and Io Crannell for a lot of fun outside of work. Annalisa is an amazing teacher, and my teaching is better for adopting some of her techniques. Franklin and Marshall is about students; there is not room to list all the students who made the demands of teaching worth the effort. Special thanks to Scott Williams, Becky Eby, Fred Duennebier, Amil Dasgupta and Mark Baron.

As in Amherst, there were many friends outside of school who made Lancaster feel like a home. Most were members of Lancaster Covenant Church. Although there are far too many people to list here, a very special thanks to Christine Schmalhofer and Cynthia Haughery for their prayers and friendship. Thanks also to Bill Haughery, Ray and Irene Randolph, Gayle and Reggie Williams, Val and Dion Roth, Bruce Gurney, Keith Hannenman, Lara Bowman, Jean Griswold, Jennifer Van Heel, and Cindy Hess. I wish I had been able to spend more time

with all of them. I am grateful to Esther Nissly, Jim Henry and Mr. Engler for their persistent hospitality.

Finally, I wound up in Illinois, where the topology is uniform. Hiking just isn't the same. Thanks to Dave Meyer for letting me work on my dissertation when circumstances left my current job somewhat undefined. Dave is one of those people who manage to salvage the best in a situation, even when the situation is pretty bad. Likewise, I've appreciated the ever-positive viewpoint and encouragement of Giles Novak. Although I cannot mention everyone in the department, thanks to Sam Finn, Guy Miller, Mel Ulmer and Dave Taylor for their support through the past several months. Life is never dull with officemates like Scott Grossman, Kathy Romer, Larry and Jennifer Kidder, and Jessie Dotson. Robert Lentz and Drew Milsom are not only a lot of fun, but also boast an admirable selection of comics and blurbs on their door. Outside the department, special thanks to Monica Palka, Jamie Hales and Elanor Bray for their prayers and friendship.

I've saved the best for last. Many, many thanks to my family for their love and support over the years. You can't really appreciate your parents until you get out on your own and realize what they went through. I have the best brothers in the world, and two wonderful sisters-in-law. Thanks to my parents, Archie and Marion, my brothers Dennis and Mark, my sisters-in-law Doreen and Sarah, and my niece and nephews, Dawn, D.J. and Alex.

Some technical credits must also be given. Although his name does not appear on the cover page, Dana Backman is rightfully a co-author on this work. Thanks to Dave Whalen for assisting me on an IRTF observing run. John Stauffer provided lists of cluster stars when we started this project. Sigma Xi, The Scientific Research Society, awarded a grant for travel funds for an IRTF observing run. Dick Joyce at KPNO and Mark Shure at the IRTF were most helpful in providing filter traces and other useful information about the telescope facilities.

Lastly, I thank Scott Kenyon, Lee Hartmann, Kevin Long, Martin Weinberg and Mike Meyer for their helpful comments over the years.

Abstract

THE EVOLUTION OF DUST IN THE TERRESTRIAL PLANET REGION OF CIRCUMSTELLAR DISKS AROUND YOUNG STARS

May 1995

Diane Dutkevitch, B.A., Wells College

M.A., University of Rochester

Ph.D., University of Massachusetts Amherst

Directed by: Professor Michael F. Skrutskie

Circumstellar disks with masses comparable to the primeval solar nebula have been discovered around numerous pre-main sequence stars; it is believed the disks are a natural byproduct of star formation. If most stars originally have massive circumstellar disks, it is very likely planetary systems are common. Orbiting planets are not directly observable owing to their relatively cool temperatures and meager surface area. However, in the early stages of planetary formation, the surface area of debris in the disk may exceed the surface area of the star by many orders of magnitude. Material in the terrestrial zone emits primarily at near-infrared wavelengths; sufficient disk debris may produce detectable excess emission at these wavelengths. As clearing mechanisms, including possible planetary formation, remove the small particles in the disk, the strong infrared emission diminishes. By observing the excess infrared emission as a function of stellar age and spectral type, timescales for inner disk processes which create or remove small particles can be established.

This dissertation presents sensitive, simultaneous, near-infrared broadband continuum observations of old pre-main sequence and young main-sequence cluster stars. The stellar ages range from 1-600 Myr, spanning the predicted epoch of

planetary formation for solar-type stars. A wide range of spectral types were observed. We detect no excess emission after an age of about 3×10^6 yr.

Using a model to predict the infrared emission from an optically thin dust disk, we find our measurements are sensitive to 10^{20}-10^{21} g of micron-radius dust grains ($\rho = 2$ g cm^{-3}) distributed within the terrestrial zone. Adapting this result to a more realistic particle size distribution, we believe we can detect debris in extra-solar systems until the terrestrial planets are 90-95% complete.

Older models of the formation of the Earth which assume orderly growth predict the Earth is 90% complete after about 80 Myr. Newer models allow runaway growth, which shortens the timescale to $\sim 10^5$ yr. If the observed clearing in the inner disk reflects the formation of terrestrial planets, our results strongly support models of planetary formation which incorporate runaway growth. Implications are discussed.

Table of Contents

List of Tables

List of Figures

Chapter 1

INTRODUCTION

1.1 Introduction

At some point we all pause to wonder how we came to inhabit our planet Earth, and what our place is in the universe. How did our planet come into being? Are there other planets like ours? Are we alone? Although it is unlikely we will know with certainty in the near future whether there are other "intelligent" life forms in the universe, we have learned a great deal about the formation of stars and our solar system, and strongly suspect that planetary systems are a common occurrence.

Ideally, we would like to view images of other planetary systems. For now, the search for other planets, and the quest to understand the process by which they form, must proceed by indirect means.

Why is it so difficult to detect planets directly? In our solar system, Jupiter is the largest planet, making it the easiest to detect from a vantage point outside our solar system. Imagine trying to detect a "Jupiter" orbiting another star. The closest stars are about 1 pc away, placing a "Jupiter" 5″ from the star. The Hubble Space Telescope, and large ground-based telescopes, have much better resolution than 5″. Unfortunately, the planet is about 10^8 times fainter than the star, which makes it extremely difficult to detect the planet.

The most promising indirect means of detecting planets orbiting other stars is to look for the tiny wobble in a star's motion resulting from its orbit about the center of mass of a planetary system. This requires extremely accurate radial

velocity and/or proper motion measurements. Such measurements are difficult, and typically require tens of years of observations (the planet's orbital period). Research programs using this approach have been underway for several years, with the intent of finding both stellar and sub-stellar companions such as brown dwarfs. Several candidates have been identified, but no sub-stellar companions to main sequence stars have been confirmed. (See, for example, Campbell, Walker and Yang, 1988; Marcy and Benitz, 1989; and Murdoch, Hearnshaw and Clark, 1993.)

Variations in the arrival time of millisecond pulses have been used to confirm the existence of at least two planets orbiting the pulsar PSR 1257+12 (Wolszczan, 1994). The variations represent Doppler shifts due to the orbit of the neutron star about the center of mass. One school of thought presumes planets around pulsars formed by accumulation of debris orbiting the neutron star after the supernova explosion.

It is currently believed our solar system formed by accumulation of material within a disk of gas and dust which was a byproduct of the birth of our Sun. There is now compelling evidence that such disks are a frequent and natural byproduct of the formation of most, if not all, solar-type stars. The detection of planets orbiting pulsars supports the notion that planets are easily created from orbiting debris. If so, then it is likely planetary systems are the norm, rather than the exception.

Although we cannot currently detect extra-solar planets directly, we can approach the problem from another angle. Instead of looking for planets, one can concentrate on the processes which are expected to produce planets. If the processes which we believe are responsible for creating our solar system appear to be common in the universe, then it is reasonable to expect planetary systems to be common. This viewpoint is reciprocal; we may learn a great deal about the formation of our own solar system by studying young stars at the stage when planetary systems may be forming.

As stated earlier, it is believed planets form within disks of gas and dust. An understanding of the evolution of these circumstellar disks is therefore critical to our understanding of planetary formation. It is difficult to observe the gas; the gas can only be detected in the very youngest stages of evolution. However, we can easily see the dust in the disks for at least the first few million years. The reader may ask, "If we can't see planets, which are large, then how can we see dust, which is small?"

For the sake of argument, assume dust particles act like blackbodies. Recall the radiation emitted by a blackbody depends on both the temperature, and the surface area. Planets are difficult to detect because they much cooler than their central star, and have much less surface area. However, circumstellar disks initially contain a great deal of gas and dust, which may emit more radiation than the central star. Some of this radiation is due to accretion; the particles lose potential energy as they approach the central star, and the lost energy is converted to radiation. Over time, the gas dissipates, the particles increase in size, and eventually may accumulate into bodies the size of planets. In a star–disk system, the star is the hottest object, but the small particles possess most of the surface area. In short, we can detect dust, while we cannot detect planets, because the total surface area of the dust is so much greater.

One can trace the evolution of processes in circumstellar disks by tracing the evolution of the small particles (i.e. surface area). At the present time, an understanding of the evolution of the small particles in circumstellar disks will provide the best observational constraints on our understanding of the formation of planetary systems.

This dissertation addresses one specific aspect of the evolution of circumstellar disks: the evolution of dust in the terrestrial planet region around young solar-type stars during the epoch of planetary formation. Although the dust may constitute

only a small fraction of the mass in a disk at the time planets are forming, it represents the majority of the radiating surface area, and is thus much more easily detected than larger bodies.

This chapter is devoted to an overview of our understanding of the formation of stars and circumstellar disks, and the subsequent evolution of disks into planetary systems. It concludes with a brief statement of the research presented in this work.

1.2 Overview of Solar-Type Star Formation

Before detailing one aspect of star–planet formation, it is helpful to describe the overall process. This section provides a brief review of the essentials of solar-type star formation, and the early stages of disk evolution. It is not intended to be complete. For a more detailed and balanced perspective, see reviews such as Shu, Adams and Lizano (1987), Cameron (1988), Wilking (1989), Wetherill (1990), and Lissauer (1993).

1.2.1 Historical Perspective

In earliest times, those who observed the heavens attempted to understand the motions of the heavenly bodies, without knowledge of the physical nature of the bodies themselves. The first modern record of the notion of a solar system as we understand it today is the work of Copernicus in the presentation of his heliocentric theory in the mid-sixteenth century. Observational proof of his theory came after Galileo's observations of the phases of Venus in the seventeenth century. In the eighteenth century, Kant and Laplace independently suggested the planets formed from a "nebula" of material around the Sun, which could account for the fact that all the planets in our solar system lie in a plane. However, they could offer no firm proof of this hypothesis.

Two centuries later, we are finally beginning to understand how planetary systems form, mostly as a result of technological developments.

Even 20 years ago, although astronomers knew much about the evolution of stars once they reached the main sequence, very little was known about star formation. Knowledge was limited because the process is heavily obscured by gas and dust. Since the coming of age of radio and infrared astronomy, we can now observe at least some of the formation process, and our knowledge continues to increase as rapid technological advances allow us to see progressively more.

1.2.2 The Birth of Solar-type Stars and Circumstellar Disks

Our first insight into the birth of stars came from the discovery at radio wavelengths of cold (typically 10 K) clouds of gas and dust in interstellar space. Sizes and masses of these "molecular clouds" range from the Dark Cloud Complexes, which are about 10–20 pc in extent and have masses of about 10^3–$10^4 M_\odot$, to Giant Molecular Clouds, about 20–80 pc in extent with masses of 10^5–$10^6 M_\odot$.

Within these clouds, denser "cores" were observed, believed to be the earliest stages of stellar formation. The cores result from the gravitational collapse of regions within the cloud. Low-mass stars generally form in the Dark Cloud Complexes, while high-mass stars are found in the Giant Molecular Clouds. The cores from which solar-type stars form have sizes ranging between roughly 0.05–0.2 pc, and masses of perhaps 0.3–10 $M_\odot$.

The visual extinction in molecular clouds is enormous, so that observations of these earliest stages of a star's life are only possible at radio, and perhaps infrared, wavelengths. Such observations have only been feasible for the past 15–20 years. Detailed observations are still difficult due to the large obscuration and confusion with ambient material, but sufficient observational information has been obtained

to enable theorists to begin to model the collapse of cores and the formation of stars.

Thermal and turbulent motions within the cloud support against collapse. Magnetic fields also play a role by inhibiting a spherically symmetric collapse of charged particles. Eventually, a temperature decrease or density enhancement allows a gravitational collapse to commence. If even a small amount of overall angular momentum is initially present in the collapsing region, conservation of angular momentum will create a flattened structure upon collapse. The most likely scenarios produce multiple star systems, circumstellar disks, or rings, depending on initial conditions. As it is highly probable there will be some small amount of angular momentum in the region of the cloud undergoing collapse, the formation of disk or ring systems (or multiple systems) is expected to be a common occurrence. This dissertation focuses on stars having circumstellar disks (or rings), from which planetary systems may evolve. For reference purposes, the initial protosun and associated "cocoon" of gas and dust is commonly referred to as the "solar nebula."

The above scenario is a simplistic view of a complicated process. The mass of the collapsing region may be several times larger than the final star–disk system, requiring a means of removing mass from the system. In addition, when a region of size 0.05–0.2 pc collapses to the size of a planetary system, conservation of angular momentum causes the orbital speed of the material to increase drastically. In fact, conservation of angular momentum should cause the star to rotate at its breakup speed! Since stars do form, there must be some mechanism to shed angular momentum. The details of this mechanism are currently one of the great mysteries of star formation.

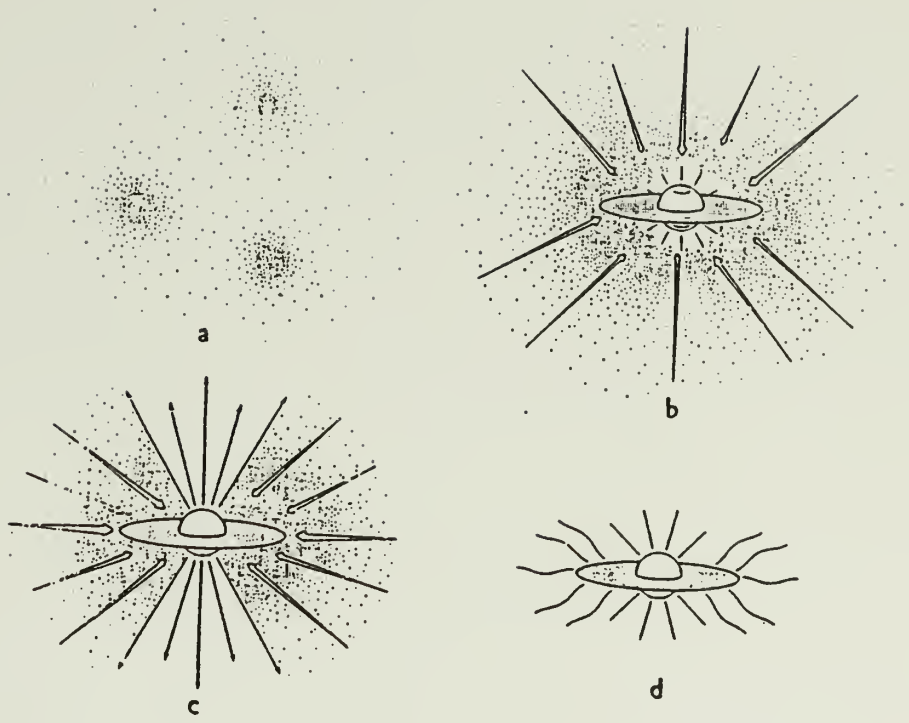

Figure 1.1. The four stages of star formation. *(a)* Cores form within molecular clouds as magnetic and turbulent support is lost. *(b)* A protostar with a surrounding nebular disk forms at the center of a cloud core collapsing from inside-out. *(c)* A stellar wind breaks out along the rotational axis of the system, creating a bipolar flow. *(d)* The infall terminates, revealing a newly formed star with a circumstellar disk. (From Shu, Adams, and Lizano, 1987.)

1.2.3 Earliest Stages of Circumstellar Disks and Outflows

The four stages in the "standard model" of star formation are illustrated in Figure 1.1 (from Shu, Adams and Lizano, 1987).

Initially protostars are not observable at wavelengths shortward of infrared or radio owing to the large visual extinction of the parent molecular cloud. Large bipolar molecular outflows associated with some of these highly obscured sources

have been observed at radio wavelengths. The outflows are perhaps 1 pc in extent, with velocities of about 10 km/sec (Snell 1989).

After 10^4–10^5 yr, enough of the cloud dissipates that protostars are seen at visible and shorter wavelengths. At this point, the signatures of collimated atomic winds tens of AU in extent, having velocities of hundreds of km/sec, are observed. Sometimes ionized jets of plasma are seen. It is believed the outflows and winds are responsible for the disruption and dissipation of the parent cloud material.

As mentioned in the previous subsection, some mechanism is required to remove mass from the collapsing cloud core to permit the formation of low-mass stars, and somehow angular momentum must be removed to prevent the forming protostar from rotating faster than its breakup speed. Outflows and winds clearly expel mass, and are also believed to remove angular momentum by some yet-unexplained process.

The spectral energy distributions (i.e. flux *vs.* wavelength) of the newly visible pre-main sequence stars differ vastly from that of main sequence stars; continuum emission far in excess of that expected from a stellar photosphere is observed at infrared and radio wavelengths. Smaller continuum excesses are also seen at X-ray and ultraviolet wavelengths. These excesses are associated with disk properties.

Dust in the disk is heated by the central star, then reemits at primarily infrared and radio wavelengths. This is known as "reprocessing" of starlight, or simply "reprocessing." Viscous accretion warms the disk and produces excess emission at infrared wavelengths and shortward. Large ultraviolet excesses arise from the regions closest to the star, where rapidly rotating disk material meets the more slowly-rotating surface of the star. This region, which is not well understood, is known as the "boundary layer."

Before launching into a discourse on the evolution of circumstellar disks, it should be emphasized that no one has seen a definitive image of a circumstellar

disk around a protostar. Excess continuum emission is sufficient to diagnose the presence of material around the star, but in itself cannot distinguish the geometry of the material. Images of the young *main* sequence star beta Pictoris show a tenuous edge-on disk of material, about ten times larger than the orbit of Pluto (Smith and Terrile, 1984). The disk geometry is presumably a remnant of the star's formation; the disk is sufficiently tenuous that it is only seen when the star itself is occulted. Images so strongly implying a disk geometry have not been obtained for protostars. Recent images of HL Tau from the Hubble Space Telescope may provide our first look at a protostellar disk (Stapelfeldt *et al.*, 1995). Regardless, the observational evidence for disks surrounding protostars is so strong their existence is now generally accepted as fact. The most compelling evidence for a disk geometry follows.

Millimeter continuum observations of pre-main sequence stars can be used to estimate the mass in circumstellar dust (Beckwith *et al.*, 1990). If one assumes the mass is distributed spherically symmetrically about the star, the calculated extinction ranges from a few hundred to a few thousand magnitudes at visible wavelengths. Since these stars are easily observed at visible wavelengths and shortward, one concludes the dust *must* be in a flattened structure, such as a disk.

Other supporting evidence for a disk geometry arises from forbidden-line observations of atomic winds. Blueshifted forbidden lines are seen, diagnostic of material approaching the observer, while the redshifted lines from the expected receding material are absent. As these winds are tens of AU in extent, a reasonable explanation for the observations is to presume the receding material is obscured by an optically thick circumstellar disk, 10–1000 AU in extent (Edwards *et al.*, 1987).

The excess continuum emission observed for pre-main sequence stars has been modeled successfully using a thin disk geometry (flat or flared). The models

assume a combination of accretion and reprocessing as the mechanism(s) for the excess luminosity (see Kenyon and Hartmann, 1987, and references within).

Observed ^{12}CO line profiles strongly suggest gas in Keplerian motion around two pre-main sequence stars, HL Tau (Sargent and Beckwith, 1991) and GG Tau (Skrutskie *et al.*, 1993).

Lastly, we *expect* flattened structures to form as a cloud core collapses, due to conservation of angular momentum. If planetary systems form by agglomeration and accretion of material, the fact that all the planets in our solar system lie nearly in a plane strongly argue for a disk geometry for the precursor material.

1.2.4 Evolution of Disks into Planetary Systems: Models

Once a disk has formed, how does it evolve with time? Eventually the disk will dissipate, possibly creating a planetary system in the process. There are few observational studies of this final stage of evolution, but numerous theoretical models. This section briefly details the general theories of planetary formation, laying the foundation for the observation studies discussed in the following sections. Much of the theory presented here refers specifically to the formation of our solar system.

Recent work suggests accretion onto the star drives the observed bipolar outflows, winds, and jets in young star–disk systems (Edwards, Ray, and Mundt, 1993). Eventually the winds disrupt and dissipate the parent molecular cloud material sufficiently to remove the source of infalling material. The star-disk system then evolves as an independent entity. Accretion tapers off, and with it, the outflows, winds, and ionized jets. At some point in time, the particle density in the disk decreases to the point where particles in the disk can stick together without collisional dissociation, permitting agglomeration into larger bodies. This is the beginning of planetary formation, if any is to occur.

It is assumed most of the mass of the disk is initially in gas, not solids, and the presence or absence of gas has a profound effect on the evolution of the disk. The nature and mass of the gas affects the composition of the bodies that form, and also the dynamics of the disk (e.g. gas drag). Unfortunately, little is known about the evolutionary history of the gas, owing to the difficulty of observations.

There are two presumed mechanisms for the creation of planets: *1.)* bodies grow by successive collisions (agglomeration or accretion), or *2.)* a gravitational instability in the disk results in a region of the disk collapsing to form a planet. Safranov (1969) was the first to discuss the agglomeration mechanism in detail; Wetherill (1990) gives a good review of the topic. Cameron (1988) reviews the study of the gravitational instability approach.

Gravitational instability is now thought to be a likely scenario for the formation of multiple star systems, but not for the formation of our solar system. The arguments prohibiting formation of planets by means of gravitational instabilities are based on the composition of the solar system, the required mass of the solar nebula, and the difficulty in explaining the formation of small bodies such as asteroids, moons and comets.

If gravitational instability does not form planetary systems, then the remaining option is planetary growth by agglomeration and accretion. The remainder of this section refers to models of disk evolution which assume growth by these mechanisms.

A number of researchers have modeled the evolution of circumstellar disks, emphasizing various combinations of expected processes. The goal of most models is to build planets from disks or rings of gas and dust, hopefully creating a planetary system similar to our own solar system.

Typical processes included in models of disk evolution are gas drag; gravitational enhancement of particle cross-section; relative velocities of particles

or bodies; probabilities of collisions; upon collision, the probabilities for *a)* fragmentation, *b)* sticking, or *c)* melting; accretion of material onto the star; radiation drag; and changes in the dynamics of the system as particles grow.

As there appears to be a natural segregation between terrestrial and Jovian planets, many models of solar system formation concentrate on either the inner or outer solar system, perhaps only one planet in particular. One test of the validity of each model is whether or not it is consistent with the overall scenario of solar system formation.

First consider models of the inner disk. In the following discussion, "planetesimals" refer to asteroid-sized bodies, while "embryos" refer to roughly lunar-sized bodies. As a matter of convenience, models of the evolution of the terrestrial planet region are typically divided into two stages: the time period needed to grow large rocky embryos, then the era in which these large embryos collide to form planets. Different techniques are required to model the two stages.

The number of bodies in a very young disk is too unwieldy to permit following each individual particle or body. One of the most common means of modeling the earliest stages of disk evolution is to treat the disk as an ideal gas, distributing the velocities of the bodies according to equipartition of energy. Although equipartition of energy in an ideal gas arises from collisions, not gravitational interactions, the gravitational interactions of *solid* bodies of unequal mass tends to equalize the kinetic energy of the particles.

Without equipartition of energy, the models predict orderly growth of embryos. The inclusion of equipartition of energy in the models leads to the possibility of runaway growth, which shortens the timescale for the formation of embryos. This topic is reviewed nicely in Wetherill (1990). Runaway *vs.* orderly growth is a function of the relative particle velocities and their gravitationally-enhanced cross-sectional areas. The gravitational cross section is

larger than the physical cross section by a factor of $1 + v_e^2/v^2$, where v is the relative velocity at infinity of the approaching body, and v_e is the escape velocity. Equipartition of energy lowers the random velocities of the larger bodies, raises the random velocities of the smaller bodies, and leaves the random velocities of the intermediate bodies relatively unchanged. As a result, the relative velocities between large and intermediate bodies is reduced, greatly increasing their gravitational cross section, which in turn leads to an enhanced growth rate. Note as the bodies grow, the escape velocity of the largest body increases, again increasing the gravitational focusing factor, which also increases the growth rate (see discussion in Wetherill, 1990).

Models of the terrestrial planet region which include gas drag, gravitational enhancement of collisional cross-section, equipartition of energy, and perfect sticking (no fragmentation on impact) result in runaway growth, which can build 10^{26}–10^{27} g planetary embryos in about 10^5 yr. Omission of equipartition of energy leads to timescales an order of magnitude larger (Wetherill, 1990). Recent work by Wetherill and Stewart (1993) demonstrates this beautifully.

The growth from embryos to planets is an exponential approach to completion. Earlier models assuming the gas-free case created an "Earth" in roughly 10^8 years (see Wetherill, 1980b, Wetherill, 1980a, and references within). In a more recent calculation, beginning with a swarm of larger embryos, three-dimensional Monte Carlo simulations produced 3 to 5 terrestrial planets in 10^7–10^8 years. This is consistent with timescales derived from geological evidence (Wetherill, 1990).

Now consider the outer regions of the solar system. The rocky cores of the Jovian planets presumably formed in a fashion analogous to the terrestrial planets. The large mass of the cores was sufficient to facilitate a rapid accumulation of material by gravitational attraction, resulting in "giant" planets.

The Jovian cores must have formed while the gaseous solar nebula was still present in order to account for the heavy abundance of hydrogen and helium in the Jovian (and Saturnian) atmospheres. This means the timescale of the formation of Jupiter is highly relevant to the formation of the Earth, as it gives a clue to the nebular gas concentration during the final stages of the Earth's formation. This indirectly determined the size and nature of the Earth's primordial atmosphere (Wetherill, 1990), which resulted from planetary outgassing or cometary impacts.

The timescale of Jupiter's formation is important for several other aspects of the formation of the solar system as a whole. First, the accretion of large amounts of gas in the formation of the Jovian planets necessarily has profound effects on the gas evolution of the disk, which in turn affects the dynamical evolution of the disk.

In addition to the gas evolution of the disk, the presence of large rocky Jovian cores has a significant impact on the evolution of the terrestrial planets. The massive cores stir planetesimals within the "feeding zone" of each giant planet, increasing the velocities of the planetesimals, and perturbing their orbits. Some of these planetesimals are ejected from the solar system. Rocky planetesimals injected into the inner terrestrial planet region will increase the collision rate there; icy planetesimals likewise perturbed will evaporate or become cometesimals or comets. These cometesimals may supply volatiles for the terrestrial planet region (Mumma *et al.*, 1993).

One possible clue to the formation time of Jupiter is the existence of the asteroid belt. It is thought the prior formation of Jupiter prohibited the creation of a terrestrial planet where the asteroids are now found. The formation of the asteroid belt is a complex issue, and only the briefest mention will be given here. A review of the topic may be found in Wetherill (1989). Assuming there was a "normal" amount of material to build planets in the asteroid region, the most likely scenario is one in which the material in the asteroid region fragmented by

mutual collisions, the smaller debris subsequently removed by gas drag or gravitational perturbations. It is likely that orbital resonances with Jupiter played a large role in the acceleration of the asteroidal bodies; the resulting increase in relative velocities could produce the necessary fragmentation, while the increase in orbital eccentricities could eject material from the asteroid region. Any scenario for the formation of the asteroid belt which relies on the prior formation of Jupiter requires Jupiter's core to form in the timescale needed to produce large planetary embryos in the outer terrestrial planet region, 10^5–10^6 yr.

Recall that models of the terrestrial planets region could produce two scenarios: orderly growth, or runaway accretion, depending on whether or not equipartition of energy was assumed. Without runaway accretion, predicted timescales for the formation of planets are unreasonably long. The need for runaway accretion becomes especially apparent when the models are applied to the Jovian planets; without runaway, formation of Neptune in particular requires many times the current age of the solar system (Lissauer, 1987)!

Lissauer (1987) found that if there was an enhancement in the nebular surface density at the distance of Jupiter, runaway accretion could produce Jupiter's core in about 10^5 yr. Such an enhancement might have occurred as a result of diffusion of water vapor from the inner disk into the Jovian planet region, and subsequent condensation into ice (Stevenson and Lunine, 1987). After the core grew to about 15–25 $M_\oplus$, it could quickly accrete gas in the surrounding region.

The formation of our solar system, and planetary systems in general, is an enormously complicated process. The discussion here hardly does justice to the work that has been done in the field; only those aspects most relevant to this work have been mentioned.

1.3 Observable Signatures of Disk Properties and Activity

Ideally, one would like to obtain as much observational information as possible about circumstellar disks and their evolution, and the timescales involved. In practice, this is not a simple task. Imaging of disks and associated phenomena is only feasible in the early stages of star–disk formation. In the early evolutionary stages, some mechanisms produce very strong diagnostic signatures, but the large extinctions and competing processes make interpretation difficult. In the later stages, the disk is possibly becoming a planetary system, and signatures of disk activity are very weak. In this section, some of the primary methods for studying disks and their evolution are mentioned.

1.3.1 Direct Imaging

The most sought-after information about star formation is direct imaging over a range of wavelengths. Large-scale structures related to the earliest stages of star–disk formation (e.g. outflows) have been imaged at optical wavelengths, and mapped at radio wavelengths. Infrared images should become common as infrared cameras come of age.

Images of the smaller disks themselves are hard to come by. At a distance of 150 pc, disks in the nearest star-forming region may be only one arcsecond or less in diameter.

1.3.2 Spectral Line Observations

Molecular line observations provide information on the gas content, mass, morphology, and rotational velocities of very young, massive disks (Sargent and Beckwith, 1991; Skrutskie *et al.*, 1993; Beckwith and Sargent, 1993). Atomic line observations provide information on winds and jets, including velocities and densities, (e.g. Edwards *et al.*, 1987; Edwards, Ray and Mundt, 1993). In the later

stages, as the gas clears and the outflows diminish, these observations become very difficult, owing to the sensitivity of current detector systems.

Spectral line observations of the T-Tauri phase of disk evolution provide information on the composition of dust and ices in the disk (e.g. Cohen and Witteborn, 1985; Brooke, Tokunaga and Strom, 1993). These observations may also be used to estimate the optical depth due to particles in the disk at the wavelength of observation. As the particle surface density decreases, these observations become progressively more difficult.

1.3.3 Continuum Observations

Accretion onto the star produces continuum emission in excess of the stellar photosphere at ultraviolet wavelengths and longward, observed with broadband measurements. The ultraviolet radiation originates in the so-called "boundary layer" where rapidly orbiting material in the innermost regions of the disk accretes onto the more slowly rotating stellar surface. This signature weakens as the gas dissipates and the smaller particles agglomerate into larger particles. Accretion signatures are not distinguishable once the accretion rate falls below about $10^{-8} M_{\odot}/\mathrm{yr}$ (Skrutskie *et al.*, 1990; see also Kenyon and Hartmann, 1987).

Solid bodies in the disk are another major source of continuum emission. Dust grains and larger bodies, heated by the central star, re-emit somewhat like blackbodies at primarily infrared and longer wavelengths (this is known as "reprocessing" of starlight). Observations using broadband filters can be used to detect reprocessing emission as an excess of continuum emission over that expected from the stellar photosphere. Dust particles are thought to vaporize at about 1500–2000 K, which places an upper limit of about 1μm to the wavelength of peak radiation from particles in the disk.

When there is confusion as to the relative contributions of infrared emission from accretion and reprocessing, the strength of any ultraviolet excess, which

arises from boundary layer emission, may be used to place limits on the accretion luminosity.

This dissertation is concerned with the late stages of disk evolution, during the epoch of planetary growth. It will be seen that one of the best methods for studying the late stages of disk evolution is to observe the dust reprocessing emission over time.

1.4 Previous Observational Studies of Disk Evolution

Many observational studies have been done on circumstellar disks around solar-type stars, mostly on the earlier stages of evolution. In this section, some of the most relevant prior studies are mentioned, leading to the research presented in this work. The list is in no way exhaustive.

1.4.1 Studies of Disks around Pre-Main Sequence Stars

This subsection presents a more-or-less chronological history of the study of disks around pre-main sequence stars. It not only includes observations that yielded information about the properties of disks, but also shows how the first gleanings of our understanding of disk evolution were deduced.

One of the first major studies was done by Cohen and Kuhi (1979), who obtained optical scanner data and infrared broadband measurements on roughly 500 pre-main sequence stars in several associations/complexes. One important conclusion was that most infrared excesses in the sources they studied required thermal emission from hot dust grains, rather than gas. Their study laid the foundation for much of the work to follow.

Cohen and Witteborn (1985) focused specifically on emission from the dust grains in the disk. They obtained 10 μm spectroscopy of 32 T-Tauri stars, where silicate grains have prominent spectral features. They found a minimum in the

optical depth at 10μm at an age of about 10^6 yr (see Lissauer, 1987). They interpreted this minimum to be a result of the beginning of agglomeration. The subsequent increase in optical depth was attributed to orbit-crossing collisions between planetesimals, leading to fragmentation which produces more small grains. In addition, for systems viewed edge-on, they presumed collisions leading to inclined orbits would produce a thickening of the disk.

Walter (1986) stumbled upon the evolutionary path of T-Tauri stars somewhat by accident. During a follow-up study of strong x-ray sources, he found a class of stars he termed the "naked" T-Tauri stars, or NTTS. On the basis of their proximity to regions of active star formation, strong Li I λ6707 absorption, and strong chromospheric and coronal activity, they were presumed to be pre-main sequence stars. However, they lacked the large infrared excesses (characteristic of dust) and wind signatures of nearby T-Tauri stars, having similar ages. As such, they could be considered diskless T-Tauri stars.

In a later paper, Walter *et al.* (1988) discussed the NTTS in some detail, focusing on 28 stars in the Taurus-Auriga complex, again from an x-ray selected sample. They found the distribution of stellar mass, spectral types, and ages of the NTTS were similar to those of the classical T-Tauri stars (cTTS). However, they did not see the the infrared excesses, extreme emission lines, or photometric variability characteristic of the cTTS. Estimating the completeness of their NTTS sample, they extrapolated the NTTS were likely to outnumber the cTTS in the Taurus-Auriga region by a ratio of 10:1. (A recent study using the ROSAT All-Sky Survey by Neuhäuser *et al.* (1995) found that in Taurus-Auriga, the wTTS outnumber the cTTS by a factor of at least 8.)

To determine the ages of their sample stars, Walter *et al.* (1988) used the convective-radiative evolutionary tracks (calculations of stellar luminosity *vs.* temperature of the contracting protostar as a function of age) adopted by Cohen

and Kuhi (1979). Cohen and Kuhi compiled the tracks from the work of several authors, striving for consistency in the treatment of convection.

Walter *et al.* found NTTS with ages less than 10^5 yr, as well as cTTS with ages greater than 5×10^6 yr. If the NTTS represent a later evolutionary stage than the cTTS, this finding implies a disk dissipation time of roughly 10^5–10^6 yr. Continuing this line of thought, they infer planets must form on timescales less than 10^6 yr. This timescale probably depends on stellar mass, and also initial and local conditions. They conclude that if planetary formation requires a longer time, then only those stars that are cTTS for long periods of time can form planetary systems. (Note: The terminology used in this paragraph was that of Walter *et al.*; it would have been more consistent with the terminology in this paper to use a phrase such as "planetary embryos" instead of "planets" in the above discussion. Disk signatures disappear once "large" bodies form.)

K. Strom *et al.* (1989) examined the evolutionary timescales of disk signatures in T-Tauri stars more carefully. They compiled optical and infrared broadband observations of 83 young stellar objects in the Taurus-Auriga molecular cloud complex, obtained from published literature (including the work of Walter and colleagues). They found that near-infrared excesses (2.2 μm), diagnostic of dust in the innermost 0.1 AU of the disk, becomes optically thin by an average age of about 3×10^6 yr. Absolute 2.2 μm flux excesses were determined by de-reddening the optical and near-infrared fluxes, then matching the observed spectral energy distribution at R ($\lambda = 0.7\mu$m) to that of a dwarf standard having the same spectral type as adopted for the pre-main sequence star.

They defined a new class of pre-main sequence stars, the weak-lined T-Tauri stars (wTTS), similar to the NTTS of Walter *et al.* (1988). The wTTS are T-Tauri stars (TTS) having an equivalent width $W(H\alpha) \leq 10$ Å.

A decrease in the equivalent width of $H\alpha$ (diagnostic of accretion) with age in the sample was noted, demonstrating that at least some of the wTTS must represent a later evolutionary stage of the cTTS. Evidence was found for at least one, possibly three disks with inner "holes", indicated by lack of near-infrared excesses, but having significant mid-infrared ($>$ 25–100 μm) excesses (see Figure 2.2). Although this study included observations covering a broad range of dust temperatures, sampling the disk to radii of nearly 100 AU, the data was not sufficient to detect optically *thin* excess emission. Most of these sources are variable, requiring simultaneous measurements to distinguish weak excesses emission arising from tenuous dust. Only portions of the data set were simultaneous measurements. Presumably the variability of the sources is caused by either starspots, or changes in accretion rates of disk material.

Extending the findings of K. Strom *et al.* (1989) to longer wavelengths, Skrutskie *et al.* (1990) obtained sensitive 10 μm ground-based broadband observations of 20 stars from the Strom *et al.* sample, seeking evidence of weak dust excesses within 1 AU of the star. For the remaining stars in the Strom *et al.* sample, 12μm measurements by IRAS (The Infrared Astronomical Satellite) were used to estimate 10 μm fluxes. A strong correlation was seen between 10 μm and 2.2 μm fluxes, reinforcing the findings of K. Strom *et al.* (1989).

The three systems with possible inner "holes" are postulated to be transition cases between the early disk stages, where an optically thick disk extends to the surface of the star, and the presumably later evolutionary stage where optically thick material is detected only at larger disk radii. The small number of observed "transition cases" argues for a rapid transition from the optically thick to optically thin case. Such a situation may well arise from the agglomeration of material into larger bodies in the inner disk, or removal of material near the star by Poynting-Robertson drag, as discussed in Section 1.5.3.

The authors also found a very strong correlation between Hα equivalent width, diagnostic of accretion, and 10 μm excess emission. This is a precursor to the findings of Edwards, Ray and Mundt (1993), who infer winds are driven by accretion. The combined results imply an observational timescale of $< 10^7$ yr for the end of the accretion epoch.

Beckwith *et al.* (1990) obtained 1.3 mm continuum measurements of 86 pre-main sequence stars in Taurus-Auriga. At this wavelength, all but the inner 1 AU of the disk is optically thin, enabling one to estimate disk masses. Free-free emission was shown to be an unlikely source for the observed emission; thermal emission from dust is the presumed source. Using the slope of the observed spectral energy distributions as a diagnostic, they concluded the shape of grains in the disk is not like that of interstellar grains, but lies somewhere between a spherical (interstellar) and fractal structure. They assume an opacity inversely proportional to wavelength, as opposed to the standard opacity assumed for interstellar grains, which varies inversely with the square of the wavelength. With this opacity law, they calculated a typical visual extinction A_V for the observed flux densities at 1.3mm assuming the material is distributed in a spherically symmetrical shell around the star. The extinction ranges from 220–5100 mag, depending on the particle motions. In contrast, all stars in the sample have observed extinctions of $A_V \leq 7$. The low observed extinction for these stars *requires* the inferred disk material lie in a flattened structure, such as a thin disk. Historically, this finding was important, as it was by far the most convincing evidence for the mere existence of circumstellar disks around pre-main sequence stars. Keep in mind no direct images of these disks had ever been achieved, which left some astronomers arguing whether the material near the star had a disk geometry or not.

Beckwith *et al.* calculated the total mass in solid particles to range between 10^{-5} and 10^{-2} $M_\odot$, implying total disk masses between 0.001 and 1 $M_\odot$ (assuming

a standard interstellar gas-to-dust ratio of 100). For those stars having disk signatures, no decrease in disk mass is seen as a function of age, up to the maximum age of 10^7 yr for their sample. Disk material was only detected for cTTS and borderline wTTS; they did not detect disk emission from stars with very weak Hα emission. This is consistent with the near-infrared observations of Walter *et al.* (1988), K. Strom *et al.* (1989), and Skrutskie *et al.* (1990). As the circumstellar material is presumed to lie in a thin disk, the disk is protected from most of the stellar wind and radiation, and should survive the T-Tauri phase, even if the winds are quite robust. They concluded that sufficient material thus remains to build planetary systems like our solar system.

Finally, within the past year Robert O'Dell of Rice University, using the Hubble Space Telescope (HST), has obtained images of ionization shells around massive young stars in Orion, but the disks are inside the shells, hidden from view. Also using the HST, Karl Stapelfeldt (of the Jet Propulsion Laboratory) and colleagues have perhaps obtained the first real image of a circumstellar disk around a pre-main sequence star. Their images of HL Tau in Taurus-Auriga are currently in press (Stapelfeldt *et al.*, 1995).

1.4.2 Previous Observations of the Late Stages of Disk Evolution

If the wTTS represent a later evolutionary stage than the cTTS, it can be argued that the process of planetary formation has begun by the time the star reaches the wTTS stage. The lack of strong disk signatures implies the disk surface area has dropped as a result of the agglomeration and accretion of material into larger bodies.

Theoretical predictions and geological evidence indicate the planet-building epoch extends into the early main sequence stage, so it is reasonable to seek evidence of disk material associated with young main sequence stars. Witteborn *et*

al. (1982) looked for 10μm excess thermal emission from fragmentation debris around the young (3×10^8 yr) and nearby (25 pc) Ursa Major Stream stars. No statistically significant excess emission was detected for any of their sample stars. Assuming a minimum particle radius of about 0.01 μm, a maximum particle radius of 50 km, and a power law particle size distribution with index $\delta = 3.5$, they were able to place an upper limit of $2.2 \times 10^{-6}\ M_\odot$ to $2.2 \times 10^{-5}\ M_\odot$ (1–10% of the rocky mass of the planets) on the mass of the debris cloud for a solar-type star. Compare their sensitivity to that needed to detect the estimated mass of the material responsible for the zodiacal light, which is only about $10^{-17} M_\odot$ (2.5×10^{16} g; Whipple, 1967)!

More sensitive infrared observations of young main sequence stars were obtained by the IRAS satellite. Tenuous, cool (50 to 125 K) material has been detected around at least 3 main sequence stars, possibly as many as 100 (see Backman and Paresce, 1993, for a review). The material is diagnosed by infrared thermal excess emission at 12–100 μm. For the three well-studied cases, α Lyrae (Vega), β Pictoris, and α Piscis Austrinus (Formalhaut), no corresponding near-infrared excess emission is observed. The material is likely to be in thin disks, 100 to 1000 AU in extent, with no detectable emission from the inner tens of AU, and may be analogous to the postulated Kuiper Belt outside our solar system (the source of short-period comets). The emission is at least 100 times stronger than that expected from the zodiacal emission from our solar system. The grains appear to be larger than typical interstellar grains.

Smith and Terrile (1987) obtained deep CCD images of what appears to be a tenuous edge-on disk around the main sequence star beta Pictoris, extending to a radius of at least 1100 AU. (The disk was originally discovered by the same authors in 1984.) It is likely this disk geometry is a remnant of the star formation process.

If interstellar gas-to-dust mass ratios hold true for disks, one expects two orders of magnitude greater disk mass in gas than dust. In this regard, Skrutskie *et al.* (1991) sought evidence of gas emission in ^{12}CO (J=1→0) for a sample of eight stars in the Ursa Major Stream. As in the Witteborn *et al.* study, the Ursa Major stream stars were chosen because they are young and nearby. The spectral types of the stars range from A2 to K3. No evidence of gas emission was found. Owing to the beam-filling factor, this study was only sensitive to material at large disk radii ($r > 350$ AU). The calculations of the authors indicate if the precursor disks are sufficiently large, then the CO mass must be less than 6×10^{24} g. Assuming the CO/H_2 ratio is characteristic of the molecular interstellar medium, the total mass remaining at large radii must be less than $3 \times 10^{-5}\ M_{\odot}$. They note that much more mass could be present but escape detection if it is in the inner regions of the disk, or if the disk is smaller than 350 AU.

1.5 Dust as a Tracer of Disk Evolution in the Planetary Formation Epoch

If it is not possible to directly observe the evolution of disks into planetary systems, what is the next best option? Secondary indicators of the processes taking place in the disk are needed. As the gas is too difficult to detect in all but the earliest stages of star formation, that leaves only emission from solid bodies in the disk.

The total emission of solids in the disk is a function of both temperature and surface area. Bodies closest to the star are hottest, and therefore emit more energy per unit surface area than bodies farther from the star. Grains near the star emit primarily at infrared wavelengths. Small grains possess the most surface area per unit mass, and comprise most of the surface area in the disk. Consider that grinding an asteroid-sized body (10^{20} g, $\rho = 3$ g cm^{-3}) into micron-sized grains

produces a total particle surface area equal to roughly 16 times the surface area of the Sun!

The large surface area-to-mass ratio of dust makes it one of the best tracers of the late stages of disk activity. The infrared excesses associated with young stars diminishes with stellar age. This diminution results from a decrease in the population of small particles (which comprise most of the surface area of the disk). The disk loses small particles to processes such as agglomeration, accretion, radiation blowout, and stellar winds.

The strength of the infrared excess produced by reprocessing of starlight is a function of the temperature of the central star, the mass of material in the disk, the size distribution of bodies, the mass surface density of the disk, and the opacities of the bodies. None of these are terribly well known, and even if they were, the modeling becomes formidable rather quickly. Instead of trying to handle all of these parameters at once, it is easier to look at a simplified picture to establish the most general conditions in the disk, after which specifics can be argued.

This section is divided into 4 parts. First it is shown that we expect most of the disk surface area to be in small particles. Next, a brief summary is given of the science we can learn by studying the evolution of dust in disks. Finally, the processes which remove and create small particles in disks are discussed briefly.

1.5.1 The Size Distribution of Solid Bodies in Circumstellar Disks

There are a few ways one can estimate the particle size distribution in circumstellar disks. One needs a lower size limit, an upper size limit, and the general distribution law. One way to go about this is to examine the size distribution of solid bodies in our own solar system. This gives information about what one might expect in the very late stages of the formation of a planetary system. Information about smaller particles may be obtained by observations of

the interstellar medium, which is presumably the raw material from which stars and planetary systems form. And, of course, models of how we believe our solar system came to be give insight as to the particle size distribution we might expect, given processes we think should be occurring within the disks.

The size distribution of particles is generally found to obey the power law $n(a) \propto a^{-\delta}$, where a is the grain radius, and $n(a)$ is the number of particles with a given radius. Only the exponent δ varies from study to study.

The size distribution of interplanetary particles in our present solar system have been studied using rocket impact and collection experiments, and micrometeor crater records on lunar rocks. Results typically indicate sub-micron and micron-sized particles (see papers within Weinberg, 1967, and Elsässer and Fechtig, 1975).

Le Sergeant and Lamy (1980) used the size distribution of micrometeor craters on lunar rocks to determine the size distribution of interplanetary particles in our solar system. With their assumption that the size of the crater is proportional to the size of the impacting particles, the size distribution of craters is identical to the size distribution of particles. They used a two-component fit for grains between 10^{-2} and 10^{3} microns in diameter. A power law with exponent $\delta = 3.85$ best fits particles with radii smaller than 6 μm; a parabolic fit with a shallower slope best represents grains with radii between 6 and 10^{3} microns. Using these results, Witteborn *et al.* (1982) assume the size distribution of interplanetary particles can be represented by a power law with the compromise index value of $\delta = 3.5$.

Mathis, Rumpl, and Nordsieck (1977) determined the size distribution of grains in the interstellar medium (ISM) from observed interstellar extinction in the wavelength range of 0.11 – 1 micron. They found a power law distribution with exponent of 3.5, which agrees well with the results of Le Sergeant and Lamy, and

the choice of Witteborn *et al.* The sizes for graphite and silicates combined range from 0.005-0.25μm.

From the theoretical standpoint, the $\delta = 3.5$ power law is characteristic of situations where the size distribution is determined by a grinding process (Dohnanyi, 1969; see also Witteborn *et al.*, 1982).

In a disk where agglomeration and collisional fracturing are presumably taking place, it is not unreasonable to assume the $\delta = 3.5$ size distribution approximately holds for the larger bodies as well.

The total surface area for a particle size distribution is determined primarily by the radius of the smallest particles:

$$S_{\rm total} = \int n(a)\pi a^2\, da \propto \int a^{2-\delta}\, da$$

where $S_{\rm total}$ is the total surface area, and $a_{\rm min}$ and $a_{\rm max}$ are the radii of the smallest and largest particles in the distribution, respectively. For $\delta = 3.5$, this becomes

$$S_{\rm total} \propto \left(\frac{1}{(a_{\rm min})^{1/2}} - \frac{1}{(a_{\rm max})^{1/2}} \right).$$

Assuming $a_{\rm max} \gg a_{\rm min}$, the total surface area is proportional to $\left(1/(a_{\rm min})^{1/2}\right)$.

If $a_{\rm min}$ is assumed to be 0.01μm, a balance between the minimum radii found for graphites and silicates in the ISM (Mathis, Rumpl, and Nordsieck, 1977), 90% of the surface area of the entire distribution will be contained in particles up to 1 μm in radius, 97% in particles with radii up to 10 μm. *Clearly, the continuum emission from solid bodies in evolved circumstellar disks will arise primarily from dust particles in the disk.*

Step back a minute and reflect on how all this relates to the research under consideration. We want to observe continuum radiation from circumstellar disks, to monitor the dust population as a function of stellar age and spectral type. Given the power law size distribution of particles in the disk, the calculated

number of grains depends strongly on the choice of a minimum grain radius. The most relevant arguments follow.

The conditions in a disk are not the same as in the ISM. Radiation pressure from the central star can remove small particles near the star ("radiation blowout"). To evaluate the effect of stellar radiation, consider first the simplistic situation in which a particle is at rest with respect to a solar-type star. How small a particle can withstand the star's radiation field? Balancing the Sun's radiation pressure at distance r with the gravitational pull of the Sun, we get:

$$\frac{L_\odot}{4\pi r^2}\frac{\pi a^2}{c}Q_{\rm pr} = \frac{GM_\odot}{r^2}\frac{4}{3}\pi a^3\rho$$

where a is the radius of the particle, r is the distance from the star, $Q_{\rm pr}$ is the pressure efficiency factor, and ρ is the density of the grain. Note the distance from the star cancels out of the equation. Assuming a particle density of 3 g cm^{-3}, and a perfect efficiency ($Q_{\rm pr} = 1$), the radiation pressure and gravitational forces balance for a 0.2 μm particle.

Burns, Lamy and Soter (1979) calculated the radiation forces on small particles in the solar system in great detail, and found that for iron, magnetite, and graphite particles, the radiation force exceeded the gravitational force for only for a narrow size range of particles, centered about a radius of 0.1 μm. For obsidian, amorphous quartz, basalt, and water ice, the radiation pressure force never exceeded the gravitational force. Although at first glance one would think that very small grains should be easily blown out by stellar radiation, small grains do not absorb the stellar radiation very efficiently, and are therefore poorly coupled to the stellar radiation field. The authors note the solar wind may be more effective at removing smaller particles from the region.

Assuming the stellar wind is effective in removing small particles, it is reasonable to assume there should be few particles with radii ≤ 0.2 microns.

Another approach is to consider a two-component particle distribution, allowing for a gap in particles with radii near 0.1 microns; this would complicate models.

Now consider how the choice of a particle size distribution affects disk models. A power law particle size distribution is not trivial to incorporate, and complicates interpretation of results. A simpler approach is to assume all the disk emission arises from particles having a uniform size distribution. The model presented in this work uses this simplification.

The choice of too small a representative grain size could lead to claims that we are sensitive to an unrealistically small amount of mass in dust. In addition, opacities become more complicated for very small grains. In light of all the considerations discussed thus far, a somewhat conservative grain radius of 1 μm was adopted throughout this work.

1.5.2 What We Can Learn from Studying Dust Emission in Disks

In the previous subsection, it was shown that most of the surface area in a circumstellar disk is contained in the small particles. It follows that *any observed continuum emission from evolved disks arises primarily from dust.* The large bodies do not possess enough surface area to be directly detected by ground-based equipment at this time.

We wish to determine the evolution of disks by observing how the continuum emission from star–disk systems evolves with stellar age. In doing so, we are really studying the evolution of the dust population in the disk. In other words, *the most basic science we can derive from this study is some understanding of the effectiveness and timescales of processes which create or destroy dust in the disks.*

During the epoch of planetary formation, the primary sources of dust are collisions between larger bodies, infall from an outer, remnant disk, and evaporation of cometesimals. The primary means of removal ("sinks") are

agglomeration into larger bodies, Poynting-Robertson (radiation) drag, and accretion onto the star. These sinks and sources will be discussed in the following subsections.

1.5.3 Mechanisms for Removal of Dust in Circumstellar Disks

One of the fundamental means of removing small particles from the disk is by agglomeration into larger particles. Growth from micron-sized grains into even millimeter-sized grains reduces the surface area by a factor of 10^3.

Another primary mechanism is accretion of small particles onto the star. Initially accretion results mostly from disk viscosity. In a very young disk, large infrared excess emission has been attributed to both accretion and reprocessing of dust (see, for example, the work of Kenyon and Hartmann, 1987, and references within).

Once the disk becomes radially optically thin, viscous accretion dwindles, but Poynting-Robertson (radiation) drag becomes extremely effective; it can remove all 1μm-radius grains within 1 AU of a 1 $L_\odot$ central star in about 10^3 yr, if there is no source of new small grains to replace those which have been removed. Larger grains require more time for removal, as do particles farther from the star. The timescale for removal can be computed as follows:

$$\tau = 10^3 \text{ yr} \left(\frac{a}{1\,\mu\text{m}} \right) \left(\frac{\rho}{1\,\text{g cm}^{-3}} \right) \left(\frac{R_i}{1\,\text{AU}} \right)^2 \left(\frac{L_\odot}{L_*} \right)$$

where τ is the time required for the body of radius a and density ρ, at an initial distance from the star of R_i, to accrete onto the central star having luminosity L_*. Since the removal time scales linearly with grain radius, it would take 10^6 yrs to remove all mm-radius particles from the inner 1 AU of a disk surrounding a 1 $L_\odot$ star.

As stated in the previous section, observational studies have determined that disk accretion signatures disappear by an age of about 10^6 yr, and the innermost

regions of the disks become optically thin by an age of about 3×10^6 yr. No optically thick near-infrared excess emission, which would indicate warm material near the star, is seen after an age of 3×10^6 yr (K. Strom *et al.*, 1989). Apparently particle growth and radiation drag have already played a major role in reducing the number of small particles in the inner disk by this age, lowering the emitting surface area of the disk. More sensitive studies may be able to discern weak infrared disk emission. Regardless, *unless there is a source of new small particles, near-infrared disk continuum emission should be quite weak after* 3×10^6 *yr.*

Remember, radiation drag becomes so efficient that unless there is a source of new small particles, all particles with radii of about 1 micron will be eliminated in a mere 10^3 years after the disk becomes radially optically thin. This is useful, as the level of near-infrared continuum emission as a function of disk age can thus be used to place constraints on sources of dust production in the disks.

1.5.4 Mechanisms That Generate Dust in Circumstellar Disks

There are three primary sources of dust production in optically thin circumstellar disks: collisions of planetesimals, infall from an outer, remnant disk, and evaporation of cometesimals. A brief overview is given here; the topic will be discussed in more detail in the discussion portion (Chapter 5) of this dissertation.

The first possible source of dust production is collisions between larger bodies. Two factors can produce collisions.

First, although most of the planetesimals will follow nearly circular orbits, the disk is not perfectly flat, and many of the orbits will be inclined to the disk midplane. Collisions are most likely to occur where the inclined orbits cross the midplane, which happens twice per orbit.

Secondly, once planetary embryos are formed, they gravitationally stir smaller bodies. The result is many smaller bodies with non-circular orbits and high relative velocities. These non-circular orbits may cross those of bodies in circular orbits.

Collisions having sufficient energy can produce fractionation; it requires about 2 eV to break a single chemical bond. The amount of dust generated by collisions is a matter of the size and relative velocities of the initial bodies, and also the material of which they are formed. Collisions may simply erode the larger body, or completely shatter it. If the larger of the two bodies has sufficient surface gravity, most dust generated in a collision will not escape to become disk debris, but will simply return to the surface of the larger body.

The collisional erosion process continues with successive generations of fragments; collision products will be ground into progressively smaller bodies. A steady-state distribution of masses of particles in collision (up to 1mm in radius) produces a particle size distribution of approximately $n(a) \propto a^{-3.5}$, where a is the particle radius, and $n(a)$ is the number of particles with radius a (Dohnanyi, 1969; see also Witteborn *et al.*, 1982).

The details of collisional generation of dust are quite complex; scientists have studied the problem in relation to the formation and evolution of the asteroid belt. Some studies involved laboratory apparatus which produced controlled collisions, with appropriate analysis of byproducts. Other studies have been more theoretical in nature, using the experimental results to constrain the theories. Some of the primary work in this field was performed in the 1960's by authors such as Gault and colleagues (Gault and Wedekind, 1969; Gault, Shoemaker, and Moore, 1963; and Dohnanyi, 1969).

Without going into mathematical detail here, cratering evidence on the Moon and other terrestrial bodies in our solar system suggest a period of heavy bombardment lasting as long as 1 billion years. Although the moon has enough surface gravity to retain most dust generated by collisions on its surface, the craters imply there were numerous km-sized planetesimals in the early solar system. Collisions between these smaller bodies may have generated significant

amounts of dust during the period of heavy bombardment. If a similar period is common around other young stars, such collisions may produce detectable levels of dust for hundreds of millions of years.

As an aside, note that it is difficult to theoretically predict dust levels resulting from collisions in the late stages of disk evolution. Recall the method for this epoch of planetary formation requires following each individual particle in the simulation (Section 1.2.4). Extending the particle sizes in the model downward to dust dimensions increases the number of particles to prohibitive values. Somewhat simpler mathematical predictions will be presented in Chapter 5.

After collisions, the second likely source of dust is an outer, remnant disk. Observations of the earliest stages of disks suggest initial sizes as large as hundreds of AU, implying a reservoir of material at large disk radii (Skrutskie *et al.*, 1993). The existence of the Oort cloud is evidence that material at large disk radii may persist into the main sequence stage. Poynting-Robertson (radiation) drag can draw this outer, remnant material into the inner disk regions. On the other hand, it is conceivable that a "Jupiter" could transfer angular momentum to particles at larger disk radii, preventing the particles from reaching the terrestrial planet region. An analogy is the "shepherding satellites" discovered in Saturn's rings.

The third source is evaporation of cometesimals. At the time the Jovian planets were forming, there were many icy planetesimals. Perturbations in the orbits of these planetesimals caused some to be ejected from the solar system, or shifted into cometary orbits. As a result, the cometary flux at that time was much larger than it is today. In addition to providing volatiles for the terrestrial planets, the cometesimals released dust into the inner disk region.

The rate at which these three processes produce small particles and the size distribution of the resulting bodies is known in only the crudest sense. The available information will be discussed in more detail in Chapter 5. The point the

reader should come away with is that there *are* processes occurring in the disk which may produce significant amounts of dust for hundreds of millions of years. One can model the processes and make predictions, but the bottom line is that the dust is the only component of the disk in the late stages of evolution which is observable with relative ease, and the only way to determine (or constrain) the evolution of the dust population in the era of planetary formation is to go out and look for dust signatures associated with stars having ages up to a few hundred million years. That is exactly what we aim to do.

1.6 Summary and Statement of Research Presented

Much work has been done in the past 20 years to advance our knowledge of the process by which our solar system formed. We believe planetary systems form by agglomeration of material within circumstellar disks; the disks are a natural byproduct of star formation.

Some of our knowledge has come through scrutiny of the geological record in our own solar system, an approach which looks backward in time. Some has come from the observation of other young stars which are at the age when they may be forming planetary systems. Actual planetary formation cannot be viewed directly, due to obscuration, lack of angular resolution, and dynamical range difficulties. As a result, much of our understanding is inferred from our assumptions of the physical processes occurring, and observable effects we attribute to these processes.

We observe thermal and accretion emission from circumstellar material, and have determined that the material must lie in a flattened structure, such as a disk. Outflows in young stars ($< 10^7$ yr) have been observed directly in some cases, and inferred in many others. The outflow diagnostics are correlated with strong thermal ("reprocessing") and accretion signatures.

Observations in Taurus-Auriga show that by an age of about 3×10^6 yr, the innermost region (within about 1 AU) of circumstellar disks around solar-type stars becomes optically thin (K. Strom *et al.*, 1989). The infrared excess thermal emission fades as the particle surface area in the disk diminishes. Planetary formation, if any is to occur, is underway by this age.

Three possible cases of disks with inner "holes" have been found around solar-type stars. It is possible these represent a transition stage in disk evolution, in which the inner regions of the disk are the first to clear or build large particles. If so, the transition must be rapid, to account for the very few such cases observed.

Evidence for tenuous cool material at large disk radii ($\geq$ 100 AU) persists for a longer period of time, into the main sequence stage.

Although there have been numerous observational studies of circumstellar disks, most have focused on the early stages of disk evolution, when disk processes produce strong signatures. Observations of the later stages of disk evolution, when the planets are forming, are far more difficult due to the weak signatures of the processes underway. As the disk evolves, small particles are removed by agglomeration, radiation drag, radiation blowout, and the solar wind. The small particles comprise most of the solid surface area in the disk, and thus thermal continuum emission decreases with disk age. When the disk becomes optically thin, wind and accretion signatures disappear. Although there should be 100 times more mass in gas than dust, even in the earliest stages of disk evolution it is difficult to obtain observations of the gas owing to confusion with ambient material and small beam-filling factors. The evolution of the gas is still one of the greatest mysteries of disk evolution.

Owing to the difficulty of observations, there is little observational information on the late stages of disk evolution, including the epoch of planetary formation. One expects the disk to contain dust, gas, ice particles, and larger bodies created

from these. Thermal emission from warm dust near the star is the easiest disk component to detect.

A quick and dirty calculation illustrates the detectability of dust. Material in the disk is heated by the central star; material closest to the star is warmest, and emits the most flux per unit surface area. Assuming a grain radius of 1 μm, density $\rho = 3$ g cm^{-3}, and grain emission efficiency $Q = 0.3$, a simple blackbody calculation reveals that approximately 10^{20} g of 1000 K dust grains will produce a flux equal to 10% of the photospheric flux of a 5800 K central star at wavelength of 3 μm. (3 μm is the wavelength of peak flux for a 1000 K grain.) A 10% excess is readily detectable for many young nearby stars, using small-aperture single-channel broadband photometry. As will be shown in the next chapter, a 1000 K dust temperature corresponds roughly to a distance of 0.1 AU from a 5800 K central star. The mass in dust is that of a typical asteroid!

Previous work was either not sufficiently sensitive or accurate enough to detect tenuous dust in the inner disk. Young stars are known to be variable, presumably owing to starspots, or for very young stars, due to variations in accretion rates. If continuum measurements at different wavelengths are made over a period of time in which the overall stellar flux changes, the resulting spectral energy distribution may mimic an infrared excess (or depletion, which is physically impossible). As a result, *simultaneous measurements are required to detect emission from tenuous dust.* Many of the previous observations were not simultaneous for all wavelengths.

Observations of dust emission arising from the inner disk as a function of stellar age and spectral type provide important constraints on dust-producing processes in the disk. Once the disk becomes optically thin, radiation drag becomes extremely efficient at removing small particles from the inner disk; it can remove all 1μm particles within 1 AU of a 1 $L_\odot$ star in about 10^3 yr, if there is no source of new particles. Radiation blowout can remove particles smaller than

about 0.5 μm, and small particles will combine to form larger particles. With such effective mechanisms for removing small particles, surface area in the disk, and the resulting continuum emission, should decline rapidly *unless* there are sufficient mechanisms to replenish the dust population. Processes which generate dust include collisions of planetesimals, infall from outer disk regions, and evaporation of cometesimals.

We will use the evolution of dust in the terrestrial planet region as a tracer of processes occurring in the disk. Given the evidence in our own solar system of a period of "heavy bombardment" lasting about 1 billion years, it is very possible that tenuous dust signatures may be observable around other stars for several hundred million years, into the early main sequence stage. Dust produced by collisions between the numerous planetesimals in that epoch may repopulate the disk with small particles.

Our approach makes use of the fact that dust in the terrestrial planet region emits primarily in the near-infrared, where "windows" in atmospheric absorption make sensitive ground-based observations possible. In addition to the high atmospheric transparency at near-infrared wavelengths, a large fraction of the disk emission may occur at these wavelengths. Depending on the steepness of the disk mass surface density law, most of the dust emission in the disk may arise from the inner few AU of the disk, despite the larger surface area of the outer regions of the disk, simply because dust luminosity scales as T^4.

The epoch of interest ranges from the age disks first become optically thin, through the period for which sufficiently high collision rates of leftover planetesimals may generate detectable levels of dust. Cluster stars were observed, as it is easier to determine the ages of clusters than of isolated stars. The details behind the choice of specific clusters is discussed in the next chapter.

This work presents sensitive, simultaneous, single-channel ground-based near-infrared broadband measurements (primarily $1.25 - 3.5\mu$m) obtained for pre-main sequence and young main sequence stars in nearby clusters having ages from about 1 Myr to 600 Myr, covering a broad range of spectral types. The clusters are the Taurus-Auriga complex (1-10 Myr), Alpha Perseus (20-80 Myr), the Pleiades (70 Myr), the Ursa Major Stream (300 Myr), the Hyades (600-670 Myr), and Praesepe (600-760 Myr). Near-infrared color excesses are used to diagnose thermal emission from warm dust; models of dust emission arising from thin disks are used to interpret the observations. The observations are sensitive enough to detect about 10^{20}g of material in micron-sized dust grains within 3 AU of the central star. The wavelengths of observation were chosen to maximize the efficiency with which dust emission can be detected, taking into consideration the dust emission itself, the transparency of the atmosphere, the ambient thermal background emission, and the sensitivity of available detectors. The following chapter details the method. No conclusive evidence of excess emission is found past an age of approximately 3×10^6 yr. This work pushes the limit of our ability to observe the signatures of planetary formation using ground-based telescopes.

Chapter 2

METHOD

2.1 Introduction

The goal of this work is to examine the evolution of the dust population in circumstellar disks, during the epoch of presumed planetary formation. Dust may be detected either by its continuum emission, or by spectral lines of materials such as silicates. As it is desirable to examine a large enough sample of stars to provide significant statistics on the dust population as a function of stellar age and spectral type, an efficient algorithm for detecting tenuous dust is required. Broadband continuum measurements require less integration time than spectral line observations, and are thus more time efficient, and also more sensitive to tenuous dust emission. Continuum observations are therefore the method of choice for this project.

This chapter discusses the characteristics of dust continuum emission, the method chosen to detect dust, the disk region to which the method is sensitive, and the sample of stars chosen for the study. (The model used to estimate the mass in dust based on the detected dust emission is discussed in Chapter 4 and Appendix C.)

2.2 The Concept

Young stars with disks are sufficiently distant that we observe them as point sources; we see the combined stellar and disk radiation. A general discussion of the

expected continuum emission from a star–disk system is presented in this section, without getting too involved in specific details. This will lead into the basic concept of how dust emission can be detected.

2.2.1 Sources of Radiation

There are two sources of flux in a star–disk system; the star and the disk. Consider first the contribution from the star alone. The photospheric spectral energy distributions (SEDs) of stars as a function of spectral type are fairly well known over a large range of wavelengths. (A spectral energy distribution is simply how flux varies with wavelength.) For most stars, the SED can be approximated by that of a blackbody with some "effective" temperature. The more massive the star, the hotter the effective temperature, and the shorter the wavelength of peak emission. The expected emission from the star can be determined from its effective temperature, and its surface area.

Now consider the contribution of the dust component. A circumstellar disk is, of course, composed of individual particles. The particles are heated by the central star, then re-radiate at their equilibrium temperature. (This is often referred to as "reprocessing" of starlight.) In the simplest case, the particles can be treated as blackbodies. Particles near the star are hotter, and thus radiate primarily at shorter wavelengths as compared to particles farther out in the disk. To obtain the total emission from the dust, one must sum the contributions from successive disk annuli (the temperature gradient is only a function of disk radius). Knowing the particle surface area and the temperature within each disk annulus, the total dust emission can be determined.

The observed spectral energy distribution is the sum of the stellar and particle emission.

2.2.2 Calculating Dust Temperatures

As stated in the previous section, there is a temperature gradient in the disk. Material near the star is hotter. Approximate dust temperatures may be determined from a simple equilibrium calculation:

$$\text{Energy absorbed by grain} = \text{Energy emitted by grain.}$$

Consider the case of an optically thin disk; each grain is heated by stellar radiation, not re-radiation by other grains. For the sake of simplicity, first assume that the grains act as perfect blackbodies. The energy absorbed by a grain is simply the stellar energy flux at the distance of the grain from the star, multiplied by the cross-sectional area of the grain:

$$\text{Energy absorbed by grain} = \left(\frac{L_*}{4\pi R^2}\right)\left(\pi a^2\right), \tag{2.1}$$

where L_* is the luminosity of the central star, R is the distance from the star to the dust grain, and a is the radius of the dust grain.

For a blackbody, the flux emitted per unit surface area is given by the familiar Stefan-Boltzmann law, so that the energy emitted from a single grain is

$$\text{Energy emitted} = 4\pi a^2 \sigma T_d^4, \tag{2.2}$$

where σ is the Stefan-Boltzmann constant, and T_d is the temperature of the dust grain (in Kelvin). Equating Expressions 2.1 and 2.2 yields a grain temperature of

$$T_d = \left(\frac{L_*}{16\pi\sigma R^2}\right)^{1/4}, \tag{2.3}$$

where L_* is the luminosity of the central star. This can be rewritten as

$$T_d(K) = 280 \text{ K } \frac{(L_*/L_\odot)^{1/4}}{(R/(1 \text{ AU}))^{1/2}}. \tag{2.4}$$

One can easily see that a particle orbiting a 1 $L_\odot$ star at a distance of 0.1 AU will have a temperature of about 10^3 K, while a particle at 3 AU will have a temperature of about 200 K.

Thus far, we have only looked at the ideal case. In reality, the particles are not perfect blackbodies; particles do not efficiently absorb or emit wavelengths larger than their physical size. Dust grains are typically 0.01 to several microns in size. Since small grains are generally cleared from circumstellar disks in short timescales, this work focuses on grains approximately one micron in size. In this simplistic case, stellar radiation, which peaks in the optical, has wavelengths smaller than the grain sizes; it will be assumed the grains absorb like perfect blackbodies.

The situation is not as simple for dust emission. Consider a dust grain orbiting the Sun near the Earth. The temperature of the Earth is roughly 300 K, with a peak emission at about 10 microns. This is comparable to or larger than the size of a typical dust grain. One must therefore take into account grain emission efficiencies when calculating the energy emitted by a grain.

The total energy emitted by the grain is the surface area of the grain multiplied by the flux per unit surface area:

$$\text{Energy emitted by grain} = 4\pi^2 a^2 \int_0^\infty B_\lambda(T_d) Q(\lambda) d\lambda, \tag{2.5}$$

where a is the particle radius, $B_\lambda(T_d)$ is the Planck function, and $Q(\lambda)$ is the particle emission efficiency law. This expression is not easily evaluated in general; it is useful to look at the trivial case in which the particles emit as perfect blackbodies, which gives a lower limit for the temperature of small grains.

The far-infrared opacity law for interstellar graphite and silicate grains is $Q \propto a/\lambda^2$ (Drain and Lee, 1984). Beckwith *et al.* (1990) examined grain opacity in

circumstellar disks in Taurus-Auriga, and found the calculations of Drain and Lee to be inadequate. They found a dust opacity decaying only as $\kappa \propto a/\lambda$, which may be a result of the different grain environment. Although the the Beckwith *et al.* opacity law is stated for wavelengths greater than 30 μm, it is the only observational measure of grain opacities in circumstellar disks, and is therefore adopted here. The grain emission efficiency assumed in this work is:

$$Q(\lambda) = \frac{1}{1 + \lambda/2a}. \tag{2.6}$$

Note that when $\lambda \ll 2a$, $Q \approx 1$.

To put this in perspective, dust grains in the terrestrial planet region (within a few AU of the star) have temperatures ranging from approximately 200-1500 K. A 200 K particle has a peak emission at 15 microns; the emission efficiency will be better than 0.8 for 200 K particles with radii larger than about 30 microns. A 1500 K particle has a peak emission at 2 microns; the emission efficiency will be better than 0.8 for 1500 K particles with radii larger than 4 microns.

As particles with radii smaller than 4 microns may constitute most of the surface area in the disk, the grain emission efficiency will certainly be an issue. The efficiency will be most important for cooler grains farther from the central star. Note that grains emit most of their energy in the near-infrared.

Getting back to the issue of determining the emission of the disk as a whole, assume for simplicity that all grains in the disk have a predetermined common size. In this case, grain temperature is only a function of distance from the central star. Consider the disk to be composed of concentric annuli; the total disk emission can be calculated knowing the grain temperature and total surface area in each annulus. This will be more clearly demonstrated in the next subsection.

2.2.3 Combined Star and Disk Emission

For a star at a distance of 100 pc, typical of the stars used in this study, 1″ on the sky corresponds to 100 AU in the star–disk system. Standard single-channel observations with beamsizes of several arcsec thus yield a composite SED of both stellar and dust emission. Figure 2.1(a) illustrates the composite SED of a 6000 K star having a dust ring at approximately 3 AU, with an equilibrium temperature of 200 K, and the dust emission efficiency law given in Equation 2.6. (For the purpose of illustration, the surface area of the dust is 50,000 times that of the 6000 K central star. Flux units are arbitrary.) Centers of the standard infrared broadband filters J (1.25 μm), K (2.2 μm), L (3.45 μm), M (4.8 μm) and N (10.0 μm) are noted. (As an historical note, these seemingly odd bandpasses are chosen to match wavelength regions for which the infrared transparency of the Earth's atmosphere is very high. These regions are commonly called "windows" in the atmosphere.) Note in Figure 2.1 the contribution from dust appears longward of 10 μm; the slope of the SED is photospheric until 10 μm.

Figure 2.1(b) illustrates the composite spectrum of a the same star with a dust ring at about 0.1 AU. The equilibrium temperature of the dust is 1000 K. The centers of the standard broadband filters are again marked. (For the purpose of illustration, the surface area of the dust is 2000 times that of the 6000 K central star.) This time, the contribution from dust is seen longward of about 1.6 μm. Note that the slope of the SED beyond 1 or 2 microns is no longer photospheric; the slope between, for example, J and K or J and L is shallower than that of the underlying photosphere.

A complete disk may be thought of as a superposition of concentric rings. The bottom frame of Figure 2.2 (from K. Strom *et al.*, 1989, and Skrutskie *et al.*, 1990) displays the SED of AA Tau, which appears to be surrounded by an optically thick disk. The dotted line indicates the expected photospheric emission for a star of

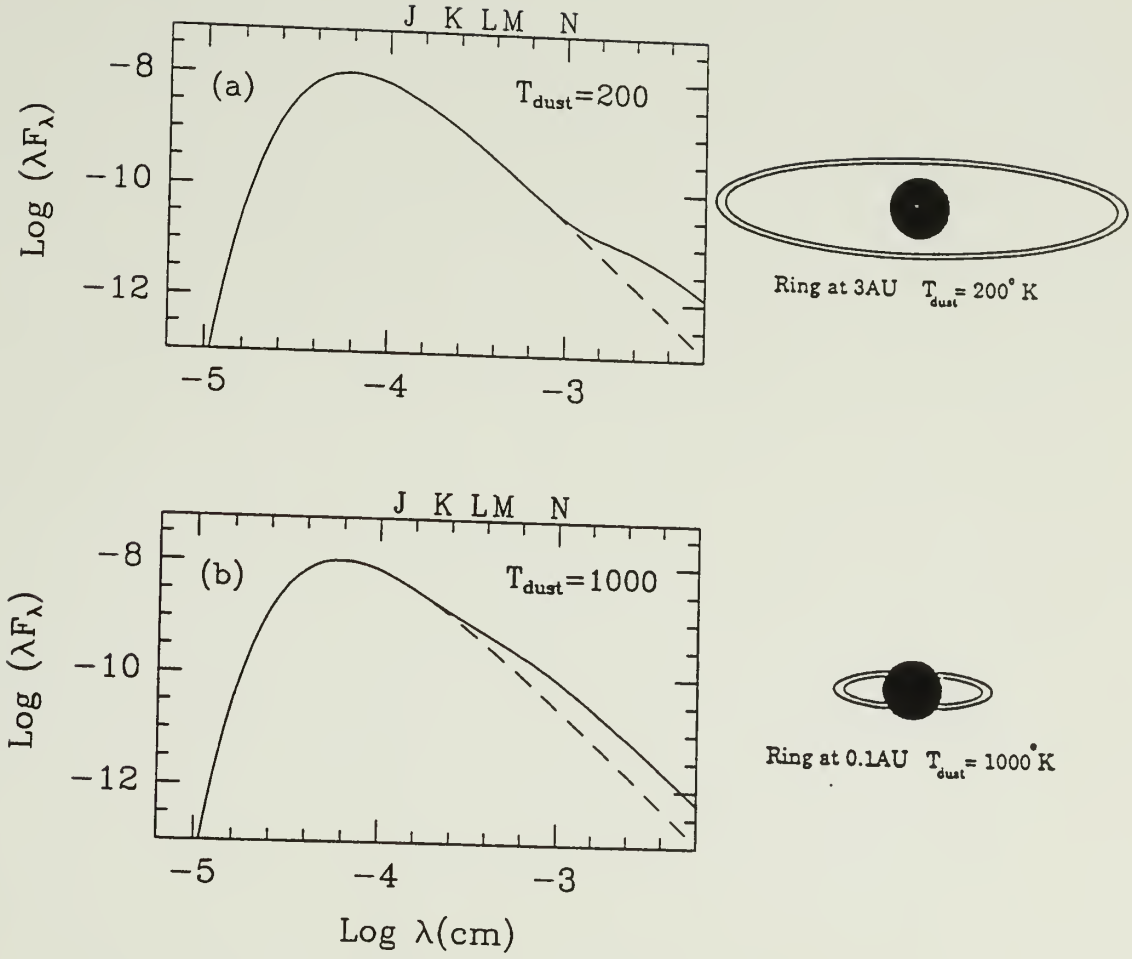

Figure 2.1. The concept. Model spectral energy distributions resulting from dust rings at two different radii. The dashed lines represent stellar emission, solid lines the sum of star plus dust. The dust emission efficiency assumed is given in Equation 2.6; the radii of the rings are approximate. *(a)* 6000 K star plus 1000 K dust ring. *(b)* 6000 K star plus 200 K dust ring. Flux units are arbitrary.

this spectral type at the distance of Taurus-Auriga. The solid line denotes the Kenyon and Hartmann (1987) prediction for a flat, optically thick reprocessing dust disk (at an inclination of $i = 60°$) surrounding the star. Points lying above this line imply additional accretion luminosity or a different geometry. Filled circles denote measured broadband fluxes. All the broadband fluxes exceed those expected for an optically thick reprocessing dust disk, diagnosing an optically thick disk extending to the surface of the star. The slope of the observed SED longward of 1 μm is clearly shallower than that of the underlying photosphere.

Consider one additional case: a disk with an inner "hole". The top frame of Figure 2.2 (from K. Strom *et al.*, 1989, and Skrutskie *et al.*, 1990) displays the SED of V819 Tau. The dotted line again indicates the expected photospheric emission. The solid line denotes the Kenyon and Hartmann prediction for an optically thick reprocessing disk surrounding the star. Filled circles represent measured broadband fluxes; J, K and L, M and N are marked. Filled circles lying between the dashed and solid lines represent optically *thin* emission. The observed SED of V819 Tau indicates optically thin emission out to about 10 μm, but optically thick emission longward of 25 μm or so. The observations suggest an optically thick outer disk, with little or no material in the inner disk; in other words, a disk with a "hole" in the center. Notice in particular the rising slope of the SED longward of 10 μm. (As a word of caution regarding this interpretation, note that a background source could produce the observed excess emission at the longest wavelengths.)

2.2.4 Detection of Dust

As illustrated in Figures 2.1 and 2.2, one can detect warm dust by the changes it produces in the *slope* of the observed SED. Warm dust close to the star creates a composite SED with a shallower slope than that of the underlying photosphere at near-infrared wavelengths (1-5 μm). Cooler dust farther from the star affects the

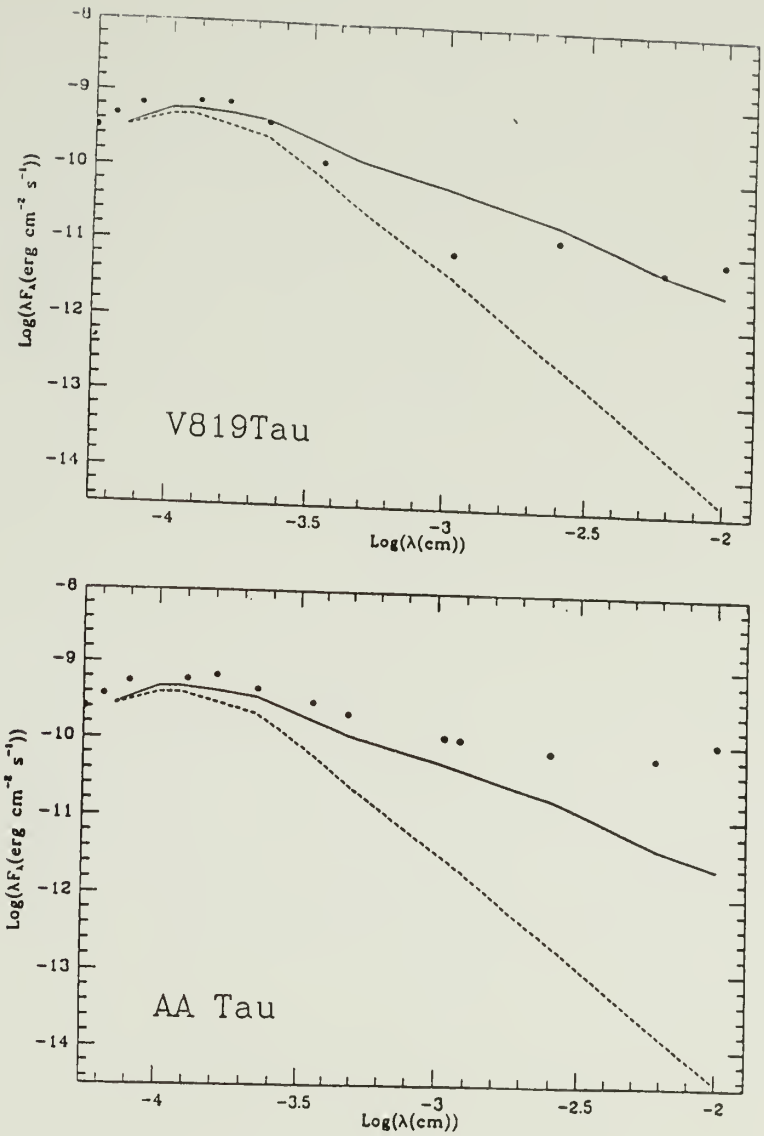

Figure 2.2. Observed SEDs of AA Tau and V819 Tau. Model and observed fluxes for two pre-main sequence stars in Taurus Auriga (from K. Strom *et al.*, 1989, and Skrutskie *et al.*, 1990). Filled circles denote observed broadband fluxes; dashed lines represent expected photospheric fluxes. Solid lines represent the expected emission from the star plus optically thick, flat, reprocessing disk ($i = 60°$). *(Top)* The observed SED for AA Tau lies above that of the predicted thick disk plus star spectrum at all wavelengths $\lambda > 1.2\mu$m, diagnostic of an optically thick disk extending to the surface of the star. *(Bottom)* The observed spectrum for V819 Tau lies *below* the thick disk plus star spectrum at wavelengths between 2.2μm and 25μm, and above at longer wavelengths. These data suggest that the *inner* disk of V819 Tau is optically thin, while the outer disk is optically thick.

slope of the SED at longer wavelengths (beyond 10 μm). A rising slope or a decrease in slope at only longer wavelengths may be diagnostic of an inner "hole" in the disk.

This method does not give information on the geometry of the warm dust near the star; it does not prove that the dust is in a disk rather than a spherical shell. The assumption that the dust lies in a disk is derived from observations of pre-main sequence stars, as discussed in Chapter 1.

One important note: if a star is variable, *simultaneous measurements are needed to detect weak excess emission.* For example, if J and K measurements were made one night, while L observations were made on another night when the star was brighter, the observed SED would have a shallower slope than the true SED at these wavelengths, mimicking a star with an infrared excess. Since it is not always known whether or not a star is variable, it is safest to acquire simultaneous measurements for each source.

2.3 Wavelengths of Observation for This Study

The goal of this project is to determine how excess radiation arising from circumstellar dust disks evolves with time, as a function of the spectral type of the central star. Excess radiation can be detected by the changes it produces in the slope of the observed SED as compared to the expected stellar SED. The shape of the SED can be determined by obtaining broadband continuum measurements. The issue now is to decide on the range of wavelengths to observe. Although it is always desirable to obtain as much information as possible for a given source, the need for efficiency urges one to observe as few wavelengths as possible, while maintaining a high likelihood for detecting any tenuous dust.

The standard optical and infrared broadband filter set is UBVRIJKLL'MNQ (0.36-20 μm); one may also obtain radio observations at mm or cm wavelengths.

To achieve adequate statistics on the evolution of dust with time as a function of the spectral type of the central star, at least 50 stars should be observed, preferably more. Also, detection of tenuous dust disks requires high precision measurements. Without trimming the observations to a minimum, the program would require more observing time than is feasible.

This section discusses the issues concerning the choice of wavelengths of observation, the wavelengths finally chosen for this study, and the limitations this choice places on the study.

2.3.1 Long-Wavelength Limit

It was seen in the previous section that dust emission affects the observed SED of a star–disk system longward of about 1-2 microns for the warmest dust, and longward of 10 microns or more for cooler dust. The longer the maximum wavelength of this study, the larger the region of the disk to which the study will be sensitive (cooler material resides at larger disk radii). However, the integration times required to obtain high-precision measurements become impractical beyond some point, defining a reasonable long-wavelength limit for this study.

The sensitivity to which one can detect dust emission is determined by the precision to which one can observe photospheric emission. In practice, at infrared wavelengths the highest precision achievable is roughly 1–2% internal precision, for ground-based work. The time required to reach this level of sensitivity increases with wavelength, owing to the transparency of the atmosphere, and thermal background emission.

Consider that a 300 K blackbody has its peak emission at 10 μm. The telescope, optics, and water vapor in the atmosphere, all of which are nearly 300 K blackbodies, produce a 10 μm flux at the detector which is many orders of magnitude larger than that received from the star of interest. Distinguishing the

stellar radiation from this enormous "background" requires long integration times. The background radiation rises steeply at wavelengths longer than about 3 μm; the required integration time increases longward of this. Figure 2.3 (from Skrutskie *et al.*, 1990) shows the 5σ sensitivity limits for one hour of integration at NASA's Infrared Telescope Facility (IRTF), and for the Infrared Astronomical Satellite (IRAS). (A 5σ sensitivity implies one can detect signals 5 times stronger than the sky fluctuations; this provides a $> 99\%$ confidence level that the detection is valid.) Also shown is the spectral energy distribution of an M0 pre-main sequence star at the distance of the Taurus-Auriga complex, and the combined SED for this star surrounded by an optically thick, flat reprocessing disk.

It can be seen from Figure 2.3 that one cannot detect the photospheres of late-type stars at a distance of about 150 pc in one hour of integration beyond a wavelength of about 10 μm. Although not shown, measurements at mm and cm wavelengths are much less sensitive to photospheric emission than infrared ground-based observations.

A 5σ detection is not a precise measurement; for this project, we desire sensitive observations of 50–100σ. Since it is desirable to observe at least 50 stars in this study, if not more, the integration times must be limited to half an hour when at all possible, 1 hour at most. The longest wavelength at which photospheric emission can be precisely detected for most members of relatively nearby clusters in 0.5 hour of integration time is 3.45-3.80 μm (L and L′). Given these time and sensitivity restrictions, L and L′ have been chosen as the standard long-wavelength limit.

The IRTF L′ filter is matched to a wavelength region for which the atmospheric transmission is "cleaner" than at L and is also less sensitive to changes in atmospheric water vapor content. Because of this, L′ (3.80 μm) will be

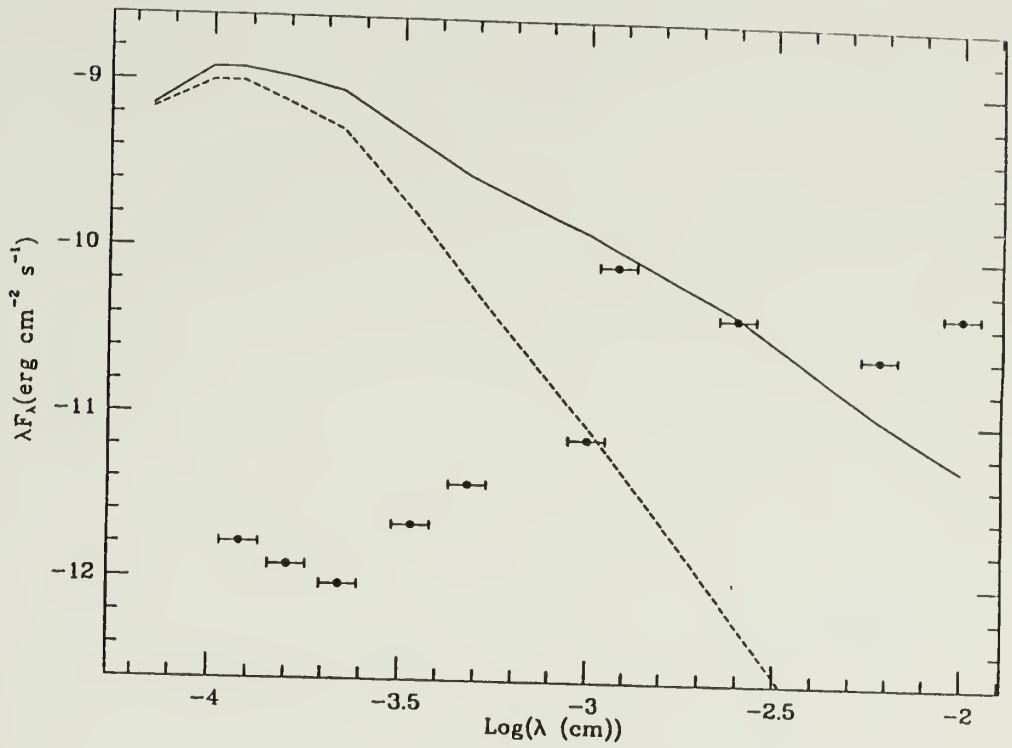

Figure 2.3. IRTF and IRAS sensitivity limits. Plot of the SED $\lambda F_\lambda vs. \lambda$ for a typical solar-type pre-main sequence star of spectral type M0 located at the distance of the Taurus-Auriga complex (dashed line). Superposed on this plot is the combined SED for this star surrounded by an optically thick, flat reprocessing disk (solid line). Also shown are the 5σ sensitivity limits achieved in 1 hour of integration on the NASA Infrared Telescope Facility ($1.6\mu\mathrm{m} \leq \lambda 10\mu\mathrm{m}$), and for *IRAS*. Note that the *IRAS* sensitivity limits lie at or above the level of excess radiation expected from a perfectly flat reprocessing disk. (From Skrutskie *et al.*, 1990).

the long-wavelength limit of choice at the IRTF. At other facilities, the standard L filter (3.45 μm) will be used.

A long wavelength cutoff of 3.5–3.8 microns limits the region of the disk to which this study is sensitive. Warm dust near the star produces a change in the slope of the SED at L and L′, but cool dust at larger radii does not (see Figure 2.1(b)). This study will not be sensitive to cool material more than about 3 AU from the central star. In other words, *this study is sensitive to material in the terrestrial planet region of the disk.* The work of Skrutskie *et al.* (1990) shows a strong correlation between 2.2 and 10 micron excess emission in circumstellar disks, which gives one some hope that much will not be lost in restricting this study to wavelengths shorter than 5 microns.

2.3.2 Short-Wavelength Limit

The next step is to decide upon the shortest wavelength for observations. To do this, it is necessary to determine the shortest wavelength at which the dust is expected to affect the observed SED of the star–disk system.

This study focuses on the late stages of disk evolution, after accretion signatures have disappeared and the disk is presumably no longer optically thick. At this time, little ultraviolet or optical excess emission is expected, in contrast with earlier stages in the formation of a protostar. Only dust reprocessing emission is expected.

Interstellar grains are known to be composed primarily of graphite and silicates (Drain and Lee, 1984). The temperature at which interstellar dust grains evaporate (the "dust destruction temperature") is $T = 1750$ K for graphite grains, $T = 1400$ K for silicate grains (private communication from Drain stated by Hillenbrand *et al.*, 1992). This corresponds to a peak dust emission at a wavelength of 1.7-2.1 μm. Although it is conceivable that large grains in a disk

near the star may survive longer, reaching higher temperatures, the dust destruction temperature represents a reasonable criterion for determining the shortest wavelengths at which dust emission will significantly alter the perceived SED of the central star.

Figure 2.4(a) illustrates the emission from a 6000 K blackbody plus a 1400 K blackbody; Figure 2.4(b) shows the same 6000 K blackbody combined with a 1750 K blackbody. In each figure the surface area of the cooler blackbody, which represents the dust, is 1200 times that of the 6000 K blackbody. The emission efficiency law given in Equation 2.6 was assumed, and the flux units are arbitrary. In the first figure, dust emission is seen longward of 1 μm, implying that observations at J (1.25 μm) still represent nearly photospheric emission. In the second figure, the 1750 K dust contributes noticeably beyond about 0.8 μm, and clearly contributes to emission at J. However, the slope of the SED between J, K and L is clearly non-photospheric. Note that a 3000 K blackbody has a peak emission of about 1 micron, implying the dust would have to be at least 3000 K for dust emission to mimic photospheric emission between 1-4 microns.

To facilitate detection of non-photospheric SEDs, it is desirable to obtain at least one measurement at a wavelength for which the observed emission is purely photospheric, or very nearly photospheric. Models by Kenyon and Hartmann predict that for disks undergoing both accretion and reprocessing, the wavelength at which the emission will be closest to photospheric emission is J (1.25 μm) (private communication). The preceding paragraph and Figures 2.4 demonstrate that for a purely reprocessing disk, measurements at J are nearly photospheric, except perhaps for the highest dust temperatures expected. (When evaluating the contribution from the highest dust temperatures, keep in mind that in Figures 2.4, the surface are of the dust has been scaled to 1200 times the surface area of the star. It is unlikely there will be that much hot dust near the star.)

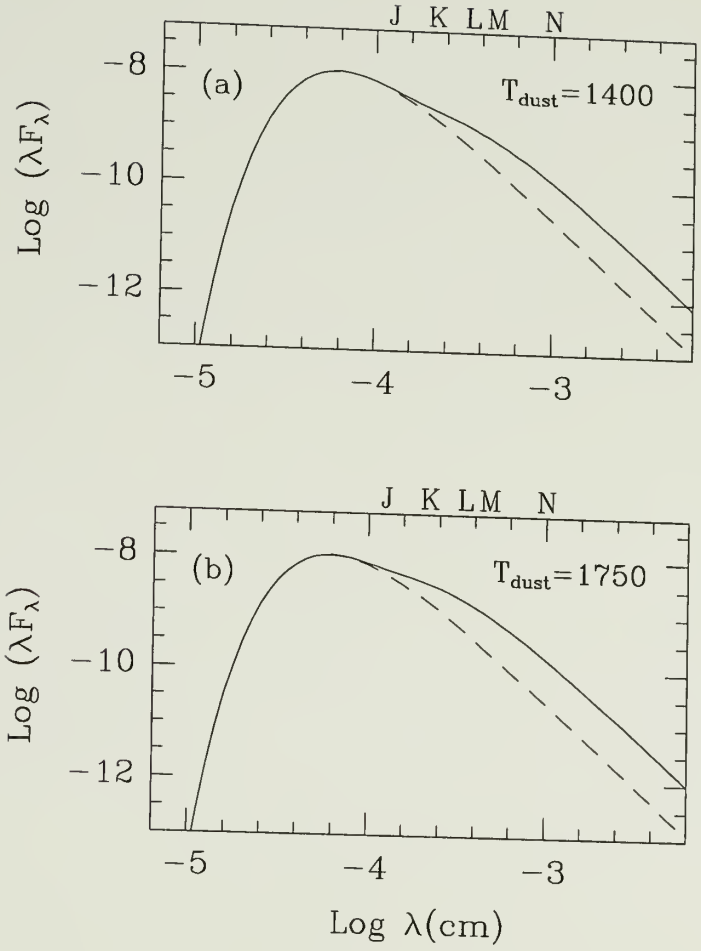

Figure 2.4. Dust destruction temperature SEDs. Model spectral energy distributions resulting from hot dust at two different evaporation temperatures. The dashed lines represent stellar emission, solid lines the sum of star plus dust. *(a)* 6000 K star plus 1400 K dust (silicate destruction temperature). *(b)* 6000 K star plus 1750 K dust (graphite destruction temperature). Flux units are arbitrary.

In picking a short-wavelength limit, there is one more consideration: the instruments needed to obtain the desired observations. An InSb detector, sensitive to 1–5μm emission, is suitable for observations at J, K and L. Observations at wavelengths shorter than J require a photomultiplier. The need for an additional instrument would reduce the efficiency of the program, and therefore the sample size.

The facts that dust emission produces a change in the observed slope of the SED beyond 1 micron, even for the hottest dust, and the need for an additional instrument to obtain measurements shortward of 1 micron, led us to choose J (1.25 μm) for the minimum wavelength of observation.

2.3.3 Wavelengths Chosen for This Project

To summarize, we wish to observe each star over the region in which dust excess emission produces a non-photospheric SED, while being efficient enough to obtain large sample statistics. J (1.25 μm) is most likely to represent the photospheric flux, with dust reprocessing emission occurring at longer wavelengths. Shorter wavelengths require a different detector, while measurements longward of about 3.5 μm require impractical integration times to achieve sufficient sensitivity to detect tenuous dust emission. In principle, one should be able to detect a warm dust excess with only three measurements, at J, K and L (or L′). *This investigation will therefore use these three wavelengths as the fundamental baseline for diagnosing thermal dust emission.*

Some bright stars (which require only short integration times), or stars for which an excess is strongly suspected, may be observed at longer wavelengths to gain information on cooler material. Unless a star seems particularly interesting, optical measurements will not be performed, since they require an additional detector, and should yield no additional information if J is photospheric.

Omission of simultaneous optical observations is admittedly a gamble. There is a possibility that J is not photospheric; the ability to perceive this would be lost without simultaneous optical data for these presumably variable sources. Unusually hot material near the star (> 3000 K) could result in a photospheric slope for the SED between J and K, or J and L. Lack of optical measurements would also eliminate the ability to determine the interstellar extinction to a star, if such information is not available in the literature.

We chose to take these risks, hoping the risks represent the exception, rather than the rule. We opted to maximize the sample of stars by minimizing our observations of each star to what we believe are the most likely wavelengths for detection of weak infrared dust emission. Minimizing the number of wavelengths observed also allows us to spend more time integrating on a given star, increasing our sensitivity to weak dust emission.

2.4 Diagnosing Excess Emission

Reprocessing emission from dust produces an apparent change in the slope of the observed SED of the central star. A shallower slope at near-infrared wavelengths is diagnostic of warm dust near the star. What is needed is a simple means of assessing the apparent change in slope of the SED, using only three broadband measurements (J, K and L) for each star.

First of all, one must devise a means to establish the slope of the SED of a stellar photosphere as a function of spectral type, using these three measurements. One of the easiest ways is to plot the flux ratios between the three wavelengths of observation. For example, one may plot

$$\frac{\text{Flux at J}}{\text{Flux at L}} \quad \textit{vs.} \quad \frac{\text{Flux at J}}{\text{Flux at K}}. \tag{2.7}$$

Since the flux ratios vary monochromatically with spectral type (at least for main sequence stars), such plots are a good means of quantifying photospheric SEDs.

In the near-infrared, it is customary to use magnitudes rather than absolute fluxes. Instead of examining flux ratios, one therefore looks at differences in magnitudes, or infrared *colors*. Recall the magnitude at J (denoted "J") is

$$J = -2.5 \log \left(\frac{\text{Observed flux at 1.25 microns}}{\text{Flux corresponding to 0 mag at 1.25 microns}} \right). \qquad (2.8)$$

The magnitudes at K and L are analogous (substitute 2.2 microns and 3.5 microns, respectively). It follows the color J-K is simply

$$J - K = 2.5 \log \left(\frac{2.2\mu\text{m mag 0 flux}}{1.25\mu\text{m mag 0 flux}} \right) - 2.5 \log \left(\frac{\text{observed } 1.25\mu\text{m flux}}{\text{observed } 2.2\mu\text{m flux}} \right). \qquad (2.9)$$

Thus, a color is just the log of the flux ratios at two wavelengths, barring a factor of 2.5, and a constant offset. It is trivial to examine the slope of a SED between 1.25–3.5 μm by plotting infrared colors against each other. Such plots are often called "color-color diagrams." Since this program uses almost exclusively measurements at J, K and L (or L′), J-K, J-L and K-L colors will be examined. (For the sake of simplicity, assume in this section that L and L′ are synonymous.) Although no illustrations of color-color plots are given in this chapter, numerous examples may be seen in Chapter 3.

Tenuous warm dust in disks will produce a shallower SED, or larger (redder) J-K, J-L, and K-L colors. Once photospheric colors are established in a given photometric system, dust can be detected by the reddening it produces in the observed infrared colors. Stars having warm dust disks should stand out on color-color diagrams. The degree to which this method is sensitive to tenuous dust is determined by how well photospheric colors can be established.

Note there are other ways to detect infrared excesses. One method is to plot infrared colors against a given magnitude, such as J, creating a color-magnitude diagram. In order to do this, the absolute flux at 1.25 microns must be determined.

A more complete method, used by K. Strom *et al.* (1989), is to obtain measurements at optical through mid-infrared wavelengths (which will cover the peak of the SED well), determine the absolute flux at each wavelength, and determine the absolute flux expected from the stellar photosphere alone, based on its spectral type and distance. This yields an *absolute* flux excess.

In contrast, the use of color-color diagrams diagnoses *relative* excesses. The primary advantages of this method over the K. Strom *et al.* approach are *a)* it requires a minimum of observations, *b)* the observations can be made using only an InSb detector, which is sensitive to 1–5 μm emission, and *c)* it does not require accurate determination of interstellar extinction to each source, which can be a very difficult and uncertain process. It will be demonstrated in Chapter 4 that interstellar reddening is not critical.

The primary disadvantage to the relative excess method is the possibility of missing an excess if the resulting SED mimics a photospheric SED in the 1-5 micron range. This will be discussed further in Chapter 5.

To summarize, the basic method chosen to search for weak dust emission is to observe all stars at a minimum of J, K and L, and create color-color plots such as J-L *vs.* J-K. Stars with tenuous warm dust disks will have non-photospheric infrared colors. As mentioned earlier, the measurements at J, K and L must be simultaneous; non-simultaneous measurements on a variable star may produce infrared colors which mimic a dust excess.

When wavelengths other than J, K and L are observed, such as M (4.5 μm) or N (10 μm), color-color plots using the additional observations will also be examined. It is not as critical to have simultaneous measurements at N, or even M, as the stars are not as variable at those wavelengths.

To establish photospheric colors, presumably diskless stars were observed at each telescope. Milky Way disk stars from the Woolley catalog (Woolley, 1970) were chosen for this purpose; halo stars are older and have lower metallicities, which might alter the infrared colors. Woolley stars with high space velocities, or having low U-B and B-V for their spectral type were presumed to be halo stars, and were not used. Known close or spectroscopic binaries and multiple systems were also excluded. Stars having infrared colors redder than those of Woolley stars are presumed to have thermal dust emission.

Observed magnitudes must be corrected for interstellar extinction (or reddening). Woolley stars are so nearby, interstellar reddening is not significant. The other stars chosen for this program belong to clusters, as discussed in the next section. Main sequence clusters will be de-reddened for interstellar extinction, which is well-known, assuming the same reddening for each star in a given cluster. For the pre-main sequence stars in Taurus-Auriga, the reddening varies widely throughout the group, and is difficult to determine accurately for any individual star. Reddening will be applied for those stars for which K. Strom *et al.* (1989) derived visual extinctions, using the extinction law for the Taurus region determined by Elias (1978). For those stars with unknown visual extinctions, the general change in infrared colors due to interstellar extinction for 1 A_V of reddening will be used as a guide to estimate probable color changes due to reddening, as opposed to thermal emission from dust. As will be shown in the next chapter, the changes in colors due to reddening are quite different from those due to thermal dust emission, and are therefore only an issue in a few cases.

Models are used to translate observed excesses on color-color plots into a physical reality. Kenyon and Hartmann (1987) modeled the expected absolute excess emission arising from optically thick flat and flared circumstellar disks; they considered both accretion and reprocessing luminosity. This dissertation is

concerned with later stages of disk evolution, after accretion is no longer significant, and the disk has become optically thin in the terrestrial planet region. M. Skrutskie has developed a simple disk model which calculates the expected infrared colors produced by optically thin disks around stars of various luminosities, presuming the disks are composed entirely of grains having a radius of 1 micron. Disk mass and the surface density distribution are allowed to vary. The model is described in detail in Appendix C.

2.5 Sample Stars

Now that method for diagnosing warm dust in circumstellar disks has been laid out, the final step is to choose the sample of stars for observation. The object of the program is to observationally determine the evolution of the dust population in the terrestrial planet region of circumstellar disks around solar-type stars, during the epoch of presumed planetary formation. This will be accomplished by quantifying the level of excess infrared emission, presumably arising from dust reprocessing, as a function of stellar age and spectral type.

The sample must cover a range of spectral types, and consist of stars with known ages. The age of star clusters can be determined by their high-mass turnoff point on a Hertzsprung-Russell diagram, whereas it is often difficult to determine the age of an isolated star. Clusters usually contain a range of spectral types, tend to be well-studied, and are relatively easy to date. Clearly, cluster stars are very appealing for this study.

The ages of the sample stars should range from late pre-main sequence through early main sequence. The work of K. Strom *et al.* (1989) revealed circumstellar disks around solar-type stars become optically thin at an age of roughly 3×10^6 years. Models of the formation of the Earth predict the Earth was $> 99\%$ formed

in $\sim 10^8$ years (Wetherill, 1992). The sample chosen should thus contain stars with ages ranging from about 1-3 million years to a few hundred million years.

We are therefore led to find clusters having ages between roughly one million and a few hundred million years. One important criterion for cluster selection is distance. The clusters should be close enough that the late-type stars can be observed with high precision in reasonable integration times. Nearby clusters also tend to be well-studied, which is an advantage. Generally studies have been done on nearby clusters to determine membership probabilities, metallicities, and so on.

One comment must be made concerning the ages of stars in clusters. In main sequence clusters, it is assumed all the stars have the same age. Pre-main sequence stars are commonly found in complexes or associations, similar to clusters. The pre-main sequence stars are young enough that the difference in ages within the complex is significant; one should not assume a common age for all the protostars in the complex. Ages of individual protostars are estimated using observed properties (such as infrared colors) and computed isochrones.

The clusters chosen for this project, along with approximate ages and distances, are given in Table 2.1.

Taurus-Auriga, the only pre-main sequence complex in the sample, is well-studied, and consists primarily of solar-type and low-mass stars. Alpha Perseus is the youngest nearby main sequence cluster in the northern hemisphere; both high- and low-mass members have been identified. The Hyades, one of the oldest clusters in this study, is one of the best-studied clusters, and historically was used to define the main sequence. All the main-sequence clusters have near-solar metallicities.

The interstellar extinction to the main sequence clusters is small. Alpha Perseus has $E(B-V) = 0.1$ (Crawford and Barnes, 1974), and the Pleiades has $E(B-V) = 0.04$ (Crawford and Perry, 1976). The Ursa Major Stream, the

Table 2.1. Clusters Observed

Cluster	Age(Myr)	Dist(pc)	Ref(age)	Ref(dist)
Taurus-Auriga	1-10	160	10	10
Alpha Perseus	20-80	140	1,3	7
Pleiades	70	125	1,9	9
Ursa Major Stream	300	25	1	4
Hyades	600-670	47	1,8	2,5
Praesepe	600-760	175	1,6	6

1) Boesgaard (1989)
2) Hanson (1975)
3) Prosser (1992)
4) Roman (1949)
5) Schwan (1990)
6) Stauffer (1982)
7) Stauffer *et al.* (1985)
8) Stauffer, Hartmann and Latham (1987)
9) Stauffer *et al.* (1989)
10) Strom *et al.* (1989)

Hyades, and Praesepe have virtually no reddening; $E(B-V)$ is assumed to be zero. Extinction for stars within Taurus-Auriga varies widely; reddening will be considered on a star-by-star basis.

Specific stars within each cluster were chosen from the following references:

- Taurus-Auriga: K. Strom *et al.* (1989).
- Alpha Perseus: Heckmann, Deickvoss and Kox (1956); Roman and Morgan (1950), Stauffer, Hartmann and Jones (1989), and Prosser (1992).
- Pleiades: Primarily Hertzsprung (1947) sources, plus one flare star; sources were actually chosen from Stauffer (1984), and Johnson and Mitchell (1958).
- Ursa Major Stream: Roman (1949).
- Hyades: Hanson (1975); Schwan (1990); Griffin *et al.* (1988).
- Praesepe: Klein-Wassink (1927); Jones and Cudworth (1983).

2.6 Summary of the Method Used

Stars in clusters ranging in age from late pre-main sequence through early main sequence ($\sim 1 - 600$ Myr) are examined for evidence of tenuous dust emission arising from the terrestrial planet region. In each cluster, as wide a range of spectral types is observed as is feasible.

Each program star is observed at a minimum of J (1.25 μm), K (2.2 μm) and L or L′ (3.45 or 3.80 μm) at high internal precision (1 or 2%). Simultaneous measurements (i.e. within an hour) are required, as the stars may be variable owing to starspots. Measurements at M and N do not generally have to be simultaneous with J, K and L, as the variability is not significant at longer wavelengths.

Many of the observed measurements must be corrected for interstellar reddening. All stars within a given main sequence cluster are treated identically. Of the clusters chosen for this program, only Alpha Perseus and the Pleiades require corrections for extinction.

Taurus-Auriga requires a more careful approach; the visible extinction throughout the complex varies by more than 1 magnitude. Each star must be corrected for extinction on an individual basis. The published visual extinctions vary with the method used to obtain them; visual extinctions in K. Strom *et al.* (1989) will be adopted. Not all program stars have a known A_V. For those stars with unknown extinctions, the expected effects of various degrees of reddening will be considered when analyzing the observed emission.

The Elias (1978) reddening law for the Taurus region is assumed when translating visual extinction into infrared extinctions for all of the program stars, even the main sequence stars. (The reddening corrections for Alpha Perseus and the Pleiades are small enough that the exact choice of reddening law is not critical.)

Plots of near-infrared *colors* are used to diagnose excess infrared emission arising from warm dust near the star. Nearby Milky Way disk stars from the Woolley catalog are observed to establish photospheric colors. At these wavelengths, stars with warm material in circumstellar disks should stand out from the main locus on color-color plots, reflecting a change in the slope of the SED from that of the photospheric emission alone. It will be seen that shifts due to interstellar reddening are quite different than those produced by dust in disks.

Models by Skrutskie, and also Kenyon and Hartmann, are used to translate observed shifts in infrared colors into estimates of disk masses. The Kenyon and Hartmann models apply to optically thick disks, and are not as relevant to this work. The Skrutskie model focuses on optically thin disks, and is the primary model used here. It assumes all grains in the disk are 1 micron in radius, but varies the luminosity of the central star, and the power law describing the surface mass distribution in the disk. The model is described in detail in Appendix C.

Finally, the evolution with stellar age of the dust in the terrestrial planet region of circumstellar disks as a function of spectral type is discussed. The findings are related to other studies and models of circumstellar disks.

Chapter 3

OBSERVATIONS

3.1 Observations

Single-channel broadband photometric measurements were obtained at the Kitt Peak National Observatory (KPNO) and at NASA's Infrared Telescope Facility (IRTF).

The KPNO infrared observations were obtained on 6-10 October 1990 and 24-28 January 1991 (UT), using the solid-nitrogen cooled InSb photometer OTTO on the 1.3 m telescope, with an 11″ aperture. Wavelengths of observation were J($\lambda_\circ$ =1.23μm, $\Delta\lambda$ = 0.23μm), K($\lambda_\circ$ =2.22μm, $\Delta\lambda$ = 0.42μm), and L($\lambda_\circ$ =3.45μm, $\Delta\lambda$ = 0.57μm). The IRTF infrared observations were obtained on 23-24 November 1989, 23-26 October 1990, and 5-6 January 1992 (UT), using the solid-nitrogen cooled InSb photometer RC2, and the liquid-helium cooled Bolometer No. 1. Each source was observed primarily at J($\lambda_\circ \approx$1.25μm, $\Delta\lambda \approx$ 0.30μm), K($\lambda_\circ$ =2.19μm, $\Delta\lambda$ = 0.44μm), and L′($\lambda_\circ$ =3.80μm, $\Delta\lambda$ = 0.70μm); additional observations at H($\lambda_\circ$ =1.64μm, $\Delta\lambda$ = 0.28μm), L($\lambda_\circ$ =3.50μm, $\Delta\lambda$ = 1.03μm), M($\lambda_\circ$ =4.69μm, $\Delta\lambda$ = 0.65μm) and/or N($\lambda_\circ$ =10.40μm, $\Delta\lambda$ = 5.07μm), were made on selected sources. A 6″ beam was used for all IRTF observations. Standard sky chopping techniques (Low and Rieke, 1974) were employed at both KPNO and the IRTF.

For a large data set, the best measure of the errors is the internal residuals in the data set itself. As the method in this program examines the relative colors of stars, the uncertainties are best defined in terms of the scatter in the observed

colors. A typical 1σ uncertainty in J-L or J-L′ for a given J-K is 0.02-0.03 magnitudes. A typical 1σ uncertainty in J-M for a given J-K is slightly larger than 0.03 mag. The details of this analysis are given in Chapter 4.

3.2 Data Reduction Method

The data were corrected for atmospheric extinction and variations in detector response as the InSb detectors cooled to solid nitrogen temperatures. The detailed method used to derive the final infrared magnitudes is described below. In this chapter the term "cluster star" refers to both cluster stars and stars from the Woolley catalog, as opposed to calibrator stars.

For each source, the individual pairs (plusbeam-minusbeam) were extracted from the electronic data, after which any pairs having obvious problems (e.g. a large spike on the stripchart) were deleted. All the pairs for a particular source were then averaged together as a whole, yielding an average signal, average UT time of observation, average airmass, and an internal signal/noise (S/N). The average signal was then converted to an instrumental magnitude.

Calibrator stars were measured every hour to provide a good record of sky transparency. Airmass curves were constructed for all calibrator stars [(catalog magnitude - instrumental magnitude) *vs.* airmass]. These plots show the corrections for a given airmass which are used to convert instrumental magnitudes of cluster stars to magnitudes relative to a given calibrator. The plots were found to be non-linear at both sites, due to changing detector response as the instrument cooled, and time variations in the atmospheric transparency. At the IRTF, where solid nitrogen temperatures were not reached until hours after observations began, slow variations as large as 0.06 mag *at the same airmass* were common. Figure 3.1 shows typical airmass curves at J and L′ at the IRTF, plus J and L at KPNO. The airmass curves are interpreted as having a constant airmass slope at a given

wavelength for a given night, with the entire airmass curve shifting upwards or downwards over the course of the night. Whenever possible, the airmass slope for the night at each wavelength is determined by looking at successive calibrator measurements at high airmass, where the airmass is changing rapidly with time, thus yielding the best measure of the (time-invariant) airmass slope. If there were insufficient calibrator measurements at high airmass, a "typical" airmass slope for each wavelength was used, as given in Table 3.1.

Table 3.1. Typical Airmass Slopes

Filter	Airmass slope (mag/airmass)
J	-0.1
H	-0.1
K	0.1
L	-0.1
L′	-0.1
M	-0.2
N	-0.2

Had the airmass curves been linear, corrections for extinction would be trivial. In that case, one would calculate a best-fit line for the airmass slope, yielding a time-independent extinction correction for a given airmass. This is the most commonly used method. However, since the variations due to atmospheric transparency and detector response were as large as 0.06 mag at a given airmass, compared to internal errors of only 0.01 to 0.02 magnitudes, a best-fit line for the night would seriously degrade the quality of the measurements. As the airmass curves varied smoothly, although not linearly, with time, it was possible to at least partially compensate for these slow variations.

Owing to the fact that the infrared magnitudes of the standard stars used are not known to the desired accuracy in the photometric systems used, relative

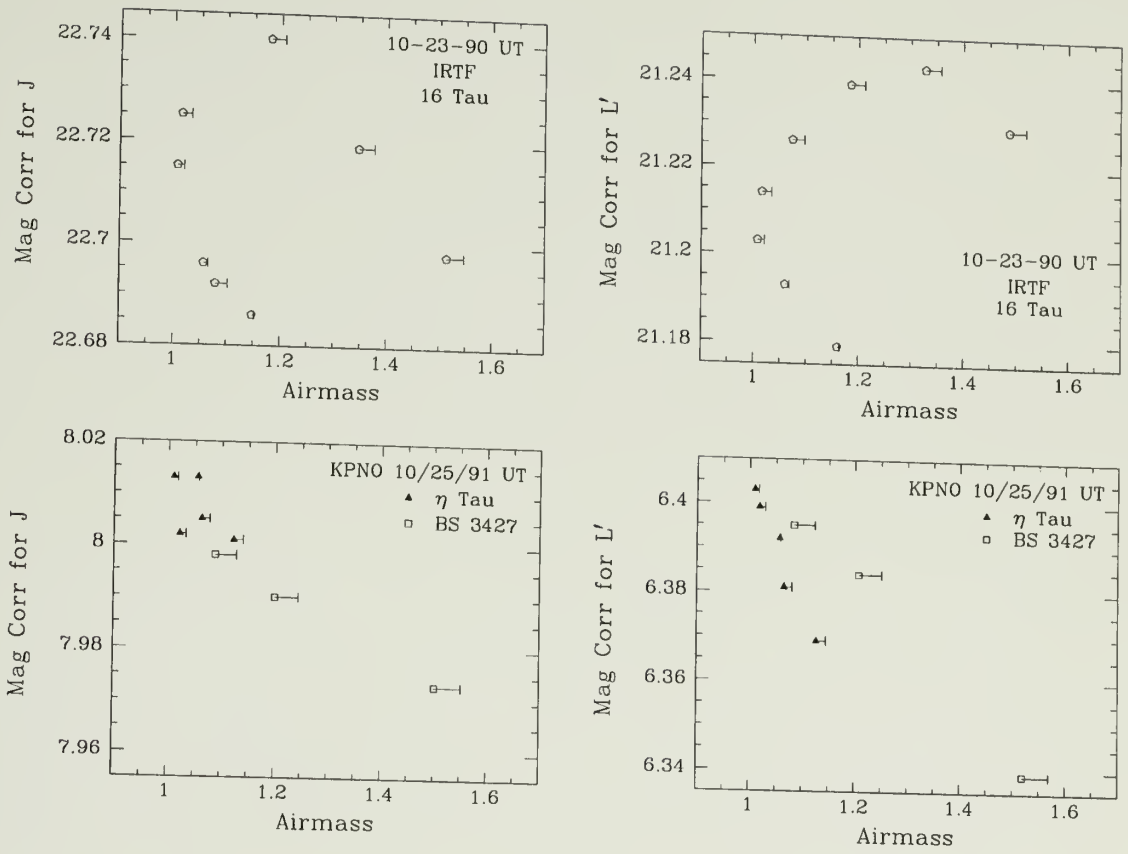

Figure 3.1. Typical airmass curves for the IRTF and KPNO. Plots show corrections to be applied to each cluster star instrumental magnitude as a function of airmass. Symbols denote different calibrators. The length of the errorbars corresponds to the time of night; an errorbar of length zero denotes the first measurement of the night, while longer errorbars denote successively later measurements. For a stable atmosphere over the course of a night, a straight line is expected for a given calibrator. The observations of BS 3427 approximate this, as do the last three observations of 16 Tau on 10-23-90 UT. Early in the evening, the detector response changes as the detector cools from liquid nitrogen to solid nitrogen temperatures. The KPNO detector was usually cold by the beginning of observations, but the IRTF curves clearly show large (0.06 mag) variations at the same airmass, largely due to detector response changes. The "loopy" IRTF curves result from the systematic variation. They can be generated by assuming a linear airmass curve with a negative slope that is sliding upwards with time. Atmospheric transparency variations were also largest in the beginning of the night, possibly due to the settling of aerosols (Young, 1974); the peculiarities in the airmass curves of η Tau probably result from this.

photometry (as opposed to absolute photometry) was employed. *Whenever possible, a single nearby calibrator was used for each cluster in order to obtain the best possible relative photometry within a cluster.* The cluster star instrumental magnitudes were converted to relative magnitudes, using the nearest calibrator measurement(s) in time and space, plus the airmass slope for that night at the wavelength of interest. If a cluster star measurement was straddled by two measurements of the same calibrator, an interpolated magnitude of the calibrator at the time of the cluster star measurement was calculated, and this interpolated calibrator magnitude was then used to determine the magnitude of the cluster star. If the calibrator was only measured before or after the cluster star, the magnitude of the cluster star was extrapolated from that single calibrator measurement. A given cluster star was reduced using the same set of calibrator measurements at all wavelengths; e.g. J and K were not determined using interpolation if L was derived using a single calibrator[1].

No filter color corrections were applied to cluster stars; the method chosen for analysis is self-calibrating.

3.3 Sources of Uncertainty

With a nearby calibrator, uncertainties in airmass correction were typically [(< 0.2 airmasses difference between cluster star and calibrator) × (0.05 mag/airmass uncertainty in slope)] = 0.01 mag, or smaller. Errors may be slightly larger for the Woolley and Ursa Major stream stars, which are scattered over the sky, and hence do not have a single nearby calibrator.

[1]Originally all the data was reduced using only the single nearest set of calibrator measurements in time. When it was determined that interpolation between calibrators reduced the scatter in the IRTF infrared data significantly, the entire infrared data set (IRTF and KPNO) was re-reduced using a modified version of a menu-driven reduction program written at UMASS by David Whalen (now at the University of Wyoming). In general, interpolation is advised when variations in atmospheric transparency and/or detector response exceed the internal accuracy of the measurements.

Sky brightness changes in a nonlinear fashion at dawn and dusk, while sky chopping/nodding techniques are designed to remove only linear changes. Measurements made too close to sunset or sunrise may therefore be inaccurate. It is typical, for example, for an airmass curve of a setting star to suddenly turn upwards at dawn (creating a positive airmass slope). The maximum estimated errors for these few stars for this effect is 0.02 mag.

Some measurements at the IRTF may have been in the nonlinear region of the detector. The new lockin amplifiers at the IRTF permit measurement of sources that are bright enough to approach the saturation region of the InSb detector, resulting in instrumental magnitudes that are too dim. A few cluster stars in our sample were bright enough to approach this saturation limit. In addition, cluster star magnitudes derived from a very bright calibrator may be erroneously bright. Measurements of the calibrator 4 Lac are borderline; based on the measured behavior of the detector near the saturation limit, errors for this calibrator are estimated to be 0.02 magnitude at most.

An additional source of error is the non-automated bias offset of the InSb photometer RC2 at the IRTF, affecting measurements at L, L′ and M. The bias offset must be adjusted manually with a potentiometer, which is difficult to perform accurately. A 1-volt offset can produce an error of 0.02 mag; a 2-volt offset was shown to produce a drop in signal of 0.08 mag. A typical offset was 0.5 V, which may translate into errors as large as 0.01 mag. Measurements at J, H, K and N are not affected.

The magnitude of external errors as a whole is best determined by the scatter in plots of an individual cluster, using a single calibrator. In the next chapter, it is shown that the typical 1σ scatter in J-L or J-L′ for a given J-K is 0.02 mag.

3.4 Relative Colors of Calibrators

The goal is to obtain precise *relative* photometry, which requires a set of calibrators whose relative magnitudes are known precisely in the photometric systems used for this study. Due to differences in photometric systems, differing colors of calibrator stars, and poorly known magnitudes of some calibrators, the published magnitudes of standard stars were not sufficient for our purposes. The published magnitudes were internally inconsistent by as much as 0.1 magnitudes, compared to an internal accuracy for each measurement of 0.01-0.02 magnitudes. Figure 3.2 illustrates the problem.

The inconsistency in the published magnitudes of the calibrators used to determine the cluster star magnitudes drastically increased the scatter in the data. As Figure 3.2 shows, the variability in the airmass curves makes them unsuitable for determining the relative magnitudes of the calibrators in the photometric system used. Another method is needed.

Best-fit lines to plots of observed colors of cluster stars *vs.* spectral type were used to derive an internally consistent set of infrared calibrator colors at each telescope. The method is described in detail in Appendix A. The adopted infrared magnitudes and colors for all calibrators are listed in Table 3.2. The J calibrator magnitudes are still only consistent to 0.1 mag. There was not enough data at N to derive relative J-N color corrections between standards. Table 3.3 gives the shifts to the J-M colors when different calibrators were used for J and M on a single source. The shifts are applied to the colors derived using the respective J and M magnitudes for the calibrators given in Table 3.2.

The adjustments to the calibrator colors effectively applies any filter transmission color correction to the calibrators. No color correction is applied to cluster stars; the clusters are allowed to self-calibrate.

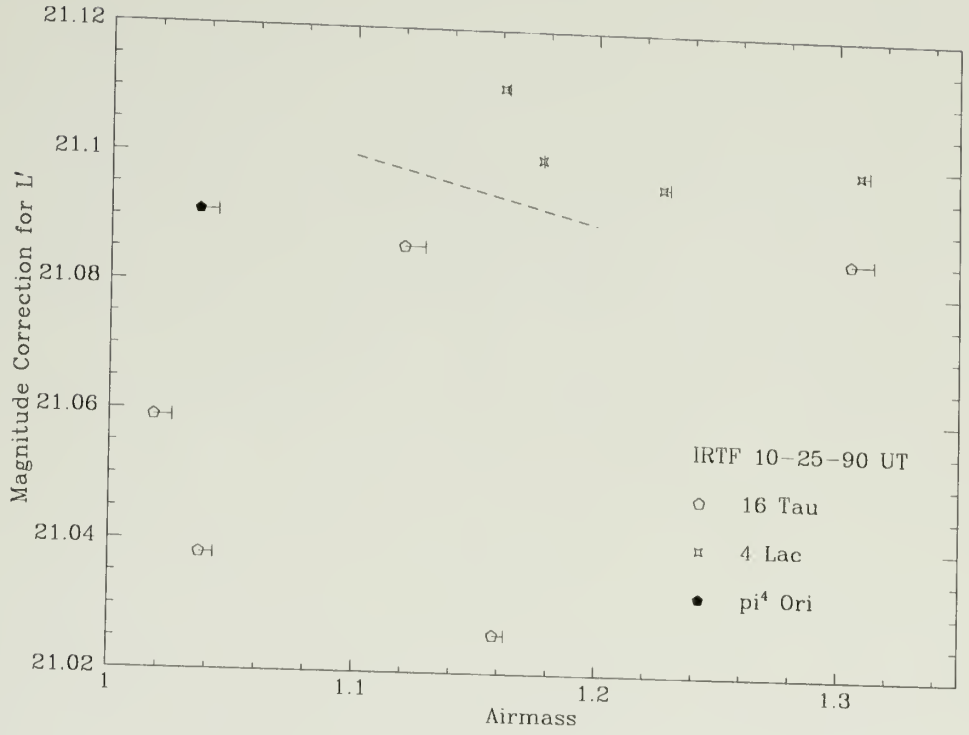

Figure 3.2. Inadequacy of published calibrator magnitudes. This figure demonstrates the difficulty in determining an internally consistent set of calibrator magnitudes. Shown are the airmass curves at L′ for three calibrators at the IRTF on the night of 25-Oct-1990. Errorbars denote the time of night, as in Figure 3.1. It is difficult to ascertain the airmass slope for the evening; a typical slope of -0.1 magnitudes/airmass was assumed, illustrated by the dotted line. If the published magnitudes for the calibrators were internally consistent, and the airmass curve for each calibrator was linear, the airmass curve created by combining all three calibrators would be a single straight line. If the calibrator magnitudes were inconsistent, but the airmass curve for each calibrator was linear, a set of three parallel lines would be seen. Note the confusion in the displayed airmass curves. The airmass curves are not linear, owing to variations in detector response and atmospheric transparency. The lone measurement of pi^4 Ori is straddled in time by two measurements of 16 Tau. Using the observation of 16 Tau at the same time of night, and the assumed airmass slope, the two calibrator are shifted about 0.035 mag with respect to each other. Using the later measurement of 16 Tau implies the published magnitudes of the calibrators agree within 0.005 mag. Note that comparing the latest measurement of 4 Lac with the earliest measurement of 16 Tau (about the same time of night) implies the published magnitudes of the two calibrators are inconsistent at a level of almost 0.1 magnitudes!

Table 3.2. Calibrator Magnitudes and Colors

Calibrator	J	J-H	J-K	J-L	J-L′	J-M	M	N
IRTF								
16 Tau (16tau)	5.520	–	-0.015	–	-0.020	-0.024	5.640	–
HD 22686 (h22686)	7.195	0.005	0.010	–	–	–	–	–
4 Lac (4lac)	4.300	0.030	0.050	0.070	0.090	0.080	4.220	–
pi^4 Ori (pi4ori)	–	-0.060	-0.100	-0.013	-0.157	–	4.320	–
HD 77281 (h77281)	7.105	–	0.075	–	0.110	–	–	–
beta Peg (bpeg)	–	–	–	–	–	–	–	-2.540
alpha Tau (atau)	–	–	–	–	–	–	–	-3.030
KPNO								
alpha Per (aper)	0.850	–	0.274	0.334	–	–	–	–
zeta Mon (zmon)	2.790	–	0.497	0.572	–	–	–	–
BS 3427 (bs3427)	4.750	–	0.528	0.582	–	–	–	–
eta Tau (ntau)	2.930	–	-0.027	0.017	–	–	–	–
beta Com (bcom)	3.190	–	0.312	0.342	–	–	–	–
eta Vir (nvir)	3.790	–	0.020	0.030	–	–	–	–

Table 3.3. Corrections to J-M for Combinations of Calibrators

J Calibrator	M Calibrator	Mag shift for J-M
16 Tau	pi^4 Ori	0.214
16 Tau	4 Lac	0.100
HD 22686	16 Tau	-0.031
HD 22686	pi^4 Ori	0.087

3.5 The Data Set

The infrared observations are presented in Tables 3.5 and 3.6, grouped by cluster. The calibrator magnitudes in Tables 3.2 and 3.3 were assumed. All the original reduced magnitudes, using the published magnitudes for calibrators, are given in Appendix B. Measurements at wavelengths not discussed in this dissertation, and measurements of stars not discussed (such as Ae/Be stars) are also recorded.

Table 3.5 presents the J through L′ observations, corrected for atmospheric extinction, showing the source name; J magnitude; infrared colors; the calibrator used; the UT date of observation; the telescope facility where the data was obtained; a flag indicating whether or not an interpolated calibrator magnitude was used (0=interpolated, 1=extrapolated); a series of two flags indicating the internal signal/noise (S/N) of measurements at L and L′ (the S/N for measurements at J, H and K was rarely less than 100); V and B-V from the literature; the visual extinction A_V (in magnitudes), if known; and a numerical code for the spectral type (1.00=B0, 2.00=A0, 2.50=A5, 2.75=A7.5,...6.00=M0). More complete information may be found in Appendix B.

Table 3.6 presents the N and M data, combined with the corresponding J through L′ observations from Table 3.5. All are corrected for atmospheric extinction. Shown are the source name; J magnitude; infrared colors; the calibrator used for J through L′; the calibrator used for M; the calibrator used for N; the UT date of observation for J through L′; the UT date of observation for M; the UT date of observation for N; the telescope facility where the data was obtained; the interpolation flag mentioned in the previous paragraph; a series of four flags indicating the internal signal/noise (S/N) of measurements at L, L′, M and N; V and B-V from the literature; the visual extinction A_V (in magnitudes), if known; and a numerical code for the spectral type (as explained in the previous paragraph). More complete information may be found in Appendix B.

The S/N flags are interpreted as follows:

The transformation equations between the IRTF and KPNO photometric systems are poorly known; therefore, the two data sets will be examined separately.

Table 3.4. Signal-to-Noise Flags

Flag	S/N
0	≥ 95
1	$75 < S/N < 95$
2	$50 < S/N \leq 75$
3	≤ 50
9	No measurement

3.6 Instrumental Problems on 1-6-92

Several stars observed at the IRTF on Jan 6, 1992, are noted as having "Instrumental problems: magnitudes may be as much as 30% in error". For a portion of that night, the airmass curves showed a 30% drop in the detected flux of some individual calibrator measurements, and subsequent reduction of cluster star measurements confirmed that cluster stars were affected as well. Under normal circumstances these measurements would be thrown away, but as they are an important part of the data set, I have decided that even a crude measurement may be useful. All these sources were among the latest-type stars in Alpha Perseus and the Pleiades, and required long integrations. As Alpha Perseus and the Pleiades are the youngest main sequence clusters in this study, and the lowest-mass stars are expected to evolve most slowly, observations of the late-type stars in these cluster are critical to my analysis. It is hoped that a future observing run will eliminate the need to retain these faulty measurements.

As stated above, a number of individual calibrator measurements showed a 30% drop in detected flux. Although no clear pattern is apparent, the consistency of the (roughly) 30% drop in flux at each wavelength suggests a filter wheel backlash problem. It was obvious which calibrator measurements were affected, but impossible to determine with certainty which cluster star measurements were affected; for a given cluster star, any combination of wavelengths may have a 30%

reduction in flux. The calibrator measurements were corrected using the airmass curves as a guide (add 0.277 mag to J, 0.293 to K, and 0.301 to L′).

In order to determine the most likely combination of wavelengths affected for any given cluster star, various color-color and color-magnitude diagrams of cluster stars were constructed. Knowing the general behavior expected in these diagrams, I altered various combinations of magnitudes by ~ 0.3 until the expected trends were seen.

Each presumably affected cluster star magnitude was then adjusted in the same manner as the calibrators for that wavelength (i.e. add 0.277 to J, etc.). Owing to the uncertainty of this process, any individual magnitude of these stars may be in error by 0.3 magnitudes, or 30%. Even if I correctly determined which magnitudes were affected by the instrumental problem, the derived magnitudes may be of lower accuracy due to the uncertainty in the determination in the "correction factor".

Table 3.5. J through L′ Magnitudes and Colors

Alpha Per

	J	J-K	J-L	J-L′	JLcal	Date(UT)	Tel	I	LL′	V	B-V	Av	SpT
AP115*	11.176	1.034	-	1.190	16tau	01-05-92	IRTF	0	90	14.13	1.640	0.31	-
AP61	10.773	0.692	-	0.767	16tau	01-06-92	IRTF	0	92	12.77	1.090	0.31	-
AP72	11.296	0.635	-	0.725	16tau	01-06-92	IRTF	0	92	12.78	0.990	0.31	-
AP75	11.090	0.838	-	1.005	16tau	01-05-92	IRTF	0	91	13.82	1.270	0.31	-
AP93	10.048	0.685	-	0.794	16tau	01-05-92	IRTF	0	90	11.99	0.930	0.31	-
HE1164	4.239	0.240	-	0.697	16tau	10-23-90	IRTF	1	90	4.20	-0.080	0.31	1.50
HE145	6.872	0.022	-	0.050	16tau	10-23-90	IRTF	1	90	6.88	0.025	0.31	1.50
HE350	9.667	0.423	-	0.460	16tau	01-05-92	IRTF	0	90	11.01	0.683	0.31	4.30
HE575	7.643	0.088	-	0.088	16tau	10-25-90	IRTF	1	90	7.85	0.104	0.31	2.00
HE609	8.283	0.300	-	0.375	16tau	01-05-92	IRTF	0	90	9.22	0.408	0.31	3.00
HE635	8.379	0.223	-	0.261	16tau	01-05-92	IRTF	0	90	9.05	0.338	0.31	2.80
HE639	7.967	0.074	-	0.117	16tau	01-05-92	IRTF	0	90	8.15	0.119	0.31	2.30
HE780	7.707	0.141	-	0.184	16tau	01-05-92	IRTF	0	90	8.09	0.166	0.31	2.10
HE848	8.878	0.361	-	0.419	16tau	01-05-92	IRTF	0	90	9.99	0.588	0.31	-
HE863*	8.215	0.339	-	0.381	16tau	01-05-92	IRTF	0	90	9.21	0.517	0.31	3.60
HD22928	3.260	-0.093	-0.103	-	aper	10-10-90	KPNO	0	09	2.99	-0.118	0.31	1.50
HD24760	3.376	-0.165	-0.212	-	aper	10-10-90	KPNO	0	09	2.88	-0.172	0.31	1.05
HE1153	6.944	-0.051	-0.043	-	aper	10-06-90	KPNO	0	19	6.89	-0.020	0.31	1.80
HE1164	4.216	0.219	0.537	-	aper	10-06-90	KPNO	0	09	4.20	-0.080	0.31	1.50
HE145	6.857	-0.037	-0.013	-	aper	10-10-90	KPNO	0	09	6.88	0.025	0.31	1.50
HE383	5.325	-0.075	-0.086	-	aper	10-10-90	KPNO	0	09	5.15	-0.061	0.31	1.30
HE606	8.365	0.184	0.191	-	aper	01-28-91	KPNO	1	29	8.98	0.330	0.31	2.80
HE625	7.332	0.026	-0.004	-	ntau	01-28-91	KPNO	1	19	7.63	0.114	0.31	1.95
HE675	6.284	-0.090	-0.108	-	aper	10-10-90	KPNO	0	09	6.06	-0.079	0.31	1.70
HE694	8.121	0.061	0.066	-	ntau	01-25-91	KPNO	0	39	8.48	0.200	0.31	2.50
HE835	4.886	-0.071	-0.081	-	aper	10-06-90	KPNO	0	09	4.66	-0.098	0.31	1.30
HE861	5.956	0.022	0.090	-	aper	10-06-90	KPNO	0	09	6.24	0.126	0.31	1.70
HE904	5.971	-0.055	-0.047	-	aper	10-10-90	KPNO	0	09	5.82	-0.040	0.31	1.80
HE906	8.189	0.116	0.109	-	ntau	01-28-91	KPNO	1	39	8.78	0.276	0.31	2.60
HE985	5.675	-0.086	-0.105	-	aper	10-06-90	KPNO	0	09	5.46	-0.104	0.31	1.80

V, B-V from Stauffer et al. (1985) and (1989), and Mitchell (1960).
Spectral types from SIMBAD.
* Not a cluster member according to Prosser (1992).

Pleiades

	J	J-K	J-L	J-L′	JLcal	Date(UT)	Tel	I	LL′	V	B-V	Av	SpT
HII1726	8.238	0.327	-	0.373	16tau	01-06-92	IRTF	0	90	9.25	0.550	0.12	3.60
HII1762	7.579	0.236	-	0.281	16tau	01-06-92	IRTF	0	90	8.27	0.360	0.12	2.90
HII189	11.433	0.861	-	0.972	16tau	01-06-92	IRTF	0	92	13.92	1.460	0.12	5.55
HII2220	7.321	0.050	-	0.080	16tau	01-06-92	IRTF	0	90	7.52	0.100	0.12	2.20
HII248	9.630	0.468	-	0.531	16tau	01-06-92	IRTF	0	90	11.02	0.770	0.12	4.40
HII2866	6.749	0.098	-	0.115	16tau	10-25-90	IRTF	1	90	6.93	0.090	0.12	2.20
HII3197	9.909	0.807	-	0.956	16tau	01-06-92	IRTF	0	90	12.10	1.070	0.12	5.30
HII659	10.340	0.638	-	0.761	16tau	01-06-92	IRTF	0	91	12.13	0.950	0.12	4.40
HII739	8.336	0.408	-	0.471	16tau	01-06-92	IRTF	0	90	9.56	0.620	0.12	4.00
HII870	10.011	0.770	-	0.935	16tau	01-06-92	IRTF	0	90	12.61	1.250	0.12	4.40
HII975	8.974	0.458	-	0.535	16tau	01-06-92	IRTF	0	90	10.56	0.810	0.12	3.80
HII980	4.188	0.122	-	0.400	16tau	10-25-90	IRTF	0	90	4.18	-0.060	0.12	1.60
T108	10.707	0.878	-	1.018	16tau	01-06-92	IRTF	0	90	13.29	1.310	0.12	-
HII1028	7.135	0.029	0.053	-	ntau	01-28-91	KPNO	1	19	7.35	0.100	0.12	2.20
HII1084	7.313	0.174	0.224	-	aper	10-10-90	KPNO	0	09	8.11	0.360	0.12	2.00
HII1234	6.779	0.007	0.026	-	aper	10-06-90	KPNO	0	09	6.82	0.020	0.12	1.95
HII1380	6.929	0.001	0.020	-	ntau	01-28-91	KPNO	1	19	6.99	0.030	0.12	2.10
HII1384	7.223	0.165	0.194	-	aper	10-10-90	KPNO	0	09	7.66	0.210	0.12	2.40
HII1431	6.713	0.035	0.048	-	aper	10-06-90	KPNO	0	09	6.81	0.060	0.12	2.00
HII2168	3.757	-0.047	-0.061	-	aper	10-10-90	KPNO	0	09	3.64	-0.080	0.12	1.80
HII2425	6.266	-0.035	-0.050	-	aper	10-10-90	KPNO	0	09	6.17	-0.050	0.12	1.80
HII2866	6.805	0.065	0.117	-	aper	10-10-90	KPNO	0	09	6.93	0.090	0.12	2.20
HII605	8.164	0.268	0.308	-	aper	10-10-90	KPNO	0	29	8.99	0.440	0.12	3.30
HII801	6.726	0.034	0.050	-	ntau	01-28-91	KPNO	0	09	6.85	0.040	0.12	2.00
HII859	6.485	-0.024	0.000	-	aper	10-06-90	KPNO	0	09	6.43	-0.020	0.12	2.00

Continued, next page.

Table 3.5. (cont.)

Pleiades (cont.)

	J	J-K	J-L	J-L'	JLcal	Date(UT)	Tel	I	LL'	V	B-V	Av	SpT
HII956	7.299	0.183	0.216	-	ntau	01-28-91	KPNO	0	09	7.96	0.320	0.12	2.70
HII980	4.162	0.078	0.269	-	aper	10-10-90	KPNO	0	09	4.18	-0.060	0.12	1.60

T108, HII3197 and HII870: V, B-V from Stauffer (1984). Remaining V, B-V from Johnson and Mitchell (1958).
Spectral types from SIMBAD.

Ursa Major

	J	J-K	J-L	J-L'	JLcal	Date(UT)	Tel	I	LL'	V	B-V	Av	SpT
HD109011	6.431	0.664	-	0.731	h22686	11-23-89	IRTF	1	00	8.09	0.930	0.00	5.20
HD110463	6.721	0.649	-	0.722	h22686	11-23-89	IRTF	1	00	8.27	0.950	0.00	5.30
HD11131	5.617	0.399	-	0.436	4lac	10-25-90	IRTF	0	90	6.76	0.610	0.00	4.00
HR1046	5.043	0.034	-	0.056	16tau	10-26-90	IRTF	0	90	5.08	0.050	0.00	2.10
HR2228	6.063	0.184	-	0.184	16tau	10-23-90	IRTF	1	90	6.52	0.270	0.00	3.00
HR647	5.299	0.272	-	0.312	16tau	10-26-90	IRTF	0	90	6.06	0.400	0.00	3.40
HR68	4.403	0.033	-	0.055	4lac	10-25-90	IRTF	0	90	4.53	0.050	0.00	2.20
HR8170	5.268	0.393	-	0.453	4lac	10-26-90	IRTF	0	90	6.40	0.530	0.00	3.80
HR8263	6.060	0.019	-	0.004	4lac	10-26-90	IRTF	0	90	6.25	0.050	0.00	2.20
HR8291	5.875	0.026	-	0.025	4lac	10-26-90	IRTF	0	90	6.10	0.060	0.00	2.20
HR8407	5.512	-0.009	-	-0.031	4lac	10-25-90	IRTF	0	90	5.60	-0.040	0.00	2.00
HR8984	4.139	0.115	-	0.134	4lac	10-25-90	IRTF	0	90	4.52	0.190	0.00	2.70
HD103287	2.364	-0.005	0.004	-	nvir	01-24-91	KPNO	0	09	2.44	0.000	0.00	2.00
HD106591	3.142	0.039	0.043	-	nvir	01-25-91	KPNO	1	09	3.31	0.080	0.00	2.30
HD109011	6.304	0.567	0.652	-	nvir	01-24-91	KPNO	0	09	8.09	0.930	0.00	5.20
HD110463	6.569	0.535	0.609	-	nvir	01-24-91	KPNO	0	09	8.27	0.950	0.00	5.30
HD111456	4.880	0.311	0.303	-	nvir	01-25-91	KPNO	1	09	5.85	0.460	0.00	3.50
HD112185	1.721	-0.012	-0.005	-	bcom	01-25-91	KPNO	1	09	1.76	-0.020	0.00	2.00
HD113139	4.177	0.218	0.248	-	nvir	01-24-91	KPNO	0	09	4.93	0.360	0.00	3.20
HD115043	5.690	0.331	0.376	-	nvir	01-24-91	KPNO	0	09	6.84	0.600	0.00	4.10
HD116842	3.668	0.078	0.101	-	nvir	01-24-91	KPNO	0	09	4.01	0.160	0.00	2.50
HD91480	4.482	0.171	0.199	-	nvir	01-25-91	KPNO	0	09	5.16	0.340	0.00	3.10
HD95418	2.333	-0.004	0.001	-	nvir	01-25-91	KPNO	0	09	2.36	-0.020	0.00	2.10
HR4865	5.608	0.024	0.032	-	bcom	01-25-91	KPNO	1	09	5.70	0.020	0.00	2.10
HR5264	3.974	0.080	0.097	-	bcom	01-25-91	KPNO	0	09	4.26	0.100	0.00	2.30
HR5373	6.184	0.034	0.057	-	nvir	01-24-91	KPNO	1	09	6.33	0.050	0.00	2.20
HR5721	5.637	0.129	0.138	-	bcom	01-25-91	KPNO	0	09	6.12	0.260	0.00	3.00
HR5793	2.202	-0.002	0.002	-	bcom	01-25-91	KPNO	0	09	2.23	-0.020	0.00	2.00

V, B-V from Johnson and Knuckles (1957), except for HD11131, which is from SIMBAD.
Spectral types from SIMBAD.

Hyades

	J	J-K	J-L	J-L'	JLcal	Date(UT)	Tel	I	LL'	V	B-V	Av	SpT
HA578	7.097	0.559	-	0.620	16tau	10-26-90	IRTF	0	90	8.51	0.841	0.00	4.50
HA178	6.367	0.356	0.403	-	aper	10-10-90	KPNO	0	09	7.54	0.679	0.00	4.50
HA361	7.402	0.540	0.606	-	aper	10-10-90	KPNO	0	09	9.01	0.939	0.00	5.20
HA382	6.841	0.365	0.431	-	ntau	01-27-91	KPNO	0	09	8.06	0.632	0.00	4.10
HA554	6.843	0.370	0.401	-	ntau	01-28-91	KPNO	0	09	8.06	0.632	0.00	4.10
HA578	7.338	0.381	0.424	-	ntau	01-28-91	KPNO	0	29	8.66	0.741	0.00	4.50
HD24357	7.090	0.476	0.584	-	aper	10-10-90	KPNO	0	09	8.51	0.841	0.00	4.50
HD26462	5.291	0.161	0.187	-	ntau	01-27-91	KPNO	0	09	5.97	0.341	0.00	3.40
HD26911	5.071	0.172	0.195	-	aper	10-10-90	KPNO	0	09	5.73	0.355	0.00	3.40
HD27962	5.608	0.200	0.216	-	aper	10-06-90	KPNO	0	09	6.32	0.399	0.00	3.50
HD28355	4.163	0.021	0.031	-	ntau	01-27-91	KPNO	0	09	4.30	0.049	0.00	2.20
HD28556	4.693	0.098	0.107	-	aper	10-06-90	KPNO	0	09	5.03	0.228	0.00	2.70
HD29310	4.938	0.145	0.170	-	aper	10-06-90	KPNO	0	09	5.40	0.262	0.00	3.00
HD29388	6.421	0.380	0.406	-	aper	10-06-90	KPNO	0	09	7.54	0.603	0.00	4.00
HD29488	4.054	0.067	0.077	-	aper	10-10-90	KPNO	0	09	4.27	0.123	0.00	2.60
HD30210	4.382	0.081	0.111	-	aper	10-06-90	KPNO	0	09	4.68	0.155	0.00	2.50
HD31845	5.024	0.055	0.078	-	ntau	01-27-91	KPNO	0	09	5.37	0.187	0.00	2.20
	5.891	0.211	0.232	-	ntau	01-25-91	KPNO	0	09	6.75	0.450	0.00	3.50

Continued, next page.

Table 3.5. (cont.)

Hyades (cont.)

	J	J-K	J-L	J-L'	JLcal	Date(UT)	Tel	I	LL'	V	B-V	Av	SpT
J291	8.528	0.661	0.757	-	ntau	01-25-91	KPNO	0	29	10.74	1.190	0.00	-
J309	8.737	0.773	0.892	-	ntau	01-24-91	KPNO	0	19	11.41	1.380	0.00	-
J330	8.689	0.633	0.653	-	ntau	01-28-91	KPNO	0	29	10.68	1.110	0.00	5.20
VB191	8.626	0.704	0.793	-	ntau	01-25-91	KPNO	0	19	11.03	1.291	0.00	5.00

V, B-V from Johnson and Knuckles (1955)(3 decimal places), and Johnson, Mitchell and Iriarte (1962)(2 decimal places).
Spectral types from SIMBAD.

Praesepe

	J	J-K	J-L	J-L'	JLcal	Date(UT)	Tel	I	LL'	V	B-V	Av	SpT
JC123	10.973	0.766	-	0.862	h77281	01-06-92	IRTF	0	90	13.28	1.360	0.00	-
KW162	9.597	0.339	-	0.379	h77281	01-05-92	IRTF	0	90	10.58	0.573	0.00	-
KW183	10.762	0.680	-	0.803	h77281	01-05-92	IRTF	0	90	12.64	1.001	0.00	-
KW232	8.514	0.275	-	0.302	h77281	01-05-92	IRTF	0	90	9.23	0.389	0.00	3.50
KW263	10.632	0.482	-	0.509	h77281	01-05-92	IRTF	0	91	11.98	0.814	0.00	-
KW265	6.577	0.003	-	0.016	h77281	01-05-92	IRTF	0	90	6.61	0.006	0.00	2.10
KW293	9.044	0.259	-	0.313	h77281	01-06-92	IRTF	0	90	9.85	0.470	0.00	-
KW299	11.341	0.653	-	0.719	h77281	01-06-92	IRTF	0	92	13.20	1.080	0.00	5.40
KW300	6.024	0.083	-	0.122	h77281	01-05-92	IRTF	0	90	6.30	0.172	0.00	2.50
KW313	10.726	0.523	-	0.541	h77281	01-06-92	IRTF	0	91	12.20	0.884	0.00	-
KW45	7.822	0.119	-	0.158	h77281	01-06-92	IRTF	0	90	8.25	0.231	0.00	3.00
KW466	9.870	0.383	-	0.371	h77281	01-06-92	IRTF	0	93	10.99	0.649	0.00	-
KW495	8.861	0.401	-	0.449	h77281	01-05-92	IRTF	0	90	9.94	0.660	0.00	3.80
KW55	9.879	0.567	-	0.627	h77281	01-05-92	IRTF	0	90	11.38	0.860	0.00	-
KW143	7.907	0.099	0.107	-	bs3427	01-25-91	KPNO	1	19	8.31	0.228	0.00	2.90
KW150	6.902	0.151	0.161	-	bs3427	01-24-91	KPNO	0	09	7.45	0.255	0.00	2.90
KW203	7.274	0.114	0.127	-	bs3427	01-28-91	KPNO	0	29	7.73	0.219	0.00	2.50
KW204	6.122	0.135	0.141	-	bs3427	01-24-91	KPNO	0	09	6.67	0.249	0.00	3.00
KW207	7.278	0.103	0.086	-	bs3427	01-25-91	KPNO	1	19	7.67	0.197	0.00	2.70
KW212	4.953	0.536	0.589	-	bs3427	01-24-91	KPNO	0	09	6.59	0.959	0.00	5.00
KW218	8.568	0.197	0.212	-	bs3427	01-25-91	KPNO	0	29	9.36	0.440	0.00	3.60
KW224	6.922	0.112	0.123	-	bs3427	01-28-91	KPNO	0	19	7.32	0.193	0.00	-
KW226	8.279	0.158	0.125	-	bs3427	01-24-91	KPNO	0	39	8.89	0.321	0.00	3.20
KW229	7.117	0.099	0.103	-	zmon	01-24-91	KPNO	0	29	7.54	0.250	0.00	-
KW232	8.460	0.231	0.215	-	bs3427	01-28-91	KPNO	0	39	9.23	0.389	0.00	3.50
KW265	6.542	0.005	0.051	-	bs3427	01-28-91	KPNO	0	29	6.61	0.006	0.00	2.10
KW265	6.597	0.003	0.058	-	bs3427	01-25-91	KPNO	0	09	6.61	0.006	0.00	2.10
KW284	6.204	0.151	0.200	-	bs3427	01-28-91	KPNO	0	09	6.78	0.261	0.00	2.90
KW284	6.217	0.157	0.171	-	zmon	01-24-91	KPNO	0	09	6.78	0.261	0.00	2.90
KW300	5.984	0.075	0.097	-	zmon	01-24-91	KPNO	0	09	6.30	0.172	0.00	2.50
KW318	8.103	0.151	0.132	-	bs3427	01-28-91	KPNO	0	29	8.65	0.291	0.00	3.00
KW328	6.431	0.095	0.110	-	bs3427	01-28-91	KPNO	0	09	6.85	0.203	0.00	2.90
KW340	7.957	0.137	0.139	-	bs3427	01-24-91	KPNO	0	19	8.48	0.259	0.00	3.00
KW348	6.403	0.101	0.140	-	bs3427	01-24-91	KPNO	0	09	6.78	0.168	0.00	2.60
KW40	7.402	0.089	0.090	-	bs3427	01-24-91	KPNO	0	19	7.79	0.220	0.00	-
KW428	5.257	0.527	0.579	-	bs3427	01-24-91	KPNO	0	09	6.90	0.963	0.00	5.00
KW429	7.954	0.147	0.153	-	bs3427	01-28-91	KPNO	0	29	8.53	0.297	0.00	3.20
KW445	7.547	0.090	0.107	-	bs3427	01-24-91	KPNO	0	29	7.96	0.208	0.00	2.70
KW449	7.492	0.112	0.125	-	bs3427	01-25-91	KPNO	1	19	7.91	0.210	0.00	2.70
KW45	7.787	0.112	0.119	-	bs3427	01-28-91	KPNO	0	29	8.25	0.231	0.00	3.00
KW50	6.306	0.115	0.123	-	bs3427	01-28-91	KPNO	0	09	6.75	0.190	0.00	2.50

V, B-V from Johnson (1952), except for JC123, which is from Jones and Cudworth (1983). (JC only good to 0.1 mag).
Spectral types from SIMBAD.

Continued, next page.

Table 3.5. (cont.)

cTTS

	J	J-K	J-L	J-L'	JLcal	Date(UT)	Tel	I	LL'	V	B-V	Av	SpT
CXTAU	9.962	1.112	-	1.658	h22686	11-23-89	IRTF	0	00	13.67	1.570	0.55	6.20
FPTAU	9.976	1.113	-	1.587	16tau	10-23-90	IRTF	1	91	13.91	1.550	0.00	6.55
GMAUR	9.498	0.992	-	1.353	h22686	11-23-89	IRTF	1	00	12.03	1.190	0.10	5.70
GOTAU	10.752	1.411	-	2.018	h22686	11-23-89	IRTF	0	02	14.89	1.460	2.44	6.00
HOTAU	11.199	1.372	-	2.026	h22686	11-24-89	IRTF	0	21	14.84	1.140	0.73	6.05
HUBBLE4	8.707	1.359	-	1.691	16tau	10-23-90	IRTF	0	90	12.73	1.680	-	5.70
LKCA8	9.800	1.522	-	2.398	16tau	10-23-90	IRTF	0	90	13.04	1.460	0.25	6.00
LKCA15	9.524	1.216	-	1.809	16tau	10-24-90	IRTF	0	90	12.09	1.320	-	5.50
SUAUR	7.295	1.274	-	2.270	16tau	10-25-90	IRTF	0	90	9.03	0.840	0.64	4.20
V773TAU	7.718	1.238	-	2.022	h22686	11-23-89	IRTF	1	00	10.65	1.370	2.04	5.20
V836TAU	9.874	1.154	-	1.709	h22686	11-23-89	IRTF	0	01	13.13	1.530	0.91	5.70
VYTAU	10.057	1.089	-	1.699	16tau	10-25-90	IRTF	0	91	13.75	1.510	1.02	6.00
ZZTAU	9.580	1.118	-	1.597	h22686	11-23-89	IRTF	0	00	14.28	1.480	0.65	6.40

V, B-V, and Av from K. Strom et al. (1989).
Spectral types from K. Strom et al. (1989) or from Scott Kenyon (private communication).

wTTS

	J	J-K	J-L	J-L'	JLcal	Date(UT)	Tel	I	LL'	V	B-V	Av	SpT
W032641	10.407	0.678	-	0.659	16tau	10-23-90	IRTF	0	93	12.05	0.900	0.30	5.10
W034903	9.936	0.819	-	0.954	16tau	10-23-90	IRTF	0	91	12.25	1.130	0.04	5.50
W035120N	10.480	0.609	-	0.712	16tau	10-23-90	IRTF	0	92	12.31	0.940	1.03	4.50
W035120N	10.482	0.626	-	0.727	16tau	10-23-90	IRTF	0	92	12.31	0.940	1.03	4.50
W035120S	10.156	0.569	-	0.649	16tau	10-23-90	IRTF	0	92	11.85	0.860	0.91	4.00
W035135S	10.878	0.651	-	0.781	h22686	11-24-89	IRTF	1	33	12.67	0.920	0.15	5.20
W035135N	11.810	0.728	-	0.839	16tau	10-24-90	IRTF	0	93	13.79	1.110	0.61	5.30
W040234	11.052	0.980	-	1.289	16tau	10-25-90	IRTF	0	92	14.67	1.370	0.38	6.20
W041529	11.198	0.730	-	0.813	16tau	10-23-90	IRTF	0	93	13.26	1.110	0.00	5.50
W041559	10.066	0.811	-	0.951	16tau	10-25-90	IRTF	0	91	12.28	1.130	0.00	5.70
W042417	8.900	0.552	-	0.628	16tau	10-23-90	IRTF	0	90	10.34	0.790	0.00	5.10
W042835	10.301	0.787	-	0.906	h22686	11-24-89	IRTF	1	03	12.53	1.180	0.15	5.50
W043124	10.635	0.705	-	0.789	h22686	11-24-89	IRTF	0	23	12.67	1.030	1.22	4.80
W043220	9.371	0.454	-	0.484	h22686	11-24-89	IRTF	0	32	10.95	0.820	0.91	3.80
W045251	9.079	0.891	-	1.034	h22686	11-23-89	IRTF	0	00	11.60	1.280	0.00	5.70
DITAU	9.441	1.055	-	1.283	h22686	11-23-89	IRTF	0	00	12.86	1.600	1.08	5.75
FFTAU	9.899	1.257	-	1.495	16tau	10-23-90	IRTF	0	90	13.67	2.060	-	5.85
HDE283572	7.501	0.584	-	0.688	16tau	10-23-90	IRTF	0	90	9.04	0.830	0.57	4.50
L155151	9.683	0.866	-	0.977	16tau	10-23-90	IRTF	0	90	12.06	1.230	0.00	5.70
L155155	10.272	0.973	-	1.090	16tau	10-23-90	IRTF	0	91	13.22	1.500	0.91	5.70
LKCA16	9.330	0.988	-	1.097	16tau	10-24-90	IRTF	0	90	12.51	1.530	1.22	5.70
LKCA19	8.962	0.766	-	0.842	16tau	10-24-90	IRTF	0	92	10.85	1.020	-	5.00
LKCA4	9.233	0.974	-	1.194	h22686	11-23-89	IRTF	0	00	12.49	1.470	0.95	5.70
LKCA4	9.254	0.984	-	1.193	16tau	10-23-90	IRTF	0	90	12.49	1.470	0.95	5.70
LKCA7	9.169	0.928	-	1.071	h22686	11-23-89	IRTF	0	00	12.55	1.390	0.76	6.00
SAO76411A	7.828	0.373	-	0.371	h22686	11-23-89	IRTF	1	00	8.85	0.590	0.00	4.10
SAO76428	8.519	0.333	-	0.368	16tau	10-23-90	IRTF	0	90	9.47	0.530	0.00	3.80
V410TAU	8.505	0.904	-	1.098	h22686	11-23-89	IRTF	0	00	10.92	1.180	0.00	5.70
V819TAU	9.591	1.153	-	1.389	h22686	11-24-89	IRTF	0	01	13.24	1.570	1.25	5.70
V819TAU	9.604	1.141	-	1.358	h22686	11-23-89	IRTF	1	00	13.24	1.570	1.25	5.70
V826TAU	9.217	0.962	-	1.085	16tau	10-23-90	IRTF	0	90	12.11	1.400	0.53	5.70
V827TAU	9.210	0.986	-	1.211	h22686	11-23-89	IRTF	0	00	12.18	1.400	0.61	6.00
V830TAU	9.472	0.948	-	1.099	16tau	10-23-90	IRTF	0	90	12.21	1.370	0.42	5.70

Note: The TTS source names beginning with "W" are a shorthand for the names given in Walter et al.(1988).
V, B-V, and Av from K. Strom et al. (1989).
Spectral types from K. Strom et al. (1989) or from Scott Kenyon (private communication).

Continued, next page.

Table 3.5. (cont.)

Woolley

	J	J-K	J-L	J-L'	JLcal	Date(UT)	Tel	I	LL'	V	B-V	Av	SpT
WL039	7.047	0.770	-	0.787	h22686	11-24-89	IRTF	1	00	9.27	1.210	0.00	5.60
WL135	5.900	0.418	-	0.459	16tau	10-23-90	IRTF	0	90	7.02	0.670	0.00	4.20
WL230	5.326	0.432	-	0.460	16tau	10-23-90	IRTF	1	90	6.46	0.670	0.00	4.60
WL6	5.258	0.325	-	0.404	16tau	10-24-90	IRTF	0	90	6.21	0.470	0.00	3.50
WL849	6.546	0.932	-	1.188	41ac	10-25-90	IRTF	0	90	10.42	1.520	0.00	6.30
WL900	6.920	0.837	-	0.960	41ac	10-25-90	IRTF	0	90	9.59	1.350	0.00	6.10
WL9112	6.369	0.572	-	0.641	16tau	10-23-90	IRTF	0	90	7.83	0.860	0.00	5.10
WL913	6.693	0.850	-	1.062	41ac	11-23-89	IRTF	1	00	9.62	1.440	0.00	6.00
WL9756A	6.789	0.655	-	0.754	41ac	11-24-89	IRTF	1	00	8.65	1.040	0.00	5.30
WL9761	4.415	0.214	-	0.257	41ac	10-25-90	IRTF	0	90	5.09	0.360	0.00	3.00
WL9771	3.408	0.066	-	0.120	41ac	10-25-90	IRTF	0	90	3.52	0.090	0.00	2.20
WL9772	8.082	0.696	-	0.744	41ac	10-26-90	IRTF	0	90	10.00	-	0.00	6.00
WL135	5.841	0.345	0.381	-	ntau	01-25-91	KPNO	0	09	7.02	0.670	0.00	4.20
WL230	5.230	0.371	0.367	-	ntau	01-25-91	KPNO	1	09	6.46	0.670	0.00	4.60
WL393	6.165	0.816	0.989	-	nvir	01-25-91	KPNO	1	09	9.63	1.520	0.00	6.20
WL408	6.340	0.819	1.056	-	bcom	01-28-91	KPNO	1	09	10.04	1.540	0.00	6.30
WL486	7.210	0.838	1.039	-	bcom	01-25-91	KPNO	0	09	11.40	1.560	0.00	6.40
WL514	5.885	0.829	0.990	-	nvir	01-25-91	KPNO	0	09	9.04	1.510	0.00	6.10
WL6	5.252	0.264	0.298	-	aper	10-06-90	KPNO	0	09	6.21	0.470	0.00	3.50
WL764	3.294	0.483	0.518	-	aper	10-10-90	KPNO	1	09	4.69	0.800	0.00	5.00
WL898	6.321	0.748	0.826	-	aper	10-10-90	KPNO	1	09	8.60	1.250	0.00	5.50
WL900	6.838	0.757	0.865	-	ntau	01-25-91	KPNO	0	09	9.59	1.350	0.00	6.10
WL913	6.658	0.793	0.923	-	ntau	01-25-91	KPNO	0	09	9.62	1.440	0.00	6.00
WL9658	5.774	0.396	0.426	-	aper	10-10-90	KPNO	1	09	6.97	0.720	0.00	4.50
WL9670A	4.166	0.288	0.307	-	aper	10-10-90	KPNO	1	09	4.99	0.460	0.00	3.50
WL9751	4.962	0.368	0.398	-	aper	10-10-90	KPNO	1	09	6.00	0.580	0.00	4.00
WL9761	4.445	0.185	0.216	-	aper	10-06-90	KPNO	0	09	5.09	0.360	0.00	3.00
WL9761	4.452	0.208	0.232	-	aper	10-10-90	KPNO	1	09	5.09	0.360	0.00	3.00
WL9771	3.364	0.033	0.050	-	aper	10-06-90	KPNO	0	09	3.52	0.090	0.00	2.50
WL9829	5.518	0.305	0.340	-	aper	10-06-90	KPNO	0	09	6.50	0.530	0.00	4.00

V, B-V and spectral types from Woolley catalog.

Table 3.6. M and N Magnitudes and Colors

Alpha Per

	J	J-K	J-L'	J-M	J-N	JLcal	Mcal	Ncal	JLdate	Mdate	Ndate	Tel	I	LL'MN	V	B-V	Av	SpT
HE1164	4.239	0.240	0.697	0.824	-	16tau	16tau	none	10-23-90	10-24-90	-	IRTF	1	9009	4.20	-0.080	0.31	1.50
HE145	6.872	0.022	0.050	-0.044	-	16tau	16tau	none	10-23-90	10-24-90	-	IRTF	1	9039	6.88	0.025	0.31	1.50
HE575	7.643	0.088	0.088	0.079	-	16tau	16tau	none	10-25-90	10-25-90	-	IRTF	1	9039	7.85	0.104	0.31	2.00

V, B-V from Stauffer et al. (1985 and 1989), and Mitchell (1960).
Spectral types from SIMBAD.

Pleiades

	J	J-K	J-L'	J-M	J-N	JLcal	Mcal	Ncal	JLdate	Mdate	Ndate	Tel	I	LL'MN	V	B-V	Av	SpT
HII2866	6.749	0.098	0.115	0.062	-	16tau	16tau	none	10-25-90	10-25-90	-	IRTF	1	9039	6.93	0.090	0.12	2.20
HII980	4.188	0.122	0.400	0.584	-	16tau	16tau	none	10-25-90	10-24-90	-	IRTF	0	9009	4.18	-0.060	0.12	1.60

V, B-V from Johnson and Mitchell (1958).
Spectral types from SIMBAD.

Ursa Major

	J	J-K	J-L'	J-M	J-N	JLcal	Mcal	Ncal	JLdate	Mdate	Ndate	Tel	I	LL'MN	V	B-V	Av	SpT
HD109011	6.431	0.664	0.731	0.717	-	h22686	pi4ori	none	11-23-89	11-23-89	-	IRTF	1	0039	8.09	0.930	0.00	5.20
HD110463	6.721	0.649	0.722	0.644	-	h22686	pi4ori	none	11-23-89	11-23-89	-	IRTF	1	0019	8.27	0.950	0.00	5.30
HD11131	5.617	0.399	0.436	0.409	-	41ac	41ac	none	10-25-90	10-25-90	-	IRTF	0	9009	6.76	0.610	0.00	4.00
HR1046	5.043	0.034	0.056	0.068	0.038	16tau	16tau	bpeg	10-26-90	10-26-90	-	IRTF	0	9003	5.08	0.050	0.00	2.10
HR2228	6.063	0.184	0.184	0.217	-0.034	16tau	16tau	bpeg	10-23-90	10-25-90	10-26-90	IRTF	1	9013	6.52	0.270	0.00	3.00
HR647	5.299	0.272	0.312	0.286	0.400	16tau	16tau	bpeg	10-26-90	10-26-90	10-26-90	IRTF	0	9003	6.06	0.400	0.00	3.40
HR68	4.403	0.033	0.055	0.054	0.126	41ac	41ac	bpeg	10-25-90	10-25-90	10-26-90	IRTF	0	9003	4.53	0.050	0.00	2.20
HR8170	5.268	0.393	0.453	0.386	-	41ac	41ac	none	10-26-90	10-26-90	-	IRTF	0	9009	6.40	0.530	0.00	3.80
HR8263	6.060	0.019	0.004	-0.002	-	41ac	41ac	none	10-26-90	10-26-90	-	IRTF	0	9009	6.25	0.050	0.00	2.20
HR8291	5.875	0.026	0.025	-0.007	-	41ac	41ac	none	10-26-90	10-26-90	-	IRTF	0	9019	6.10	0.060	0.00	2.20
HR8407	5.512	-0.009	-0.031	-0.053	-	41ac	41ac	none	10-25-90	10-25-90	-	IRTF	0	9019	5.60	-0.040	0.00	2.00
HR8984	4.139	0.115	0.134	0.120	-	41ac	41ac	none	10-25-90	10-25-90	-	IRTF	0	9009	4.52	0.190	0.00	2.70

V, B-V from Johnson and Knuckles (1957), except for HD11131 -- from SIMBAD.
Spectral types from SIMBAD.

Continued, next page.

Table 3.6. (cont.)

Hyades

	J	J-K	J-L'	J-M	J-N	JLcal	Mcal	Ncal	JLdate	Mdate	Ndate	Tel	I	LL'MN	V	B-V	Av	SpT
HA578	7.097	0.559	0.620	0.506	-	16tau	16tau	none	10-26-90	10-26-90	-	IRTF	0	9029	8.51	0.841	0.00	4.50

V, B-V from Johnson and Knuckles (1955) (3 decimal places), and Johnson, Mitchell and Iriarte (1962) (2 decimal places).
Spectral types from SIMBAD.

wTTS

	J	J-K	J-L'	J-M	J-N	JLcal	Mcal	Ncal	JLdate	Mdate	Ndate	Tel	I	LL'MN	V	B-V	Av	SpT
W034903	9.936	0.819	0.954	0.867	-	16tau	16tau	none	10-23-90	10-25-90	-	IRTF	0	9139	12.25	1.130	0.04	5.50
W042417	8.900	0.552	0.628	0.537	-	16tau	16tau	none	10-23-90	10-24-90	-	IRTF	0	9039	10.34	0.790	0.00	5.10
W043220	9.371	0.454	0.484	0.459	-	h22686	16tau	none	11-24-89	10-26-90	-	IRTF	0	3239	10.95	0.820	0.91	3.80
W045251	9.079	0.891	1.034	0.892	-	h22686	pi4ori	none	11-23-89	11-23-89	-	IRTF	0	0039	11.60	1.280	0.00	5.70
DITAU	9.441	1.055	1.283	1.166	1.808	h22686	pi4ori	atau	11-23-89	11-23-89	11-24-89	IRTF	0	0033	12.86	1.600	1.08	5.75
FFTAU	9.899	1.257	1.495	1.382	-	16tau	16tau	none	10-23-90	10-26-90	-	IRTF	0	9039	13.67	2.060	-	5.85
FPTAU	9.976	1.113	1.587	1.847	3.459	16tau	pi4ori	atau	10-23-90	11-24-89	11-24-89	IRTF	1	9133	13.91	1.550	0.00	6.55
HDE283572	7.501	0.584	0.688	0.716	-	16tau	16tau	none	10-23-90	10-24-90	-	IRTF	0	9019	9.04	0.830	0.57	4.50
LKCA16	9.330	0.988	1.097	1.143	-	16tau	16tau	none	10-24-90	10-25-90	-	IRTF	0	9039	12.51	1.530	1.22	5.70
LKCA19	8.962	0.766	0.842	0.906	-	16tau	16tau	none	10-24-90	10-26-90	-	IRTF	0	9239	10.85	1.020	-	5.00
LKCA4	9.233	0.974	1.194	1.134	-	h22686	pi4ori	none	11-23-89	11-23-89	-	IRTF	0	0039	12.49	1.470	0.95	5.70
LKCA7	9.169	0.928	1.071	1.069	-	h22686	pi4ori	none	11-23-89	11-23-89	-	IRTF	0	0039	12.55	1.390	0.76	6.00
SAO76411A	7.828	0.373	0.371	0.227	0.756	h22686	pi4ori	atau	11-23-89	11-23-89	11-24-89	IRTF	1	0033	8.85	0.590	0.00	4.10
SAO76428	8.519	0.333	0.368	0.317	-	16tau	16tau	none	10-23-90	10-24-90	-	IRTF	0	9039	9.47	0.530	0.00	3.80
V410TAU	8.505	0.904	1.098	1.015	-	h22686	pi4ori	none	11-23-89	11-23-89	-	IRTF	0	0039	10.92	1.180	0.00	5.70
V819TAU	9.604	1.141	1.358	1.244	-	h22686	pi4ori	none	11-23-89	11-23-89	-	IRTF	1	0039	13.24	1.570	1.25	5.70
V826TAU	9.217	0.962	1.085	1.110	-	16tau	16tau	none	10-23-90	10-24-90	-	IRTF	0	9039	12.11	1.400	0.53	5.70
V827TAU	9.210	0.986	1.211	1.082	-	h22686	pi4ori	none	11-23-89	11-23-89	-	IRTF	0	0039	12.18	1.400	0.61	6.00
V830TAU	9.472	0.948	1.099	1.019	-	16tau	16tau	none	10-23-90	10-24-90	-	IRTF	0	9039	12.21	1.370	0.42	5.70

Note: The TTS source names beginning with "W" are a shorthand for the names given in Walter et al.(1988).
V, B-V and SpT from K. Strom et al.(1989), or Scott Kenyon (private communication).

Continued, next page.

Table 3.6. (cont.)

cTTS

	J	J-K	J-L'	J-M	J-N	JLcal	Mcal	Ncal	JLdate	Mdate	Ndate	Tel	I	LL'MN	V	B-V	Av	SpT
CXTAU	9.962	1.112	1.658	1.915	4.067	h22686	pi4ori	atau	11-23-89	11-23-89	11-24-89	IRTF	0	0033	13.67	1.570	0.55	6.20
FPTAU	9.976	1.113	1.587	1.847	3.459	16tau	pi4ori	atau	10-23-90	11-24-89	11-24-89	IRTF	1	9133	13.91	1.550	0.00	6.55
GMAUR	9.498	0.992	1.353	1.441	-	h22686	pi4ori	none	11-23-89	11-23-89	-	IRTF	1	0039	12.03	1.190	0.10	5.70
GOTAU	10.752	1.411	2.018	2.250	4.201	h22686	pi4ori	atau	11-23-89	11-23-89	11-24-89	IRTF	0	0233	14.89	1.460	2.44	6.00
HOTAU	11.199	1.372	2.026	2.480	-	h22686	pi4ori	none	11-24-89	11-24-89	-	IRTF	0	2139	14.84	1.140	0.73	6.05
HUBBLE4	8.707	1.359	1.691	1.698	-	16tau	16tau	none	10-23-90	10-24-90	-	IRTF	0	9039	12.73	1.680	-	5.70
LKCA8	9.800	1.522	2.398	2.620	-	16tau	16tau	none	10-23-90	10-26-90	-	IRTF	0	9029	13.04	1.460	0.25	6.00
LKCA15	9.524	1.216	1.809	2.159	-	16tau	16tau	none	10-24-90	10-26-90	-	IRTF	0	9039	12.09	1.320	-	5.50
SUAUR	7.295	1.274	2.270	2.591	4.789	16tau	16tau	atau	10-25-90	10-25-90	10-25-90	IRTF	0	9000	9.03	0.840	0.64	4.20
V773TAU	7.718	1.238	2.022	2.230	-	h22686	pi4ori	none	11-23-89	11-23-89	-	IRTF	1	0029	10.65	1.370	2.04	5.20
V836TAU	9.874	1.154	1.709	1.921	-	h22686	pi4ori	none	11-23-89	11-23-89	-	IRTF	0	0139	13.13	1.530	0.91	5.70
VYTAU	10.057	1.089	1.699	1.980	-	16tau	16tau	none	10-25-90	10-25-90	-	IRTF	0	9139	13.75	1.510	1.02	6.00
ZZTAU	9.580	1.118	1.597	1.697	3.129	h22686	pi4ori	atau	11-23-89	11-23-89	11-24-89	IRTF	0	0033	14.28	1.480	0.65	6.40

V, B-V and SpT from K. Strom et al. (1989), or Scott Kenyon (private communication).

Woolley

	J	J-K	J-L'	J-M	J-N	JLcal	Mcal	Ncal	JLdate	Mdate	Ndate	Tel	I	LL'MN	V	B-V	Av	SpT
WL039	7.047	0.770	0.787	0.733	-	h22686	pi4ori	none	11-24-89	11-24-89	-	IRTF	1	0039	9.27	1.210	0.00	5.60
WL135	5.900	0.418	0.459	0.413	-	16tau	16tau	none	10-23-90	10-25-90	-	IRTF	0	9019	7.02	0.670	0.00	4.20
WL230	5.326	0.432	0.460	0.455	-	16tau	16tau	none	10-23-90	10-25-90	-	IRTF	1	9009	6.46	0.670	0.00	4.60
WL6	5.258	0.325	0.404	0.393	0.441	16tau	41ac	bpeg	10-24-90	10-25-90	10-26-90	IRTF	0	9003	6.21	0.470	0.00	3.50
WL849	6.546	0.932	1.188	1.112	-	41ac	41ac	none	10-25-90	10-25-90	-	IRTF	0	9009	10.42	1.520	0.00	6.30
WL900	6.920	0.837	0.960	0.937	-	41ac	41ac	none	10-25-90	10-25-90	-	IRTF	0	9019	9.59	1.350	0.00	6.10
WL9112	6.369	0.572	0.641	0.573	-	16tau	16tau	none	10-23-90	10-25-90	-	IRTF	0	9009	7.83	0.860	0.00	5.10
WL913	6.693	0.850	1.062	0.997	-	41ac	41ac	none	11-23-89	11-23-89	-	IRTF	1	0009	9.62	1.440	0.00	6.00
WL9756A	6.789	0.655	0.754	0.702	-	41ac	41ac	none	11-24-89	11-24-89	-	IRTF	1	0029	8.65	1.040	0.00	5.30
WL9761	4.415	0.214	0.257	0.215	-	41ac	41ac	none	10-25-90	10-25-90	-	IRTF	0	9009	5.09	0.360	0.00	3.00
WL9771	3.408	0.066	0.120	0.097	0.222	41ac	41ac	bpeg	10-25-90	10-25-90	10-26-90	IRTF	0	9002	3.52	0.090	0.00	2.20
WL9772	8.082	0.696	0.744	0.696	-	41ac	41ac	none	10-26-90	10-26-90	-	IRTF	0	9039	10.00	- 0	0.00	6.00

V, B-V, and Spectral type from Woolley catalog.

Continued, next page.

Table 3.6. (cont.)

Ae\Be stars

	J	J-K	J-L'	J-M	J-N	JLcal	Mcal	Ncal	JLdate	Mdate	Ndate	Tel	I	LL'MN
ABAUR	6.168	1.856	3.110	3.507	5.544	16tau	16tau	atau	10-25-90	10-25-90	10-25-90	IRTF	0	9000
BD46	8.500	1.909	3.271	3.664	4.974	41ac	41ac	bpeg	10-26-90	10-26-90	10-26-90	IRTF	0	9001
HD245185	9.370	1.287	2.453	3.020	6.607	16tau	16tau	atau	10-26-90	10-26-90	10-25-90	IRTF	0	9030
HD250550	8.513	2.009	3.365	3.799	5.944	16tau	16tau	atau	10-26-90	10-26-90	10-25-90	IRTF	0	9012
HIORI	10.608	1.382	2.572	3.132	5.582	16tau	16tau	atau	10-25-90	10-25-90	10-25-90	IRTF	0	9001
HKORI	9.700	2.203	3.886	4.515	6.907	16tau	16tau	atau	10-25-90	10-25-90	10-25-90	IRTF	0	9133
LKHA208	10.578	1.235	3.165	4.083	7.750	16tau	16tau	atau	10-25-90	10-25-90	10-25-90	IRTF	0	9000
LKHA233	11.246	2.783	5.223	6.026	8.762	41ac	41ac	bpeg	10-26-90	10-26-90	10-25-90	IRTF	0	9032
LKHA257	11.252	1.661	2.787	3.042	4.746	41ac	41ac	bpeg	10-26-90	10-26-90	10-26-90	IRTF	0	9001
RMON	9.652	3.750	6.279	7.136	9.467	16tau	16tau	atau	10-26-90	10-26-90	10-26-90	IRTF	0	9033
RRTAU	9.562	2.546	3.972	4.367	6.012	16tau	16tau	atau	10-26-90	10-26-90	10-25-90	IRTF	0	9001
SUAUR	7.295	1.274	2.270	2.591	4.789	16tau	16tau	atau	10-25-90	10-25-90	10-25-90	IRTF	0	9022

Chapter 4

RESULTS

4.1 Introduction

The goal of this work is to determine observationally the evolution of the dust population in circumstellar disks around young stars. As discussed in previous chapters, particularly Chapter 2, thermal dust emission produces a shallower slope in the observed spectral energy distribution (SED) of the star–disk system than would be expected from the stellar photosphere alone, resulting in near-infrared colors which are redder than photospheric colors. In this chapter the near-infrared colors of the five main sequence clusters and one pre-main sequence cluster comprising the sample for this study are examined graphically for the diagnostic excess emission. Correlations of infrared colors with stellar age and spectral type are sought.

A quantitative measure of the sensitivity of this study to circumstellar dust grains is presented by comparing the observed colors with those predicted for a star having a circumstellar disk, giving particular attention to the case when the disk is optically thin. It will be seen that the observations presented are sufficient to detect a mass in μm-sized grains as small as $10^{20} - 10^{21}$ g, the mass of a typical asteroid!

The basic results and concepts are first presented with the JKLL′ (1–4 μm) data set, which constitutes the majority of the database. Observations in the 5–10 μm range (M and N) are presented separately afterwards. Measurements at

these longer wavelengths are difficult and time-consuming owing to relatively poor atmospheric transmission and high ambient thermal background. As a result, only the brightest stars could be observed at M and N. The M and N observations support the findings of the JKLL' data, but the data set is far more limited.

Throughout this chapter, the data sets from each of the two telescope facilities are examined separately, as the photometric systems at the two telescopes are different. The transformation equations between the two photometric systems are not well known, making it difficult to combine the data sets with confidence. Fortunately, this presents no real difficulty in the interpretation of the results.

Only the observed colors and model predictions are presented in this chapter. Basic results are stated, but the interpretation of the results will be discussed in Chapter 5.

4.2 The JKLL′ (1–4μm) Results

4.2.1 The Pre-Main Sequence Stars

Large infrared color excesses arising from thermal dust emission are easily seen in the pre-main sequence classical T-Tauri stars (cTTS). Figure 4.1 displays the observed J-L′ *vs.* J-K colors of both the cTTS and wTTS (weak-lined T-Tauri stars), along with nearby Milky Way disk stars from the Woolley catalog. The Woolley stars are presumed to represent diskless main sequence standards; also, they are all within 25 pc, so that interstellar extinction is minimal. The data were corrected for atmospheric extinction and interstellar reddening, when known, using the Elias (1978) reddening law for the Taurus region.[1] A_V are given in the data tables in Chapter 3. From Figure 4.1, it is seen that the wTTS colors are generally

[1]No attempt has been made to convert Elias's reddening law, which was derived in the CIT photometric system, to the KPNO or IRTF photometric systems. Fortunately, the success in de-reddening the wTTS indicates the reddening law works just fine as is.

consistent with those of main sequence stars. The wTTS and Woolley stars form a well-defined locus. The cTTS have infrared colors that are much larger (redder) than the main sequence stars, and do not form a well-defined locus. Note the large displacement of the cTTS in the direction of positive J-L′ from an imaginary extension of the main sequence locus. This is the diagnostic signature of a thermal dust excess.

Interstellar extinction will also cause observed colors to appear redder than the intrinsic photospheric colors. However, the effect of interstellar reddening is noticeably different from the effect of thermal dust emission arising from circumstellar material. An arrow in Figure 4.1 illustrates the change in J-L′ *vs.* J-K color resulting from 1 magnitude of visual extinction (1 A_V). (This arrow is commonly called the "reddening vector.") Note the shift is *parallel* to the locus of Woolley and wTTS. This is clearly demonstrated by the two lone wTTS stars far to the right of the main sequence locus, FF Tau and Hubble 4. The visual extinction to these stars is not yet known, so no interstellar reddening correction was applied. Note that despite the large apparent reddening, there is no vertical displacement from an imaginary extension of the main sequence locus. This is important; it clearly shows that reddening should not mimic an infrared excess for the color indices chosen. This is not necessarily true for other choices of color indices, such as J-H *vs.* H-K.

Only one wTTS shows a vertical displacement suggestive of an optically thin excess, W040234 (J-K = 0.899, J-L′ = 1.191). Walter *et al.* (1988) assigns a spectral type M2 to this star. Although the main sequence locus appears to be a straight line in Figure 4.1, Bessell and Brett (1988) found a natural turnup in the locus at spectral types in the M range. It is conceivable that W040234 is a late-type star which naturally resides on the upturned portion of the main sequence. In that case, the excess might not be due to dust. Spots are another

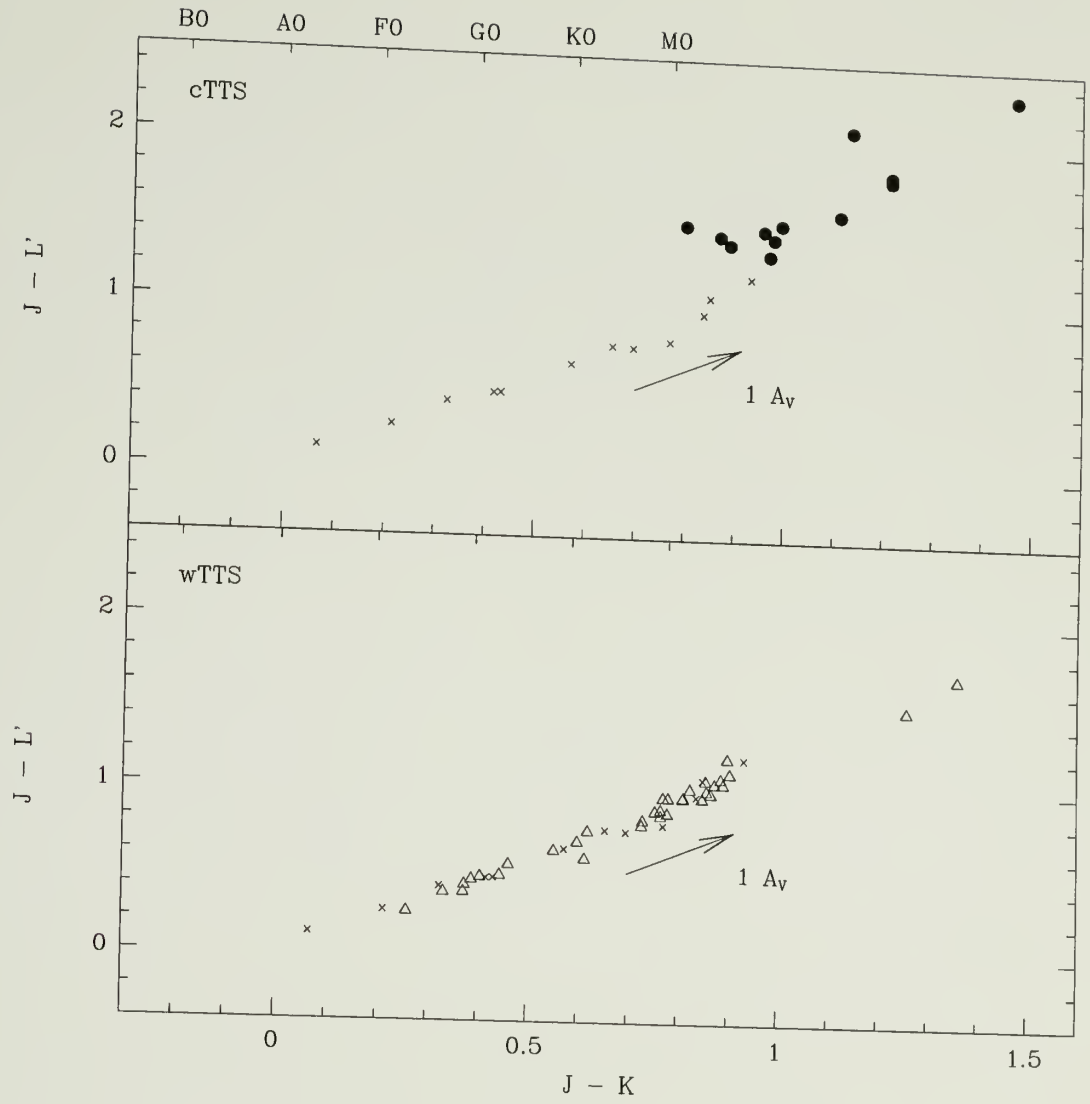

Figure 4.1. TTS and Woolley JKLL′ colors. J-L′ vs. J-K for the cTTS and wTTS in Taurus-Auriga, all observed at the IRTF. In both frames, the photospheric colors of main sequence stars are determined by the observed colors of nearby Woolley disk stars, pictured as"x"es. The effect of 1 A_V of interstellar reddening is shown. TTS with known interstellar extinction were de-reddened. (a) The observed colors of cTTS are displayed by filled circles. Note the cTTS are all significantly redder than the Woolley colors, and do not form a tight locus. (b) The observed colors of the wTTS are displayed as open triangles. In contrast to the cTTS, the wTTS appear to have colors similar to the Woolley stars, forming a tight locus. Note that the two reddest wTTS appear to lie along an extension of the line formed by the other wTTS and Woolley stars.

possible source of an infrared excess, as discussed briefly in Section 4.4, and Chapter 5. Using the evolutionary tracks of D'Antona and Mazzitelli (1994), Michael R. Meyer of the University of Massachusetts at Amherst has determined the age of W040234 to be between 1-3 Myr (private communication).

According to ages provided by Meyer, the oldest cTTS observed, GO Tau, has an age of 3×10^6 yr. For the sample observed, no stars with age greater than 3×10^6 yr show evidence of excess emission. Some of the wTTS which show no evidence of excess emission are as young as 0.3–1 Myr of age. A general table of individual ages has not been included in this work.

Table 4.1 summarizes the interesting stars noted in this subsection.

Table 4.1. Interesting Stars

Star	*Explanation for Excess*
HE1164	Be star (ff emission)
HII980	Be star (ff emission)
W040234	Uncertain; possible thermal excess

4.2.2 The Main Sequence Stars

Figures 4.2 display the J-L or J-L' colors *vs.* J-K for each of the individual main sequence clusters, plus nearby Milky Way disk stars chosen from the Woolley catalog. The data were corrected for atmospheric extinction and interstellar reddening. Reddening values may be found in the data tables in Chapter 3. Figures 4.3 display the same data, but simultaneously. In each case, Part *(a)* presents the KPNO data, part *(b)* the IRTF data.

It can be seen from Figures 4.2 and 4.3 that between the two telescope facilities, the range of spectral types observed for each cluster is fairly broad. The dimmer late-type stars were observed at the IRTF, while the brighter stars were observed at KPNO. The coverage in spectral type shown for Alpha Per and the

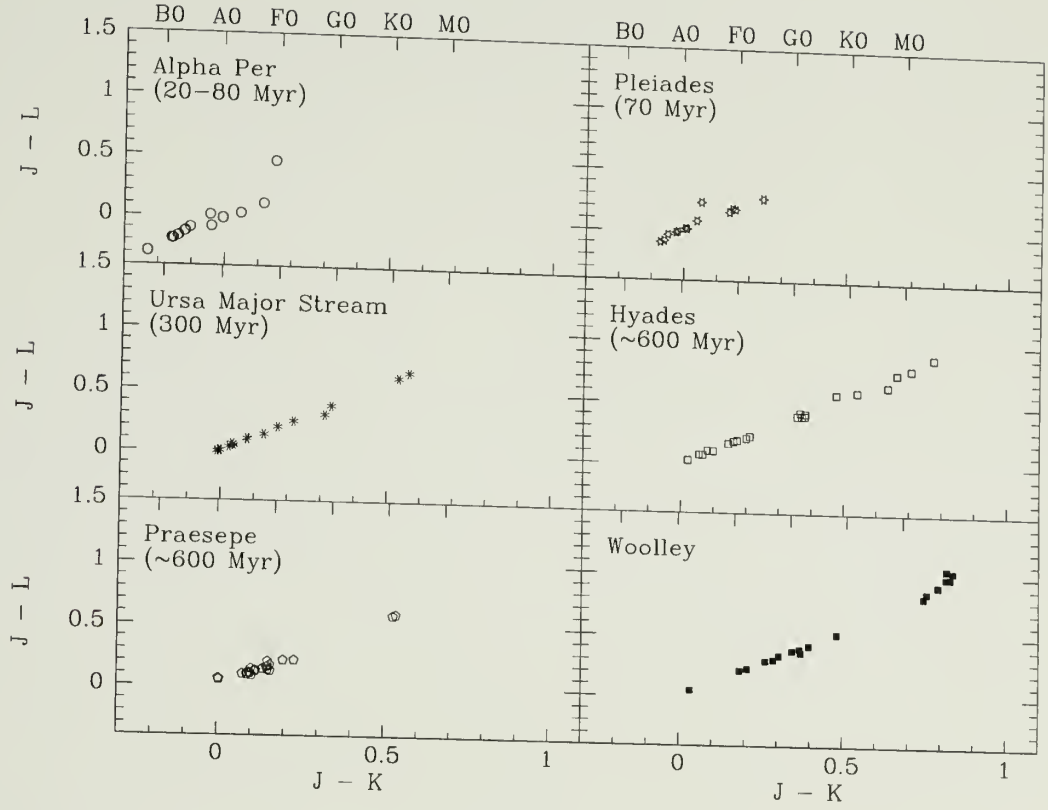

Figure 4.2. Main sequence JKLL′ colors, separated by cluster. (a) J-L′ vs. J-K for all the KPNO data. Note that for the most part, in each cluster the stars form a tight linear locus. One star in Alpha Persei and one star in the Pleiades strongly deviate from this trend.

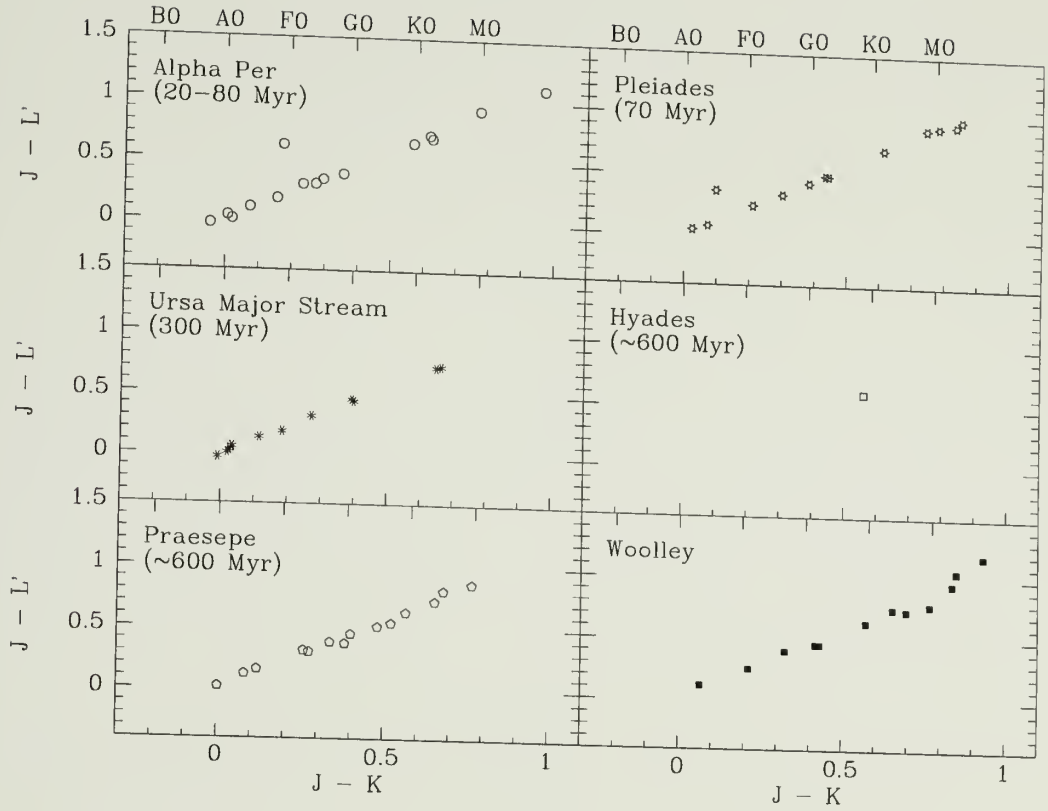

Figure 4.2. (cont.) (b) J-L′ vs. J-K for all the main sequence IRTF data. Again, with the exception of one star in Alpha Persei and one in the Pleiades, the stars form a tight linear locus in each cluster. Note that only one star was observed in the Hyades.

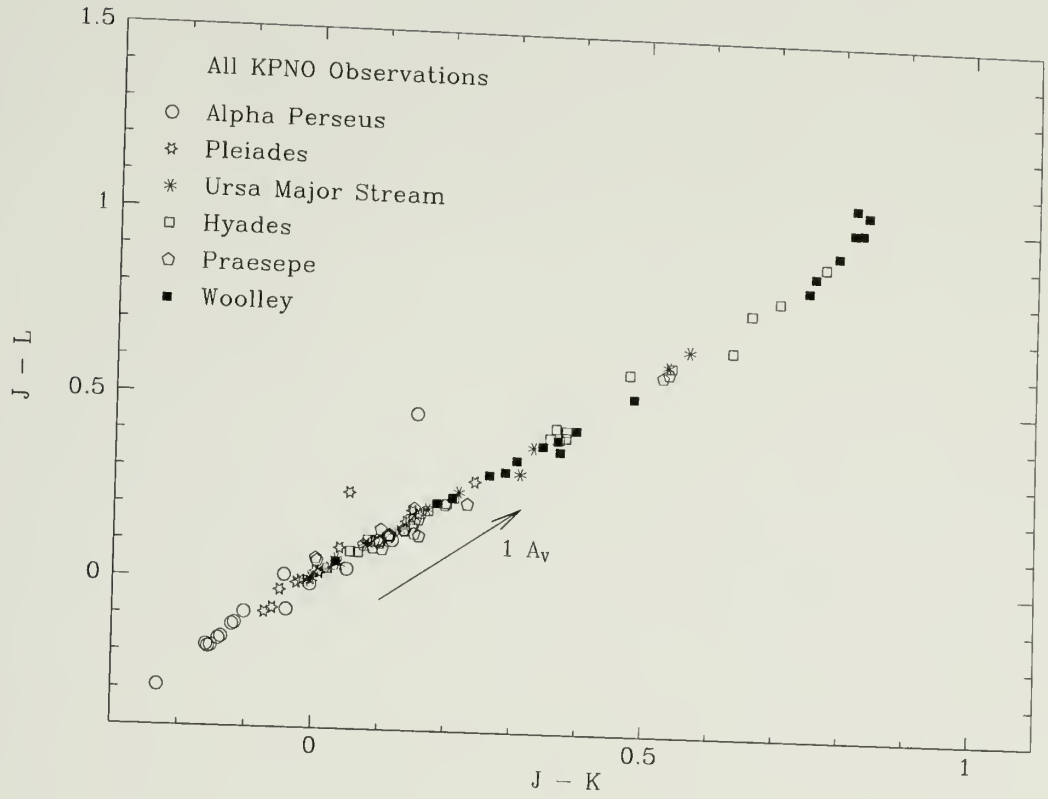

Figure 4.3. Main sequence JKLL′ colors, combined by telescope. (a) All J-L vs. J-K for the main sequence cluster stars observed at KPNO. Clusters are differentiated by symbol. The effect of 1 A_V of interstellar reddening is shown. Note how tight a locus is formed by the majority of the stars. Only two stars deviate significantly from the locus, HE1164 and HII980. Note they sit well *above* the main sequence locus. They are both Be stars; the reddening is caused by free-free emission, not thermal dust emission.

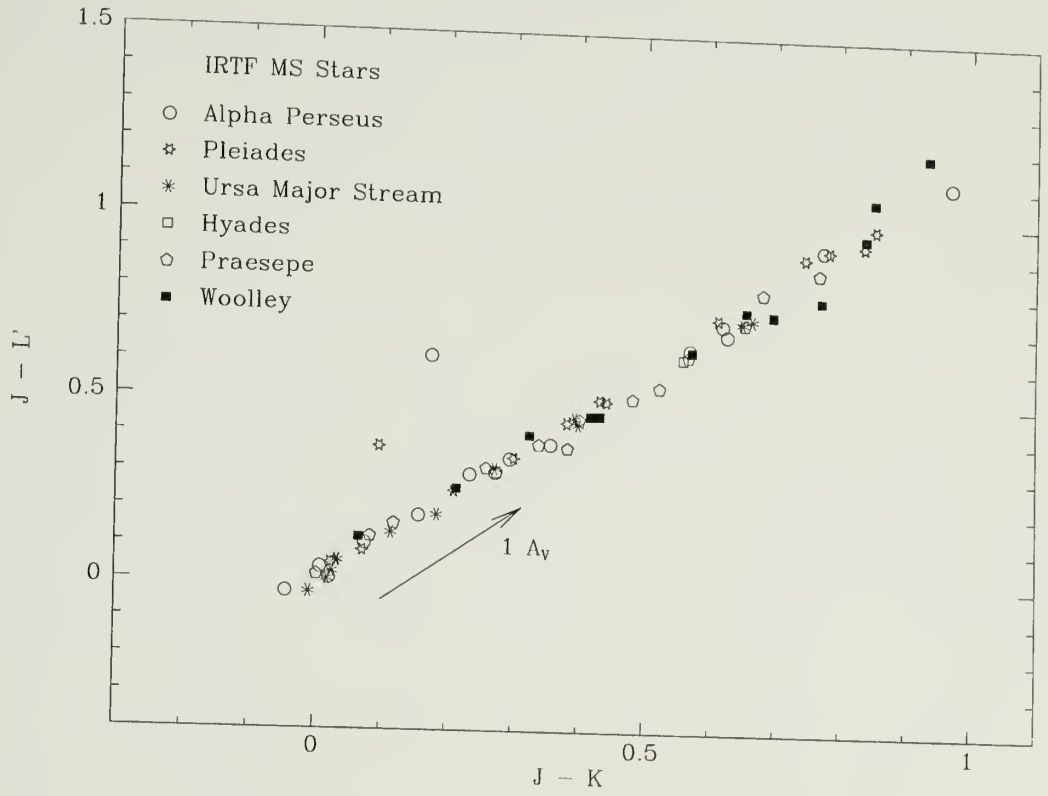

Figure 4.3. (cont.) (b) All J-L′ vs. J-K for the main sequence cluster stars observed at the IRTF. Clusters are differentiated by symbol. The effect of 1 A_V of interstellar reddening is shown. Again, note how tight a locus is formed by the majority of the stars. The same two Be stars as in Figure (a) deviate significantly from the main sequence locus.

Pleiades is somewhat deceptive; a number of the observations of late-type stars in Alpha Per and the Pleiades made at the IRTF are questionable. A possible problem with backlash in the dewar filter wheel reduced the flux by 30% for an apparently random selection of measurements at all wavelengths. Normally such data would be thrown away, but the measurement were important enough that much effort was expended to retrieve them. If the visual result truly reflects the success of that effort, the retrieval process worked reasonably well. The process used to correct these data was described in the previous Chapter.

With the exception of two Be stars, HE1164 in Alpha Per and HII980 in the Pleiades, the stellar colors form a very well-defined locus in each photometric system. The observed excess in the Be stars is produced by free-free emission, not thermal dust emission. However, the Be stars have been left in the data set to demonstrate how stars with infrared excesses may be diagnosed.

The Woolley stars are presumed to represent diskless standards; the stellar colors of all the main sequence cluster stars agree well with the Woolley colors. No infrared emission in excess of a stellar photosphere is apparent for any of the clusters, even the youngest cluster, Alpha Perseus, which is 20–80 Myr of age.

The main sequence locus is better defined in Figures 4.3 than in Figures 4.1. Assuming the use of the Elias reddening law is appropriate for all the stars in this program, it is clear from the reddening vector displayed in Figures 4.3 that interstellar reddening moves the infrared colors *along* the main sequence locus. Except in the case of very large extinctions for late-type stars, the effects of reddening are thus not visually apparent on a diagram of J-L (or J-L′) *vs.* J-K (for the exception, recall the natural turnup in the main sequence locus for very late-type stars). The beauty of this result is that it implies the chosen method does not, in general, require accurate reddening determination for the sources. The

same is not true if one wishes to determine *absolute* excess fluxes, the method employed by K. Strom *et al.* (1989).

Compare the effect of reddening to the behavior of the Be stars. The Be stars have infrared colors which deviate highly from the main sequence colors. A line connecting the two Be stars shows the path a B star would follow in moving off the main sequence locus. The infrared excess emission from the Be star is such that the the star does not move along the main sequence, as for interstellar extinction, but is vertically displaced from the main sequence locus. This is the signature we seek. One must be a little careful in this analogy, in that this work focuses on thermal dust emission, while the excess infrared emission in Be stars arises from free-free (gas) emission, not dust. The effects of thermal dust emission are best observed in the cTTS stars. Again, the colors are displaced vertically from the main sequence locus.

The collective IRTF data set, including both the TTS and the main sequence stars, is displayed in Figure 4.4. The vertical deviations from the main sequence locus for the two Be stars and the cTTS are clearly seen.

4.2.3 Comparison of Observed Colors with Model Predictions

By visual inspection of the J-L *vs.* J-K color plots, it has been determined that no obvious signature of thermal dust emission is observed after a stellar age of approximately 3×10^6 yr. A model is required to place an upper limit on the amount of dust which can reside near the star, given the observed results.

The model used is described in detail in Appendix C. Dust grains are heated by the central star, then radiate according to a specified emission efficiency law at their equilibrium temperature. In this model, shadowing of grains by other grains (optical depth) is taken into account when calculating the grain equilibrium temperature. A "bow-tie" disk geometry is assumed, with disk scale height

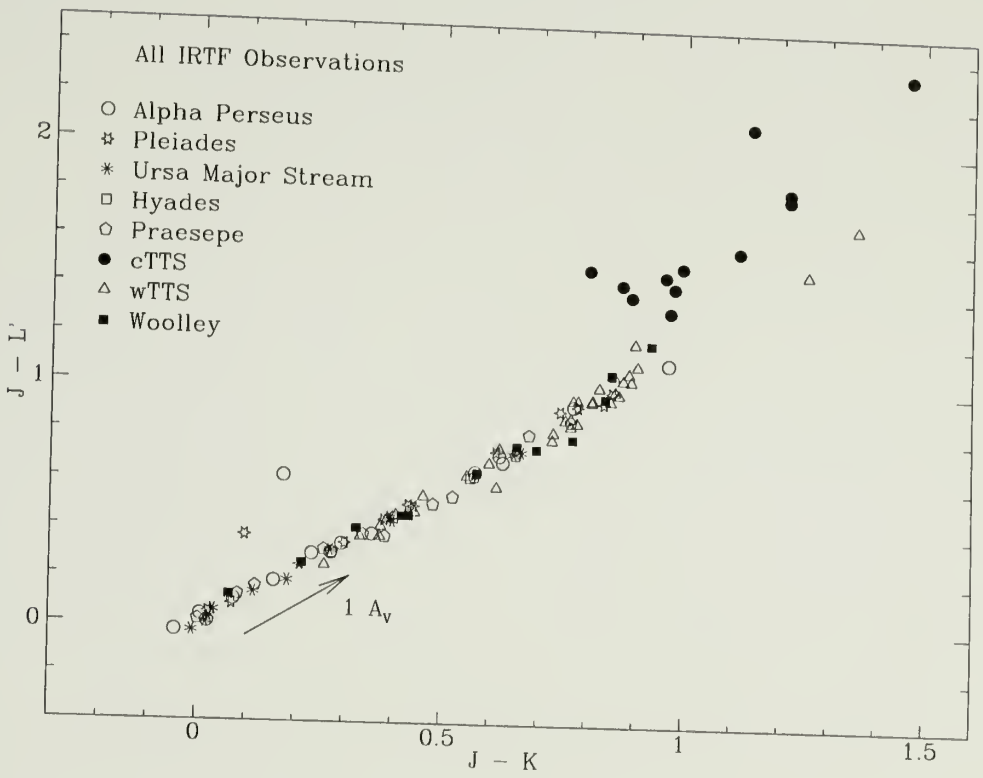

Figure 4.4. J-L′ vs. J-K for the entire IRTF data set. Clusters are differentiated by symbol. The effect of 1 A_V of interstellar reddening is shown. The vertical deviations from the main sequence locus for the two Be stars and the cTTS are clearly seen.

proportional to distance from the star. To simplify the model, all dust grains in the disk are presumed to have radius 1 μm, as discussed in Section 1.5.1. The choice of grain emission efficiency law is discussed in Chapter 2. The model calculates the expected infrared colors of the central star plus disk emission as a function of total dust mass.

A power law is assumed for the surface mass density. A disk mass surface density established by Poynting-Robertson drag decreases linearly with distance from the star (Link *et al.*, 1975). Link *et al.* determined that the spatial density of dust in our Solar System between 0.08 and 1.5 AU obeys a power law with index of approximately -1.3. If the mass surface density is defined to be $\sigma(r) = \sigma_0 r^{-\alpha}$, examination of the cases where $\alpha = 1$ and $\alpha = 2$ bracket these physically realistic cases.

The model parameters chosen are:

Table 4.2. Model Parameters

Dust destruction temperature	1800 K
Disk inner radius	Set by dust destruction temp
Disk outer radius	3 AU
Mass surface density law	$\sigma(r) = \sigma_0 r^{-\alpha}$, $\alpha = 1, 2$
Scale height of disk	$h(r) = h_0 r$; $h_0 = r(1\ \mathrm{AU}) = 5 \times 10^{11}$ cm
Effective T of central star	15,000 10,000 7000 5000 4000 3000 K
Stellar radius	4.90 2.75 1.25 0.90 0.75 0.50 $R_\odot$
Stellar luminosity	$L_* = 4\pi R_*^2 \sigma T^4$
Particle size distribution	Uniform; particle radius $a = 1\mu$m
Particle density	$\rho = 2$ g cm^{-3}
Total disk mass	$10^{18} - 10^{26}$ g
Grain emission efficiency	$1/(1 + (\lambda/2a)), \approx 2a/\lambda$ for $\lambda \gg a$

Before examining the model results, one more thing needs to be done. Since we are looking for vertical displacements on the plots, the plots presented thus far do not display the data in the most useful form. The slope of the main sequence locus makes it difficult to discern the relatively small vertical displacements within

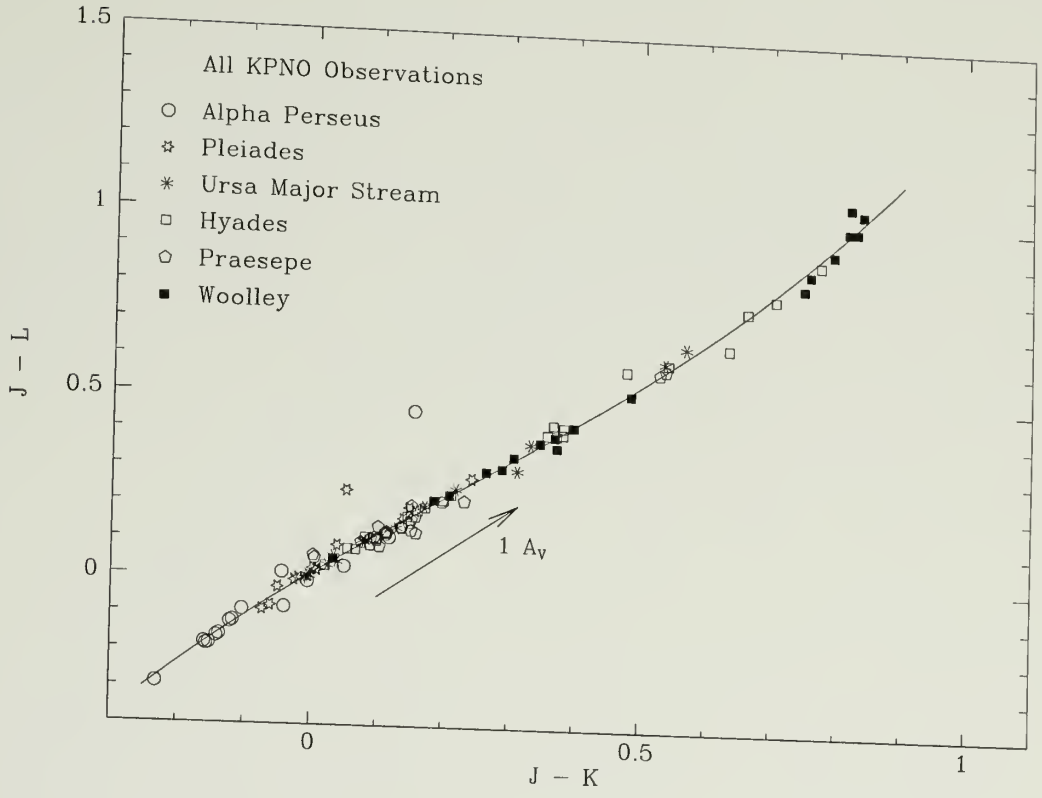

Figure 4.5. Third order polynomial fit to main sequence JKLL′ colors. (a) Third order polynomial fit to all the KPNO J-L vs. J-K results. The two Be stars were not included in data used for the best-fit routine.

the main sequence locus. The data is better viewed if the slope of the main sequence is removed, after which the vertical scale may be expanded. To accomplish this, a third-order polynomial fit was performed to the main sequence stars only (no Be stars or TTS). The corresponding fits to the KPNO and IRTF data are shown in Figures 4.5.

The residual J-L and J-L′ *vs.* J-K colors for the main sequence stars alone are shown in Figures 4.6 and 4.7. Superimposed on the residuals are the calculated model colors. Two mass surface density laws are displayed. Figures 4.6 shows the results for a disk with a surface mass density which decreases linearly with radial

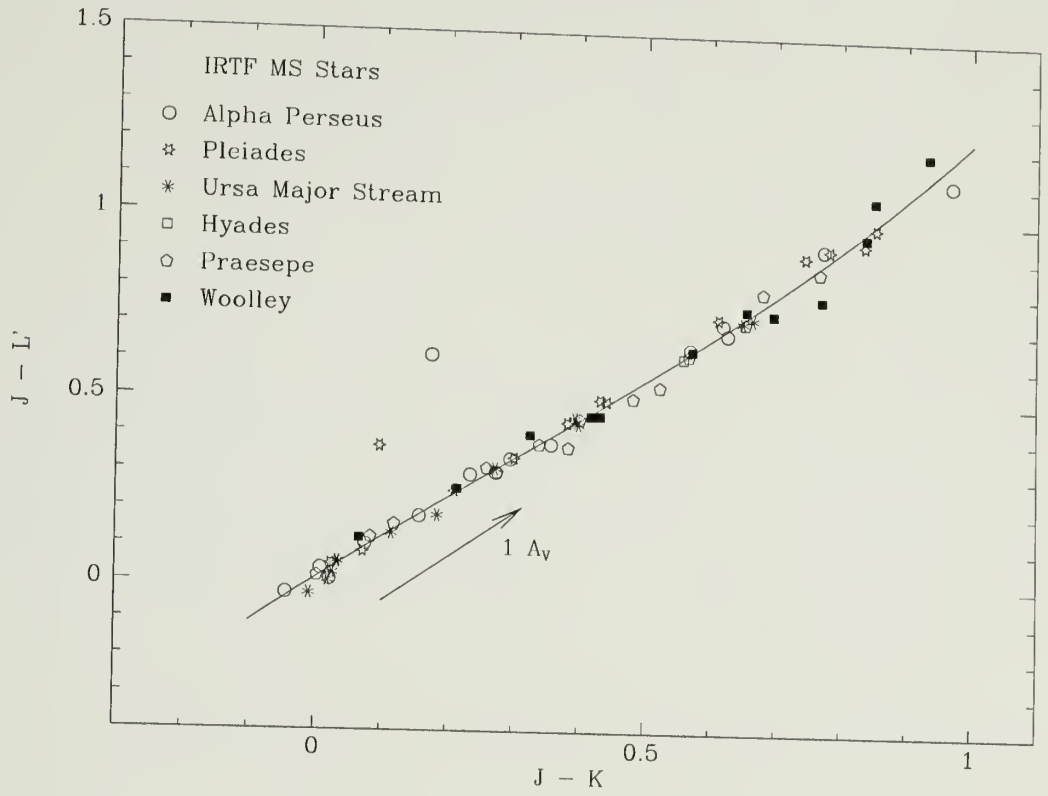

Figure 4.5. (b) (cont.) Third order polynomial fit to all the IRTF J-L′ vs. J-K main sequence results. The TTS and the two Be stars were not included in data used for the best-fit routine.

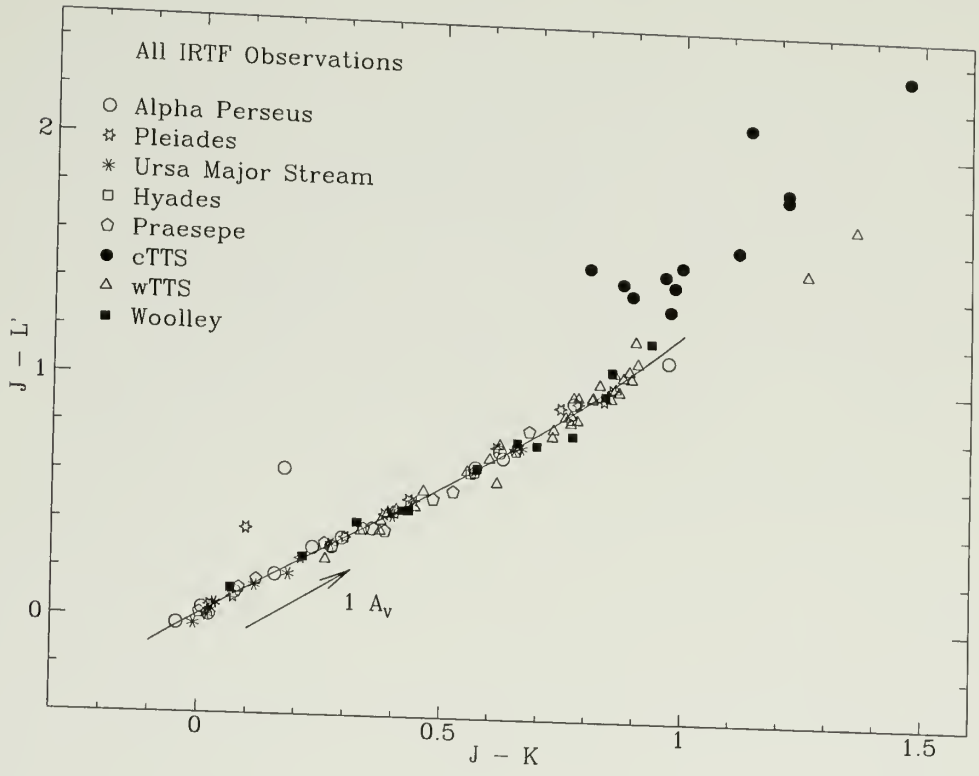

Figure 4.5. (cont.) (c) Same as in (b), but showing the entire IRTF data set.

distance from the star ($\sigma(r) \propto r^{-1}$). Figure 4.7 shows the results for a disk with a surface mass density which decreases with the square of radial distance from the star ($\sigma(r) \propto r^{-2}$). Lastly, Figure 4.8 displays the IRTF main sequence stars combined with the wTTS for the case where mass surface density decreases as $\sigma(r) \propto r^{-2}$.

It is only fair to state at this point that the well-behaved curves displayed in the figures are not the true model output. The problems arises because the disk may be optically thin to an observer looking at the disk face-on, yet radially optically thick from the perspective of a dust grain looking toward the star. The model was really designed to examine the optically thin case, and cannot be

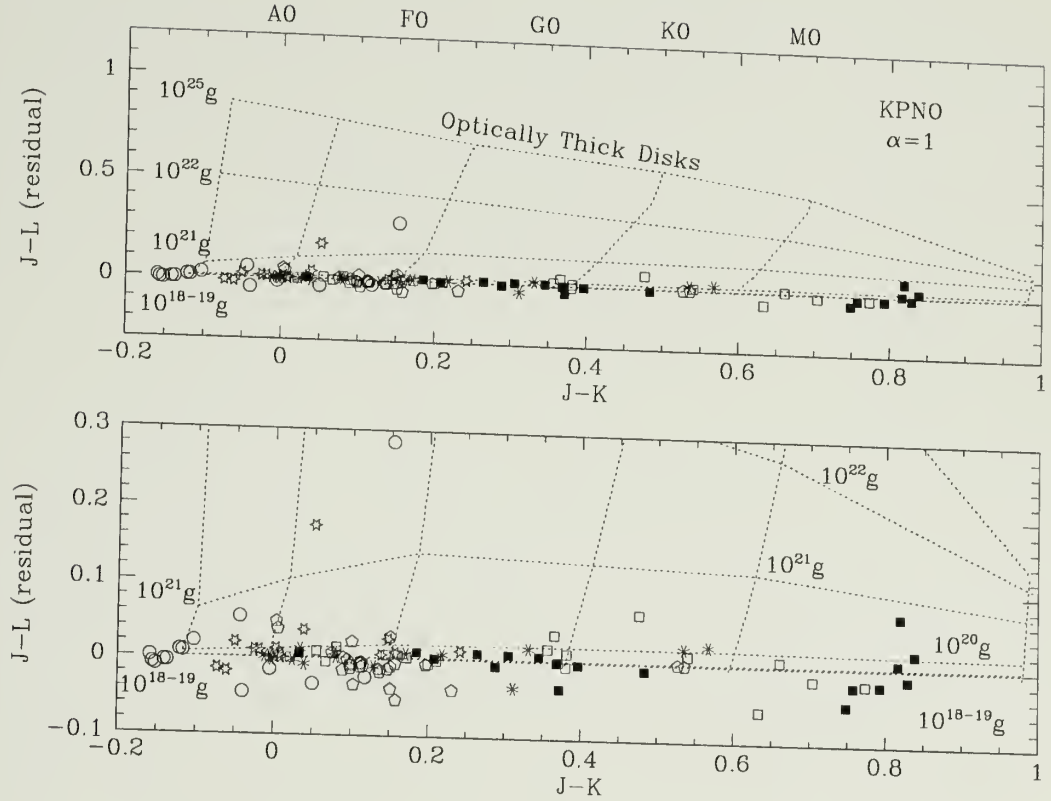

Figure 4.6. JKLL′ model results, MS stars, $T_{dest} = 1800$, $\alpha = 1$. Residual colors from the third-order polynomial fit, shown in Figures 4.5, are shown. Symbols are the same. Superimposed on the residuals are models of warm dust emission arising from material within 3 AU of the central star. The model assumes all grains have radius 1 μm, a dust destruction temperature of 1800 K, an emission efficiency law of $[1/(1 + \lambda/2a)]$, and takes into account possible shadowing of grains by other grains. Disk surface density decreases as r^{-1}. The horizontal dashed lines are lines of constant dust mass. The vertical dashed lines represent lines of constant dust temperature, from left to right, 13000 K, 9000 K, 7000 K, 6000 K, 5000 K, and 3000 K (a) The results for the KPNO data set.

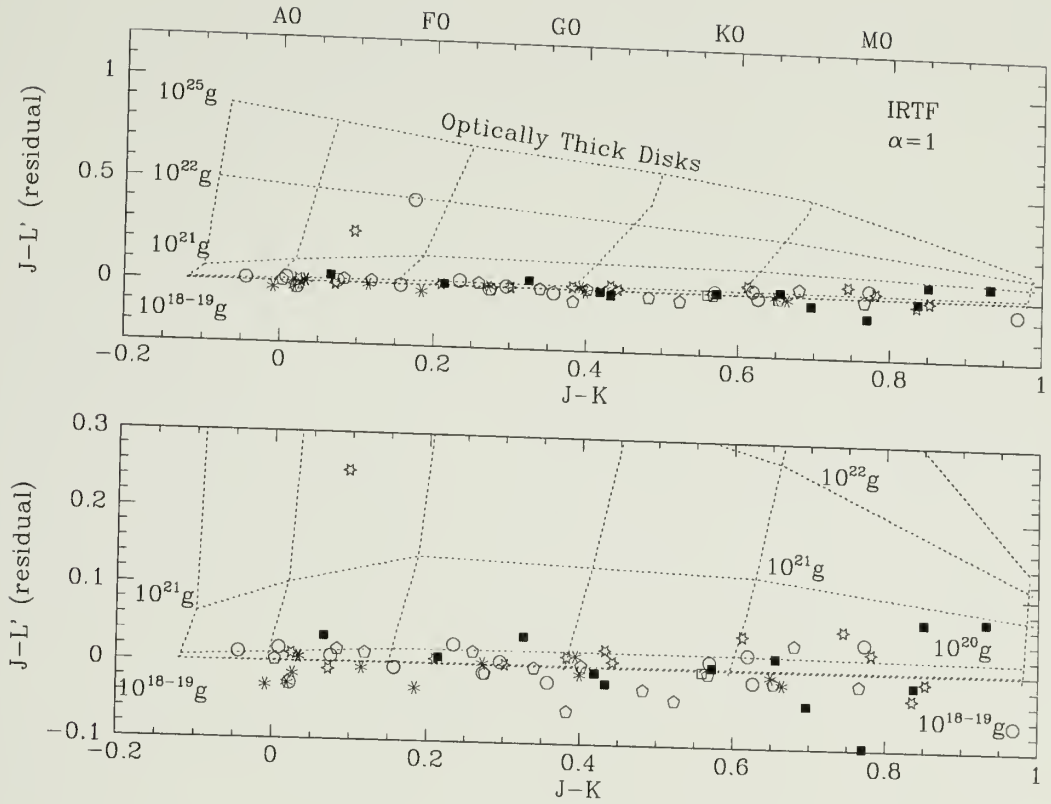

Figure 4.6. (cont.) (b) Residual colors and model results for the IRTF main sequence stars, again with $T_{dest} = 1800$ and $\alpha = 1$.

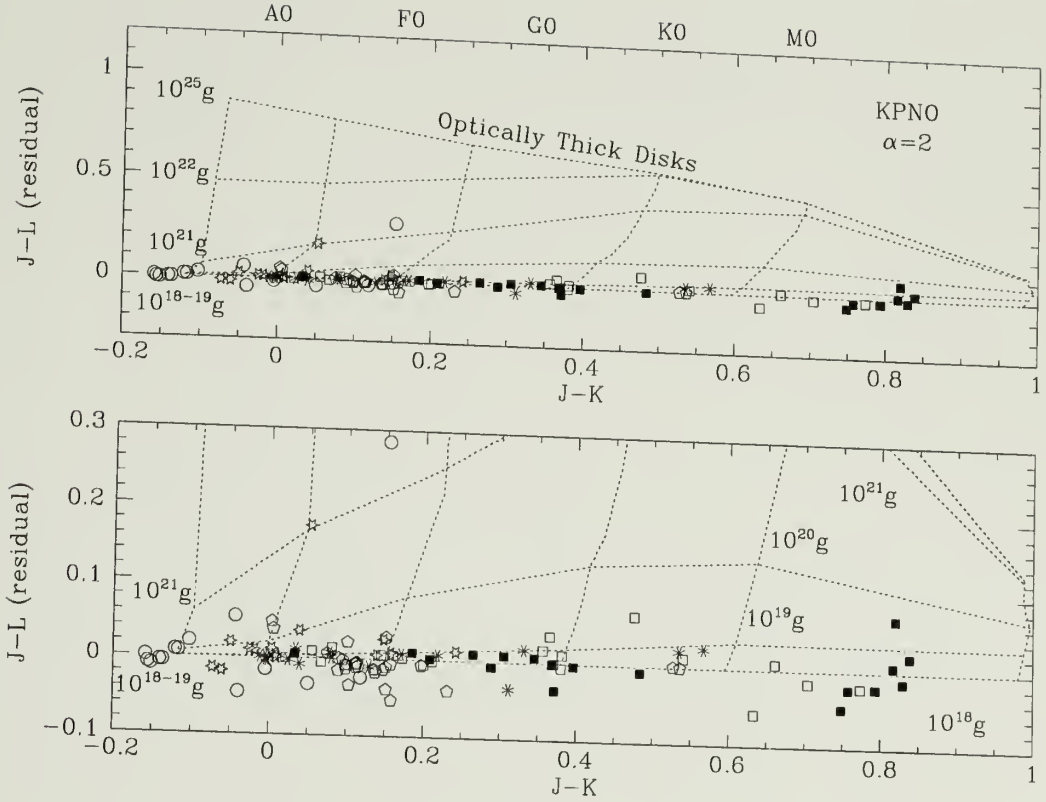

Figure 4.7. JKLL′ model results, MS stars, $T_{dest} = 1800$, $\alpha = 2$. Residual colors from the third-order polynomial fit, shown in Figures 4.5, are shown. Symbols are the same. Superimposed on the residuals are models of warm dust emission arising from material within 3 AU of the central star. The model assumes all grains have radius 1 μm, a dust destruction temperature of 1800 K, an emission efficiency law of $[1/(1 + \lambda/2a)]$, and takes into account possible shadowing of grains by other grains. Disk surface density decreases as r^{-2}. The horizontal dashed lines are lines of constant dust mass. The vertical dashed lines represent lines of constant dust temperature, from left to right, 13000 K, 9000 K, 7000 K, 6000 K, 5000 K, and 3000 K. (a) The results for the KPNO data set.

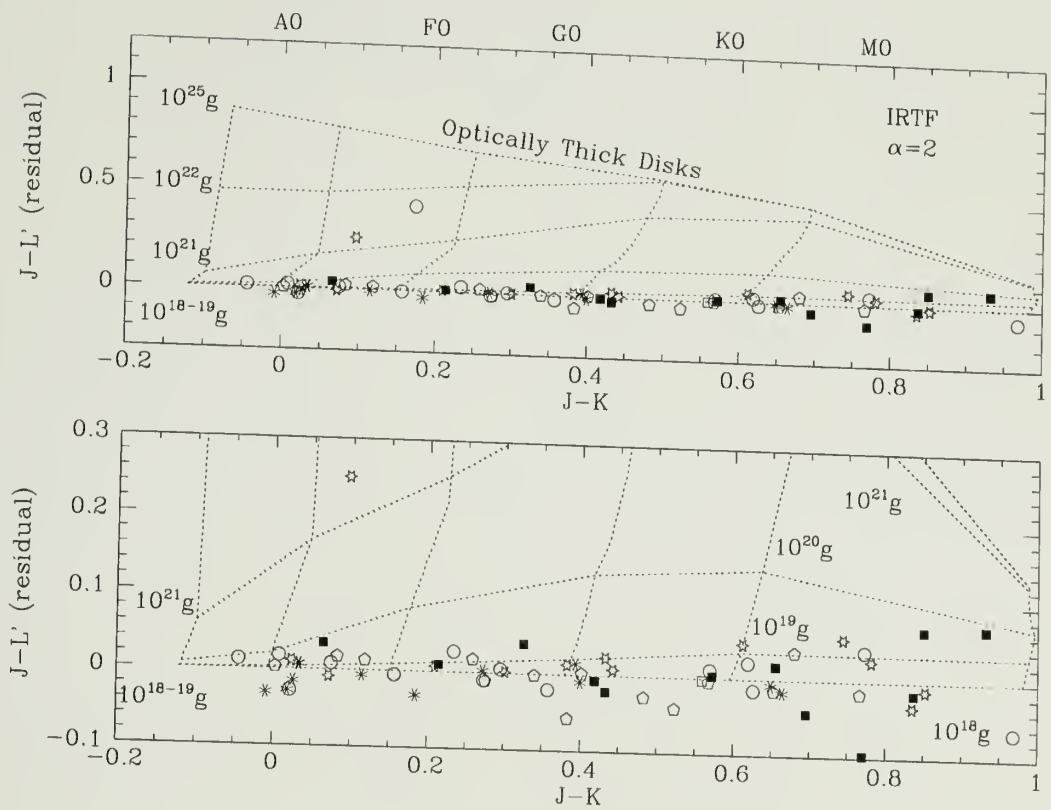

Figure 4.7. (cont.) (b) Residual colors and model results for the IRTF main sequence stars, again with $T_{dest} = 1800$ and $\alpha = 2$.

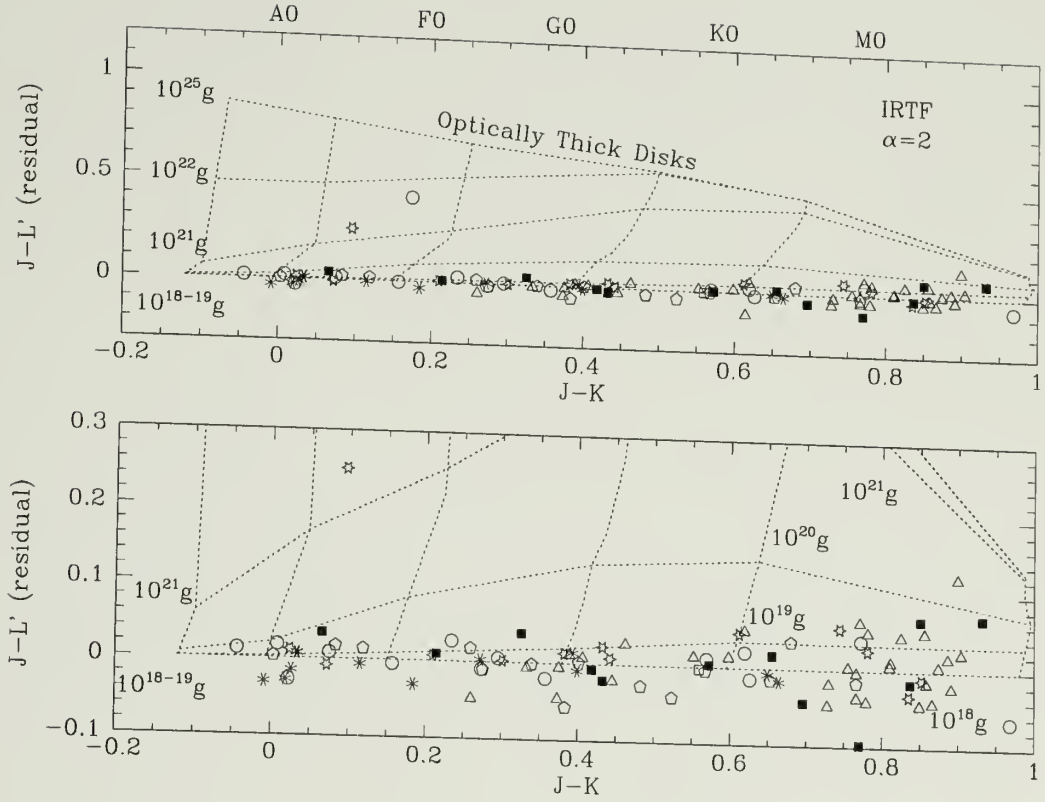

Figure 4.8. JKLL′ model results, wTTS included, $T_{dest} = 1800$, $\alpha = 2$. Residual colors from the third-order polynomial fit, shown in Figure 4.5(b). All the IRTF main sequence stars, plus the wTTS, are shown. The key for symbols is as in Figure 4.4. Superimposed on the residuals are models of warm dust emission arising from material within 3 AU of the central star. The model assumes all grains have radius 1 μm, a dust destruction temperature of 1800 K, an emission efficiency law of $[1/(1 + \lambda/2a)]$, and takes into account possible shadowing of grains by other grains. Disk surface density decreases as r^{-2}. The horizontal dashed lines are lines of constant dust mass. The vertical dashed lines represent lines of constant dust temperature, from left to right, 13000 K, 9000 K, 7000 K, 6000 K, 5000 K, and 3000 K.

trusted in the intermediate case, and perhaps the optically thick case. The graph displayed was cleaned up by assuming the optically thin and thick results were correct, and interpolating the regions where the model obviously went non-physical. More comments will be made on this subject in Chapter 5.

The typical 1σ scatter in the J-L′ residuals is about 0.02 magnitudes for the KPNO main sequence stars, and slightly more than 0.03 magnitudes for the corresponding IRTF stars. With this level of scatter, as can be seen in the figures, the observations are sensitive to a mass of 10^{21} g for a surface mass density law scaling as r^{-1}. If the surface density law is steeper, more particles reside closer to the star, resulting in higher dust temperatures and larger flux excesses. The models show that if the mass surface density scales as r^{-2}, the observations are sensitive to about 10^{20} g in micron-sized grains. This is the mass of a typical asteroid! Keep in mind the model is not sensitive to larger grains, which have less surface area per unit mass. Much more mass can reside in the disk and remain undetectable, as long as it is in larger grains or bodies. The sensitivity of the model to various parameters is discussed in the following chapter.

As stated earlier, none of the main sequence stars show any clear evidence of thermal excess emission. For the model parameters displayed in this chapter, one may conclude that none of the main sequence stars observed show evidence of warm material in the disk having a total surface area in excess of that equivalent to $10^{20} - 10^{21}$ grams of micron-sized grains, distributed according to the surface density laws shown. Only one wTTS, W040234 (J-K = 0.90, J-L′(residual) $\sim$ 0.12), shows an excess characteristic of a dust disk with mass 10^{20} g, assuming a mass surface density law falling off as R^{-2}. Although the excess appears to be significant, one must allow for the possibility that the perceived excess is nothing more than statistical scatter.

4.3 The M and N (5–10μm) Results

Most of the cluster stars were too faint for observations at M (4.8μm) and N (10.0μm). At these wavelengths, thermal emission from terrestrial sources overwhelms the stellar emission, requiring very long integration times. Measurements at M were only made on very bright infrared sources, such as the cTTS and Be stars, which have large infrared excesses, or the Ursa Major Stream Stars, which are nearby. The TTS are still relatively faint; the S/N for TTS at M is typically < 50. A mere handful of sources were observed at N. Only stars with huge infrared excesses, such as Ae/Be stars, had S/N > 50 at N. (The observations of Ae/Be stars are presented in Chapter 3 and Appendix B, but are not discussed in this work.) Despite the lower quality of the measurements at these wavelengths, the same trends are seen as for the shorter wavelengths.

As the background to interpret the figures has already been stated in the previous sections, very little commentary will be given in this section.

Figures 4.9 and 4.10 display the J-M *vs.* J-K colors of just the main sequence stars, then the entire data set. The trends seen are identical to those of the J-L and J-L′ *vs.* J-K colors.

Figure 4.11 displays all the J-N *vs.* J-K data. There is not enough data to establish a main sequence at N. Clearly, the cTTS have excess emission. It is possible the two wTTS, SAO76411A and DI Tau have excess emission; of the two, DI Tau (J-K = 0.825, J-N = 1.499) is a more likely candidate. Note that DI Tau is a binary system. As neither SAO76411A nor DI Tau show evidence of excess emission at L′ or M, excess emission at N would be particularly interesting. IRAS (12-100 micron) data reveals excess emission in the 12 to 100 micron range for these stars, although the 12-25 micron excess is not well established for SAO76411A (see K. Strom *et al.*, 1989).

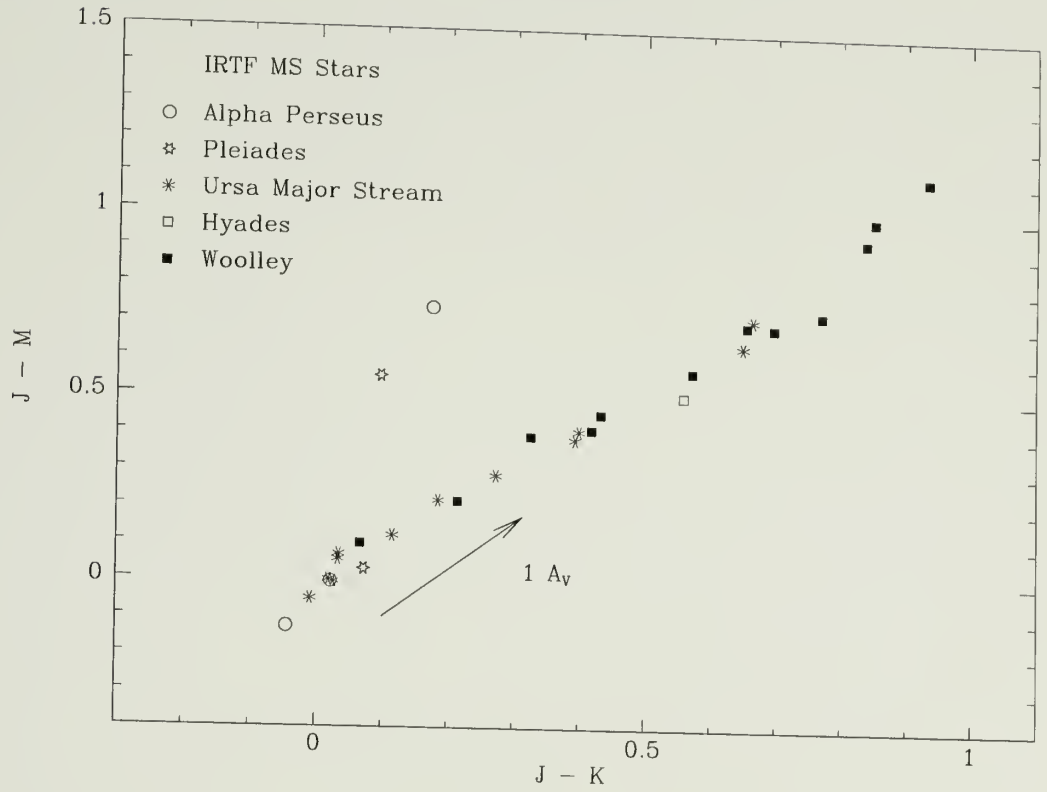

Figure 4.9. JKM results, main sequence stars only. All J-M vs. J-K for the main sequence cluster stars observed at IRTF. Clusters are differentiated by symbol. The effect of 1 A_V of interstellar reddening is shown. Although the data set is smaller for these longer wavelengths, the scatter is comparable to that in Figure 4.3(b). As before, the two Be stars, HE1164 and HII980 deviate significantly from the main sequence locus.

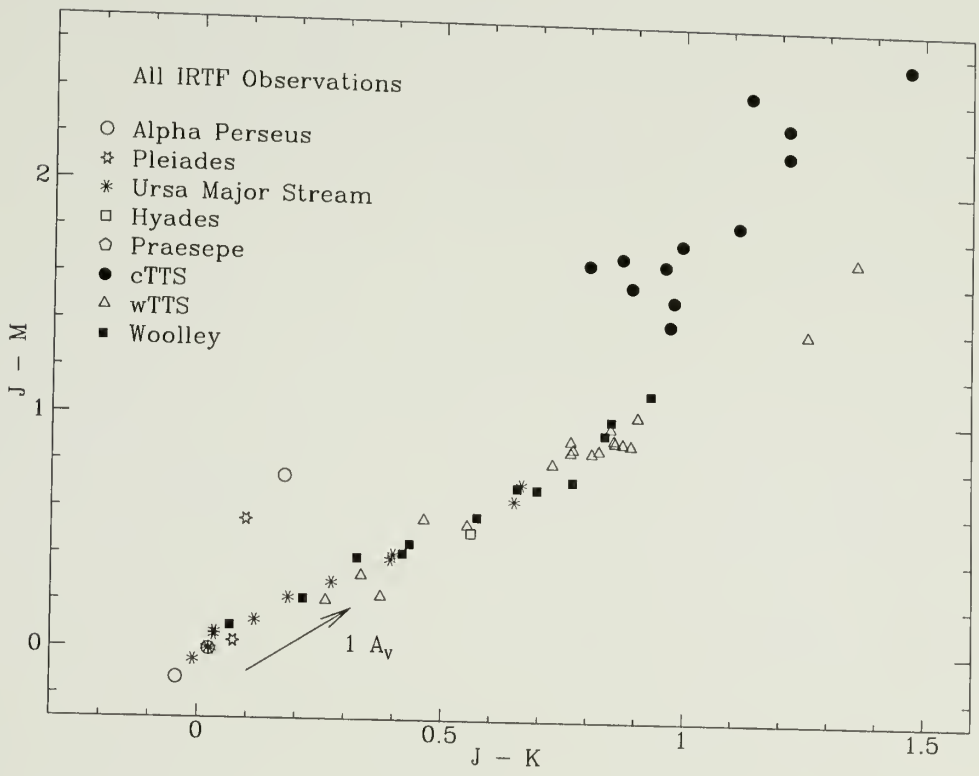

Figure 4.10. JKM results, the full IRTF data set. J-M vs. J-K for the entire IRTF data set. Clusters are differentiated by symbol. The effect of 1 A_V of interstellar reddening is shown. The vertical deviations from the main sequence locus for the two Be stars and the cTTS are clearly seen. Compare to Figure 4.4.

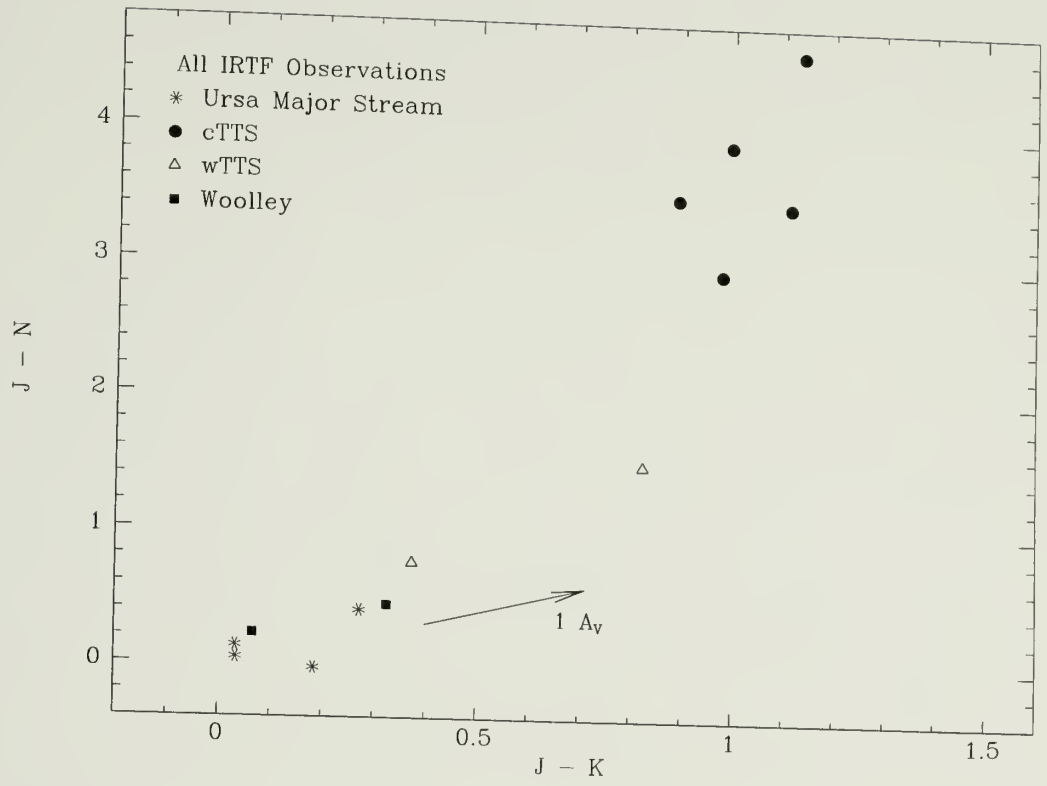

Figure 4.11. JKN results, the full IRTF data set. J-N vs. J-K for the entire IRTF data set. Clusters are differentiated by symbol. The effect of 1 A_V of interstellar reddening is shown. The vertical deviations from the main sequence locus for the cTTS are clearly seen. Compare to Figures 4.4 and 4.10.

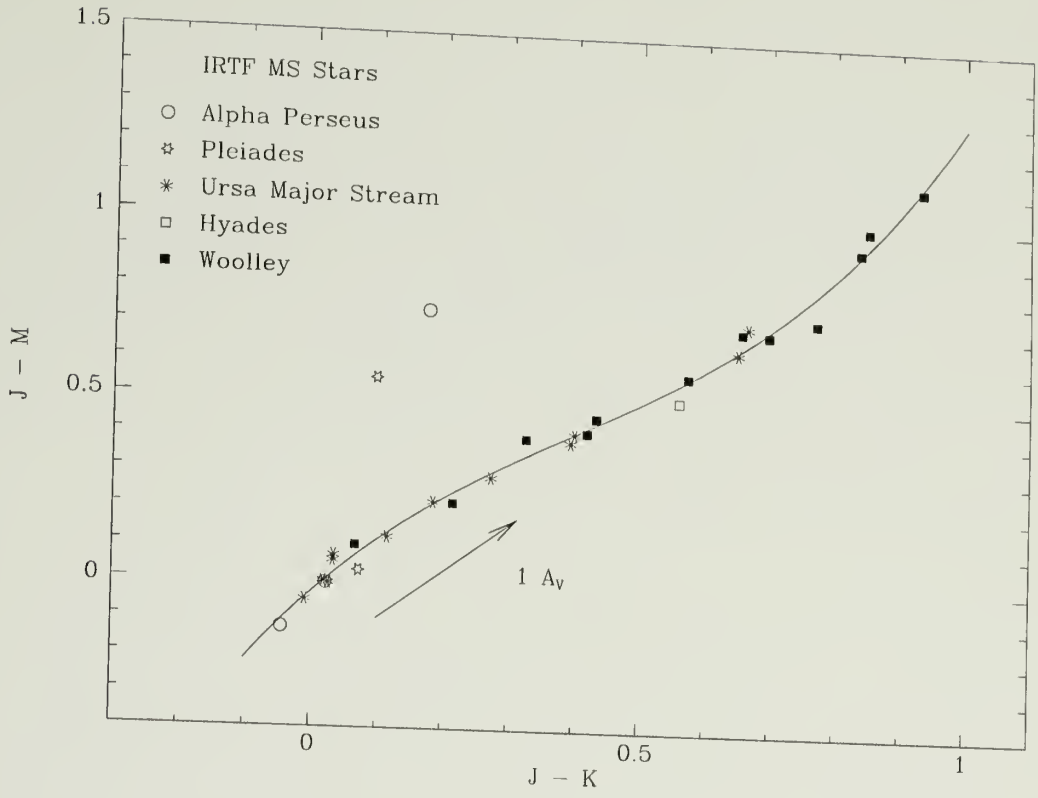

Figure 4.12. Third order polynomial fit to JKM MS colors. (a) Third order polynomial fit to all the IRTF J-M vs. J-K main sequence results. The two Be stars were not included in data used for the best-fit routine.

Once again, a third order polynomial fit is performed, using only the main sequence stars, to remove the slope from the J-M *vs.* J-K colors to facilitate examination of the vertical scatter in the data. The resulting fit is displayed in Figures 4.12. The curvature to the fit is pronounced; it may or may not be real.

Finally, the residual J-M colors are displayed in Figure 4.13. Superimposed on the residuals are the model predictions for the infrared colors arising from thermal dust emission in a circumstellar disk. Only the case with surface density falling off with the square of the distance from the star ($\alpha = 2$) is shown. The results are in agreement with the results at L and L′; the observations are sensitive to

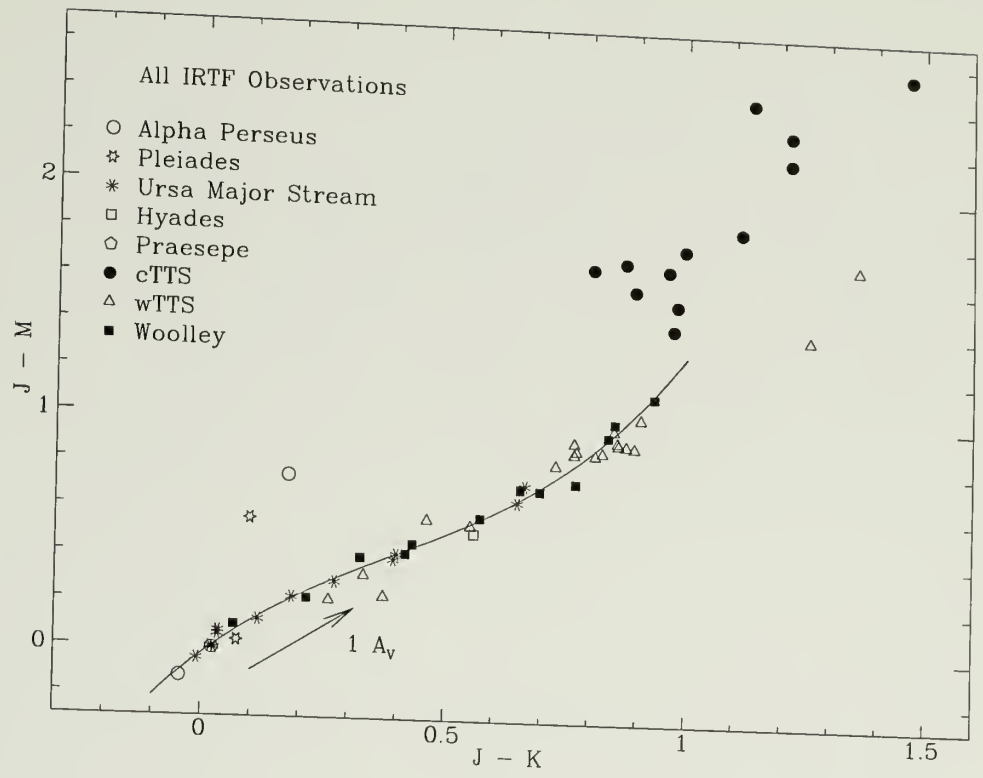

Figure 4.12. (cont.) (b) Same as in (a), but showing the entire IRTF data set.

approximately 10^{20} g of material in small grains. The 1σ scatter in the J-M residuals is slightly larger than 0.03 magnitudes.

4.4 Summary of Results

The photospheric colors of the main sequence star observed, and the majority of the weak-lined T-Tauri stars, form a well-defined locus. The classical T-Tauri stars are not confined to a well-defined locus, and display colors which are much redder than the main sequence locus. Based on visual inspection of plots of J-L or J-L′ *vs.* J-K colors, thermal emission from circumstellar dust is seen in classical T-Tauri stars, and possibly one relatively young weak-lined T-Tauri star. No

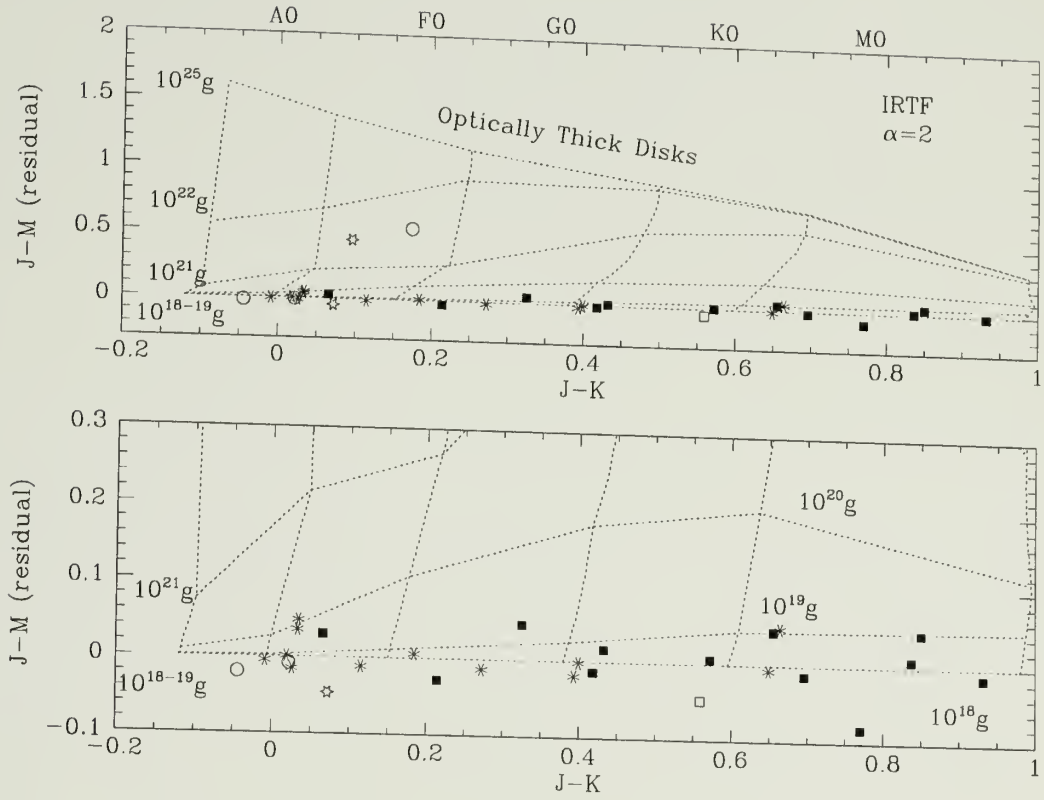

Figure 4.13. JKM model results, $T_{dest} = 1800$, $\alpha = 2$. Residual J-M vs. J-K colors from the third-order polynomial fit, shown in Figures 4.12. Symbols are the same. Compare to Figure 4.7(b). Superimposed on the residuals are models of warm dust emission arising from material within 3 AU of the central star. The model assumes all grains have radius 1 μm, a dust destruction temperature of 1800 K, an emission efficiency law of $[1/(1 + \lambda/2a)]$, and takes into account possible shadowing of grains by other grains. Disk surface density decreases as r^{-2}. The horizontal dashed lines are lines of constant dust mass. The vertical dashed lines represent lines of constant dust temperature, from left to right, 13000 K, 9000 K, 7000 K, 6000 K, 5000 K, and 3000 K.

excess emission is seen for any of the main sequence stars. The youngest main sequence cluster is Alpha Perseus, having an age of 20-80 Myr. The oldest star showing obvious evidence of excess emission is GO Tau, a cTTS, having an age of 3×10^6 yr.

One wTTS, W040234, shows possible evidence of thermal dust emission. This star has spectral type M2. The main sequence locus turns upwards for very late-type main sequence stars, so it is possible the perceived excess is merely an illusion. Late-type stars have more absorption lines than early-type stars, resulting in redder broadband colors. The star may normally sit a little high on the plots; scatter could displace it even more. Spots could also possibly mimic an excess, as spots have additional absorption lines which cause them to be redder. (The behavior of spots which act as blackbodies is discussed in Chapter 5.) On the other hand, the star has age ranging from 1-3 Myr, which is intermediate between the young cTTS with large excesses, and the older wTTS, with no excesses. This is the age at which infrared excess emission is expected to decline, and we may have caught the star just before its dust disk disappears below the detection limit.

Based on a simple model of a circumstellar disk composed of micron-sized dust grains, the observations are sensitive to a mass in dust of $10^{20} - 10^{21}$ g of material, the mass of a typical asteroid. The models are sensitive to surface area, rather than mass. Note that much more mass may be present in the disk in the form of larger grains or bodies, yet escape detection.

The next chapter discusses the implications of these findings.

Chapter 5

DISCUSSION

5.1 Introduction

This project was undertaken in the hope of finding tenuous dust signatures associated with old pre-main sequence and young main sequence stars. The previous chapter presented graphic results of near-infrared colors for such stars; no near-infrared excess emission, diagnostic of warm dust emission arising from the innermost regions of the disk, was seen for stars past an age of 3×10^6 yrs. Model predictions for the excess emission which would arise at these wavelengths from the inner 3 AU of an optically thin circumstellar disk imply that if all the material in the disk was composed of grains 1 micron in radius, our measurements are sensitive enough to detect a mere 10^{20} to 10^{21} grams of material, the mass of a 40-km diameter asteroid.

Whereas the previous chapter simply presented the results, this chapter discusses the findings, and the trustworthiness of the method used. A handful of mechanisms other than thermal dust emission which might produce near-infrared excesses are noted. A brief summary of how the results from this program compare to related observing programs is given, and also a discussion of how the findings presented in the previous chapter relate to our current theoretical understanding of the formation of our solar system. The chapter concludes with a discussion of what we expected to see, compared with what was actually observed.

5.2 Limitations of the Model

Although the basic philosophy of the model is described in Appendix C, some of the shortcomings were not discussed. The model was designed to examine the near-infrared emission arising from the inner disk regions of an optically thin disk.

The terms "optically thin" and "optically thick" are relative. The disk may be optically thin when viewed face-on, but radially optically thick from the perspective of a dust grain viewing the central star. The model estimates a "typical" optical depth towards the star from the perspective of a dust grain at the midplane of the disk. Dust grains which are not at the midplane will see a different optical depth.

Once the total cross-sectional area of the grains within a given annulus exceeds the cross-sectional area of the surface of the annulus itself, the emission efficiency of the grains is abruptly shifted from the chosen emissivity law to $Q(\lambda) = 1$. It is possible this abrupt transition can contribute to non-physical results.

As stated in the appendix, the model does not take into account heating of grains by emission from other grains. If the disk is optically thin, heating of grains by other grains should be insignificant compared to heating by the central star. Once the disk is no longer optically thin, or is in the transition region, this simplification may not be appropriate.

The model may only be considered valid for the optically thin case. Graphic results support this admonition. The model results presented in Chapter 4 look very clean and consistent, but the plots have been cleaned up by hand. The actual results were by no means this nice. The progression of infrared excesses is not monotonic; once the disk is no longer optically thin, the excess emission exhibits loops and other nonphysical results. In some cases the models predict emission in excess of that expected from an opaque disk. The model is well-behaved up to dust masses of about 2×10^{21} g. The optically thick case is acceptable, but it was

not handled as carefully as in models by other authors. Regardless, the purpose of the model was to provide a means by which we could estimate the sensitivity of our observations to tenuous dust disks. The model is successful in accomplishing that end.

One other point which should be mentioned is that every telescope facility has its own photometric system, a convolution of all the optical elements in the light path, and the responsivity of the detector and electronics. The model is only a theoretical representation of what one might expect from a given facility for a perfect blackbody "star" having an appropriate effective temperature. In the presentation of the model results, the stellar effective temperatures were matched to the corresponding J-K colors for the spectral types at that particular telescope facility.

Likewise, the calculated J-L (or J-L′) excess emission had to be "matched" to the corresponding observed J-L′ colors. Recall that the slope of the original plots of J-L *vs.* J-K was removed by fitting a third-order polynomial to the set of photospheric colors, leaving "residual" J-L colors evenly scattered about J-L=0. The calculated J-L colors were likewise flattened to match the residual data set. The model results were examined to determine the largest total mass in grains which produced no perceivable excess. The results for that mass were then used as a zero point for all other calculated excesses.

5.3 Shortcomings of the Method

The method employed to diagnose near-infrared excess emission was chosen primarily for its efficiency. As stated in earlier chapters, the method is not foolproof. The spectral energy distributions of the stars are sampled at only 3 wavelengths, and then only the relative strength of the emission at those wavelengths is examined. Although one hopes the method is trustworthy, based on

the reasonings given in Chapter 2, it is still possible to be fooled in certain cases. If the near-infrared colors of a given star mimic those of a main-sequence star of *any* spectral type, no infrared excess will be detected, even if the star has a warm dust disk. To put it another way, if the excess emission produced by warm or hot dust moves the near-infrared colors of a star along the locus of photospheric colors, the excess will be undetectable. As an analogy, it was shown in the previous chapter that interstellar reddening produces displacements *along* the main sequence locus.

How likely is it that an excess could be missed? Wien's law tells us that if the temperature of dust exceeds 1500 K, the dust emission peaks at wavelengths shorter than 2 microns. In this case, the dust may produce significant emission at J, so that the observed emission of star plus dust will not be photospheric at J. If that is true, then the perceived excesses at K and L will be weaker, and thus harder to detect.

A model trial was performed assuming a dust destruction temperature of 2500 K and a disk surface density law of $\sigma(r) = r^{-2}$. This steep density law favors the hottest particles. Although not displayed in this document, the results were not very different from the case in which $T_{\rm dest} = 1800$ K, shown in Figures 4.7. For the hottest stars, 10^{19} g of dust would be detectable. However, for most stars, 10^{20} g of dust grains would be required for detection, the same limit as for the case of $T_{\rm dust} = 1800$ K. The implied result is that hot dust does not alter the infrared colors in stars cooler than spectral type F or so. So yes, it is possible for hot dust to escape detection in cool stars.

Before worrying about this flaw in the method, is it prudent to question how much hot dust one would expect to find near the star.

Hot dust emission may result from two possible scenarios. First, very small grains, sometimes more like large molecules, can be raised to high temperatures with the absorption of a single photon. It is difficult to predict the number of

molecule-sized particles in the inner regions of the disk, and their effects. The range of temperatures for such grains would be wide, and they can cool by emitting single photons.

Secondly, one expects larger particles to vaporize more slowly as a result of their low surface area - to - mass ratio. It is possible that larger particles may persist closer to the star, achieving higher temperatures than the normal vaporization temperature.

It is unlikely there are vast amounts of large hot particles near the star. Even large grains would slowly evaporate, requiring a supply of new large grains. Large particles are least affected by radiation drag, and require the longest timescales to drift to the innermost regions of the disk. A micron-sized grain at an initial distance of 1 AU from a central star like our Sun will spiral into the star in fewer than 10^3 years; a millimeter-sized grain requires 10^6 years.

Lastly, it must be restated that the method chosen is not sensitive to cool material outside the terrestrial planet region of the disk. The excess arising from such cool material occurs outside the wavelength region investigated in this study.

5.4 Sources Other than Dust That May Produce Near-IR Emission

5.4.1 Starspots

One possible source of near-infrared excess emission which must be investigated is starspots. Spots are typically on the order of 500-2000 K cooler than the surrounding photosphere, possibly due to the inhibition of convection by the strong magnetic fields in the spot region. Since spots are cooler, they will have redder broadband colors than the surrounding photosphere. One way to approach the investigation of spots is to treat them as simple blackbodies. The percentage of the stellar surface they cover is left as a free parameter. In reality, if the spots have more absorption lines than the surrounding photosphere, the additional

absorption lines could make the spot colors even redder than their corresponding blackbody colors.

Blackbody models of spot colors are easy to produce. One must simply choose a spot temperature, then sum the blackbody emission from the chosen percentages of spot and standard photosphere. To translate fluxes into magnitudes, zero magnitude fluxes can be estimated by assuming the flux from a 10,000 K blackbody defines 0 magnitude at all wavelengths.

The calculated results for the case of two different spot temperatures are shown in Figures 5.1 and 5.2. In each figure, the blackbody colors of stellar photospheres with no spots are depicted by open circles. The photospheric temperatures are, from left to right, 15000 K, 12500 K, 10000 K, 9000 K, 8000 K, 7000 K, 6000 K, 5000 K, 4500 K, 4000 K, 3500 K, and 3000 K. The resultant colors of stars having spots are shown by open four-pointed symbols. The percentage of the stellar surface covered by spots is noted in each frame. In Figure 5.1, the spots are 1000 K cooler than the surrounding photosphere. Figure 5.2 illustrates the case when the spots are 2000 K cooler than the surrounding photosphere.

It will take a little effort on the part of the reader to associate the proper 4-pointed symbol with its corresponding filled circle. Starting with the case of 25% coverage, the trend should be fairly obvious. The resultant star plus spot colors for the case of a 3000 K photosphere cannot be seen on the plots; they are off-scale.

In each case the presence of spots on the surface of the star reddens the total observed colors, as expected. A larger percentage of spot coverage increases the reddening. The effects are more pronounced for cooler stars.

Note, that for the case of spots 1000 K cooler than the surrounding photosphere, the addition of spots reddens the colors *along* the line of photospheric colors, as in the case of interstellar reddening.

When the spots are 2000 K cooler, the addition of spots produces vertical displacements from the locus of photospheric colors, for stars 4500 K and cooler.

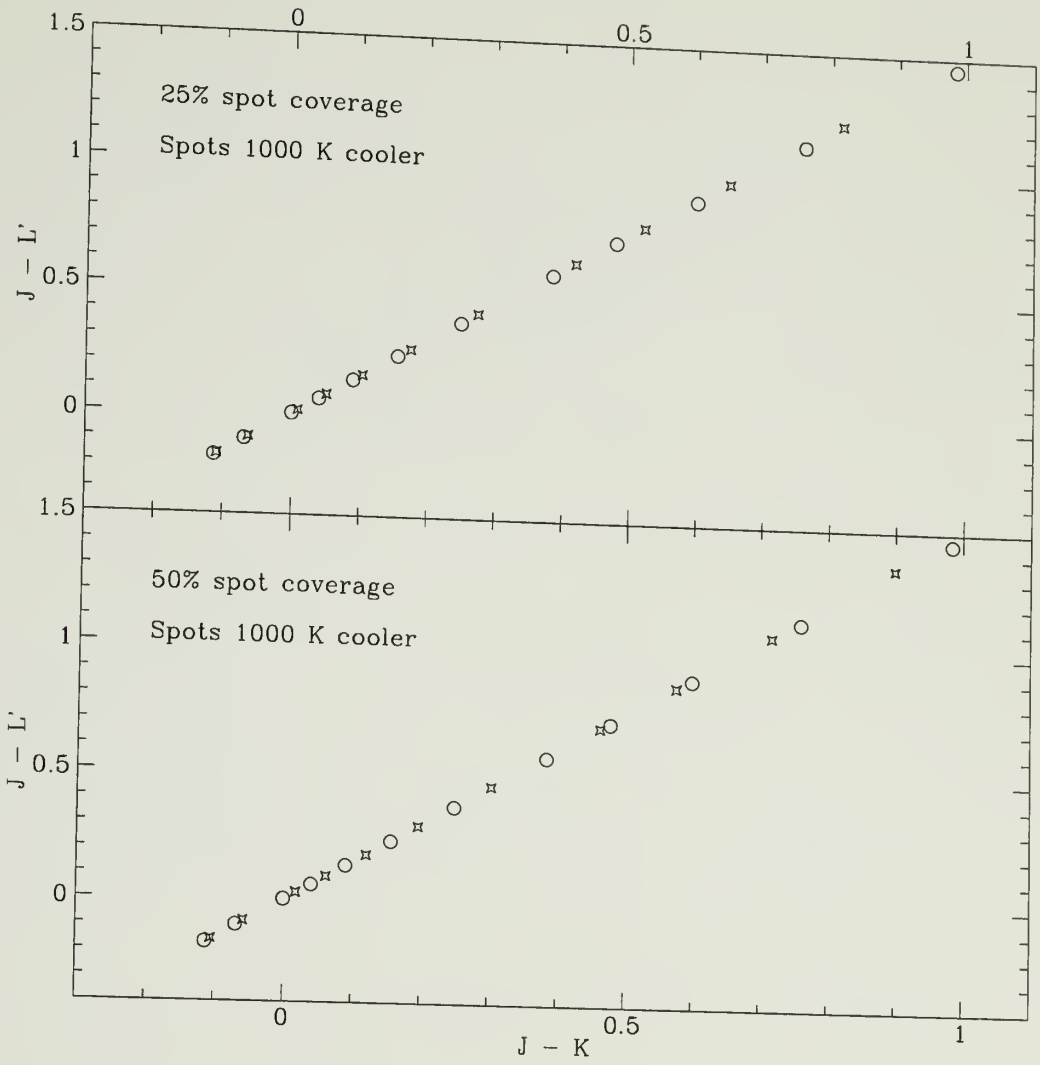

Figure 5.1. Spot models, spots 1000 K cooler than photosphere. Calculated J-L′ vs. J-K colors for perfect blackbody photospheres, denoted by open circles, and also photospheres having spots 1000 K cooler than the photosphere, illustrated with open 4-pointed symbols. The photospheric temperatures are 15000 K, 12500 K, 10000 K, 9000 K, 8000 K, 7000 K, 6000 K, 5000 K, 4500 K, 4000 K, 3500 K, and 3000 K. The correlation of 4-pointed symbol with corresponding circle is easiest to discern in the upper frame. The resultant colors for a 3000 K photosphere plus spots are off-scale. In each case the presence of spots reddens the observed colors. The effect is more pronounced for greater spot coverage, and for cooler stars. Note that spots move the resultant colors *along* the line of photospheric colors.

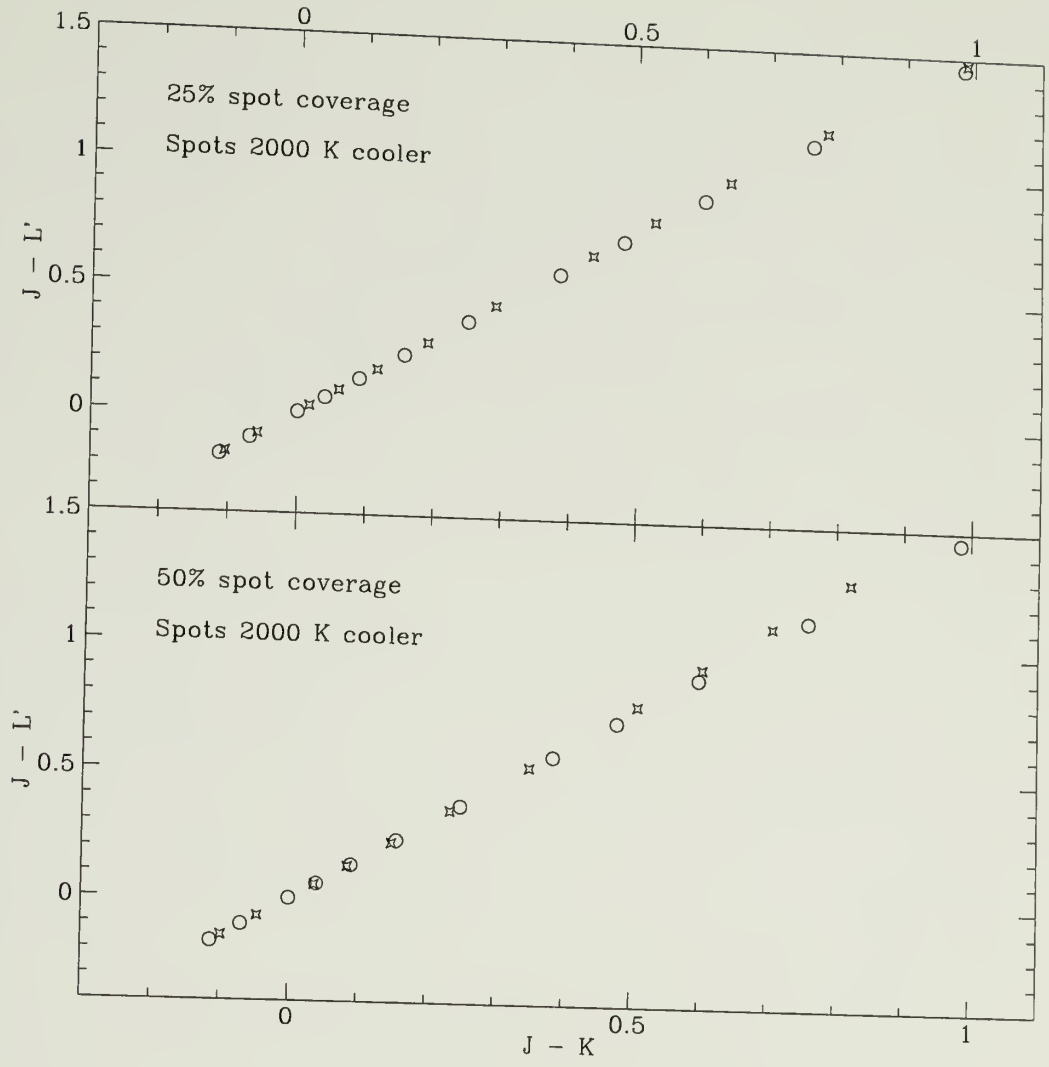

Figure 5.2. Spot models, spots 2000 K cooler than photosphere. Calculated J-L′ vs. J-K colors for perfect blackbody photospheres, denoted by open circles, and also photospheres having spots 2000 K cooler than the photosphere, illustrated with open 4-pointed symbols. The photospheric temperatures are 15000 K, 12500 K, 10000 K, 9000 K, 8000 K, 7000 K, 6000 K, 5000 K, 4500 K, 4000 K, 3500 K, and 3000 K. The correlation of 4-pointed symbol with corresponding circle is easiest to discern in the upper frame. The resultant colors for a 3000 K photosphere plus spots are off-scale. In each case the presence of spots reddens the observed colors. The effect is more pronounced for greater spot coverage, and for cooler stars. For stars cooler than about 5000 K, the spots produce vertical deviations from the photospheric locus.

The effects are easily seen for the case of 50% spot coverage. It is not clear that such cool stars could have spots 2000 K cooler.

The axis limits in Figures 5.1 and 5.2 have been chosen to coincide with that of the plots in Chapter 4. The small deviations from the photospheric locus produced by spots are within the scatter of the data. Therefore, *perfect blackbody spots do not produce observable near-infrared excess emission,* even in the extreme case of 50% spot coverage.

The above assumes that stellar photospheres and spots are pure blackbodies. In reality, as photospheres become cooler, the number of absorption lines increases, owing to the presence of molecules. Molecular lines are plentiful in the infrared. Absorption lines decrease the stellar flux, and numerous absorption lines will therefore affect the broadband colors. Spectral lines of molecules not observed in the the solar photosphere have been observed in sunspots (see Grevesse and Sauval, 1991, for a review of the infrared solar spectrum). If starspots have more absorption lines than the surrounding photosphere, the effect of starspots will be to make the infrared colors appear even redder. The spot models displayed in this section may therefore underestimate the true effect of spots.

As an interesting exercise, the spot models can be used to predict the effect of a dust excess. Instead of assuming the spots are 500 or 1000 K cooler than the photosphere, pretend the spots are an absolute temperature of either 500 K, 1000 K, or 1500 K. These temperatures are more consistent with the temperatures of dust in the inner disk regions of a solar-type star. The relative percentage of spot surface area compared to "normal photospheric" surface area will represent the relative percentage of dust surface area to stellar surface area. The results are shown in Figures 5.3, 5.4, and 5.5.

Looking at Figures 5.3 – 5.5, a fundamental change from Figures 5.1 and 5.2 is immediately apparent. In the case of 500 K spots, no effect is seen when spots are

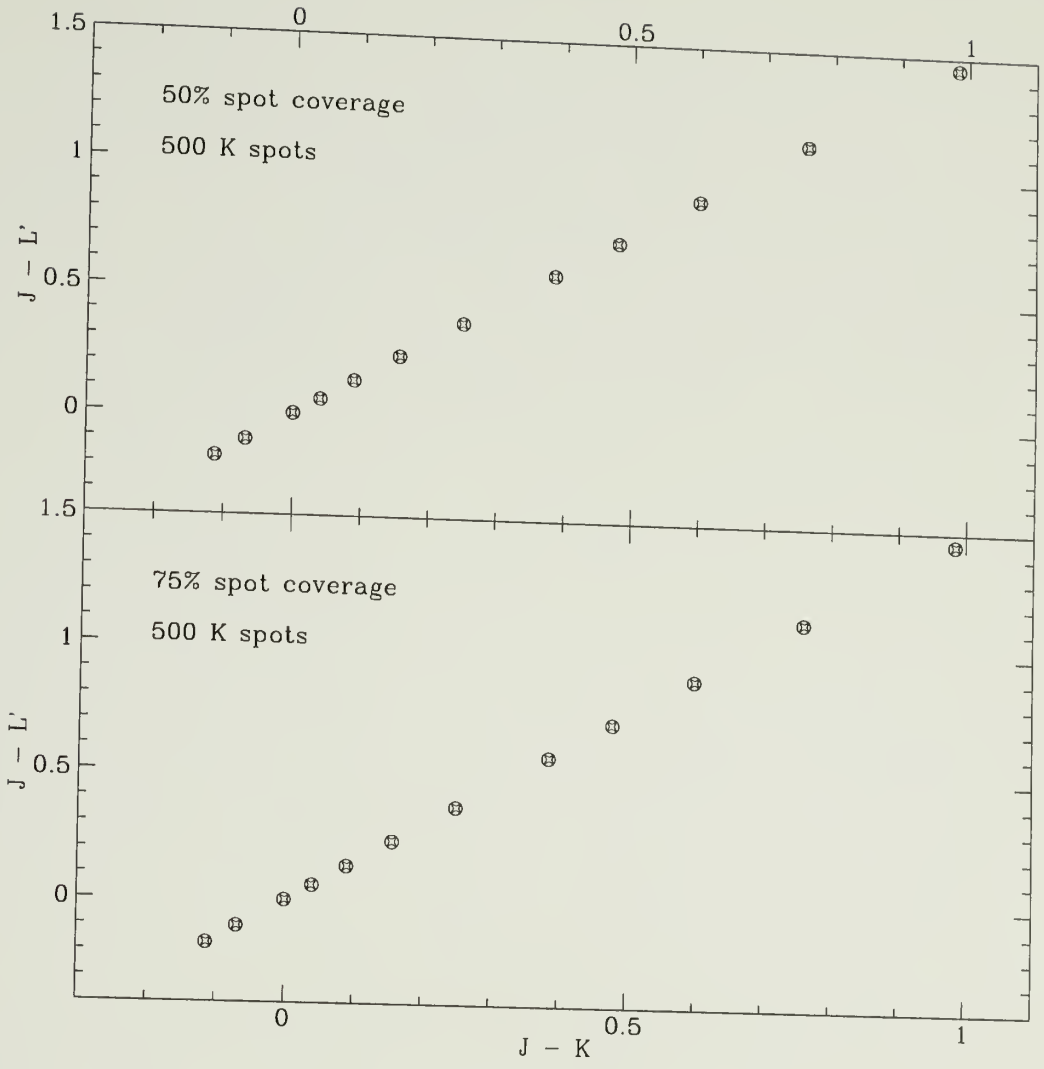

Figure 5.3. Spot models, 500 K spots. Calculated J-L′ vs. J-K colors for perfect blackbody photospheres, denoted by open circles, and also photospheres having 500 K spots, illustrated with open 4-pointed symbols. The upper frame shows the case in which 50% of the stellar surface is covered with spots; the lower frame assumes 75% coverage. The photospheric temperatures shown are 15000 K, 12500 K, 10000 K, 9000 K, 8000 K, 7000 K, 6000 K, 5000 K, 4500 K, 4000 K, 3500 K, and 3000 K. The addition of 500 K spots produces no noticeable effect, even for 75% spot coverage. The circles and stars appear to be coincident.

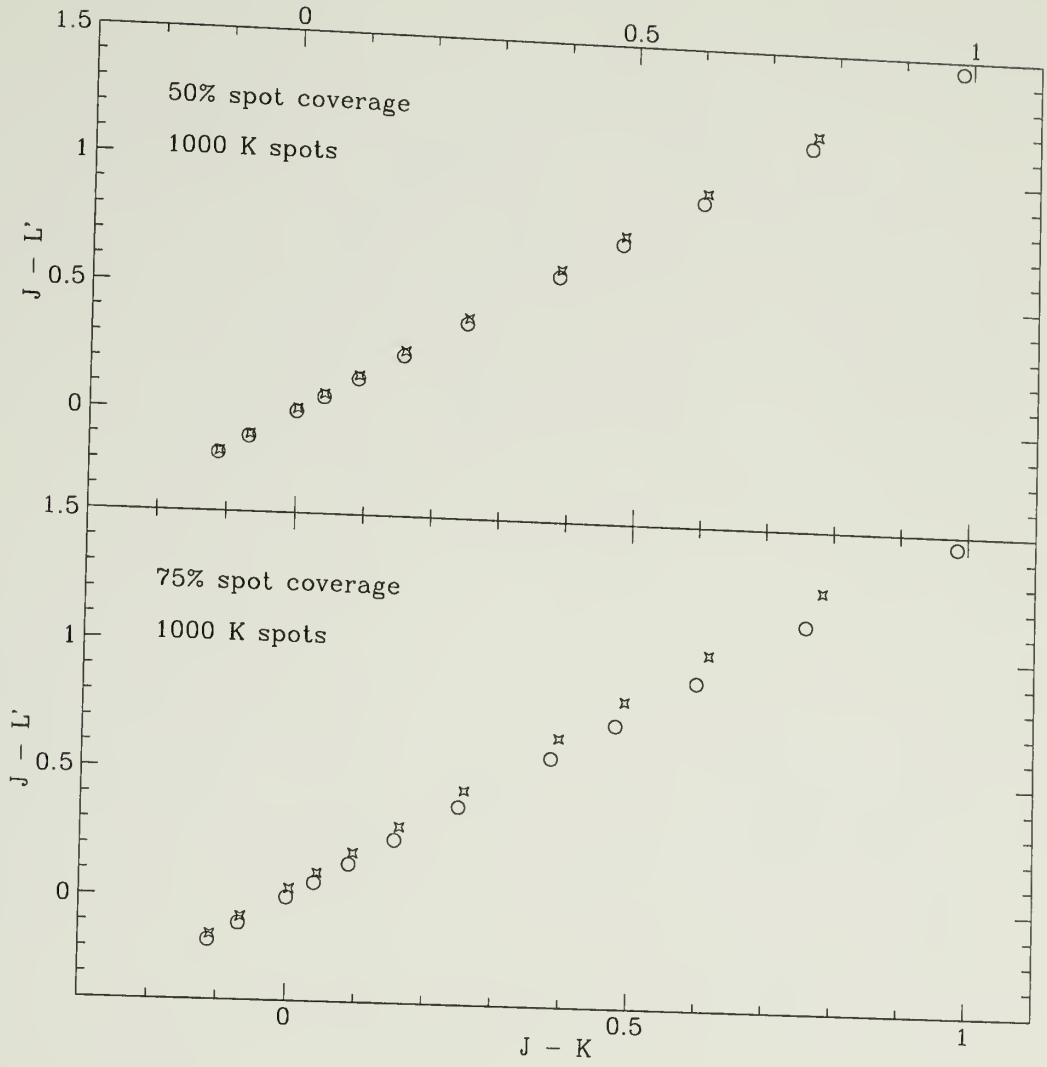

Figure 5.4. Spot models, 1000 K spots. Calculated J-L′ vs. J-K colors for perfect blackbody photospheres, denoted by open circles, and also photospheres having 1000 K spots, illustrated with open 4-pointed symbols. The photospheric temperatures shown are 15000 K, 12500 K, 10000 K, 9000 K, 8000 K, 7000 K, 6000 K, 5000 K, 4500 K, 4000 K, 3500 K, and 3000 K. The correlation of 4-pointed symbol with corresponding circle is easiest to discern in the upper frame. The resultant colors for a 3000 K photosphere plus spots are off-scale. In each case the presence of spots reddens the observed colors. The effect is more pronounced for greater spot coverage, and for cooler stars. The effect for 75% coverage is strong enough to produce a vertical deviation larger than the scatter in the data set.

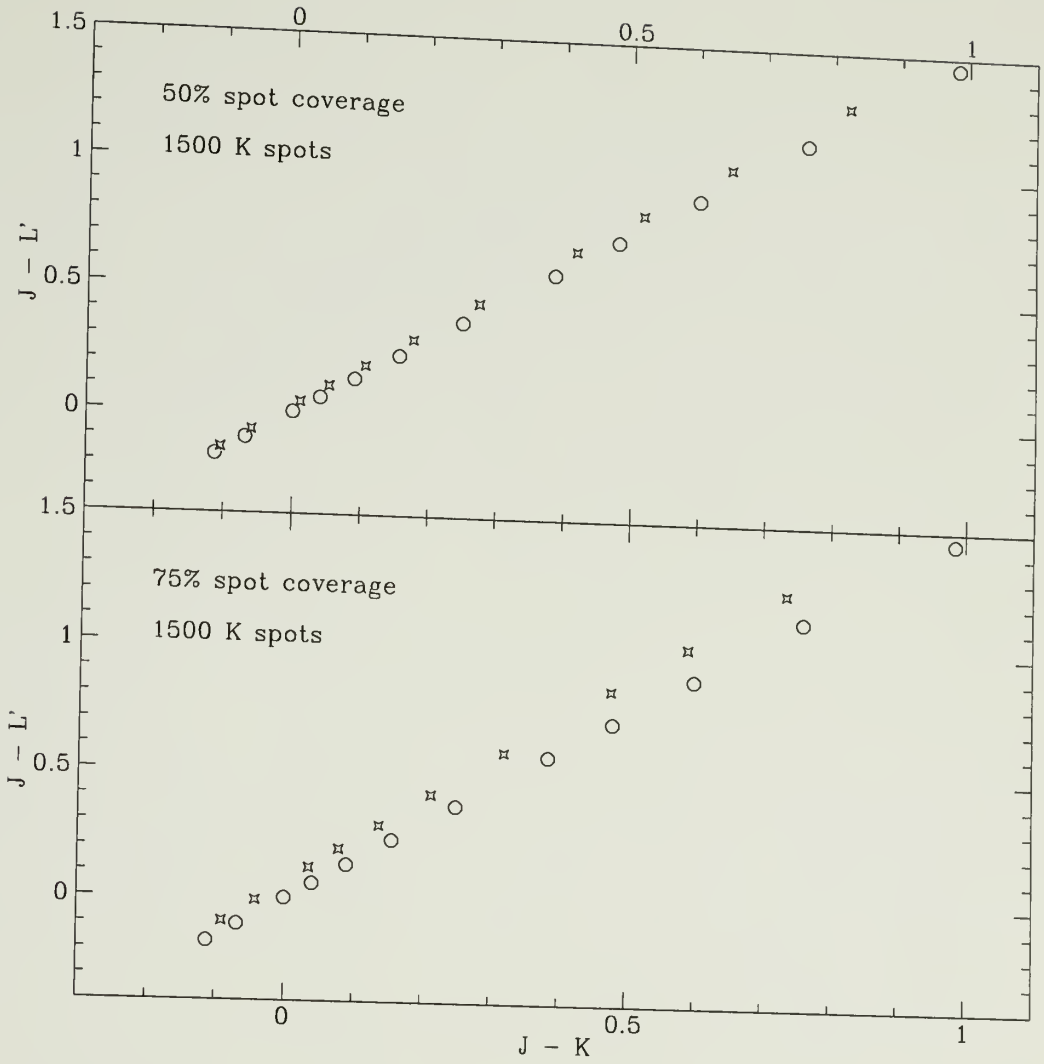

Figure 5.5. Spot models, 1500 K spots. Calculated J-L′ vs. J-K colors for perfect blackbody photospheres, denoted by open circles, and also photospheres having 1000 K spots, illustrated with open 4-pointed symbols. The photospheric temperatures shown are 15000 K, 12500 K, 10000 K, 9000 K, 8000 K, 7000 K, 6000 K, 5000 K, 4500 K, 4000 K, 3500 K, and 3000 K. The correlation of 4-pointed symbol with corresponding circle is easiest to discern in the upper frame. The resultant colors for a 3000 K photosphere plus spots are off-scale. In each case the presence of spots reddens the observed colors. The effect is more pronounced for greater spot coverage, and for cooler stars. The effect for 75% coverage is strong enough to produce a vertical deviation larger than the scatter in the data set. The effects are stronger than for the case of 1000 K spots.

added. In the case of 1000 and 1500 K spots, the spots no longer move the colors along the line of photospheric colors; a *vertical* deviation is clearly seen. The case of 75% spot coverage for 1000 K spots produces vertical deviations from the photospheric locus which would be barely discernible in real data for stars with spectral type G or later. (This is based on a comparison of these plots to Figure 4.5(b), matching the filled circles representing photospheric colors with the best-fit line in Figure 4.5(b).) The deviations for the case of 75% coverage with 1500 K spots would be easily seen in stars with spectral type G or later; the deviations might be discernible for stars as early as spectral type F.

To say 1000 or 1500 K spots cover 50% of the stellar surface is equivalent to saying there are 1000 or 1500 K dust grains near the star which have a total surface area equal to that of the star. Seventy-five percent spot coverage is equivalent to dust grains having a total of three times the surface area of the central star. Assuming 75% spot coverage, a central star which is a twin of the Sun, and that dust has a density of 2 g cm^{-3} and a radius of 1 μm, this surface area yields a mass in dust grains of 1.2×10^{19} g. This is in crude agreement with the model predictions of Chapter 4, perhaps an order of magnitude lower. A true disk is composed of particles having a range of temperatures; these models are too simple to predict the effect of a true disk. For a star like the Sun, most of the dust in the inner disk will be cooler than 1500 K, some cooler than 1000 K.

The astute reader will notice an apparent contradiction between Figures 5.4 and 5.5 and the disk model results in Figures 4.6 and 4.7. The spot models predict that dust should be easiest to detect around low-mass stars. Bear in mind the mass in dust in Figures 5.4 and 5.5 is not constant with spectral type; the mass in dust is related to the surface area of the star. An A0 star certainly has more surface area than an M0 star. The plots then imply a small amount of dust near an M0 star may produce a larger excess than a greater amount of dust near an A0

star. One would think it would thus be a cinch to detect disks around M stars. However, the disk model results do not bear this out. Why?

Note in Figure 5.3 that 500 K spots produce no observable excess. Crudely speaking, portions of the disk with $T > 500$ K will contribute most of the observed infrared excess. Assume a uniform mass surface density for the disk, that the disk is optically thin, and the grains act as perfect blackbodies. The dust destruction radius for an A0 star would be 0.18 AU, and a 500 K dust grain would reside at a distance of 2.3 AU from the A0 star. In comparison, the dust destruction radius for an M0 star is a mere 0.006 AU, but a 500 K dust grain would reside at a distance of 0.07 AU. Using these inner and outer disk radii to calculate the total disk surface area for each star, one finds the disk around the A0 star has more than 10^3 times the surface area than the disk around the M0 star. In short, although ~ 1000 K dust is inherently easier to detect near cooler stars, there will be much less dust to detect.

The important point to be learned from this exercise is that while stellar spots have temperatures and surface areas which do not result in observed near-infrared excess emission, dust near the stars can produce non-photospheric near-infrared broadband colors.

5.4.2 Low Mass Companions

It has been estimated that more than half the stars in the universe may belong to binary or multiple star systems. The exact statistics are not known. Given these odds, one must consider what effects low-mass companions may have on observed colors. Like spots, low mass companions can be modeled as blackbodies, with the understanding that true low-mass companions will have absorption lines which may make them inherently redder.

Low mass companions have a smaller surface area than the higher mass star; an M0 star (with effective temperature 3480 K) has only about 40% the surface

area of the Sun (Allen, 1976; likewise throughout paragraph). An M5 star (with effective temperature 2800 K) has 10% the surface area of the Sun. An M2 star has 25% the surface area of the Sun. When using the spot models to predict the effects of low-mass companions, 25% spot coverage is predicts the effect for a companion having 33% the area of the hotter star.

Models showing the expected colors for photospheres having 25% coverage of 2000 and 2500 K spots are shown in Figure 5.6. The deviations from photospheric colors lie well within the scatter of the date in Figures 4.5. The effects for 3000 K, 4000 K and 5000 K spots, not shown, are even smaller. One concludes from this exercise that *low-mass companions modeled as perfect blackbodies cannot produce observable near-infrared excess emission.*

As stated earlier, physical low-mass stars have absorption lines which make them inherently redder. However, their small radiating surface area and cool temperatures will still make them very difficult to detect. Also, the additional absorption lines reduces the total flux from the star.

5.4.3 Effects of Gas on Infrared Colors

Gas emission may create near-infrared color excesses, owing to free-free emission. Although it is difficult to discern the source of the excess based on only broadband measurements at three wavelengths, other diagnostics can pinpoint the source of the emission. If there is strong free-free emission, one would expect to find strong emission lines as well, such as $H\alpha$. The specific emission lines depend on the temperature of the emitting gas.

Two early-type stars in the data set displayed large near-IR excesses, HE 1164 and HII 980. Both of these are Be stars. B stars showing emission lines in their spectra. Although Be stars are still not fully understood, it is believed they rotate rapidly and have an extended disk-like circumstellar envelope. The basic concept

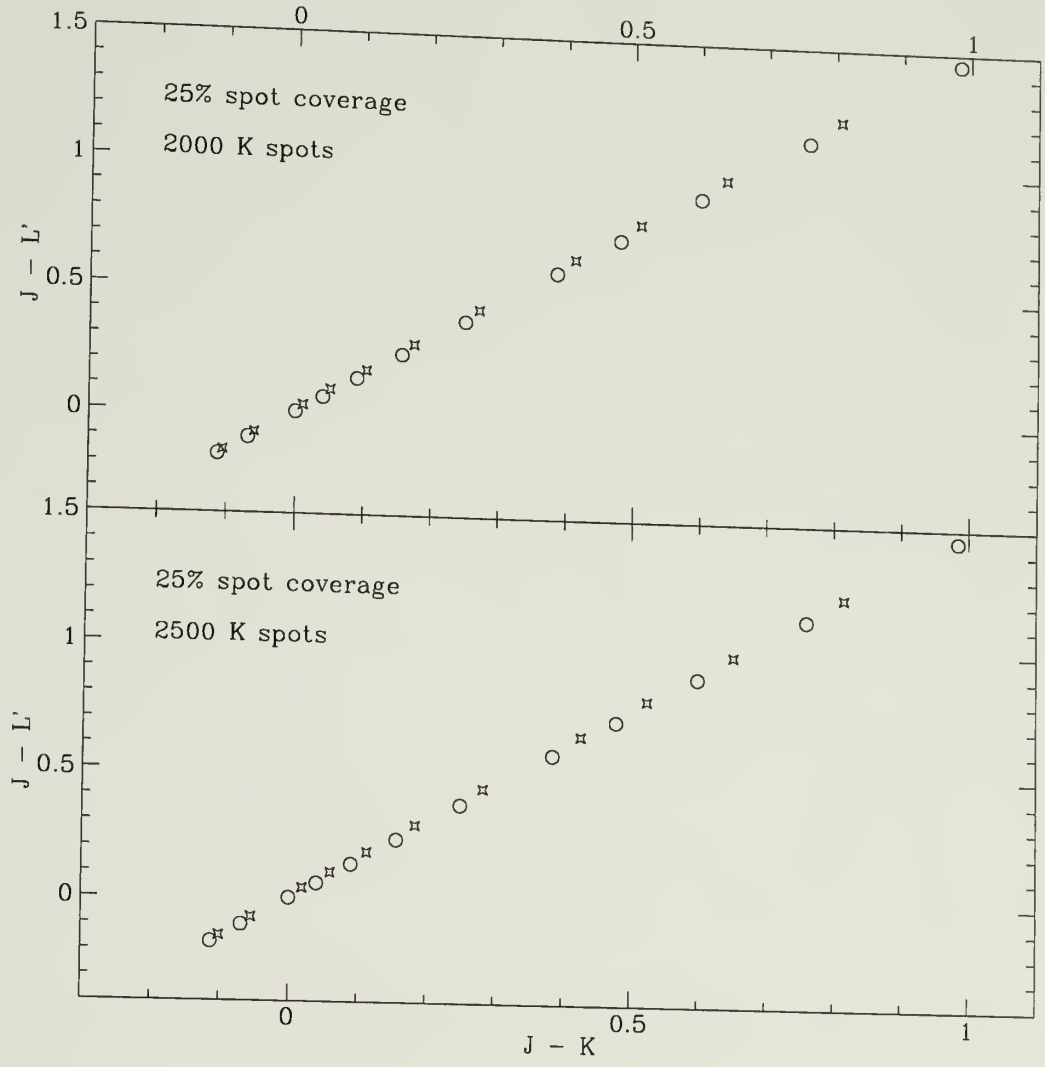

Figure 5.6. Spot models, 2000 and 2500 K spots. Calculated J-L′ vs. J-K colors for perfect blackbody photospheres, denoted by open circles, and also photospheres having 25% coverage of 2000 K and 2500 K spots, illustrated with open 4-pointed symbols. The photospheric temperatures shown are 15000 K, 12500 K, 10000 K, 9000 K, 8000 K, 7000 K, 6000 K, 5000 K, 4500 K, 4000 K, 3500 K, and 3000 K. The addition of such spots, mimicking the addition of a low-mass companion, produces only tiny vertical displacements from the locus of single photospheres. The tiny displacements would be lost in the scatter of observed photospheric colors.

was put forth by Struve (1931); a review talk on model atmospheres of Be stars may be found in Poeckert (1982).

The nature of the infrared excess in HE 1164 was examined by Allen (1973). Allen performed a detailed study of the spectral energy distributions of 248 early-type emission-line stars and related objects, focusing on the near-infrared magnitudes. He divided the 248 sources into four basic categories, based on plausible explanations for the continuum emission observed, including interstellar reddening, symbiotic stars, free-free radiation, and circumstellar dust. Models were used to place upper limits on possible contributions from free-free and blackbody emission. Allen classified HE 1164 as what he calls "type F," in which the observed infrared excesses can be successfully explained by free-free emission alone.

Although Allen did not examine HII 980, it is also a Be star, and has an even weaker infrared excess than HE 1164. If the infrared excess of HE 1164 could be accounted for by free-free emission alone, it is reasonable to presume the weaker excess of HII 980 can also be explained by free-free emission. Looking at Figures 4.3, note that a line drawn through both HE 1164 (spectral type B5Ve) and HII 980 (spectral type B6IVe) intersects the locus of photospheric colors in the B range, suggesting the same mechanism is responsible for the excesses seen in the two stars.

5.5 Theoretical Estimates of the Time Evolution of Disk Surface Area

5.5.1 Background

Safronov (1969) was the first to publish a detailed, formal theory for the formation of the planets from a protoplanetary cloud. Much has been done since that monumental work.

To date, no one has formally tackled the problem in its entirety; it is much too difficult. Rather, individual pieces of the problem at various evolutionary stages

have been attacked. For example, a particular model may address only the formation of the Earth, and maybe then only one isolated era in the formation.

We want to know how the (particle) surface area of the disk evolves with time, which requires determination of the the total mass of the inner disk, and the particle size distribution, as a function of time. The period of interest is the era in which disk accretion signatures have disappeared, and the process of planetary formation, if any is to occur, has begun. Large bodies cannot form until the gas has significantly dissipated, as the gas damps the motions of the particles, inhibiting collisions. This issue is discussed in papers such as Weidenschilling (1980 and 1984).

A brief overview of some of the models was given in Chapter 1, and will not be repeated here. Only highlights of interest will be discussed.

5.5.2 Models of Terrestrial Planet Formation

It is hopeless to use an N-body formulation for a large number of particles. In the very early stages of disk evolution, when all the particles are small, models often treat the particles as an ideal gas in a box. Later, when particles grow and gravitational interactions are important, models focus on the larger bodies. The large bodies are treated as an N-body problem, while the small particles (the tail of the mass distribution) are ignored. Since the intent of the models is usually to predict the rate of growth of the largest bodies, this method is perfectly reasonable. Once very large bodies have formed, the smallest particles do not contribute significantly to the growth of planets.

We, however, want to know the size distribution of the smallest particles even after large bodies have formed, as the small particles possess most of the surface area in the disk. No models to date have calculated the fate of the smallest particles.

Probably the best work to date has been done by Wetherill and Stewart (1993), who find that runaway growth can produce planetary embryos in 10^5 years. As discussed in Chapter 1, inclusion of equipartition of energy in the model leads to the possibility of runaway growth, reducing the timescales for terrestrial planetary formation by about an order of magnitude. Wetherill and Stewart carry out their calculations to an age of only about 10^5 yr.

Without runaway growth, by definition there is a slow, steady building of planets, which looks exponential in nature. This is best visualized with a figure from Wetherill (1980a). His Figure 5(b) is shown here in Figure 5.7. (Note: the figure is an adaptation of Figure 9 from Wetherill 1980b.) The figure refers to a numerical simulation of the formation of the Earth, and displays the fraction of mass in the four largest bodies as a function of time. The asymptotic approach to completion of the Earth is easily seen. The newer (runaway) models predict faster growth than this; Wetherill (1992) claims the Earth is $> 99\%$ grown in about 10^8 yr.

We are interested in disk surface area as a function of time. Since the theory of the formation of terrestrial planets has not been tackled in its entirety, and no models consider the smallest particles in the late stages of planetary formation, it is not very useful to formally adopt any one of the particular published models.

A better way to approach the investigation is to simply tabulate the surface area of the disk, as a function of what fraction of the Earth's mass is left in "small" particles, adopting a particle size distribution law, and picking minimum and maximum particle radii. This information may then be applied to any particular model.

5.5.3 Disk Surface Area as a Function of Time

Planets grow by agglomeration and accumulation. Regardless of the model adopted, as planets grow, the disk mass remaining as small particles diminishes

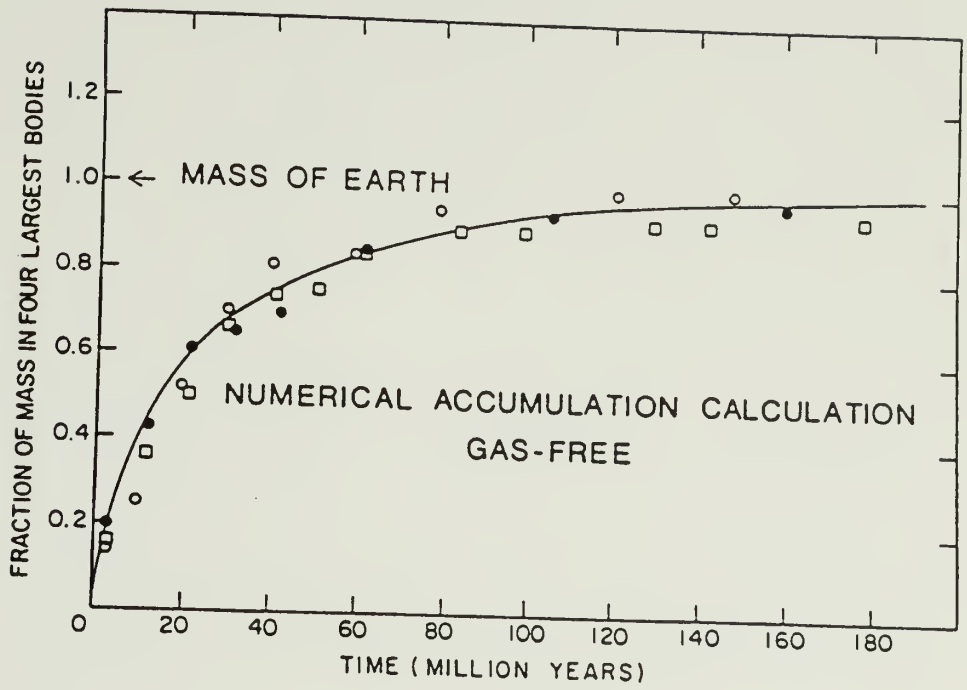

Figure 5.7. Wetherill model of Earth accumulation. Figure 5(b) from Wetherill (1980a), an adaptation of Figure 9 in Wetherill (1980b), showing theoretical predictions of the accumulation of the Earth as a function of time. The model is a three-dimensional numerical calculation assuming gas-free accumulation.

with time. Exactly how the mass in mass in small particles changes with time is unknown. Also unknown is the particle size distribution for the smallest particles. However, we can make some assumptions, and estimate the surface area in the disk as a function of time.

First consider the particle size distribution. Models which predict timescales for accumulation of planetesimals into protoplanets and planets sometimes calculate the particle size distributions. Although the models do not keep track of the smallest particles, for the size range included in the models, the particle size distribution may be quite consistent for all but the largest bodies. A good example of this is found in Wetherill and Stewart (1993). Wetherill and Stewart find their fragmentation tail has approximately a power-law size distribution with exponent -3.3. It is reasonable to assume a similar size distribution should hold for the smallest particles, until forces such as radiation drag and radiation blowout become significant.

Dohnanyi (1969) determined the size distribution law of particles in the asteroid belt, assuming collisional equilibrium. He found a steady-state power-law size distribution with exponent -3.5. This power law is still frequently quoted by authors as a "typical" power law for particles undergoing collisions in a planetary disk.

Adopting Dohnanyi's particle size distribution, note that most of the surface area will result from the small particles in the disk. To use this power law to estimate a disk surface area, one must choose a mass in small particles, and also a minimum and maximum particle radius. For a given mass, the calculated area will depend strongly on the minimum and maximum particle sizes.

Minimum particles sizes may be estimated from rocket studies of the interplanetary medium in our own solar system, or by calculations which estimate the processes which create and remove particles. Both methods have their

strengths and shortcomings. The calculations involve many assumptions, while rocket experiments suffer from the difficulty of distinguishing between interplanetary material and terrestrial material (sometimes from the rocket itself). (In this regard, Kessler (1984) found the particulate emission from solid rocket motors to range in size (diameter?) from 0.1 microns to 20 microns.)

A satellite study by Alvarez (1967) found a minimum particle radius of 5.8 μm. In a later study, Explorer 46 satellite data implied submicron particles as small as 0.1 μm (Singer, Stanley and Kassel, 1984; see also Singer and Stanley, 1980); the evidence suggests these particles are released directly from comets. The small particles should be short-lived in their orbits, owing to radiation pressure. There is probably a small population of very small particles, about 0.01 microns in size, which do not interact readily with the radiation from the central star.

Given the above, the minimum particle radius should lie somewhere between 0.01 and 6 microns.

The maximum particle radius is somewhat of a judgment call. The largest bodies will clearly be the size of terrestrial planets, but the size distribution breaks down for large bodies. Looking at the model results of Wetherill and Stewart (1993), the mass distribution law seems to break down at a mass of 10^{23} g, which corresponds to a radius of 2×10^7 cm (assuming a density of 3 g cm^{-3}). It is therefore reasonable to choose a maximum particle radius somewhere between tens of km to 200 km.

Using these limits as a guide, one can get a feeling for the expected surface area of the disk as a function of time by seeing how the surface area changes as the parameters are varied. Consider first of all that the total mass in the terrestrial planet region of our solar system adds to approximately two earth masses (2 $M_\oplus$, where 1 $M_\oplus$ is 6×10^{27} g). As the terrestrial planets grow, the mass in the fragmentation tail will decrease. The mass in the fragmentation tail can be

expressed as some fraction of the completed terrestrial planetary masses. If the formation of the terrestrial planets is 90% complete, approximately 0.2 $M_\oplus$ of material will remain as a fragmentation tail in the terrestrial zone. If the process is 95% complete, only 0.1 $M_\oplus$ will be left in "small" bodies.

Table 5.1 summarizes the disk surface area arising from the fragmentation tail, assuming a particle size distribution with power law index -3.5, and a particle density of 3 g cm^{-3}. With these assumptions, the total disk surface area due to the fragmentation tail (which is most of the disk surface area) can be calculated by:

$$A_T = \frac{3M_T}{\rho(a_{\max}^{1/2} - a_{\min}^{1/2})}\left(\frac{1}{a_{\min}^{1/2}} - \frac{1}{a_{\max}^{1/2}}\right) \tag{5.1}$$

Table 5.1. Disk Surface Area Due to Fragmentation Tail

M_T ($M_\oplus$)	M_T (g)	$a_{\min}$ (cm)	$a_{\max}$ (cm)	A_T (cm^2)
0.2	1.2×10^{27}	5×10^{-4}	2×10^{6}	3.8×10^{25}
0.2	1.2×10^{27}	10^{-4}	2×10^{6}	8.5×10^{25}
0.2	1.2×10^{27}	10^{-4}	10^{6}	1.2×10^{26}
0.2	6.0×10^{27}	5×10^{-5}	2×10^{7}	3.8×10^{25}
0.1	6.0×10^{26}	5×10^{-4}	2×10^{6}	1.9×10^{25}
0.1	6.0×10^{26}	10^{-4}	2×10^{6}	4.2×10^{25}
0.1	6.0×10^{26}	10^{-4}	10^{6}	6.0×10^{25}
0.1	6.0×10^{26}	5×10^{-5}	2×10^{7}	1.9×10^{25}

We wish to compare the surface areas in Table 5.1 to the detection limit established by the model results presented in Chapter 4. The results in Chapter 4 predicted a sensitivity to $10^{20} - 10^{21}$ g in micron-sized grains, assuming a grain density of 2 g cm^{-3}. The total surface area of such grains is $1.5 \times 10^{24} - 1.5 \times 10^{25}$ cm^2. Thus, *we can detect a tenuous disk if the total surface area of the particles in the terrestrial zone is at least* $1.5 \times 10^{24} - 1.5 \times 10^{25}$ *cm*^{2}. (Although the particle size distribution will affect the optical depth of the disk, in the optically thin case, the difference in optical depths should not significantly alter the result.)

From the results in Table 5.1, it is clear the disk material is within the detection limit of the data set when the terrestrial planets are up to 90-95% complete, for the parameters chosen.

How does this relate to the age of the planetary system? That will depend on the model of planetary formation. In the case shown in Figure 5.7, the Earth is 90% grown at an age of about 80 million years, and 95% grown at about 110 million years. We should then be able to detect tenuous dust disks up to an age of roughly 10^8 years. We don't!

However, if runaway growth occurs, the timescales for planetary formation are considerably shorter. Wetherill (1992) finds the Earth is >99% grown within about 10^8 yr, incorporating runaway growth. Wetherill and Stewart (1993) state that after 114300 years, only 10% of the present mass of the Earth is contained in the fragmentation tail. Restated, the Earth is 90% grown in only 10^5 yr, a timescale reduced by a factor of 700 from the 80 million years estimated for orderly growth (Wetherill 1980a and 1980b)! *If disk clearing is a result of planetary formation, it appears our data support the theory of runaway growth,* as we detect no dust signatures after an age of only 3×10^6 yr. Wetherill and Stewart did not publish results of their models beyond a protostellar age of 114300 years, so we cannot yet compare our results directly with their models. Given a fairly broad range of parameters, we should be able to detect a disk up until the planets are at least 90-95% formed.

It is important to keep in mind that the parameters of a forming planetary system are not well known. The particle size distribution, minimum particle sizes, and even maximum particle sizes are all estimates. The parameters given here cannot be considered more than a crude estimate. In particular, the disk surface area depends strongly on the rate at which micron-size and sub-micron size particles are removed from the disk and replenished, rates which are unknown.

In Chapter 1 it was mentioned that one of the reasons we believed we would observe tenuous dust signatures in stars having ages of perhaps hundreds of millions of years was that our Moon shows cratering evidence which suggests a period of "heavy bombardment" lasting until an age of about a billion years. How is this reconciled with the notion of rapid formation of the terrestrial planets? Although the initial accumulation of material in a body may be rapid, the final accumulation of material onto the planets is a very slow process. In fact, the process continues to this day on our own planet.

5.6 Results from Related Observing Programs

5.6.1 The Pre-Main Sequence Stars

In Chapter 1, some of the results of earlier observing programs were mentioned as motivation for pursuing the study detailed in this document. For closure, the results of this program will be discussed in the light of those and other related programs. Consider first the pre-main sequence stars.

K. Strom *et al.* (1989) compiled broadband optical and near-infrared data, acquired by other groups, for pre-main sequence stars in Taurus-Auriga. They found few stars older than about 3×10^6 yr having evidence of optically thick emission at 2.2 microns. Our sample of pre-main sequence stars was chosen from the K. Strom *et al.* sample. Whereas their investigation could only distinguish between optically thin and optically thick excesses, our observations were sensitive enough to detect optically thin excess emission. Our results agreed completely with the earlier results; no excess emission was seen in any stars older than about 3×10^6 yr, despite the increased sensitivity.

Skrutskie *et al.* (1990) extended the work of K. Strom *et al.* to longer wavelengths, observing a subset of the K. Strom *et al.* sample at 10 microns with a bolometer. Ten microns fluxes for the remaining stars were estimated from IRAS

12 micron fluxes. Excess emission at 2 microns and 10 microns correlated very well, again supporting the observation that optically thick near-infrared excess emission disappears by a stellar age of 3×10^6 yr.

Beckwith *et al.* (1990) observed continuum emission in a sample of pre-main sequence stars in Taurus-Auriga at a wavelength of 1.3 mm, which is sensitive to cooler material farther out in the disk. Observations at mm wavelengths are much less sensitive to disk material; their sensitivity was sufficient to detect about $10^{-4} M_\odot$ ($33 M_\oplus$) in small particles.

Interestingly, the Beckwith *et al.* results defy the near-infrared results, and show no correlation of excess with age. Comparing our results with those of Beckwith where the sample set overlaps, stars with considerable near-infrared excesses may have no detectable emission at 1.3 mm, and stars with no near-infrared excesses may have detectable 1.3 mm emission. Before jumping to conclusions, be forewarned that the sensitivity of the 1.3 mm observations was widely variable.

Of the Beckwith *et al.* stars with upper flux limits only, ZZ Tau has the lowest upper limit of all (15 mJy), with no detection. This (along with FW Tau) was the most sensitive observation in their entire data set. In contrast, ZZ Tau has a large near-infrared excess, which is easily detected. In the reverse scenario, V819 Tau has virtually no near-infrared attributed to disk material (most or all of the excess can be explained by reddening), yet it was detected above the 3σ level at 1.3 mm (with a flux of 34 mJy). These are but two examples of many.

One other way to discuss the pre-main sequence stars is in relation to their $H\alpha$ emission. Although there are a number of classifications in use, K. Strom *et al.* defined "weak-lined" T-Tauri stars (wTTS) to be those with $H\alpha$ equivalent widths smaller than 10 $\AA$, and dubbed the remaining T-Tauri stars "classical" T-Tauri stars (cTTS). All the cTTS have significant near-infrared excess, while all the

wTTS have little or no near-infrared excess (after reddening corrections). The 1.3 mm fluxes show no correlation with $H\alpha$ equivalent width.

IRAS data is not sensitive enough to detect stellar photospheres in the far-infrared (12-100 microns), but can detect strong excesses. IRAS fluxes are provided in K. Strom *et al.* for all their sample stars. Examination of our sample stars which overlap with the Beckwith *et al.* sample set shows that an IRAS (12-100 micron) excess does not necessarily correlate with either near-infrared excess or 1.3 mm detection. Weak-lined T-Tauri stars with no near-infrared excess may have clear far-infrared excesses; the 1.3 mm emission may or may not be detectable.

Can a coherent picture be created from this information? Not really. The primary difficulty lies in the detection limits at various wavelengths. Sensitivity is greatest at near-infrared wavelengths, while one must work with mostly upper flux limits at the longer wavelengths. It has been suggested in previous papers (K .Strom *et al.*) that the lack of near-infrared excesses, coupled with detected far-infrared excesses, may be diagnostic of a circumstellar disk which has cleared in the inner regions (i.e. a disk with a hole). This is quite compatible with strong radiative clearing processes in the inner disk, coupled with slower timescales for Jovian planet-building. (As mentioned in a later section, it is possible a "Jupiter" may prevent material from the outer disk from reaching the inner disk.)

It is more difficult to explain a large near-infrared excess, with no far-infrared or mm emission. In many cases, the far-infrared or mm emission may be just below the detection limit; the sensitivities are much lower for longer-wavelength observations. The upper flux limits for many of the Beckwith *et al.* non-detections are well above the detected flux levels. It is very possible that a higher sensitivity would have resulted in a 1.3 mm detection. The one curious case is ZZ Tau, which was not detected at even the 15 mJy level. In this regard, K. Strom *et al.* note in

their Tables 4 and 5 that a strong far-infrared source lies 45″ to the south of ZZ Tau, making it impossible to determine the 60 and 100 micron flux from ZZ Tau alone. Beckwith *et al.* used an 11″ beam with a 30″ chop. The direction of the chop was not stated. If the chop was north-south, it is possible their ZZ Tau data is contaminated by the strong source to the south.

One cannot infer much from current data which implies a near-infrared excess, but no strong far-infrared or mm excess for a particular pre-main sequence star. Hopefully improved space-based observations, such as will be made using the ISO satellite, will improve our understanding of puzzles like this.

To briefly summarize the pre-main sequence results, first, observations pertaining to the inner disk may not reflect the properties of the disk as a whole. Secondly, observations sensitive to the outer disk regions lack the sensitivity needed for true comparison to data exploring inner disk conditions. Lastly, we expected to see tenuous dust emission in the inner disk for perhaps hundreds of millions of years. The surprising result that the near-infrared emission drops below the detection level after a mere 3×10^6 yr suggests the clearing processes in the inner disk are quite rapid.

5.6.2 The Main Sequence Stars

Before models incorporating runaway growth became popular, the "standard model" predicted long timescales for planetary formation in our solar system. Figure 5.7 from a 1980 review paper by Wetherill demonstrates a typical model assuming orderly growth. The long timescales predicted by orderly growth, along with cratering evidence within our solar system, suggested that the surface area of debris in a circumstellar disk may be great enough to permit detection at near-infrared wavelengths up to stellar ages of hundreds of millions of years. This was the motivation behind our own work.

Realizing the potential for detection of disk material around young main sequence stars, Witteborn *et al.* (1982) searched for fragmentation debris associated with 13 stars in the Ursa Major Stream, roughly 300 million years in age. Our Sun is embedded in the Ursa Major Stream, so the stars are close and bright. Witteborn *et al.* opted for observations at 10 microns (N), but found no significant (3σ) excess emission in any of the observed stars. They predicted "normal" (photospheric) fluxes from V-N as given by Johnson (1966) and extrapolations based on effective temperature and the Planck function. Their measurements were sensitive to $2 \times 10^{-5} M_{\odot}$ in debris, based on a particle size distribution with power law index of -3.5, a maximum particle radius of 50 km, and a minimum particle radius of 0.1 microns. We also looked at Ursa Major stars, and saw no near-infrared excess emission, in keeping with the Witteborn *et al.* results. Our work was sensitive to a smaller mass in material, and provided a better means of assessing excesses. Our experience with using V-L (or N) to predict infrared magnitudes has produced crude results at best.

Choosing another tactic, Skrutskie *et al.* (1991) looked for remnant gas disks around Ursa Major Stream stars, again preying upon the nearness of the cluster stars. Observations of the ^{12}CO ($J = 1 \rightarrow 0$) transition at 115 GHz (3 mm) yielded only upper limits to the gas in circumstellar disks (or shells). If the disks have radii greater than 350 AU, the upper limit to the disk mass is $3 \times 10^{-5} M_{\odot}$. Their results are consistent with our non-detection of near-infrared excesses.

Far-infrared data from the IRAS satellite has revealed excess emission associated with many main sequence stars. The phenomenon was first seen for α Lyrae (Vega), as reported by Aumann *et al.* in 1984. Since that discovery, various authors have searched the IRAS database for evidence of far-infrared excess associated with other stars, attempting to find a pattern to the excesses. Excellent studies are Aumann (1988) and a master's thesis by Gary Kleiman

(1993). Backman and Paresce (1992) review the topic. In most cases, it is not known whether the far-infrared excess emission arises from a circumstellar disk, or a shell. Only β Pictoris has been imaged to reveal a distinct disk of material. Aumann (1988) found that far-infrared excesses associated with A, F, and G stars is the exception, rather than the rule. The stars with excesses can be as old as 1-5 Gyr, which is most likely past the age of active planet formation (Backman and Paresce, 1992). This strongly contrasts our finding that the near-infrared excess disappears by an age of only 3×10^6 yr.

5.7 Implications for the Persistence of an Outer, Remnant Disk

5.7.1 Observational Evidence for the Persistence of an Outer Disk

The results from other observing programs quoted in the previous section provide strong evidence for the persistence of disk material in the outer disk well into the main sequence stage. The coldest material is quite difficult to detect; mm observations are subject to beam-filling factors and thermal background, while far-infrared observations are only possible from spacecraft.

The Beckwith *et al.* (1990) 1.3 mm continuum results clearly show that cool material may reside around a pre-main sequence star even when no warm material is detected. The oldest star in their sample had an age of 4×10^7 yr (Elias 1), which had a strong 1.3 mm flux. Six of their sample stars had an age greater than 3×10^6 yr, four of which had better than 3σ detections at 1.3 mm. Our near-infrared data showed no thermal excess emission after an age of 3×10^6 yr.

The IRAS far-infrared (12-100 micron) results are enticing; a fine review is found in Backman and Paresce (1992). IRAS was quite successful at detecting cool (50-125 K) material around many stars. The biggest question is whether or not the material lies in a disk, which would suggest possible planetary formation, or whether the material is simply distributed in a shell. In only one case has the

matter been definitively resolved; Smith and Terrile (1984) used a coronograph to image an edge-on disk of material surrounding β Pictoris.

The β Pic disk extends from radii less than 100 AU to radii greater than 1000 AU. The best images of the β Pic disk were unpublished (Smith and Terrile), but the relevant information may be found in Backman and Paresce (1992). The IRAS data is sensitive to material around β Pic lying between 30 and 100 AU from the star. This region corresponds to the hypothetical Kuiper belt in our solar system, believed to be the origin of short-period comets. β Pic has no near-infrared excess.

The β Pic system is an irrefutable case of a disk of material around a star, with no evidence of disk material in its terrestrial zone. The failure to detect evidence of terrestrial material may mean that planetary formation has proceeded to a point where little fragmentation debris remains, or that planetary formation never occurred at all. The present data does not allow one to distinguish between the two possibilities. Since β Pic is of spectral type A, which implies an age of roughly 10^8 yr, models incorporating runaway growth certainly allow for near-completion of planetary formation in this system. This can easily account for the failure to detect warm material near the star.

The β Pic system lends support to the evolutionary scenario in which disks clear from the inside out, i.e. the inner regions clear first. Such a scenario was also proposed in Skrutskie *et al.* (1990), based on near-infrared and IRAS data for pre-main sequence stars. Whether or not disks with cleared inner regions represents an evolutionary trend, one can certainly say that a star may show no evidence of material in the terrestrial zone, yet possess substantial material in an outer disk.

5.7.2 Could a "Jupiter" Isolate the Inner Disk?

Knowing that material around some stars may persist at large disk radii, with no corresponding evidence of material in the inner regions, the question arises why

radiation drag does not draw some of the smaller particles to the inner disk regions. The β Pic disk is a perfect example. The outer edge of the disk is at least 1000 AU from the star; the inner edge may extend to less than 100 AU. No near-infrared thermal excess indicative of material in the terrestrial zone has been detected.

One possibility is that radiation drag does not draw in sufficient material for detection. Another scenario derives from observations of Saturn and its ring system.

In 1979, when the Voyager I spacecraft flew by Saturn, the images transmitted to Earth showed Saturn's rings to be composed of at least a thousand ringlets, rather than just a few rings. The F ring had a "braided" pattern which could not be explained. The phenomenon posed quite a puzzle to astronomers at the time, and was a popular subject for even cartoonists of the day. The mystery of both the numerous ringlets and the twisted appearance of the F ring was solved with the discovery of "shepherding satellites" seen within the rings on images from both Voyager I, and later, Voyager II. These small satellites confine ring material by transfer of angular momentum.

Although no rigorous arguments will be given, it may be possible for a large forming planet, perhaps a Jovian planet, to act as a one-sided shepherd, transferring angular momentum to particles farther out in the disk. This would effectively isolate the outer disk from the inner disk, preventing the outer disk from resupplying the inner disk with dust particles. As discussed in Section 1.2.4, it is likely the core of Jupiter formed in $10^5 - 10^6$ yrs. This is much shorter than the 3×10^6 year timescale in which near-infrared dust signatures disappear.

5.8 Detectability of Dust in Our Solar System from Afar

Scattered light from the dust in the plane of our own solar system can be viewed after sunset or before sunrise as the beautiful zodiacal light and

gegenschein. How easily could we detect this dust if we could move our telescopes to an extra-solar planet?

Whipple (1967) estimates the total mass of the zodiacal cloud within a radius of 3.5 AU to be 4.5×10^{19} g, assuming a mean space density of 2×10^{-22} g cm^{-3} within $i < 20°$ of the ecliptic. (Whipple remarks shortly afterwards that this estimate is probably too high, since the outer regions are less dense, and guesses the true mass may be only 2.5×10^{19} g. The higher number will be adopted here to provide an upper limit.) This number cannot be compared directly to the model results in Chapter 4, as the particles in the zodiacal cloud are not all 1 micron in radius.

To convert Whipple's mass estimate into the surface area produced by micron-radius grains, a particle density, particle size distribution law, minimum particle radius, and maximum particle radius must be chosen.

It is customary to assume a power law particle size distribution, i.e. $n(a) = ka^{-\delta}$, where $n(a)$ is the number of particles having radius a within an interval da, k is the normalization constant, and δ is the index of the power law. As discussed in Section 5.5.3, a widely accepted index for the power law is -3.5.

To get an upper limit on the detectability of the zodiacal material, assume the material is made up of only small particles. A paper presented by Alvarez (1967) at the same conference as Whipple's work announced detection of interplanetary particles ranging in size from 5.8 μm to 4.9 mm. The range of particle densities and particle size distributions obtained from experimental studies of interplanetary dust near the Earth is quite broad. As discussed in Section 5.5.3, interplanetary particles may be as small as 0.01 microns. It is likely radiation blowout will quickly remove any particles with radii smaller than 0.5 microns.

With a minimum particle size of 5.8 μm, a maximum particle size of 4.9 mm (Alvarez 1967), a particle density of 3 g cm^{-3}, and a particle size distribution

index of $\delta = 3.5$, the surface area produced by 4.5×10^{19} g of zodiacal material is equivalent to only 2.7×10^{17} g of dust in the micron-radius grains of Chapter 4. This is a factor of 10^3 or more below the mass detection limit of $10^{20} - 10^{24}$ g derived in Chapter 4.

Table 5.2 displays this result, along with results for two other sets of parameters. Here ρ is the particle density of real zodiacal dust, δ is the index of the particle size distribution, $a_{\rm min}$ is the minimum particle radius, $a_{\rm max}$ is the maximum particle radius, and $M_{\rm zod}$ is the total mass of the zodiacal cloud within 3.5 AU of the Sun, assuming the mass is composed entirely of micron-radius grains having a density of 3 g cm^{-3}. $M_{\rm zod}$ may be compared directly with the mass detection limits presented in Chapter 4.

Zodiacal dust may be less dense than 3 g cm^{-3}; one example examines the case when $\rho = 1$ g cm^{-3}. In the last case, a minimum particle radius of 0.5 microns was assumed, typical of that predicted by radiation blowout. The results of the three sets of parameters are comparable. The model results of Chapter 4 require a minimum of $M_{\rm zod} = 10^{20} - 10^{21}$ g for the zodiacal dust to be detectable.

Table 5.2. Mass of Zodiacal Cloud in Micron-Radius Grains

ρ(g cm^{-3})	δ	$a_{\rm min}$ (μm)	$a_{\rm max}$ (mm)	$M_{\rm zod}$ (10^{17} g)
3	3.5	5.8	4.9	2.7
1	3.0	5.8	4.9	1.9
3	3.5	0.5	4.9	3.0

Thus, if we could observe the solar system from the vantage point of a distant star, we would not be able to detect the near-infrared excess from the zodiacal cloud. If circumstellar disks evolve on timescales typical of the disk from which our solar system formed, we would not expect to detect near-infrared excesses in stars the age of the Sun.

5.9 Implications for the Rate of Evaporation of Cometesimals

One of the issues which can be examined using the results of this work is the rate at which cometesimals evaporate in young planetary systems. This has particular relevance in the study of the formation of planetary atmospheres.

One way to produce a planetary atmosphere is by outgassing. The author's non-astronomical observations in Hawaii's Volcanos National Park (a classic pleasure after observing runs on Mauna Kea) attest to the persistence of outgassing even billions of years after the formation of the Earth.

Another way to create an atmosphere is by capture of gases after the formation of the planet. The evolution of the gas in circumstellar disks is not well known, owing to the difficulty of the observations. However, one source of gas in the disk is the evaporation of cometesimals. In our own solar system, cometesimals should have been plentiful at the time the Jovian planets were forming. Icy planetesimals were common in the Jovian planet region, and massive Jovian cores routinely perturbed the orbits of the icy planetesimals. Many were flung beyond the orbit of Neptune; many must have been coaxed into the inner solar system.

The cometesimals are composed of both ice and rock. As cometesimals evaporate, both gas and dust are released. The observations presented in this dissertation may be used to place an upper limit on the dust released by cometesimals. This can in turn be used to glean some information about the gas released. The following perusal presents some simple arguments for thought.

Studies of Comet Halley revealed that comets are more like "icy mudballs" than "dirty snowballs." Regardless of the initial percentages of ice and rock, the gases in a comet evaporate more easily than the rock. Very old comets are mostly rock. Most comets survive only 1000 trips near the Sun.

For the sake of argument, suppose that a typical cometesimal has a radius of 1 km, a period of 100 years, and an average density of 0.2 g cm^{-3} (as for Comet

Halley; Seeds, 1994). The total initial mass of the comet is then 8×10^{14} g. Assume that with each passage near the Sun it loses 0.1% of its mass, 10% of which is in the form of dust. Loosely speaking, it then follows that with each passage, the comet loses 8×10^{11} g of material, 8×10^{10} g in dust. Call it 10^{12} g for simplicity.

The models presented in Chapter 4 imply that 10^{20} g of micron-radius dust within 3 AU of the central star should be detectable. In order to supply 10^{20} g of dust to the terrestrial planet region in 10^3 years (the timescale in which radiation drag clears the terrestrial planet region of dust), roughly 10^8 cometesimal passages are needed in 10^3 yr, or 10^5 cometesimal passages per year.

This rate of dust production also implies, with the chosen parameters, that 10^{21} g of gas would be generated every 10^3 years. Only a fraction of that would be swept up by any particular terrestrial planet under formation, probably 10% at most. That leaves roughly 10^{20} g of gas to be swept up by a planet like the Earth every 10^3 yr.

For a crude estimate of the mass of the Earth's atmosphere, assume the atmosphere is 100 km thick, and has a density of 1.3×10^{-3} g cm^{-3}. Using

$$M_{\rm atm} = 4\pi R_{\rm Earth}^2 \rho \, dr,$$

where $M_{\rm atm}$ is the mass of the Earth's atmosphere, $R_{\rm Earth}$ is the mass of the Earth, dr is the thickness of the Earth's atmosphere, and ρ is the density of the Earth's atmosphere, one finds that $M_{\rm atm} = 7 \times 10^{22}$ g, or roughly 10^{23} g.

If a planet like the Earth swept up gas from cometesimals at the rate of 10^{20} g per 10^3 yr, it would take 10^6 yr to sweep up enough gas to equal the mass of the current Earth atmosphere.

A million years may be a perfectly reasonable timescale for producing an atmosphere, but a cometesimal flux of 10^5 per year for a million years is a very high flux. Perhaps such a high rate was possible during the formation of the

Jovian planets. Certainly such a rate is inconceivable in the recent past of our solar system.

The reader is left to reproduce the calculations presented with the parameters of his or her choice. It is certain that at least some portion of the Earth's atmosphere is a result of outgassing. The arguments presented here are intended to provoke thought on the role of cometesimal evaporation in the role of planetary atmospheres.

5.10 Summary

We obtained sensitive broadband near-infrared observations of young cluster stars, searching for excesses indicative of tenuous dust in the terrestrial zone of circumstellar disks. Starspots and low-mass companions should not produce detectable excesses at our sensitivity levels; infrared excesses arising from free-free emission can be flagged by information from other databases.

When we started this program, we fully expected to see dust signatures for stars up to perhaps hundreds of millions of years in age. Instead, we found the excesses disappeared by an age of only 3×10^6 yr. If all the debris is composed of micron-radius grains with density 2 g cm^{-3}, our observations are sensitive to about $10^{20} - 10^{21}$ g of material.

The best current explanation for the early demise of dust signatures is that the terrestrial planets form via runaway growth. In this case, the fragmentation tail diminishes much more quickly than for orderly growth. Published results for models which incorporate runaway growth in the terrestrial zone do not extend to an age of 3×10^6 yr, which makes it impossible to compare our results directly with the model results. However, orderly growth predicts that planets may be 90% complete at an age of about 80 million years, while runaway growth permits 90% completion at little more than 10^5 years. Depending on the parameters chosen, we

should be sensitive to disk debris in the terrestrial zone until the terrestrial planets are at least 90-95% complete.

Our data set is not complete in that we lack observations of late-type stars in our youngest main sequence cluster, Alpha Perseus. As the late-type stars are expected to evolve more slowly than their higher-mass siblings, it is conceivable we missed tenuous dust signatures in this cluster (age 20-80 million years).

Results of observing programs at longer wavelengths (far-infrared and mm) often show implicit evidence of disk material at large radii, even when there is no detectable thermal emission from inner disk regions. In the case of the main-sequence A star β Pictoris, an edge-on disk of material extending over 1000 AU from the star has been definitively imaged, yet no near-infrared excess emission is observed. One envisions a disk with a "hole." To put this in perspective, someone observing our solar system from a distant stellar system would not detect a near-infrared excess from the dust in the zodiacal cloud, yet we believe there is cold material well beyond the orbits of Neptune and Pluto, from which the short-period comets originate.

It is not yet known whether a "hole" in a disk represents an evolutionary trend in which in the inner regions of the disk are the first to clear. When no warm material is detected around a star, it is impossible to determine whether planetary formation has occurred, or whether the inner regions are truly devoid of material. It is possible the formation of a Jovian-type planet could prevent material in an outer disk from reaching the terrestrial zone.

Chapter 6

CONCLUSIONS

6.1 Background and Objective

As infrared and radio astronomy come of age, the investigation of how stars and planetary systems form has become one of the foremost topics of observational and theoretical astronomy. The possibility of extra-solar planets, perhaps harboring intelligent life, tickles the imagination. Although extra-solar planets have been detected orbiting a supernova remnant, no planets have been detected around main-sequence stars like our Sun. It is likely we will hear of such detections within a decade or so. All evidence seems to imply planets are a natural byproduct of the birth of stars. Currently it is not feasible to detect planets directly, or observe the formation process directly. We can, however, observe secondary indicators of the processes occurring as new stars are born. In this work, we sought to determine timescales of terrestrial planet formation around young stars in clusters by looking for weak near-infrared excess emission arising from debris in the circumstellar disks. Planets presumably form by accumulation and agglomeration of material in the disks.

Planets are much cooler than the stars/protostars which they orbit, and have much less surface area. As a result, they are much dimmer than the central star, to the point where direct detection is currently all but impossible. However, the precursors to the final planets are more easily detected. It is believed that circumstellar disks form naturally by conservation of angular momentum when cores of molecular clouds collapse to form protostars. Direct images of disks are

few, but the evidence for numerous disks is convincing. Planets may form form by accumulation and agglomeration of the dust and gas in the circumstellar disks. During the epoch of planetary formation, the disk is composed of gas, dust, growing planetesimals, protoplanets, and collisional debris. The disk material in the terrestrial planet region has temperatures on the order of hundreds of Kelvin, having peak thermal emission at near-infrared wavelengths. The total surface area of the debris may easily exceed the surface area of the central star by a factor of 10 or 100 or more. The cooler temperatures of the disk material, and the increased surface area makes the disk ideally suited for detection at infrared wavelengths. In the very early stages of star formation, when infall contributes significantly to the luminosity, the infrared emission from the disk may exceed the infrared output from the central star. As the disk material is accreted, and accumulated into planets, the disk surface area decreases, and the infrared emission from the disk/planetary system fades. Eventually, the observed infrared emission will be that expected from the stellar photosphere itself.

Theoretical models and fossil evidence in our own solar system provide a good idea of the timescales of disk evolution and planetary formation. However, observational evidence from forming planetary systems is needed to constrain the models. By observing the infrared emission from young stars having a range of ages covering the predicted timescales, one may deduce the evolutionary trends of the disk emission, and glean information about the timescales of planetary formation.

6.2 Method and Observations

A tenuous dust disk in the terrestrial zone of a young star can be detected by means of the near-infrared radiation it emits. Sensitive near-infrared observations can be made with ground-based telescopes, owing to the high transparency of the atmosphere at certain near-infrared wavelengths, known as atmospheric

"windows." Broadband filters have been developed to match the wavelength ranges of the windows; the filters include J (centered on 1.25 μm), K (2.2 μm), L (3.45 μm), L′ (3.80 μm), M (4.8 μm), and N (10 μm). Disk emission at 1.25 μm (J) is most likely to be photospheric; excess emission arising from a circumstellar extending to an inner radius defined by the temperature at which dust vaporizes normally appears at wavelengths of 2 μm (K) and longward. Excess emission may be diagnosed by the resulting change in the slope of the spectral energy distribution longward of 1 micron. We chose to evaluate the change in the slope of the spectral energy distribution by plotting broadband colors, primarily J-K and J-L (or J-L′), which is equivalent to using flux ratios.

Sample stars were chosen from clusters, which are easy to date, and have well-known properties. As tenuous dust signatures were expected for perhaps hundreds of millions of years, the sample stars range in age from pre-main sequence, near the age for which optically thick disk signatures are known to diminish, to about 600 Myr. The pre-main sequence stars were chosen from the Taurus-Auriga complex (1-10 Myr). The main sequence stars were chosen from the clusters Alpha Perseus (20-80 Myr), the Pleiades (70 Myr), the Ursa Major Stream (300 Myr), the Hyades, and Praesepe (both ~600 Myr). All of these clusters are relatively nearby, well-studied, have near-solar metallicities, and have a wide range of spectral types.

6.3 Results

J-L (or J-L′) *vs.* J-K color-color plots were used to evaluate near-infrared excess emission, as illustrated in Chapter 4. The main sequence cluster stars form a tight locus, representing photospheric colors. The scatter in the locus defines our sensitivity to weak excess emission. No infrared excess emission is observed for any main sequence stars; the youngest cluster has an age of 20-80 Myr. (Although we

observed nearby, presumably diskless main sequence stars chosen from the Woolley catalog to define a main sequence locus, we later discovered this had been unnecessary, as the cluster stars themselves defined a photospheric locus.)

Young T-Tauri stars show classic optically thick near-infrared emission, which is easily seen on our color-color plots as a vertical deviation from the photospheric locus. Reddening affects are also observed, but at the wavelengths used, reddening shifts the observed colors along the direction of the photospheric locus, rather than displacing the colors vertically above the photospheric locus. This is fortunate, as it implies accurate extinction measurements are not critical. No definitive infrared excess emission is observed for pre-main sequence stars beyond an age of about 3×10^6 yr. The age of the stars was determined from calculated isochrones; the quoted age thus depends on the model adopted.

A model of the expected dust emission arising from optically thin disks was used to place upper limits on the amount of material in circumstellar disks. Although the model also calculates emission from disks which are optically thick, the model is only reliable in the optically thin case. Assessing the scatter in our data and the model predictions, we conclude our measurements are sensitive enough to detect as little as $10^{20} - 10^{21}$ g in micron-radius dust grains distributed over the terrestrial zone. The model assumes a grain density of 2 g cm^{-3}, and allows for a disk mass surface density falling off as either R^{-1} or R^{-2}. These and other model parameters are discussed in Chapter 4 and Appendix C.

6.4 Discussion and Conclusions

We observe no near-infrared thermal emission characteristic of tenuous dust disks beyond a stellar age of about 3×10^6 yr. We originally expected to see dust signatures for perhaps hundreds of millions of years, based on model predictions of terrestrial planet formation, and cratering evidence in our own solar system.

The model predictions for infrared emission from thermal dust disks were based on a population of micron-radius dust grains. In order to compare our model results directly to models of planetary formation, our results must be converted to those from a more realistic particle size distribution. Assuming the disk is truly optically thin, the optical depth in the disk should not change much if a power law particle size distribution is substituted for the uniform distribution. This being the case, one may presume we are sensitive to emitting disk surface area, rather than particle mass. Using our best estimate for a power law particle size distribution (index −3.5), and likely minimum and maximum particle radii, we believe we should be able to detect tenuous dust disks up until the time when the terrestrial zone is at least 90-95% complete.

According to older models of planetary formation, which assume orderly growth of planetesimals and protoplanets, the Earth was 90% complete after about 80 million years (see Wetherill 1980 and 1980a). Surprisingly, we detected no evidence of tenuous dust after only 3×10^6 yr. Newer models of terrestrial planetary formation include equipartition of energy, which leads to the possibility of runaway growth (see Wetherill, 1990, and Wetherill and Stewart, 1993). With runaway growth, Wetherill and Stewart calculate the Earth is 90% formed after a mere 10^5 yr. This is more compatible with our observed results.

If the disappearance of the dust signatures signifies planetary formation, our data appear to support models incorporating runaway growth, rather than older models assuming orderly growth. We detect no emission beyond 3×10^6 yr from the terrestrial zone, yet we should be able to detect tenuous dust signatures for at least 80 million years, if the older models (orderly growth) are correct.

Since most models of planetary formation apply to the formation of the Earth, the timescales quoted here should be assumed to apply to G stars. If timescales of planetary formation scale with stellar lifetimes, one would expect disks around

hotter stars to evolve more quickly, and disks around cooler stars to evolve more slowly. Our data set lacks low-mass stars in our youngest main-sequences cluster, Alpha Perseus, having an age of 20-80 million years. Alpha Per is distant enough that observations of the lowest-mass stars would have required as much as an hour per star. It is conceivable we would have detected weak excesses in some of the low-mass stars if we had performed such observations.

Although our data are sensitive only to warm material in the terrestrial zone, data from other observing programs clearly show that material may persist in an outer disk even when the inner disk appears to be clear of material. It is not yet known whether this represents an evolutionary trend, in which the inner regions of the disk are the first to clear. (As discussed in Chapter 4, two wTTS in our sample might have excess emission at 10 microns, although they have no excess emission at 4 or 5 microns.) In cases where a disk is detected, but the inner region appears to be devoid of dust, one cannot discern whether planetary formation is complete, or never occurred in the first place.

6.5 Future Directions

The results of this program are quite useful in providing constraints on current models of planetary formation, but there are still loose ends which need to be tied up.

Observations of the late-type stars in our earliest main sequence cluster (Alpha Per) are lacking, which constitutes a rather important hole in our data set. If disks around low-mass stars evolve more slowly, it is possible tenuous dust signatures will be observed for some of the low-mass stars in this cluster.

The interpretation of the near-infrared colors of some pre-main sequence stars in Taurus-Auriga is ambiguous. The ambient material in this region is quite variable, which makes it difficult to accurately assess reddening in some cases.

Also, the infrared colors of diskless low-mass pre-main sequence stars is not well determined in the photometric system used. The upshot is that for a handful of sources, we cannot distinguish between reddening effects and the normally redder colors of low-mass stars. In order to clarify the ambiguity, one would have to accurately determine the reddening to each source, verify the reddening law in each corresponding region of the cloud, obtain the highest-quality spectra of each source to accurately determine the spectral classification, and determine normal photospheric colors of late-type stars in the IRTF (RC2) photometric system. It is unlikely we will ever have a truly convincing understanding.

Ideally, one would like to find a bright cluster of very young (1-10 million years) stars with little ambient material, possessing stars with a wide range of spectral types. The effects of reddening would then be minimal.

New spacecraft will improve the current infrared data set for both pre-main sequence and main sequence stars. No images shortward of 4 microns are planned; the detectors on the satellites will be sensitive to cooler regions of the disk than those studied by us.

Appendix A

RELATIVE COLORS OF THE CALIBRATOR STARS

A.1 Definition of the Problem

The magnitude at a particular wavelength of a given calibrator star is a function of the photometric system used. The published magnitudes for the calibrator stars used in this program reflect a variety of photometric systems. Unfortunately, the transformation equations between the various systems are not well known, especially at wavelengths longer than K(2.2μm).

When published magnitudes for standards were originally used to reduce the cluster star data, large shifts were seen in the colors of the cluster stars as a function of the calibrator used. This effectively increased the scatter in the data by as much as a factor of 5. In order to obtain the maximum information from the data set, the relative colors of the calibrators should be known to at least the accuracy of the measurements being made. An internally consistent set of calibrators is needed for each telescope facility.

The standard method for determining relative magnitudes of calibrators is to obtain measurements of each calibrator at the telescope of interest over the course of at least a few hours, covering a range of airmasses, then note the relative instrumental magnitudes as a function of airmass for the evening. Ideally, one would like to measure both calibrators at the same airmass at the same time of night; there is only one opportunity to do this in a given night. This method could

not be successfully employed for this data set. Although some calibrators were observed over the course of several hours, there was little overlap in time of different calibrators. The non-linear nature of the airmass curves made it impossible to accurately determine the relative magnitudes of the calibrators when the times of observation did not overlap, as described in Section 3.2. Although determination of the relative *magnitudes* of the calibrators was not possible at the desired accuracy for this project, there was sufficient information to determine the relative *colors* of the calibrators, using plots of infrared colors vs. spectral type for the cluster and Woolley stars observed. This was possible owing to the fact that no excess infrared emission was observed from any of the main sequence stars in the sample. The following sections detail the method.

A.2 Published Magnitudes

The magnitudes for the standard stars were originally obtained from unpublished catalogs, which were usually a compilation from several other catalogs and private communications. Most were obtained from the IRTF Photometry Manual. The catalogs did not always note the photometric system assumed. Table A.1 lists the original calibrator magnitudes used in the data reduction, including the photometric system, if known. Dashes indicate magnitudes not needed for this data set.

A.3 The Relative J-K, J-L′, and K-L′ Colors of the Calibrators.

Figure A.1 shows the reddening-corrected K-L′ *vs.* spectral type (SpT) for the highest-quality measurements of the main sequence stars observed at the IRTF, derived using the calibrator magnitudes in Table A.1, and the Elias (1978) reddening law for the Taurus region, as given in Table A.2. Cluster star

Table A.1. Published Magnitudes of Calibrators

Calibrator	J	H	K	L	L′	M	N
IRTF							
16 Tau	5.52b	–	5.51b	–	5.64c	5.64c	–
HD 22686	7.195b	7.190b	7.185b	–	–	–	–
4 Lac	4.30b	4.27b	4.25b	4.23b	4.21c	4.22c	–
pi^4 Ori	4.04b	4.10b	4.14b	4.17b	4.17c	4.32c	–
HD 77281	7.105b	–	7.030b	–	6.995b	–	–
beta Peg	–	–	–	–	–	–	-2.54c
alpha Tau	–	–	–	–	–	–	-3.03c
KPNO							
alpha Per	0.85a	–	0.54a	0.50a	–	–	–
zeta Mon	2.79	–	2.32	2.22b	–	–	–
BS 3427	4.75	–	4.23	4.20	–	–	–
eta Tau	2.93a	–	2.94a	2.92a	–	–	–
beta Com	3.19	–	2.88	2.87	–	–	–
eta Vir	3.79b	–	3.77b	3.76b	–	–	–

(a) Johnson system.
(b) CIT system. (Published L magnitudes were adopted for L′.)
(c) MKO (Mauna Kea Observatories) system.

magnitudes, visual extinction, and spectral types are from Table B.1. For plotting purposes, the standard OBAFGKM system was converted to numbers, with O=0, B=1, A=2, F=3, G=4, K=5, and M=6. An A0 star would thus be assigned the number 2.00, an A2 star the number 2.20, an A7.5 star the number 2.75, and so on.

The symbols in Figure A.1 indicate which calibrator star was used to reduce that particular main sequence star. Obvious shifts in color *vs.* spectral type as a function of calibrator are seen. Similar shifts are seen for J-K *vs.* Spectral type and J-L′ *vs.* Spectral type. These shifts can be calculated, and removed. Since photospheric colors are required for this method, the T-Tauri stars, which are known to have non-photospheric emission, cannot be used.

For any given calibrator, the plots of infrared color *vs.* spectral type have a linear region. If points outside this region are removed, including the late-type stars, the earliest-type stars, the Be stars, and some poor-quality measurements, a

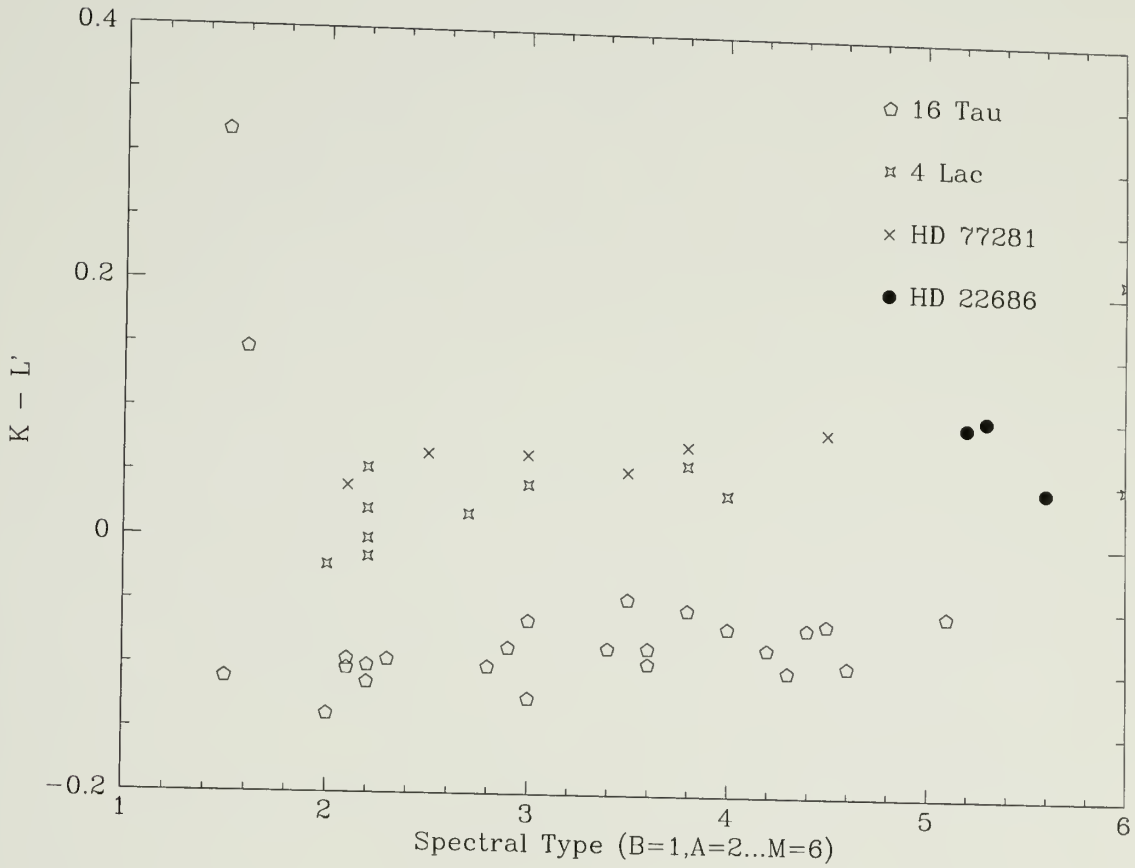

Figure A.1. Shifts in colors using published magnitudes for calibrators. Shown are the reddening-corrected K-L′ colors *vs.* spectral type for the highest quality observations of main sequence cluster stars at the IRTF. Symbols distinguish the calibrators used to derive the cluster star colors; published magnitudes for these calibrators were used in the data reduction. Note the shift in colors as a function of the calibrator used, particularly for 16 Tau. Internal inconsistencies in the assumed calibrator magnitudes create the appearance of increased scatter in the observed cluster star colors.

Table A.2. Elias (1978) Reddening Law for the Taurus Region

$$
\begin{aligned}
A_J &= 0.31A_V \\
A_H &= 0.18A_V \\
A_K &= 0.092A_V \\
A_L &= 0.052A_V \\
A'_L &= 0.047A_V \\
A_M &= 0.029A_V \\
A_M &= 0.019A_V
\end{aligned}
$$

best-fit line can be calculated for each calibrator. The results of the least-squares fit for the IRTF data are shown in Figures A.2. The results of the least-squares fit for the KPNO data are shown in Figures A.3. The data has been corrected for interstellar extinction.

Since the slopes of the best-fit lines vary between the calibrators, a particular spectral type must be chosen for comparison. In general, the shifts in colors between calibrators was evaluated at SpT=3.5, an average spectral type. In the IRTF data set, the fit for HD 22686 is very poor, since there are only 3 points available for which to calculate a fit, all at nearly the same spectral type. The shifts for HD 22686 were thus evaluated at SpT=5.37, the average spectral type for the three points. Similarly, in the KPNO data set, shifts for zeta Mon and beta Com were evaluated at SpT=2.70 and SpT=2.28, respectively.

One calibrator at each telescope must be chosen as the "standard" to which all others are compared. The Elias (Elias *et al.*, 1982) standards 4 Lac (IRTF) and eta Vir (KPNO) were chosen for this purpose. Table A.3 lists the adjustments to the published colors of each calibrator which will bring them into agreement with either 4 Lac or eta Vir in their respective photometric system at the spectral type given in the previous paragraph. The adjustments should be added to the

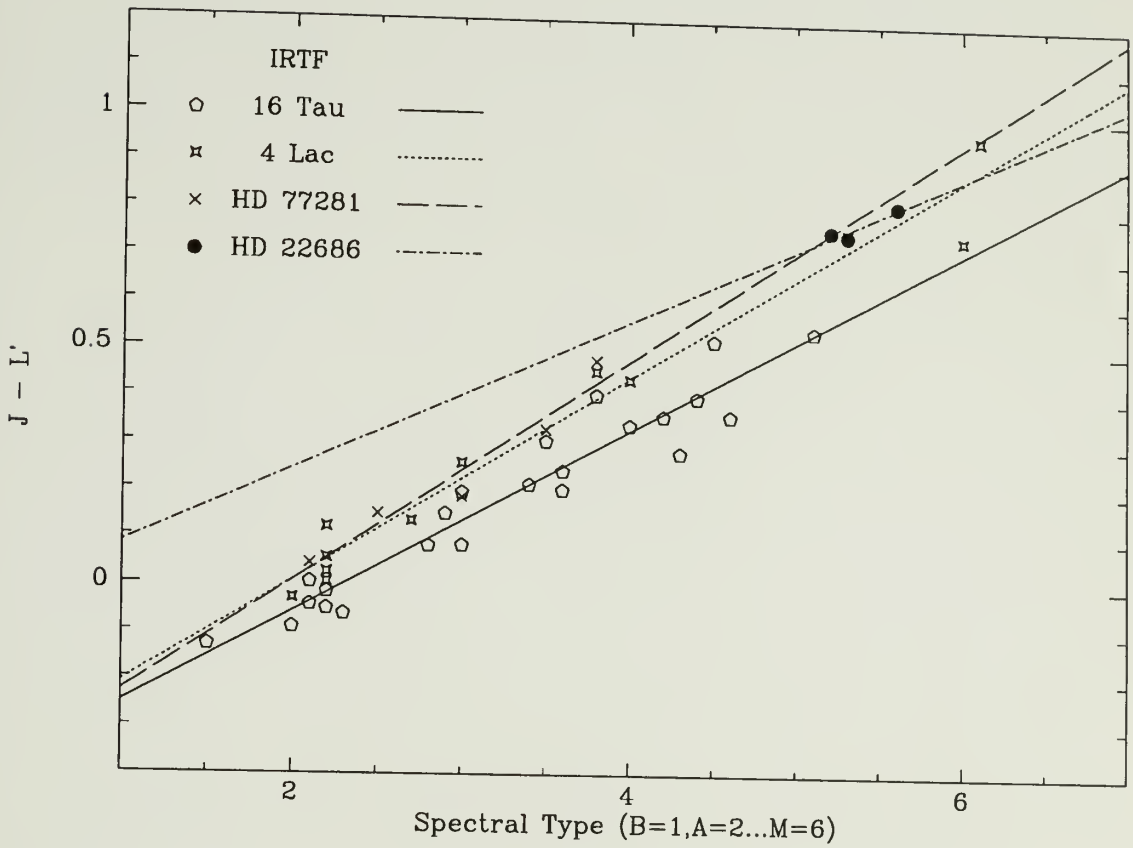

Figure A.2. Best-fit lines to determine the relative IRTF calibrator JKL′ colors. (a) Shown are the first-order least-squares fits for each IRTF calibrator for the linear region of the J-L′ colors *vs.* spectral type. Only the highest quality measurements of main sequence cluster stars obtained at the IRTF were used for the fit. Note the poor fit for the standard HD 22686.

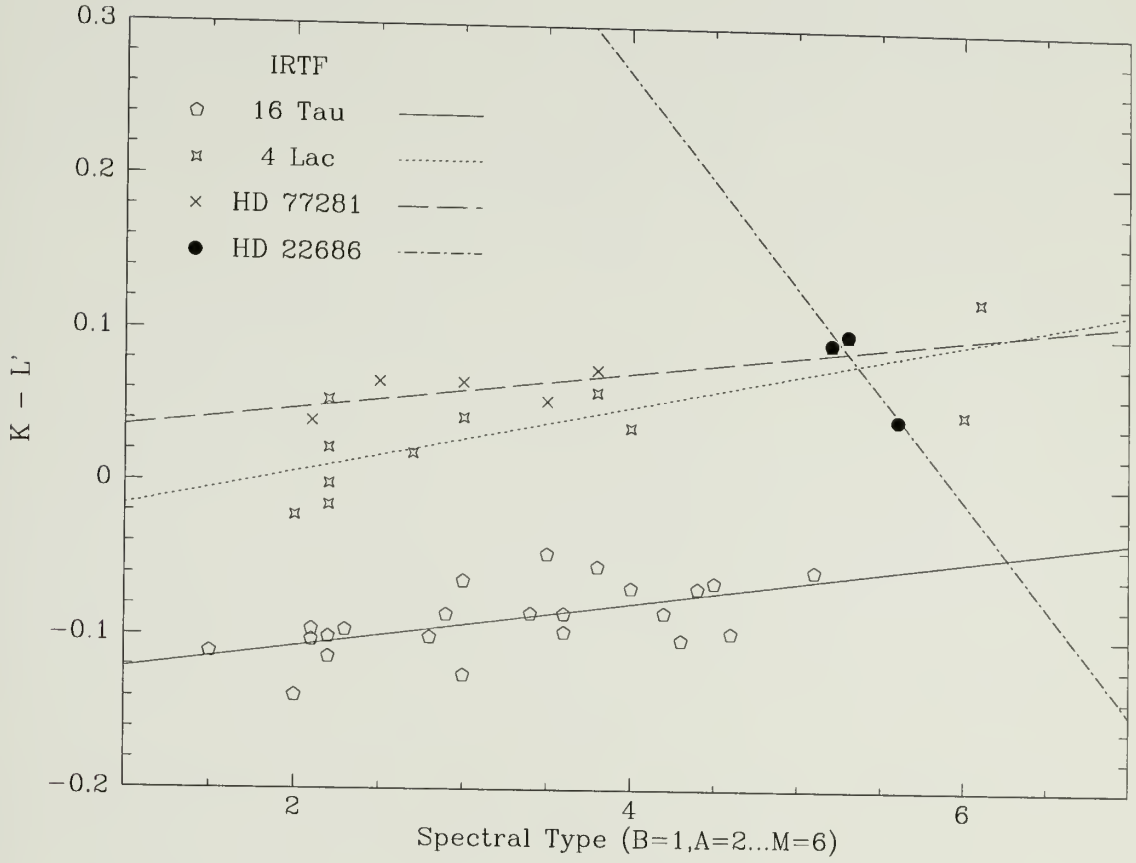

Figure A.2. (cont.) (b) First-order least-squares fits for each IRTF calibrator for the linear region of the K-L′ colors *vs.* spectral type. Only the highest quality measurements of main sequence cluster stars obtained at the IRTF were used for the fit. Note the poor fit for the standard HD 22686.

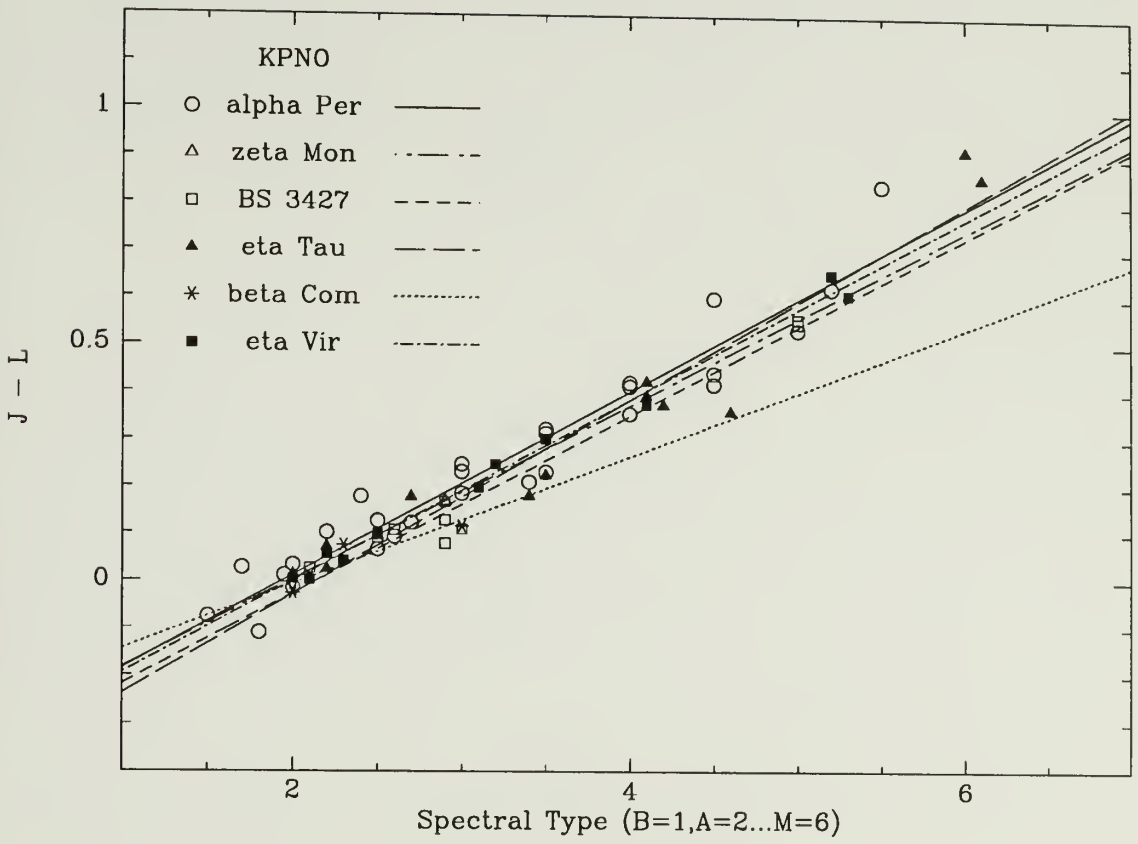

Figure A.3. Best-fit lines to determine the relative KPNO calibrator JKL colors. (a) Shown are the first-order least-squares fits for each KPNO calibrator for the linear region of the J-L colors *vs.* spectral type. Only the highest quality measurements of main sequence cluster stars obtained at the KPNO were used for the fit. Note the poor fit for the standard beta Com.

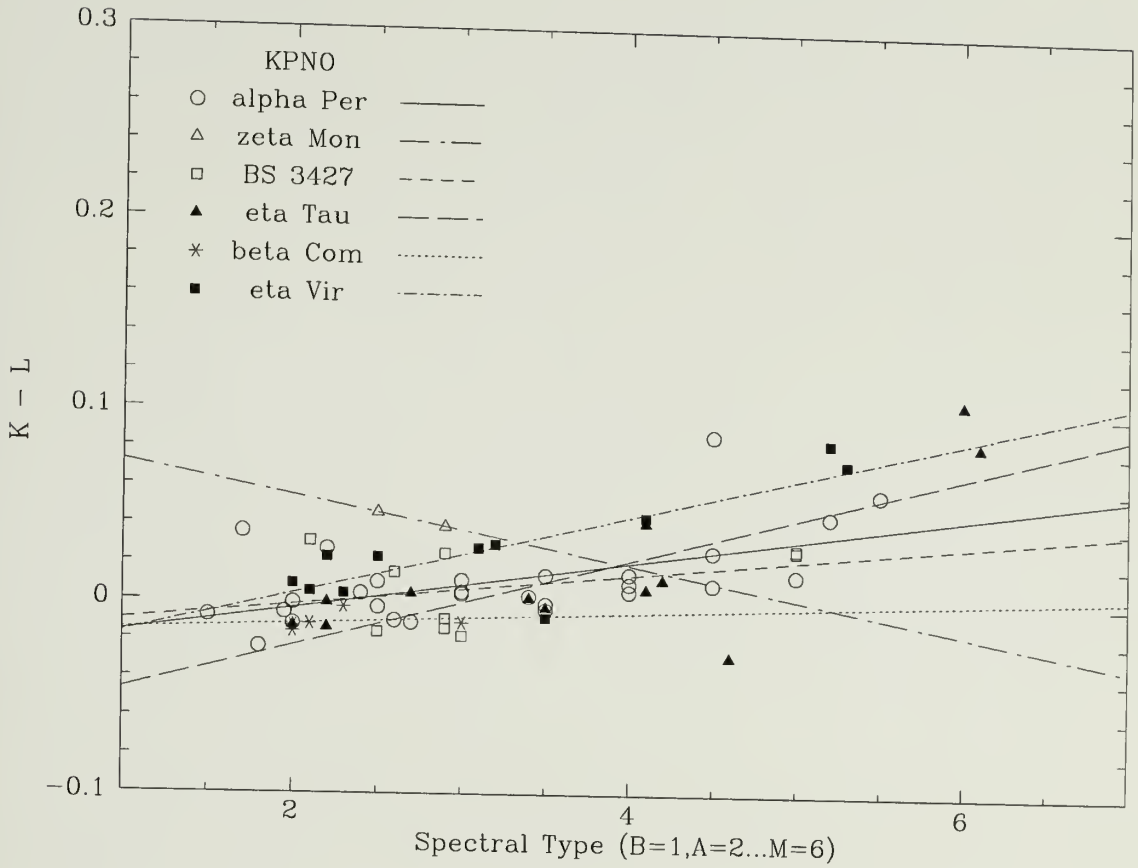

Figure A.3. (cont.) (b) First-order least-squares fits for each KPNO calibrator for the linear region of the K-L colors *vs.* spectral type. Only the highest quality measurements of main sequence cluster stars obtained at the KPNO were used for the fit. Note the poor fit for the standard zeta Mon.

published colors for the calibrators. The resulting colors from these adjustments are given in Table 3.2.

The errors in the adjustments depend on the spectral type of the star, and may be estimated from Figures A.2 and A.3. The maximum errors appear to be about 0.02 magnitudes for any given infrared color.

Table A.3. Adjustments to Calibrators for J through L′

Calibrator	J-K	J-L	J-L′
IRTF			
16 Tau	-0.025	–	0.100
HD 22686	0.000	–	-0.027
4 Lac	–	–	–
pi^4 Ori	-0.000	–	-0.027
HD 77281	0.000	–	-0.027
KPNO			
alpha Per	-0.036	-0.016	–
zeta Mon	0.027	0.002	–
BS 3427	0.008	0.032	–
eta Tau	-0.017	0.007	–
beta Com	0.002	0.022	–
eta Vir	–	–	–

Two cases require a word of explanation. The adjustments to HD 22686 as calculated did not appear believable. Recall there were only three measurements of HD 22686 available for calculation of a best-fit line. Since HD 22686 is an Elias A0 star, and HD 77281 is an Elias A2 star, the adjustments calculated for HD 77281 were also adopted for HD 22686.

The calibrator pi^4 Ori was too bright for observation at J. It was almost always used to calibrate L, L′ and M in conjunction with HD 22686 at J, H and K. On a very few occasions, pi^4 Ori was used to calibrate H, K, L, L′ and M, using HD 22686 for J only. As a result, it was not possible to evaluate the adjustments for pi^4 Ori to 4 Lac using a best-fit line. It has spectral type B2III, and is an Elias

standard. The adjustments for HD 77281 were again adopted, despite the difference in spectral types, since both are early-type Elias standards. The adjustments to pi^4 Ori can therefore be regarded as no more than a guess.

A.4 The Relative J-M and J-N Colors of the Calibrators.

M measurements were not always simultaneous with J through L′ measurements, which sometimes resulted in the use of one calibrator for J through L′, and another for M. Likewise, there are very few calibrators for N, also resulting in combinations of calibrators for a given cluster star (most N calibrators are much too bright to be used as calibrators at J, H, and K). It was therefore necessary to consider adjustments to the J-M and J-N calibrator colors for the various combinations of calibrators used.

The adjustments to the calibrators were computed in two steps. First, reddening-corrected plots of L′-M and L′-N *vs.* spectral type were constructed, using all available measurements, regardless of quality. Points in the non-linear region were removed, and best-fit lines to were constructed for each calibrator, as described in the previous section. The plots are shown in Figures A.4 and A.5. The L′-M colors were adjusted to agree with those of 4 Lac at a spectral type of 3.5, with the exception of pi^4 Ori, which was evaluated at SpT=5.37. There is not enough data at N to compute shifts between calibrators; the published N magnitudes are therefore adopted.

Secondly, the shifts computed for L′-M were combined with the previously determined shifts for J-L′ to determine the resultant shift in J-M. The adjustments are tabulated in Table A.4.

It should be noted that there are only three data points for pi^4 Ori, and one for the combination 16 Tau (L′) with 4 Lac (M). Errors may be estimated from

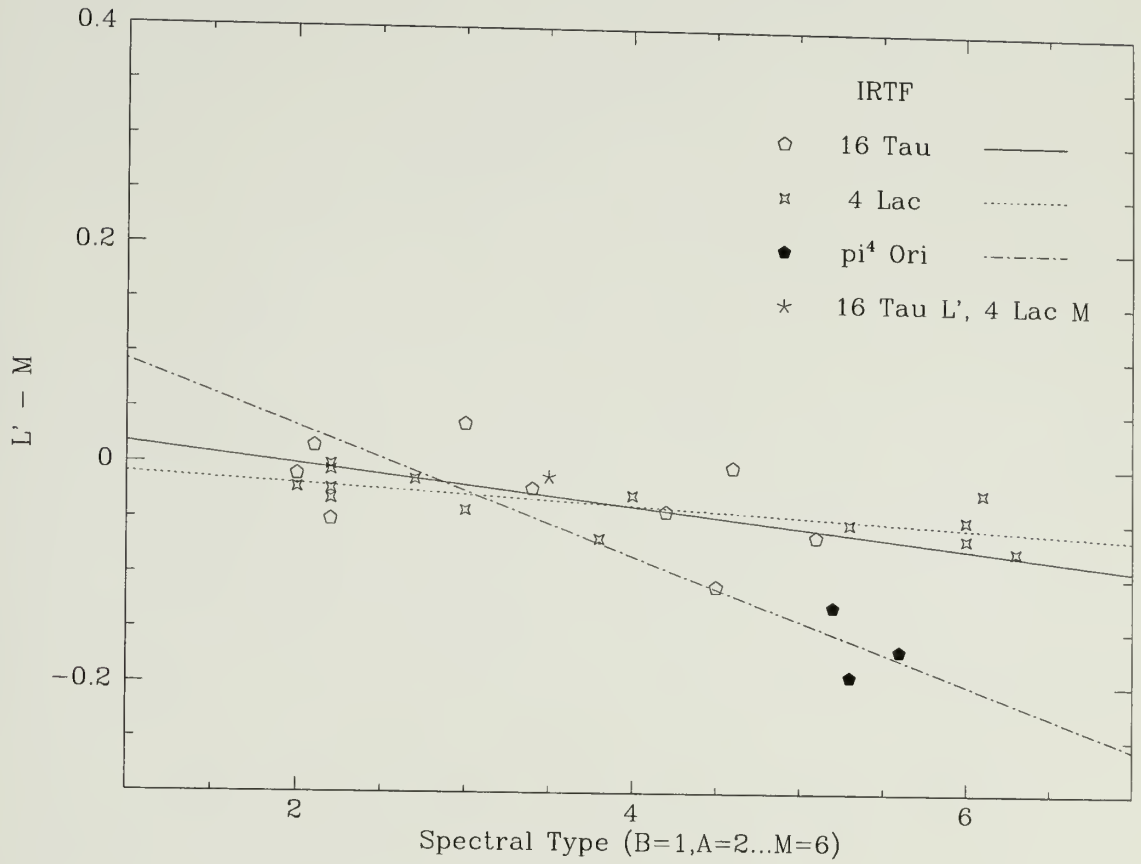

Figure A.4. Best-fit lines to determine the relative IRTF calibrator L′M colors. Shown are the first-order least-squares fits for each IRTF calibrator for the linear region of the L′-M colors *vs.* spectral type. All quality measurements of main sequence cluster stars obtained at the IRTF were used for the fit. Note the poor fit for the standard pi^4 Ori.

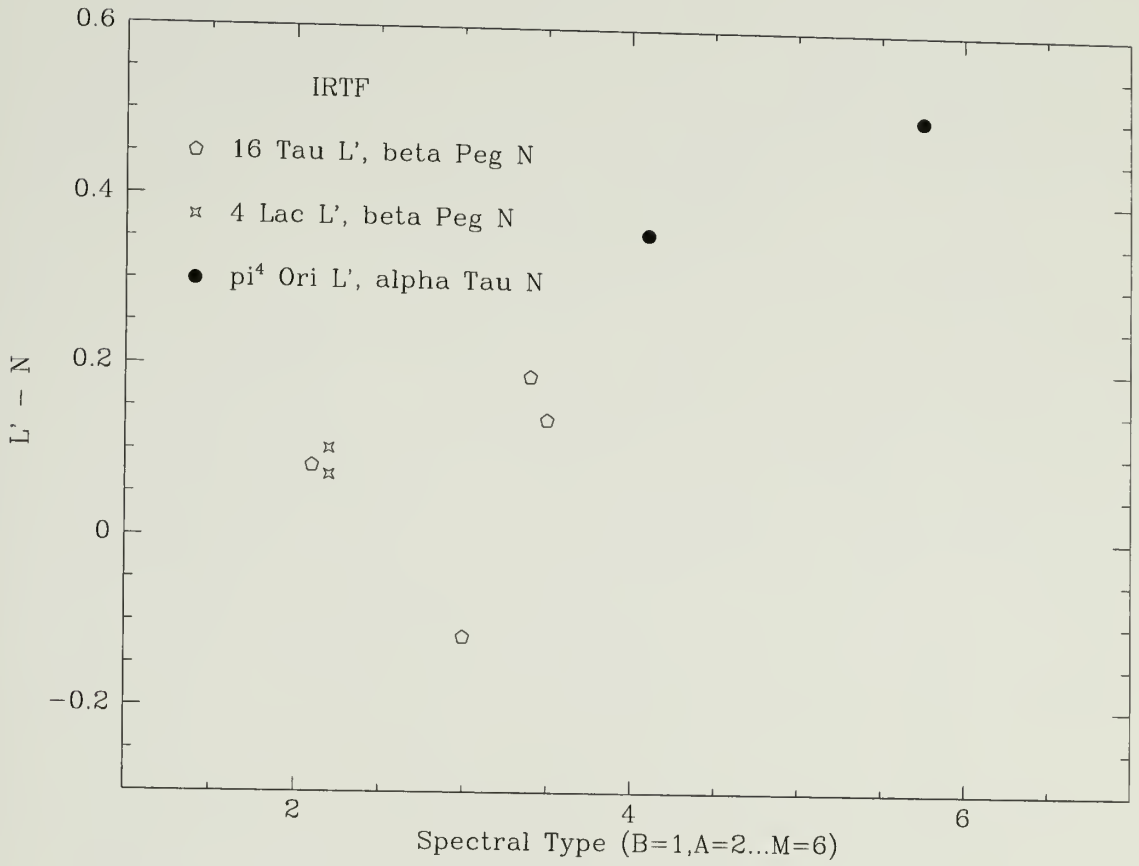

Figure A.5. Best-fit lines to determine the relative IRTF calibrator LN colors. Shown are the L'-N colors *vs.* spectral type for all quality measurements of Woolley, Ursa Major, and wTTS obtained at the IRTF. There are not enough data points to perform a least-squares fit. Because of this, the published magnitudes at N are adopted in this work.

Table A.4. Adjustments to Calibrators for J-M

J Calibrator	M Calibrator	Shift for J-L′	Shift for L′-M	Shift for J-M
IRTF				
4 Lac	4 Lac	–	–	–
16 Tau	16 Tau	0.100	-0.004	0.096
16 Tau	pi^4 Ori	0.100	0.113	0.214
16 Tau	4 Lac	0.100	–	0.100
HD 22686	16 Tau	-0.027	-0.004	-0.031
HD 22686	pi^4 Ori	-0.027	0.113	0.087

Figure A.4; the adjustments to J-M in Tables A.4 and 3.3 should only be trusted to about 0.05 mag.

Appendix B

THE COMPLETE ORIGINAL DATA SET

This appendix gives all of the original reduced magnitudes for all the sources observed during this program, even those wavelengths and sources which are not discussed in the text. Published magnitudes of calibrators, as given in Table A.1, were used in the reduction. The data have been corrected for extinction as a function of airmass; they have not been corrected for reddening.

Table B.1 lists the source name; J through N magnitudes; calibrator used to reduce the J through M observations; calibrator used to reduce the N observations; UT date of observation; the telescope at which the measurement was made; a flag which denotes whether or not the magnitude was derived by interpolating in time between two calibrator measurements, or by extrapolating (0=interpolated, 1=extrapolated; see Chapter 3); flags which indicates the internal signal/noise of the measurement (see Table 3.4) at L, L′, M and N (the S/N at J, H, and K was rarely less than 100); V and B-V from the literature; visual extinction A_V (in magnitudes); a numerical code to denote the spectral type (1.00=B0, 2.00=A0, 2.50=A5, 2.75=A7.5,...6.00=M0); and the spectral type from the literature.

Table B.2 lists miscellaneous comments about the data set, including any problems that may have arisen, and exact signal/noise when less than 100 for any given wavelength.

Table B.1. The Complete Original Data Set

Alpha Per

	J	H	K	L	L'	M	N	JMcal	Ncal	Date(UT)	Tel	I	LL'MN	V	B-V	Av	SpT	SpT	Notes
AP115*	11.176	-	10.117	-	10.086	-	-	16tau	none	01-05-92	IRTF	0	9099	14.13	1.640	0.31	-	-	
AP61	10.773	-	10.056	-	10.106	-	-	16tau	none	01-06-92	IRTF	0	9299	12.77	1.090	0.31	-	-	
AP72	11.296	-	10.636	-	10.671	-	-	16tau	none	01-06-92	IRTF	0	9299	12.78	0.990	0.31	-	-	
AP75	11.090	-	10.227	-	10.185	-	-	16tau	none	01-05-92	IRTF	0	9199	13.82	1.270	0.31	-	-	
AP93	10.048	-	9.338	-	9.354	-	-	16tau	none	01-05-92	IRTF	0	9099	11.99	0.930	0.31	-	-	4
HE1164	-	-	3.927	-	-	3.511	-	16tau	none	10-24-90	IRTF	0	9909	4.20	-0.080	0.31	1.50	B5Ve	
HE1164	4.239	-	3.974	-	3.642	-	-	16tau	none	10-23-90	IRTF	1	9099	4.20	-0.080	0.31	1.50	B5Ve	19
HE145	-	-	-	-	-	7.012	-	16tau	none	10-24-90	IRTF	0	9939	6.88	0.025	0.31	1.50	B5	18,19,20
HE145	6.872	-	6.825	-	6.922	-	-	16tau	none	10-23-90	IRTF	1	9099	6.88	0.025	0.31	1.50	B5	
HE350	9.667	-	9.219	-	9.307	-	-	16tau	none	01-05-92	IRTF	0	9099	11.01	0.683	0.31	4.30	G3	
HE575	7.643	-	7.530	-	7.655	7.660	-	16tau	none	10-25-90	IRTF	1	9039	7.85	0.104	0.31	2.00	A0V	
HE609	8.283	-	7.958	-	8.008	-	-	16tau	none	01-05-92	IRTF	0	9099	9.22	0.408	0.31	3.00	F0V	16,17
HE635	8.379	-	8.131	-	8.218	-	-	16tau	none	01-05-92	IRTF	0	9099	9.05	0.338	0.31	2.80	A8V	
HE639	7.967	-	7.868	-	7.950	-	-	16tau	none	01-05-92	IRTF	0	9099	8.15	0.119	0.31	2.30	A3Vn	
HE780	7.707	-	7.541	-	7.623	-	-	16tau	none	01-05-92	IRTF	0	9099	8.09	0.166	0.31	2.10	A1Vn(V:)	
HE848	8.878	-	8.492	-	8.559	-	-	16tau	none	01-05-92	IRTF	0	9099	9.99	0.588	0.31	-	-	
HE863*	8.215	-	7.851	-	7.934	-	-	16tau	none	01-05-92	IRTF	0	9099	9.21	0.517	0.31	3.60	F6	
HD22928	3.260	-	3.317	3.347	-	-	-	aper	none	10-10-90	KPNO	0	0999	2.99	-0.118	0.31	1.50	B5III SB	
HD24760	3.376	-	3.505	3.572	-	-	-	aper	none	10-10-90	KPNO	0	0999	2.88	-0.172	0.31	1.05	B0.5V SB,VB	
HE1153	6.944	-	6.959	6.971	-	-	-	aper	none	10-06-90	KPNO	0	1999	6.89	-0.020	0.31	1.80	B8V	
HE1164	4.216	-	3.961	3.663	-	-	-	aper	none	10-06-90	KPNO	0	0999	4.20	-0.080	0.31	1.50	B5Ve	
HE145	6.857	-	6.858	6.854	-	-	-	aper	none	10-10-90	KPNO	0	0999	6.88	0.025	0.31	1.50	B5	
HE383	5.325	-	5.364	5.395	-	-	-	aper	none	10-10-90	KPNO	0	0999	5.15	-0.061	0.31	1.30	B3V (SB?)	
HE606	8.365	-	8.145	8.158	-	-	-	aper	none	01-28-91	KPNO	1	2999	8.98	0.330	0.31	2.80	A8V	
HE625	7.332	-	7.289	7.343	-	-	-	ntau	none	01-28-91	KPNO	1	1999	7.63	0.114	0.31	1.95	B9.5V	
HE675	6.284	-	6.338	6.376	-	-	-	aper	none	10-10-90	KPNO	0	0999	6.06	-0.079	0.31	1.70	B7V	
HE694	8.121	-	8.043	8.062	-	-	-	ntau	none	01-25-91	KPNO	0	3999	8.48	0.200	0.31	2.50	A5V	
HE835	4.886	-	4.921	4.951	-	-	-	aper	none	10-06-90	KPNO	0	0999	4.66	-0.098	0.31	1.30	B3V (B3IV?)	
HE861	5.956	-	5.898	5.850	-	-	-	aper	none	10-06-90	KPNO	0	0999	6.24	0.126	0.31	1.70	B7V	
HE904	5.971	-	5.990	6.002	-	-	-	aper	none	10-10-90	KPNO	0	0999	5.82	-0.040	0.31	1.80	B8V (SB:)	
HE906	8.189	-	8.056	8.087	-	-	-	ntau	none	01-28-91	KPNO	1	3999	8.78	0.276	0.31	2.60	A6Vn	
HE985	5.675	-	5.725	5.764	-	-	-	aper	none	10-06-90	KPNO	0	0999	5.46	-0.104	0.31	1.80	B8IIImnp(var)	

V, B-V from Stauffer et al. (1985) and (1989), and Mitchell (1960).
Spectral types from SIMBAD.

Continued, next page.

Table B.1. (cont.)

Pleiades

	J	H	K	L	L'	M	N	JMcal	Ncal	Date(UT)	Tel	I	LL'MN	V	B-V	Av	SpT	SpT	Notes
HII1726	8.238	-	7.886	-	7.965	-	-	16tau	none	01-06-92	IRTF	0	9099	9.25	0.550	0.12	3.60	F6V	
HII1762	7.579	-	7.318	-	7.398	-	-	16tau	none	01-06-92	IRTF	0	9099	8.27	0.360	0.12	2.90	A9V	
HII189	11.433	-	10.547	-	10.561	-	-	16tau	none	01-06-92	IRTF	0	9299	13.92	1.460	0.12	5.55	K5.5e;pg	38
HII2220	7.321	-	7.246	-	7.341	-	-	16tau	none	01-06-92	IRTF	0	9099	7.52	0.100	0.12	2.20	A2V	
HII248	9.630	-	9.137	-	9.199	-	-	16tau	none	01-06-92	IRTF	0	9099	11.02	0.770	0.12	4.40	G4V	
HII2866	6.749	-	6.626	-	6.734	6.783	-	16tau	none	10-25-90	IRTF	1	9039	6.93	0.090	0.12	2.20	A2V	
HII3197	9.909	-	9.077	-	9.053	-	-	16tau	none	01-06-92	IRTF	0	9099	12.10	1.070	0.12	5.30	K3e:	38
HII659	10.340	-	9.677	-	9.679	-	-	16tau	none	01-06-92	IRTF	0	9199	12.13	0.950	0.12	4.40	G4V	
HII739	8.336	-	7.903	-	7.965	-	-	16tau	none	01-06-92	IRTF	0	9099	9.56	0.620	0.12	4.00	G0V	
HII870	10.011	-	9.216	-	9.176	-	-	16tau	none	01-06-92	IRTF	0	9099	12.61	1.250	0.12	4.40	G4V:pg	38
HII975	8.974	-	8.491	-	8.539	-	-	16tau	none	01-06-92	IRTF	0	9099	10.56	0.810	0.12	3.80	F8V	
HII980	-	-	-	-	-	3.700	-	16tau	none	10-24-90	IRTF	0	9909	4.18	-0.060	0.12	1.60	B6IVe	
HII980	4.188	-	4.041	-	3.888	-	-	16tau	none	10-25-90	IRTF	0	9099	4.18	-0.060	0.12	1.60	B6IVe	18,19
T108	10.707	-	9.804	-	9.789	-	-	16tau	none	01-06-92	IRTF	0	9099	13.29	1.310	0.12	-	-	38
HII1028	7.135	-	7.089	7.089	-	-	-	ntau	none	01-28-91	KPNO	1	1999	7.35	0.100	0.12	2.20	A2V	
HII1084	7.313	-	7.103	7.073	-	-	-	aper	none	10-10-90	KPNO	0	0999	8.11	0.360	0.12	2.00	A0V	21
HII1234	6.779	-	6.736	6.737	-	-	-	aper	none	10-06-90	KPNO	0	0999	6.82	0.020	0.12	1.95	B9.5V	
HII1380	6.929	-	6.911	6.916	-	-	-	ntau	none	01-28-91	KPNO	1	1999	6.99	0.030	0.12	2.10	A1V	
HII1384	7.223	-	7.022	7.013	-	-	-	aper	none	10-10-90	KPNO	0	0999	7.66	0.210	0.12	2.40	A4V	
HII1431	6.713	-	6.642	6.649	-	-	-	aper	none	10-06-90	KPNO	0	0999	6.81	0.060	0.12	2.00	A0V	
HII2168	3.757	-	3.768	3.802	-	-	-	aper	none	10-10-90	KPNO	0	0999	3.64	-0.080	0.12	1.80	B8III	
HII2425	6.266	-	6.265	6.300	-	-	-	aper	none	10-10-90	KPNO	0	0999	6.17	-0.050	0.12	1.80	B8V	
HII2866	6.805	-	6.704	6.672	-	-	-	aper	none	10-10-90	KPNO	0	0999	6.93	0.090	0.12	2.20	A2V	
HII605	8.164	-	7.860	7.840	-	-	-	aper	none	10-10-90	KPNO	0	2999	8.99	0.440	0.12	3.30	F3V	23
HII801	6.726	-	6.675	6.683	-	-	-	ntau	none	01-28-91	KPNO	0	0999	6.85	0.040	0.12	2.00	A0V	9
HII859	6.485	-	6.473	6.469	-	-	-	aper	none	10-06-90	KPNO	0	0999	6.43	-0.020	0.12	2.00	A0Vn	
HII956	7.299	-	7.099	7.090	-	-	-	ntau	none	01-28-91	KPNO	0	0999	7.96	0.320	0.12	2.70	A7V	10
HII980	4.162	-	4.048	3.877	-	-	-	aper	none	10-10-90	KPNO	0	0999	4.18	-0.060	0.12	1.60	B6IVe	

T108, HII3197 and HII870: V, B-V from Stauffer (1984). Remaining V, B-V from Johnson and Mitchell (1958).
Spectral types from SIMBAD.

Continued, next page.

Table B.1. (cont.)

Ursa Major

	J	H	K	L	L'	M	N	JMcal	Ncal	Date(UT)	Tel	I	LL'MN	V	B-V	Av	SpT	SpT	Notes
HD109011	6.431	5.874	5.767	5.659	5.673	5.801	-	h22686	none	11-23-89	IRTF	1	0039	8.09	0.930	0.00	5.20	K2V;Var?	26
HD110463	6.721	6.172	6.072	5.969	5.972	6.164	-	h22686	none	11-23-89	IRTF	1	0019	8.27	0.950	0.00	5.30	K3V	27
HD11131	5.617	-	5.218	-	5.181	5.208	-	41ac	none	10-25-90	IRTF	0	9009	6.76	0.610	0.00	4.00	G0	16,17
HR1046	5.043	-	4.984	-	5.087	5.071	5.005	16tau	bpeg	10-26-90	IRTF	0	9003	5.08	0.050	0.00	2.10	A1V	
HR2228	-	-	-	-	-	-	6.097	none	bpeg	10-26-90	IRTF	0	9993	6.52	0.270	0.00	3.00	F0V	12
HR2228	-	-	-	-	-	5.942	-	16tau	none	10-25-90	IRTF	0	9919	6.52	0.270	0.00	3.00	F0V	
HR2228	6.063	-	5.854	-	5.979	-	-	16tau	none	10-23-90	IRTF	1	9099	6.52	0.270	0.00	3.00	F0V	
HR647	5.299	-	5.002	-	5.087	5.109	4.899	16tau	bpeg	10-26-90	IRTF	0	9003	6.06	0.400	0.00	3.40	F4V	32
HR68	-	-	-	-	-	-	4.277	none	bpeg	10-26-90	IRTF	0	9993	4.53	0.050	0.00	2.20	A2V;SB	
HR68	4.403	-	4.370	-	4.348	4.349	-	41ac	none	10-25-90	IRTF	0	9009	4.53	0.050	0.00	2.20	A2V;SB	16,17,18,19
HR8170	5.268	-	4.875	-	4.815	4.882	-	41ac	none	10-26-90	IRTF	0	9009	6.40	0.530	0.00	3.80	F8V;SB	16,17
HR8263	6.060	-	6.041	-	6.056	6.062	-	41ac	none	10-26-90	IRTF	0	9009	6.25	0.050	0.00	2.20	A2V	
HR8291	5.875	-	5.849	-	5.850	5.882	-	41ac	none	10-26-90	IRTF	0	9019	6.10	0.060	0.00	2.20	A2V	
HR8407	5.512	-	5.521	-	5.543	5.565	-	41ac	none	10-25-90	IRTF	0	9019	5.60	-0.040	0.00	2.00	A0IV(or_B9p)	16,17
HR8984	4.139	-	4.024	-	4.005	4.019	-	41ac	none	10-25-90	IRTF	0	9009	4.52	0.190	0.00	2.70	A7V	16,17,18,19
HD103287	2.364	-	2.369	2.360	-	-	-	nvir	none	01-24-91	KPNO	0	0999	2.44	0.000	0.00	2.00	A0V	3
HD106591	3.142	-	3.103	3.099	-	-	-	nvir	none	01-25-91	KPNO	1	0999	3.31	0.080	0.00	2.30	A3V	
HD109011	6.304	-	5.737	5.652	-	-	-	nvir	none	01-24-91	KPNO	0	0999	8.09	0.930	0.00	5.20	K2V	2
HD110463	6.569	-	6.034	5.960	-	-	-	nvir	none	01-24-91	KPNO	0	0999	8.27	0.950	0.00	5.30	K3V	2
HD111456	4.880	-	4.569	4.577	-	-	-	nvir	none	01-25-91	KPNO	1	0999	5.85	0.460	0.00	3.50	F5V	
HD112185	1.721	-	1.735	1.748	-	-	-	bcom	none	01-25-91	KPNO	1	0999	1.76	-0.020	0.00	2.00	A0p	
HD113139	4.177	-	3.959	3.929	-	-	-	nvir	none	01-24-91	KPNO	0	0999	4.93	0.360	0.00	3.20	F2V	3
HD115043	5.690	-	5.359	5.314	-	-	-	nvir	none	01-24-91	KPNO	0	0999	6.84	0.600	0.00	4.10	G1Va	2
HD116842	3.668	-	3.590	3.567	-	-	-	nvir	none	01-24-91	KPNO	0	0999	4.01	0.160	0.00	2.50	A5V	3
HD91480	4.482	-	4.311	4.283	-	-	-	nvir	none	01-25-91	KPNO	0	0999	5.16	0.340	0.00	3.10	F1V	
HD95418	2.333	-	2.337	2.332	-	-	-	nvir	none	01-25-91	KPNO	0	0999	2.36	-0.020	0.00	2.10	A1V	
HR4865	5.608	-	5.586	5.598	-	-	-	bcom	none	01-25-91	KPNO	1	0999	5.70	0.020	0.00	2.10	A1V	
HR5264	3.974	-	3.896	3.899	-	-	-	bcom	none	01-25-91	KPNO	0	0999	4.26	0.100	0.00	2.30	A3V	
HR5373	6.184	-	6.150	6.127	-	-	-	nvir	none	01-24-91	KPNO	1	0999	6.33	0.050	0.00	2.20	A2V	3
HR5721	5.637	-	5.510	5.521	-	-	-	bcom	none	01-25-91	KPNO	0	0999	6.12	0.260	0.00	3.00	F0V	
HR5793	2.202	-	2.206	2.222	-	-	-	bcom	none	01-25-91	KPNO	0	0999	2.23	-0.020	0.00	2.00	A0V	

V, B-V from Johnson and Knuckles (1957), except for HD11131, which is from SIMBAD.
Spectral types from SIMBAD.

Continued, next page.

Table B.1. (cont.)

Hyades

	J	H	K	L	L'	M	N	JMcal	Ncal	Date(UT)	Tel	I	LL'MN	V	B-V	Av	SpT	SpT	Notes
HA578	7.097	-	6.513	-	6.577	6.687	-	16tau	none	10-26-90	IRTF	0	9029	8.51	0.841	0.00	4.50	G5	
HA178	6.367	-	5.975	5.948	-	-	-	aper	none	10-10-90	KPNO	0	0999	7.54	0.679	0.00	4.50	G5V	
HA361	7.402	-	6.826	6.780	-	-	-	aper	none	10-10-90	KPNO	0	0999	9.01	0.939	0.00	5.20	K2V	
HA382	6.841	-	6.459	6.417	-	-	-	ntau	none	01-27-91	KPNO	0	0999	8.06	0.632	0.00	4.10	G1V	
HA382	6.843	-	6.456	6.449	-	-	-	ntau	none	01-28-91	KPNO	0	0999	8.06	0.632	0.00	4.10	G1V	39
HA554	7.338	-	6.940	6.921	-	-	-	ntau	none	01-28-91	KPNO	0	2999	8.66	0.741	0.00	4.50	G5	
HA578	7.090	-	6.578	6.490	-	-	-	aper	none	10-10-90	KPNO	0	0999	8.51	0.841	0.00	4.50	G5	
HD24357	5.291	-	5.113	5.111	-	-	-	ntau	none	01-27-91	KPNO	0	0999	5.97	0.341	0.00	3.40	F4V	39
HD26462	5.071	-	4.863	4.860	-	-	-	aper	none	10-10-90	KPNO	0	0999	5.73	0.355	0.00	3.40	F4V	
HD26911	5.608	-	5.372	5.376	-	-	-	aper	none	10-06-90	KPNO	0	0999	6.32	0.399	0.00	3.50	F5V	
HD27962	4.163	-	4.125	4.139	-	-	-	ntau	none	01-27-91	KPNO	0	0999	4.30	0.049	0.00	2.20	A2IV	39
HD28355	4.693	-	4.559	4.570	-	-	-	aper	none	10-06-90	KPNO	0	0999	5.03	0.228	0.00	2.70	A7V	
HD28556	4.938	-	4.757	4.752	-	-	-	aper	none	10-06-90	KPNO	0	0999	5.40	0.262	0.00	3.00	F0V	
HD29310	6.421	-	6.005	5.999	-	-	-	aper	none	10-06-90	KPNO	0	0999	7.54	0.603	0.00	4.00	G0	
HD29388	4.054	-	3.951	3.961	-	-	-	aper	none	10-10-90	KPNO	0	0999	4.27	0.123	0.00	2.60	A6V	
HD29488	4.382	-	4.265	4.255	-	-	-	aper	none	10-06-90	KPNO	0	0999	4.68	0.155	0.00	2.50	A5Vn	
HD30210	5.024	-	4.952	4.953	-	-	-	ntau	none	01-27-91	KPNO	0	0999	5.37	0.187	0.00	2.20	A2m	39
HD31845	5.891	-	5.663	5.666	-	-	-	ntau	none	01-25-91	KPNO	0	0999	6.75	0.450	0.00	3.50	F5V	
J291	8.528	-	7.850	7.778	-	-	-	ntau	none	01-25-91	KPNO	0	2999	10.74	1.190	0.00	-	-	
J309	8.737	-	7.947	7.852	-	-	-	ntau	none	01-24-91	KPNO	0	1999	11.41	1.380	0.00	-	-	
J330	8.689	-	8.039	8.043	-	-	-	ntau	none	01-28-91	KPNO	0	2999	10.68	1.110	0.00	5.20	K2III	
VB191	8.626	-	7.905	7.840	-	-	-	ntau	none	01-25-91	KPNO	0	1999	11.03	1.291	0.00	5.00	K0	

V, B-V from Johnson and Knuckles, 1955 (3 decimal places), and Johnson, Mitchell and Iriarte, 1962 (2 decimal places).
Spectral types from SIMBAD.

Praesepe

	J	H	K	L	L'	M	N	JMcal	Ncal	Date(UT)	Tel	I	LL'MN	V	B-V	Av	SpT	SpT	Notes
JC123	10.973	-	10.207	-	10.084	-	-	h77281	none	01-06-92	IRTF	0	9099	13.28	1.360	0.00	-	-	
KW162	9.597	-	9.258	-	9.191	-	-	h77281	none	01-05-92	IRTF	0	9099	10.58	0.573	0.00	-	-	
KW183	10.762	-	10.082	-	9.932	-	-	h77281	none	01-05-92	IRTF	0	9099	12.64	1.001	0.00	-	-	
KW232	8.514	-	8.239	-	8.185	-	-	h77281	none	01-05-92	IRTF	0	9099	9.23	0.389	0.00	3.50	F5V	
KW263	10.632	-	10.150	-	10.096	-	-	h77281	none	01-05-92	IRTF	0	9199	11.98	0.814	0.00	-	-	
KW265	6.577	-	6.574	-	6.534	-	-	h77281	none	01-05-92	IRTF	0	9099	6.61	0.006	0.00	2.10	A1V;Blue strag	
KW293	9.044	-	8.785	-	8.704	-	-	h77281	none	01-06-92	IRTF	0	9099	9.85	0.470	0.00	-	-	4
KW299	11.341	-	10.688	-	10.595	-	-	h77281	none	01-06-92	IRTF	0	9299	13.20	1.080	0.00	5.40	K4V	
KW300	6.024	-	5.941	-	5.875	-	-	h77281	none	01-05-92	IRTF	0	9099	6.30	0.172	0.00	2.50	A5m;SB2	
KW313	10.726	-	10.203	-	10.158	-	-	h77281	none	01-06-92	IRTF	0	9199	12.20	0.884	0.00	-	-	
KW45	7.822	-	7.703	-	7.637	-	-	h77281	none	01-06-92	IRTF	0	9099	8.25	0.231	0.00	3.00	F0Vn	

Continued, next page.

Table B.1. (cont.)

Praesepe (cont.)

	J	H	K	L	L'	M	N	JMcal	Ncal	Date(UT)	Tel	I	LL'MN	V	B-V	Av	SpT	SpT	Notes
KW466	9.870	-	9.487	-	9.472	-	-	h77281	none	01-06-92	IRTF	0	9399	10.99	0.649	0.00	-	-	
KW495	8.861	-	8.460	-	8.385	-	-	h77281	none	01-05-92	IRTF	0	9099	9.94	0.660	0.00	3.80	F8V	
KW55	9.879	-	9.312	-	9.225	-	-	h77281	none	01-05-92	IRTF	0	9099	11.38	0.860	0.00	-	G	
KW143	7.907	-	7.816	7.832	-	-	-	bs3427	none	01-25-91	KPNO	1	1999	8.31	0.228	0.00	2.90	A9V	22
KW150	6.889	-	6.754	-	-	-	-	bs3427	none	01-28-91	KPNO	0	9999	7.45	0.255	0.00	2.90	A9Vn	
KW150	6.902	-	6.759	6.773	-	-	-	bs3427	none	01-24-91	KPNO	0	0999	7.45	0.255	0.00	2.90	A9Vn	11
KW203	7.274	-	7.168	7.179	-	-	-	bs3427	none	01-28-91	KPNO	0	2999	7.73	0.219	0.00	2.50	A5V	5
KW204	6.122	-	5.995	6.013	-	-	-	bs3427	none	01-24-91	KPNO	0	0999	6.67	0.249	0.00	3.00	F0III	11
KW204	6.125	-	5.996	-	-	-	-	bs3427	none	01-28-91	KPNO	0	9999	6.67	0.249	0.00	3.00	F0III	5
KW207	7.278	-	7.183	7.224	-	-	-	bs3427	none	01-25-91	KPNO	1	1999	7.67	0.197	0.00	2.70	A7Vn	1,23
KW212	4.953	-	4.425	4.396	-	-	-	bs3427	none	01-24-91	KPNO	0	0999	6.59	0.959	0.00	5.00	K0III	
KW212	4.955	-	-	-	-	-	-	bs3427	none	01-25-91	KPNO	0	9999	6.59	0.959	0.00	5.00	K0III	
KW212	4.956	4.529	4.427	-	-	-	-	bs3427	none	01-28-91	KPNO	0	9999	6.59	0.959	0.00	5.00	K0III	
KW217	9.251	-	9.003	-	-	-	-	bs3427	none	01-28-91	KPNO	0	9999	10.23	0.513	0.00	3.50	F5V	
KW218	8.568	-	8.379	8.388	-	-	-	bs3427	none	01-25-91	KPNO	0	2999	9.36	0.440	0.00	3.60	F6V	
KW224	6.922	-	6.818	6.831	-	-	-	bs3427	none	01-28-91	KPNO	0	1999	7.32	0.193	0.00	-	Am	7
KW226	8.279	-	8.129	8.186	-	-	-	bs3427	none	01-24-91	KPNO	0	3999	8.89	0.321	0.00	3.20	F2V	
KW226	8.281	-	-	-	-	-	-	bs3427	none	01-25-91	KPNO	0	9999	8.89	0.321	0.00	3.20	F2V	
KW227	8.682	-	8.490	-	-	-	-	bs3427	none	01-28-91	KPNO	0	9999	9.49	0.414	0.00	3.60	F6V	
KW229	7.108	-	-	-	-	-	-	bs3427	none	01-25-91	KPNO	0	9999	7.54	0.250	0.00	-	Am	
KW229	7.117	-	7.045	7.016	-	-	-	zmon	none	01-24-91	KPNO	0	2999	7.54	0.250	0.00	-	Am	23
KW232	8.460	-	8.237	8.277	-	-	-	bs3427	none	01-28-91	KPNO	0	3999	9.23	0.389	0.00	3.50	F5V	8
KW265	6.542	6.565	6.545	6.523	-	-	-	bs3427	none	01-28-91	KPNO	0	2999	6.61	0.006	0.00	2.10	A1V	5
KW265	6.597	-	6.602	6.571	-	-	-	bs3427	none	01-25-91	KPNO	0	0999	6.61	0.006	0.00	2.10	A1V	
KW268	8.927	-	8.639	-	-	-	-	bs3427	none	01-28-91	KPNO	0	9999	9.89	0.477	0.00	3.50	F5V	
KW284	6.204	-	6.061	6.036	-	-	-	bs3427	none	01-28-91	KPNO	0	0999	6.78	0.261	0.00	2.90	A9V	4
KW284	6.211	-	-	-	-	-	-	bs3427	none	01-25-91	KPNO	0	9999	6.78	0.261	0.00	2.90	A9V	
KW284	6.217	-	6.087	6.048	-	-	-	zmon	none	01-24-91	KPNO	0	0999	6.78	0.261	0.00	2.90	A9V	24
KW300	5.975	-	-	-	-	-	-	bs3427	none	01-25-91	KPNO	0	9999	6.30	0.172	0.00	2.50	A5m	
KW300	5.984	-	5.935	5.889	-	-	-	zmon	none	01-24-91	KPNO	0	0999	6.30	0.172	0.00	2.50	A5m	24
KW318	8.103	-	7.960	8.003	-	-	-	bs3427	none	01-28-91	KPNO	0	2999	8.65	0.291	0.00	3.00	F0V	5
KW328	6.431	-	6.344	6.353	-	-	-	bs3427	none	01-28-91	KPNO	0	0999	6.85	0.203	0.00	2.90	A9III	7
KW340	7.957	-	7.828	7.850	-	-	-	bs3427	none	01-24-91	KPNO	0	1999	8.48	0.259	0.00	3.00	F0Vn	11
KW348	6.403	-	6.310	6.295	-	-	-	bs3427	none	01-24-91	KPNO	0	0999	6.78	0.168	0.00	2.60	A6Vn	
KW40	7.402	-	7.321	7.344	-	-	-	bs3427	none	01-24-91	KPNO	0	1999	7.79	0.220	0.00	-	Am	
KW428	5.257	-	4.738	4.710	-	-	-	bs3427	none	01-24-91	KPNO	0	0999	6.90	0.963	0.00	5.00	K0III	
KW428	5.257	4.836	4.731	-	-	-	-	bs3427	none	01-28-91	KPNO	0	9999	6.90	0.963	0.00	5.00	K0III	6
KW428	5.261	-	-	-	-	-	-	bs3427	none	01-25-91	KPNO	0	9999	6.90	0.963	0.00	5.00	K0III	
KW429	7.954	-	7.815	7.833	-	-	-	bs3427	none	01-28-91	KPNO	0	2999	8.53	0.297	0.00	3.20	F2Vn	7
KW445	7.547	-	7.465	7.472	-	-	-	bs3427	none	01-24-91	KPNO	0	2999	7.96	0.208	0.00	2.70	A7V	
KW445	7.552	-	-	-	-	-	-	bs3427	none	01-25-91	KPNO	0	9999	7.96	0.208	0.00	2.70	A7V	

Continued, next page.

Table B.1. (cont.)

Praesepe (cont.)

	J	H	K	L	L'	M	N	JMcal	Ncal	Date(UT)	Tel	I	LL'MN	V	B-V	Av	SpT	SpT	Notes
KW449	7.492	-	7.388	7.399	-	-	-	bs3427	none	01-25-91	KPNO	1	1999	7.91	0.210	0.00	2.70	A7Vn	
KW45	7.787	-	7.683	7.700	-	-	-	bs3427	none	01-28-91	KPNO	0	2999	8.25	0.231	0.00	3.00	F0Vn	
KW50	6.306	-	6.199	6.215	-	-	-	bs3427	none	01-28-91	KPNO	0	0999	6.75	0.190	0.00	2.50	A5V	

V, B-V from Johnson (1952), except for JC123, which is from Jones and Cudworth (1983). (JC only good to 0.1 mag).
Spectral types from SIMBAD.

cTTS

	J	H	K	L	L'	M	N	JMcal	Ncal	Date(UT)	Tel	I	LL'MN	V	B-V	Av	SpT	SpT	Notes
CXTAU	9.938	-	-	-	-	-	5.895	h22686	atau	11-24-89	IRTF	2	9993	13.67	1.570	0.55	6.20	M2	
CXTAU	9.962	9.090	8.850	8.464	8.277	8.134	-	h22686	none	11-23-89	IRTF	0	0039	13.67	1.570	0.55	6.20	M2	15
FPTAU	-	-	-	8.558	8.434	8.343	6.517	pi4ori	atau	11-24-89	IRTF	0	1033	13.91	1.550	0.00	6.55	M5.5	
FPTAU	9.976	-	8.838	-	8.489	-	-	16tau	none	10-23-90	IRTF	1	9199	13.91	1.550	0.00	6.55	M5.5	
GMAUR	9.461	-	-	-	-	-	-	h22686	none	11-24-89	IRTF	1	9999	12.03	1.190	0.10	5.70	K7	25
GMAUR	9.498	8.738	8.506	8.206	8.118	8.144	-	h22686	none	11-23-89	IRTF	1	0039	12.03	1.190	0.10	5.70	K7	
GOTAU	10.733	-	-	-	-	-	6.551	h22686	atau	11-24-89	IRTF	1	9993	14.89	1.460	2.44	6.00	M0	
GOTAU	10.752	9.741	9.341	8.838	8.707	8.589	-	h22686	none	11-23-89	IRTF	0	0239	14.89	1.460	2.44	6.00	M0	15
HOTAU	11.199	10.264	9.827	9.260	9.146	8.806	-	h22686	none	11-24-89	IRTF	0	2139	14.84	1.140	0.73	6.05	M0.5	15
HUBBLE4	-	-	7.327	-	-	7.105	-	16tau	none	10-24-90	IRTF	0	9939	12.73	1.680	-	5.70	K7 (V,B-V:)	
HUBBLE4	8.707	-	7.323	-	7.116	-	-	16tau	none	10-23-90	IRTF	0	9099	12.73	1.680	-	5.70	K7 (V,B-V:)	
LKCA8	-	-	8.300	-	-	7.276	-	16tau	none	10-26-90	IRTF	0	9929	13.04	1.460	0.25	6.00	M0:V	
LKCA8	9.800	-	8.253	-	7.502	-	-	16tau	none	10-23-90	IRTF	0	9099	13.04	1.460	0.25	6.00	M0:V	4
LKCA15	-	-	8.112	-	-	7.461	-	16tau	none	10-26-90	IRTF	0	9939	12.09	1.320	-	5.50	K5:V	
LKCA15	9.524	-	8.283	-	7.815	-	-	16tau	none	10-24-90	IRTF	0	9099	12.09	1.320	-	5.50	K5:V	
SUAUR	7.295	-	5.996	-	5.125	4.800	2.506	16tau	atau	10-25-90	IRTF	0	9000	9.03	0.840	0.64	4.20	G2III	
V773TAU	7.718	6.831	6.480	5.851	5.669	5.575	-	h22686	none	11-23-89	IRTF	1	0029	10.65	1.370	2.04	5.20	K2	15
V773TAU	7.741	-	-	-	-	-	-	h22686	none	11-24-89	IRTF	1	9999	10.65	1.370	2.04	5.20	K2	
V836TAU	9.874	9.017	8.720	8.232	8.138	8.040	-	h22686	none	11-23-89	IRTF	0	0139	13.13	1.530	0.91	5.70	K7V;(SJK)	15
V836TAU	9.883	-	-	-	-	-	-	h22686	none	11-24-89	IRTF	0	9999	13.13	1.530	0.91	5.70	K7V;(SJK)	
VYTAU	10.057	-	8.943	-	8.458	8.173	-	16tau	none	10-25-90	IRTF	0	9139	13.75	1.510	1.02	6.00	M0	35
ZZTAU	9.563	-	-	-	-	-	6.451	h22686	atau	11-24-89	IRTF	1	9993	14.28	1.480	0.65	6.40	M4	
ZZTAU	9.580	8.735	8.462	8.136	7.956	7.970	-	h22686	none	11-23-89	IRTF	0	0039	14.28	1.480	0.65	6.40	M4	15

Interpolation flag: For J and N, 2=N interp, J not interp. If N not interp, just use 1 regardless of J.
V, B-V, and Av from K. Strom et al. (1989).
Spectral types from K. Strom et al. (1989) or from Scott Kenyon (private communication, marked "SJK").

Continued, next page.

Table B.1. (cont.)

wTTS

	J	H	K	L	L'	M	N	JMcal	Ncal	Date(UT)	Tel	I	LL'MN	V	B-V	Av	SpT	SpT	Notes
W032641	10.407	-	9.704	-	9.848	-	-	16tau	none	10-23-90	IRTF	0	9399	12.05	0.900	0.30	5.10	K1	
W034903	-	-	9.096	-	-	9.176	-	16tau	none	10-25-90	IRTF	0	9939	12.25	1.130	0.04	5.50	K5	34
W034903	9.936	-	9.092	-	9.082	-	-	16tau	none	10-23-90	IRTF	0	9199	12.25	1.130	0.04	5.50	K5	
W035120N	10.480	-	9.846	-	9.868	-	-	16tau	none	10-23-90	IRTF	0	9299	12.31	0.940	1.03	4.50	G5	
W035120N	10.482	-	9.831	-	9.855	-	-	16tau	none	10-23-90	IRTF	0	9299	12.31	0.940	1.03	4.50	G5	
W035120S	10.156	-	9.562	-	9.607	-	-	16tau	none	10-23-90	1RTF	0	9299	11.85	0.860	0.91	4.00	G0	36
W035135S	10.878	10.331	10.227	10.156	10.070	-	-	h22686	none	11-24-89	IRTF	1	3399	12.67	0.920	0.15	5.20	K2	14,15
W035135N	11.810	-	11.057	-	11.071	-	-	16tau	none	10-24-90	IRTF	0	9399	13.79	1.110	0.61	5.30	K3	
W040234	11.052	-	10.047	-	9.863	-	-	16tau	none	10-25-90	IRTF	0	9299	14.67	1.370	0.38	6.20	M2	
W041529	11.198	-	10.443	-	10.485	-	-	16tau	none	10-23-90	IRTF	0	9399	13.26	1.110	0.00	5.50	K5	4
W041559	10.066	-	9.230	-	9.215	-	-	16tau	none	10-25-90	IRTF	0	9199	12.28	1.130	0.00	5.70	K7	
W042417	-	-	8.271	-	-	8.459	-	16tau	none	10-24-90	IRTF	0	9939	10.34	0.790	0.00	5.10	K1	28,31
W042417	8.900	-	8.323	-	8.372	-	-	16tau	none	10-23-90	1RTF	0	9099	10.34	0.790	0.00	5.10	K1	4
W042835	10.301	9.627	9.514	9.410	9.368	-	-	h22686	none	11-24-89	IRTF	1	0399	12.53	1.180	0.15	5.50	K5	15
W043124	10.635	10.058	9.930	9.769	9.819	-	-	h22686	none	11-24-89	IRTF	0	2399	12.67	1.030	1.22	4.80	G8	15
W043220	-	-	8.901	-	-	8.881	-	16tau	none	10-26-90	IRTF	0	9939	10.95	0.820	0.91	3.80	F8	4
W043220	9.371	9.008	8.917	8.852	8.860	-	-	h22686	none	11-24-89	IRTF	0	3299	10.95	0.820	0.91	3.80	F8	15
W045251	9.079	8.342	8.188	8.066	8.018	8.274	-	h22686	none	11-23-89	IRTF	0	0039	11.60	1.280	0.00	5.70	K7	15
W045251	9.086	-	-	-	-	-	-	h22686	none	11-24-89	IRTF	0	9999	11.60	1.280	0.00	5.70	K7	
DITAU	9.420	-	-	-	-	-	7.633	h22686	atau	11-24-89	IRTF	2	9993	12.86	1.600	1.08	5.75	K7.5(SJK)	Bin
DITAU	9.441	8.586	8.386	8.230	8.131	8.362	-	h22686	none	11-23-89	IRTF	0	0039	12.86	1.600	1.08	5.75	K7.5(SJK)	Bin 15
FFTAU	-	-	8.630	-	-	8.613	-	16tau	none	10-26-90	IRTF	0	9939	13.67	2.060	-	5.85	K7,M0V	4,35
FFTAU	9.899	-	8.617	-	8.504	-	-	16tau	none	10-23-90	IRTF	0	9099	13.67	2.060	-	5.85	K7,M0V	
FPTAU	-	-	-	8.558	8.434	8.343	6.517	pi4ori	atau	11-24-89	IRTF	0	1033	13.91	1.550	0.00	6.55	M5.5	
FPTAU	9.976	-	8.838	-	8.489	-	-	16tau	none	10-23-90	IRTF	1	9199	13.91	1.550	0.00	6.55	M5.5	
HDE283572	-	-	6.821	-	-	6.881	-	16tau	none	10-24-90	IRTF	0	9919	9.04	0.830	0.57	4.50	G51V	29
HDE283572	7.501	-	6.892	-	6.913	-	-	16tau	none	10-23-90	IRTF	0	9099	9.04	0.830	0.57	4.50	G51V	4
L155151	9.683	-	8.792	-	8.806	-	-	16tau	none	10-23-90	IRTF	0	9099	12.06	1.230	0.00	5.70	K7	
L155155	10.272	-	9.274	-	9.282	-	-	16tau	none	10-23-90	1RTF	0	9199	13.22	1.500	0.91	5.70	K7	
LKCA16	-	-	8.358	-	-	8.283	-	16tau	none	10-25-90	IRTF	0	9939	12.51	1.530	1.22	5.70	K7V	
LKCA16	9.330	-	8.317	-	8.333	-	-	16tau	none	10-24-90	IRTF	0	9099	12.51	1.530	1.22	5.70	K7V	
LKCA19	-	-	8.176	-	-	8.152	-	16tau	none	10-26-90	1RTF	0	9939	10.85	1.020	-	5.00	K0V	4
LKCA19	8.962	-	8.171	-	8.220	-	-	16tau	none	10-24-90	IRTF	0	9299	10.85	1.020	-	5.00	K0V	
LKCA4	9.233	8.449	8.259	8.107	8.012	8.186	-	h22686	none	11-23-89	IRTF	0	0039	12.49	1.470	0.95	5.70	K7:V	15
LKCA4	9.254	-	8.245	-	8.161	-	-	16tau	none	10-23-90	IRTF	0	9099	12.49	1.470	0.95	5.70	K7:V	
LKCA4	9.356	-	-	-	-	-	-	h22686	none	11-24-89	IRTF	0	9999	12.49	1.470	0.95	5.70	K7:V	
LKCA7	9.165	-	-	-	-	-	-	h22686	none	11-24-89	IRTF	0	9999	12.55	1.390	0.76	6.00	M0(SJK)	
LKCA7	9.169	8.431	8.241	8.117	8.071	8.187	-	h22686	none	11-23-89	IRTF	0	0039	12.55	1.390	0.76	6.00	M0(SJK)	15
SAO76411A	-	-	-	-	-	-	7.072	none	atau	11-24-89	IRTF	0	9993	8.85	0.590	0.00	4.10	G1	29,30,33
SAO76411A	7.828	7.514	7.455	7.437	7.430	7.688	-	h22686	none	11-23-89	IRTF	1	0039	8.85	0.590	0.00	4.10	G1	25
SAO76428	-	-	8.119	-	-	8.298	-	16tau	none	10-24-90	IRTF	0	9939	9.47	0.530	0.00	3.80	F8	
SAO76428	8.519	-	8.161	-	8.251	-	-	16tau	none	10-23-90	IRTF	0	9099	9.47	0.530	0.00	3.80	F8	

Continued, next page.

Table B.1. (cont.)

wTTS (cont.)

	J	H	K	L	L'	M	N	JMcal	Ncal	Date(UT)	Tel	I	LL'MN	V	B-V	Av	SpT	SpT	Notes
V410TAU	8.365	-	-	-	-	-	-	h22686	none	11-24-89	IRTF	0	9999	10.92	1.180	0.00	5.70	K7	
V410TAU	8.505	7.768	7.601	7.443	7.380	7.577	-	h22686	none	11-23-89	IRTF	0	0039	10.92	1.180	0.00	5.70	K7	15
V819TAU	9.591	8.686	8.438	8.264	8.175	-	-	h22686	none	11-24-89	IRTF	0	0199	13.24	1.570	1.25	5.70	K7V(SJK)	15
V819TAU	9.604	8.718	8.463	8.289	8.219	8.447	-	h22686	none	11-23-89	IRTF	1	0039	13.24	1.570	1.25	5.70	K7V(SJK)	15
V826TAU	-	-	8.248	-	-	8.203	-	16tau	none	10-24-90	IRTF	0	9939	12.11	1.400	0.53	5.70	K7V	
V826TAU	9.217	-	8.230	-	8.232	-	-	16tau	none	10-23-90	IRTF	0	9099	12.11	1.400	0.53	5.70	K7V	
V827TAU	9.199	-	-	-	-	-	-	h22686	none	11-24-89	IRTF	0	9999	12.18	1.400	0.61	6.00	M0(SJK)	
V827TAU	9.210	8.422	8.224	8.120	7.972	8.215	-	h22686	none	11-23-89	IRTF	0	0039	12.18	1.400	0.61	6.00	M0(SJK)	15
V830TAU	-	-	8.403	-	-	8.549	-	16tau	none	10-24-90	IRTF	0	9939	12.21	1.370	0.42	5.70	K7	28
V830TAU	9.472	-	8.499	-	8.473	-	-	16tau	none	10-23-90	IRTF	0	9099	12.21	1.370	0.42	5.70	K7	

Note: The TTS source names beginning with "W" are a shorthand for the names given in Walter et al. (1988).
V, B-V, and Av from K. Strom et al. (1989).
Spectral types from K. Strom et al. (1989) or from Scott Kenyon (private communication, marked "SJK").

Woolley

	J	H	K	L	L'	M	N	JMcal	Ncal	Date(UT)	Tel	I	LL'MN	V	B-V	Av	SpT	SpT	Notes
WL039	7.047	6.377	6.277	6.190	6.233	6.401	-	h22686	none	11-24-89	IRTF	1	0039	9.27	1.210	0.00	5.60	dK6	15
WL135	-	-	-	-	-	5.583	-	16tau	none	10-25-90	IRTF	0	9919	7.02	0.670	0.00	4.20	dG2	
WL135	5.900	-	5.457	-	5.541	-	-	16tau	none	10-23-90	IRTF	0	9099	7.02	0.670	0.00	4.20	dG2	
WL230	-	-	-	-	-	4.967	-	16tau	none	10-25-90	IRTF	0	9909	6.46	0.670	0.00	4.60	G6V	
WL230	5.326	-	4.869	-	4.966	-	-	16tau	none	10-23-90	IRTF	1	9099	6.46	0.670	0.00	4.60	G6V	
WL6	-	-	-	-	-	-	4.817	none	bpeg	10-26-90	IRTF	0	9993	6.21	0.470	0.00	3.50	dF5	
WL6	5.258	-	4.908	-	4.954	-	-	16tau	none	10-24-90	IRTF	0	9099	6.21	0.470	0.00	3.50	dF5	
WL6	5.260	-	4.953	-	-	4.965	-	41ac	none	10-25-90	IRTF	0	9909	6.21	0.470	0.00	3.50	dF5	16,17
WL849	6.546	-	5.614	-	5.358	5.434	-	41ac	none	10-25-90	IRTF	0	9009	10.42	1.520	0.00	6.30	dM3	16,17
WL900	6.920	-	6.083	-	5.960	5.983	-	41ac	none	10-25-90	IRTF	0	9019	9.59	1.350	0.00	6.10	dM1	16,17
WL9112	-	-	-	-	-	5.892	-	16tau	none	10-25-90	IRTF	0	9909	7.83	0.860	0.00	5.10	K1V	
WL9112	6.369	-	5.772	-	5.828	-	-	16tau	none	10-23-90	IRTF	0	9099	7.83	0.860	0.00	5.10	K1V	37
WL913	6.693	6.042	5.843	5.681	5.631	5.696	-	41ac	none	11-23-89	IRTF	1	0009	9.62	1.440	0.00	6.00	dM0	
WL9756A	6.789	6.229	6.134	6.086	6.035	6.087	-	41ac	none	11-24-89	IRTF	1	0029	8.65	1.040	0.00	5.30	K3V	12
WL9761	4.415	-	4.201	-	4.158	4.200	-	41ac	none	10-25-90	IRTF	0	9009	5.09	0.360	0.00	3.00	F0V	
WL9771	3.408	-	3.342	-	3.288	3.311	-	41ac	none	10-25-90	IRTF	0	9009	3.52	0.090	0.00	2.20	A2V	
WL9771	-	-	-	-	-	-	3.186	none	bpeg	10-26-90	IRTF	0	9992	3.52	0.090	0.00	2.20	A2V	
WL9772	8.082	-	7.386	-	7.338	7.386	-	41ac	none	10-26-90	IRTF	0	9039	10.00	-	0.00	6.00	dM0	16,17
WL135	5.841	-	5.479	5.467	-	-	-	ntau	none	01-25-91	KPNO	0	0999	7.02	0.670	0.00	4.20	dG2	
WL230	5.230	-	4.842	4.870	-	-	-	ntau	none	01-25-91	KPNO	1	0999	6.46	0.670	0.00	4.60	G6V	
WL393	6.165	-	5.349	5.176	-	-	-	nvir	none	01-25-91	KPNO	1	0999	9.63	1.520	0.00	6.20	dM2	
WL408	6.340	-	5.523	5.306	-	-	-	bcom	none	01-28-91	KPNO	1	0999	10.04	1.540	0.00	6.30	dM3	

Continued, next page.

Table B.1. (cont.)

Woolley (cont.)

	J	H	K	L	L'	M	N	JMcal	Ncal	Date(UT)	Tel	I	LL'MN	V	B-V	Av	SpT	SpT	Notes
WL486	7.210	-	6.374	6.193	-	-	-	bcom	none	01-25-91	KPNO	0	0999	11.40	1.560	0.00	6.40	dM4	
WL514	5.885	-	5.056	4.895	-	-	-	nvir	none	01-25-91	KPNO	0	0999	9.04	1.510	0.00	6.10	M1V	
WL6	5.252	-	4.952	4.938	-	-	-	aper	none	10-06-90	KPNO	0	0999	6.21	0.470	0.00	3.50	dF5	
WL764	3.294	-	2.775	2.760	-	-	-	aper	none	10-10-90	KPNO	1	0999	4.69	0.800	0.00	5.00	K0V	1,22
WL898	6.321	-	5.537	5.479	-	-	-	aper	none	10-10-90	KPNO	1	0999	8.60	1.250	0.00	5.50	dK5	1,21
WL900	6.838	-	6.064	5.980	-	-	-	ntau	none	01-25-91	KPNO	0	0999	9.59	1.350	0.00	6.10	dM1	
WL913	6.658	-	5.848	5.742	-	-	-	ntau	none	01-25-91	KPNO	0	0999	9.62	1.440	0.00	6.00	dM0	
WL9658	5.774	-	5.342	5.332	-	-	-	aper	none	10-10-90	KPNO	1	0999	6.97	0.720	0.00	4.50	dG5	1,23
WL9670A	4.166	-	3.842	3.843	-	-	-	aper	none	10-10-90	KPNO	1	0999	4.99	0.460	0.00	3.50	F5V	1,23
WL9751	4.962	-	4.558	4.548	-	-	-	aper	none	10-10-90	KPNO	1	0999	6.00	0.580	0.00	4.00	dG0	1,23
WL9761	4.445	-	4.224	4.213	-	-	-	aper	none	10-06-90	KPNO	0	0999	5.09	0.360	0.00	3.00	F0V	
WL9761	4.452	-	4.208	4.204	-	-	-	aper	none	10-10-90	KPNO	1	0999	5.09	0.360	0.00	3.00	F0V	1,24
WL9771	3.364	-	3.295	3.298	-	-	-	aper	none	10-06-90	KPNO	0	0999	3.52	0.090	0.00	2.50	A2V	
WL9829	5.518	-	5.177	5.162	-	-	-	aper	none	10-06-90	KPNO	0	0999	6.50	0.530	0.00	4.00	dG0	

V, B-V and spectral types from Woolley catalog.

Ae\Be stars and S190

	J	H	K	L	L'	M	N	JMcal	Ncal	Date(UT)	Tel	I	LL'MN	Notes
ABAUR	6.168	-	4.287	-	3.158	2.757	0.624	16tau	atau	10-25-90	IRTF	0	9000	19,20
BD46	8.500	-	6.591	-	5.229	4.836	3.526	41ac	bpeg	10-26-90	IRTF	0	9001	
HD245185	-	-	-	-	-	-	2.763	none	atau	10-25-90	IRTF	0	9990	2
HD245185	9.370	-	8.058	-	7.017	6.446	-	16tau	none	10-26-90	IRTF	0	9039	4
HD250550	-	-	-	-	-	-	2.569	none	atau	10-25-90	IRTF	0	9992	
HD250550	8.513	-	6.479	-	5.248	4.810	-	16tau	none	10-26-90	IRTF	0	9019	
HD37490	4.661	-	4.454	-	4.188	3.938	3.085	16tau	atau	10-25-90	IRTF	0	9001	18,19
HIORI	10.608	-	9.201	-	8.136	7.572	5.026	16tau	atau	10-25-90	IRTF	0	9133	
HKORI	9.700	-	7.472	-	5.914	5.281	2.793	16tau	atau	10-25-90	IRTF	0	9000	
LKHA208	-	-	-	-	-	-	2.828	none	atau	10-25-90	IRTF	0	9992	
LKHA208	10.578	-	9.318	-	7.513	6.591	-	16tau	none	10-26-90	IRTF	0	9039	
LKHA233	11.246	-	8.463	-	6.023	5.220	2.484	41ac	bpeg	10-26-90	IRTF	0	9001	
LKHA257	11.252	-	9.591	-	8.465	8.210	6.506	41ac	bpeg	10-26-90	IRTF	0	9033	
RMON	-	-	-	-	-	-	0.185	none	atau	10-25-90	IRTF	0	9991	
RMON	9.652	-	5.877	-	3.473	2.612	-	16tau	none	10-26-90	IRTF	0	9009	4,20
RRTAU	-	-	-	-	-	-	3.550	none	atau	10-25-90	IRTF	0	9992	
RRTAU	9.562	-	6.991	-	5.690	5.291	-	16tau	none	10-26-90	IRTF	0	9029	4
SUAUR	7.295	-	5.996	-	5.125	4.800	2.506	16tau	atau	10-25-90	IRTF	0	9000	
V594CAS	-	-	-	-	-	-	1.817	none	bpeg	10-26-90	IRTF	0	9990	
S190A	12.388	-	9.963	-	8.115	-	-	10per	none	01-06-92	IRTF	0		
S190B	14.403	-	9.565	-	5.967	-	-	10per	none	01-06-92	IRTF	0		

Table B.2. Notes to Table B.1

1	Beginning of night.
2	End of night; near daylight.
3	End of night; near daylight. Airmass curve positive.
4	Near low point (dip) on airmass curve.
5	Airmass curve unstable.
6	Airmass curve previously unstable; should be stable by this measurement.
7	Thin clouds seen intermittently previously.
8	Thin clouds previously. Seems to be OK now.
9	Stripchart gets noisy 1/2 hr after this measurement.
10	Stripchart gets noisy right after this source.
11	Calibrator for K 2-3% low on airmass curve.
12	Measurement of calibrator at L' was noisy .
13	Sky noisy for calibrator.
14	Only used 3 pairs for J; signal at L' seems to be decaying with time.
15	Calibrator for L and L' and/or M measurements was pi4ori.
16	Measurement of calibrator at J possibly in nonliner region of detector.
17	Measurement of calibrator at K possibly in nonliner region of detector.
18	Measurement of source at J possibly in nonliner region of detector.
19	Measurement of source at K possibly in nonliner region of detector.
20	Measurement of source at L' possibly in nonliner region of detector.
21	Calibrator > 1/2 hr away in time.
22	Calibrator >= 45 min away in time.
23	Calibrator >= 1 hr away in time.
24	Calibrator >= 1-1/2 hr away in time.
25	J calibrator >= 1 hr away in time, and bs9512.
26	J calibrator >= 1.5 hr away in time, and bs9512.
27	J calibrator >= 2 hr away in time, and bs9512.
28	K calibrator >= 1 hr away in time.
29	K calibrator >= 1.5 hr away in time.
30	M calibrator 0.85 hr away in time.
31	M calibrator 1.4 hr away in time.
32	HR647? Looks like a double star on TV; noisy.
33	Too bright to do at visible wavelengths other than B.
34	M is so weak, hard to tell whether or not there are bad differences.
35	Mars nearby?
36	Possible source not centered properly on boresight.
37	Possible telescope tracking problem.
38	Instrumental problems; as much as 30% error possible; best guess.
39	Bad weather most of night; hard to get calibrator measurements.

Appendix C

THE MODEL

This model, developed by Michael Skrutskie, estimates the thermal dust emission arising from a circumstellar disk, and the resultant infrared colors for the star-disk system, as a function of the total mass in dust grains. Unlike previous models of circumstellar disks, this model focuses on optically thin disks. The model is unreliable in the thin/thick transition region, and is not as fine as previous models for the optically thick case, such as Kenyon and Hartmann (1987). The model sums the expected emission from concentric disk annuli within a specified distance of the star, taking into account the temperature and luminosity of the central star, shadowing of particles by other particles (optical depth), the grain opacity law (or emission efficiency), the disk surface mass density law, and the total mass of the disk. A "bow-tie" disk geometry and a power law particle size distribution are assumed. Although some assumptions may be simplistic, the model is "exact" for the optically thin case, and gives rough estimates for the mass in dust responsible for producing observed near-infrared color excesses even out to the optically thick case.

The disk emission is calculated assuming the disk is viewed face-on; this view angle produces the maximum possible infrared excess. In the end, all grains in the disk were assumed to have radius 1μm (uniform particle size distribution); the choice of this size is discussed in Section 1.5.1.

The basic geometry of the system is illustrated in Figure C.1. The stellar radius is R_*. A "bow tie" disk geometry is assumed, with disk scale height

$$h(r) = h_{\circ} r, \tag{C.1}$$

such that $h(1\ \mathrm{AU}) = h_{\circ}$. The inner disk radius is denoted by R_{min}; the outer disk radius is not shown in the figure.

Dust grains evaporate when the temperature exceeds some critical limit; the "dust destruction temperature" varies with grain material. Grains cannot survive very near the star, which sets a physical limit to the minimum disk radius. The minimum disk radius is the distance from the star at which the equilibrium temperature of a dust grain equals the dust destruction temperature, R_{dest}. The model allows minimum disk radii which are greater than R_{dest}, if desired.

The central star radiates as a blackbody having temperature T_{*}. The grains absorb starlight as perfect blackbodies and are heated by the starlight. The warmed grains emit as blackbodies tempered by an emission efficiency law chosen by the user. In order to calculate the grain equilibrium temperature, an estimate is needed of the amount of starlight which reaches the grains at a given disk radius, taking into account the fact that dust grains at smaller disk radii block some of the starlight. Consider the disk to be composed of concentric annuli. Knowing the disk geometry and surface density law, a typical optical depth from the star to an annulus at a given disk radius can be calculated. The optical depth is determined by the blockage due to grains at smaller disk radii. This model ignores heating by neighboring dust grains.

The disk, with outer radius R_{max} and inner radius R_{min}, is divided into 50 equally-spaced logarithmic intervals (concentric annuli). The more closely-spaced annuli are near the star. Trial runs of the model show that the results do not change significantly (order-of-magnitude) when the calculations are extended beyond a disk radius of 3 AU. The model results presented in this work all assume an outer disk radius of 3 AU.

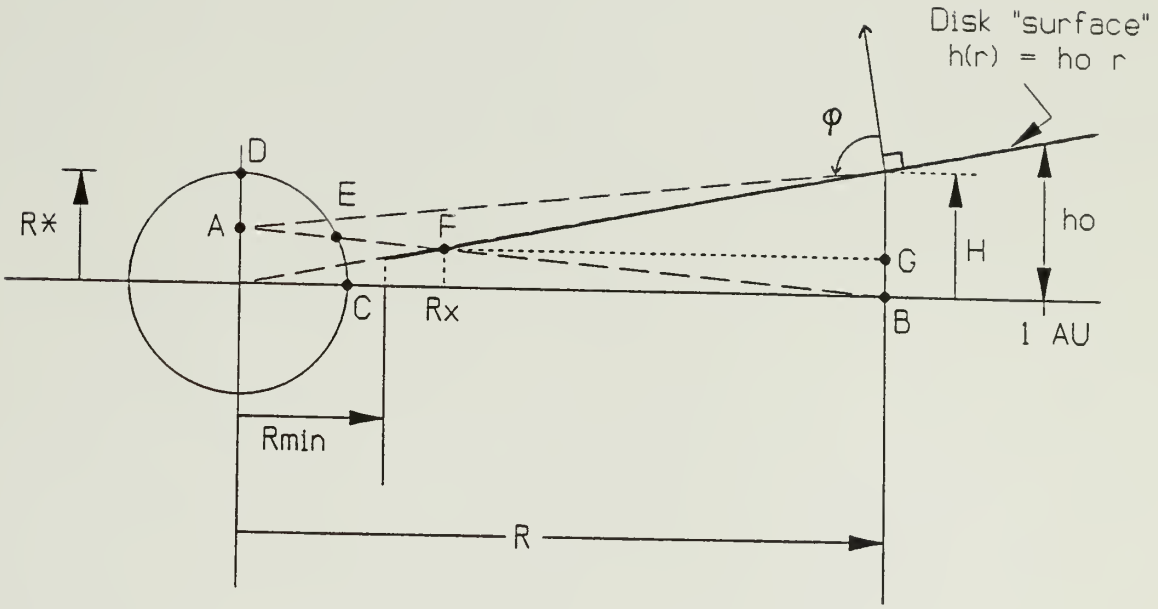

Figure C.1. The model geometry. The stellar radius is R_*. A "bow tie" disk geometry is assumed, with disk scale height $h(r) = h_\circ r$, such that $h(1\ \mathrm{AU}) = h_\circ$. The disk "surface" is drawn with a solid line style. The inner disk radius is at distance R_{min}; although not shown, the maximum disk radius used in the computations is 3 AU. The points $A, B, C, D,, E, F$ and G are described in the text. The optical depth to the central star at disk radius R due to dust grains at smaller disk radii is calculated along the line segment FG. The scale height of the disk at radius R is $h(R) = H$.

Imagine a particular disk annulus at distance R from the star, having width dr, and height $H = h(R)$ above the midplane (so the total height of the annulus is $2H$). The stellar flux is attenuated by dust grains at disk radii less than R. Within the annulus, the optical depth to the star varies with height above the midplane. Since the star is not a point source, the optical depth to the star is also a function of where one is looking on the stellar surface.

Strictly speaking, one must also consider the curvature of the stellar surface, and the resulting diminution of stellar flux near the limb resulting from projection effects. Instead of tackling the problem rigorously, an approximate optical depth for the entire annulus to a portion of the stellar surface midway between the center and upper limb is calculated. It is assumed all dust grains within the annulus are at the same temperature (see Kenyon and Hartmann, 1987, for a discussion on why this is a reasonable assumption).

The stellar flux at distance R is simply $L_*/4\pi R_*^2$. This will be attenuated by a factor of $e^{-\tau}$, where τ is the optical depth to the star. The line of sight used to calculate the optical depth, described below, is shown in Figure C.1.

Point A in Figure C.1 is located at a distance $R_*/2$ from the center of the star, in a direction perpendicular to the plane of the disk. Point B is the intersection of the annulus with the midplane of the disk. From the perspective of a dust grain at point B (ignoring the presence of the rest of the disk), the most intensive stellar flux arises from point C, the weakest from point D, owing to projection effects from the curved stellar surface. One may therefore loosely argue that flux arising from Point E therefore represents an "typical" stellar flux. This will hold true for dust grains at other locations within the annulus.

The line of sight AB intersects the top "surface" of the disk at point F, at disk radius R_x. Line segment BF represents the line of integration for calculating the optical depth perceived by a dust grain at point B to point E, the portion of the

stellar surface representing an "average" stellar flux. The resulting optical depth is a reasonable estimate of the optical depth for any grain within the annulus. To make the calculations a little simpler, instead of using line segment BF for the line of integration, a line parallel to the disk midplane, line segment FG is used to calculate the representative optical depth to the annulus at radius R. (Note: if the intersection of line segment AB with the bow-tie function for the surface of the disk occurs at a radius smaller than the inner radius of the disk (i.e. point R_x is closer than $R_{\rm min}$), the optical depth is calculated over a line segment parallel to the disk midplane from radius $R_{\rm min}$ to radius R.)

The disk surface mass density law is given by

$$\sigma(r) = \sigma_\circ r^{-\alpha}, \tag{C.2}$$

where $\sigma_\circ = \sigma(1\mathrm{AU})$. Typical examples are $\alpha = 0$ (uniform disk), $\alpha = 1$ and $\alpha = 2$. Within each annulus, the particles are assumed to be distributed uniformly.

The optical depth is defined to be

$$d\tau = nA\,dl,$$

where n is the number of particles per unit volume, A is the cross-sectional area of a particle, and dl is a line segment along the line of sight. Using Equations C.1 and C.2, this becomes

$$d\tau = \frac{\sigma(r)}{2h(r)m}\pi a^2\,dr,$$

where m and a are the mass and radius of a dust grain, and dr is along line segment FG in Figure C.1. If a grain has density ρ, the optical depth can then be written as

$$\tau = \frac{3\sigma_\circ}{8h_\circ\rho a}\int_{R_x}^{R} r^{-(\alpha+1)}\,dr.$$

The model performs the integral numerically.

The maximum possible attenuation occurs when the disk acts like a solid sheet. This is just the flux dilution from the projection onto the disk surface,

$\cos\phi$, where ϕ is defined in Figure C.1. If the calculated attenuation is larger than this, the attenuation for a solid surface is used; $\cos\phi$ is substituted for $e^{-\tau}$.

Once the stellar flux incident on the grains in the annulus is known, the equilibrium temperature of the grain can be calculated. It is assumed the grains are perfect absorbers of the starlight, since most of the stellar emission is at wavelengths much smaller than the grains. The emission efficiency of the grains is very important for the emitted spectrum, however, as the emitted radiation is primarily at wavelengths similar to or larger than the grain size. The equilibrium temperature is determined by conservation of energy:

$$\text{Energy absorbed by grain} = \text{Energy emitted by grain},$$

which is given by

$$\frac{L_*}{4\pi R^2}\pi a^2 e^{-\tau} = 4\pi a^2 \int_0^\infty \pi B_\lambda(T) Q(\lambda)\, d\lambda \tag{C.3}$$

where $B_\lambda(T)$ is the Planck function, and $Q(\lambda)$ is the grain emission efficiency law. The emission efficiency law adopted is

$$Q(\lambda) = \frac{1}{1 + (\lambda/2a)^\beta}.$$

However, when the total cross-section of the emitting particles within an annulus exceeds the surface area of the annulus itself, the annulus is presumed to emit as a perfect blackbody, and the emission efficiency is set to $Q(\lambda) = 1$. For the model results presented in this work, $\beta = 1$.

As there is no simple analytical solution to Equation C.3, the temperature is determined empirically. Thirty logarithmically-spaced wavelength bins are used in the calculation, covering a range of approximately 0.14 – 400 μm. Smaller bins are used for shorter wavelengths.

Once the equilibrium temperature of the dust grains in the annulus has been determined, the emission from the grains in each annulus as a function of

wavelength can be calculated. If the surface area of the grains in an annulus exceeds the surface area of the annulus (i.e. an optically thick disk), the surface area of the disk is substituted for the total emitting area. The emission from each grain is given by the right-hand side of Equation C.3. The total dust emission from the disk is determined by summing over all disk annuli. Lastly, the infrared colors arising from the combined emission of star and disk are determined as a function of the stellar temperature, stellar luminosity, total dust mass, and disk mass surface density law.

REFERENCES

Allen, C.W. (1976) *Astrophysical Quantities,* Third Edition (London: Athlone Press).

Allen, D.A. (1973) *Mon. Not. R. Astr. Soc.,* **161**, 145.

Alvarez, J.M. (1967) in *The Zodiacal Light and the Interplanetary Medium,* Ed. J. Weinberg, NASA SP-150, p. 123.

Aumann, H.H. (1988) *Astron. J.,* **96**, 1415.

Backman, D.E. and Paresce, F. (1993) in *Protostars and Planets III,* Eds. E.H. Levy, J.I. Lunine, and M.S. Matthews (Tucson: University of Arizona Press).

Beckwith, S.V.W. and Sargent, A.I. (1993) *Astrophys. J.,* **402**, 280.

Beckwith, S.V.W., Sargent, A.I., Chini, R.S., and Güsten, R. (1990) *Astrophys. J.,* **99**, 924.

Bessell and Brett (1988) *Pub. A.S.P.,* **100**, 1134.

Boesgaard, A.M. (1989) *Astrophys. J.,* **336**, 798.

Brooke, T.Y., Tokunaga, A.Y. and Strom, S.E. (1993), *Astron. J.,* **106**, 656.

Burns, J.A., Lamy, P.L. and Soter, S. (1979) *Icarus,* **40**, 1.

Cameron, A.G.W. (1988) *Ann. Rev. Astron. Astrophys.,* **26**, 441.

Campbell, B., Walker, G.A.H. and Yang, S. (1988) *Astrophys. J.,* **331**, 902.

Cohen, M. and Witteborn, F.C. (1985) *Astrophys. J.,* **294**, 345.

Cohen, M. and Kuhi, L.V. (1979) *Astrophys. J.,* **41**, 743.

Crawford, D.L. and Barnes, (1974) *Astron. J.,* **79**, 687.

Crawford, D.L. and Perry, C.L. (1976) *Astron. J.,* **81**, 419.

D'Antona, F. and Mazzitelli, I. (1994) *Astrophys. J. (Suppl.),* **90**, 467.

Dohnanyi, J.S. (1969) *J. Geophys. Res.*, **74**, 2531.

Drain, B.T., and Lee, H.M. (1984) *Astrophys. J.*, **285**, 89.

Edwards, S., Cabrit, S., Strom, S.E., Heyer, I., Strom, K.M. and Anderson, E. (1987) *Astrophys. J.*, **321**, 473.

Edwards, S., Ray, T. and Mundt, R. (1993) in *Protostars and Planets III*, Eds. E.H. Levy, J.I. Lunine, and M.S. Matthews. (Tucson: University of Arizona Press).

Elias, J.H. (1978) *Astrophys. J.*, **224**, 857.

Elsässer, H. and Fechtig, H. (Eds.) (1975) *Interplanetary Dust and Zodiacal Light*, Proceedings of IAU Colloquium No. 31 (Berlin: Springer-Verlag).

Gault, D.E. and Wedekind, J.A. (1969) *J. Geophys. Res.*, **74**, 6780.

Gault, D.E., Shoemaker, E.M. and Moore, H.J. (1963) NASA Tech. Note TN D-1767.

Grevesse, N. and Sauval, A.J. (1991) in *The Infrared Spectral Region of Stars*, Eds. C. Jaschek and Y. Andrillat (Cambridge: Cambridge University Press).

Griffin, R.F., Gunn, J.E., Zimmerman, B.A. and Griffin, R.E.M. (1988) *Astron. J.*, **96**, 172.

Hanson, R.B. (1975) *Astron. J.*, **80**, 379.

Heckmann, V.O., Deickvoss, W. and Kox, H. (1956) *Astr. Nach.*, **283**, 109.

Hertzsprung, E. (1947) *Ann. Leiden Obs.*, **19**, Part 1A.

Hillenbrand, L.H., Strom, S.E., Vrba, F.J., and Keene, J. (1992) *Astrophys. J.*, **397**, 613.

Johnson, H.L. (1952) *Astrophys. J.*, **116**, 640.

Johnson, H.L. (1966) *Ann. Rev. Astron. Astrophys.*, **4**, 193.

Johnson, H.L. and Knuckles, C.F. (1955) *Astrophys. J.*, **122**, 209.

Johnson, H.L. and Knuckles, C.F. (1957) *Astrophys. J.*, **126**, 113.

Johnson, H.L. and Mitchell, R.I. (1958) *Astrophys. J.*, **128**, 31.

Johnson, H.L., Mitchell, R.I. and Iriarte, B. (1962) *Astrophys. J.*, **136**, 75.

Jones, B.F and Cudworth, K. (1983) *Astron. J.*, **88**, 215.

Kenyon, S.J. and Hartmann, L. (1987) *Astrophys. J.*, **323**, 714.

Kessler, D.J. (1984) in *Properties and Interactions of Interplanetary Dust,* Eds. R.H. Giese and P. Lamy (Lancaster: D. Reidel), p. 97.

Kleiman, G. (1993) *Possible Links between Infrared Excesses in Dwarf Stars and Duplicity,* MS thesis, University of Massachusetts, Amherst.

Klein-Wassink, W.J. (1927) *Groningen Pub.,* No. 41.

Le Sergeant D'Hendecourt, L.B. and Lamy, P.L. (1980) *Icarus,* **43**, 350.

Link, H., Leinert, C., Pitz, E. and Salm, N. (1975) in *Interplanetary Dust and Zodiacal Light,* IAU Colloquium No. 31, Eds. Elsässer, H. and Fechtig, H. (Berlin: Springer-Verlag), p. 24.

Lissauer, J.J. (1987) *Icarus,* **69**, 249.

Lissauer, J.J. (1993). *Ann. Rev. Astron. Astrophys.*, **31**, 129.

Marcy, G.W., and Benitz, K.J. (1989) *Astrophys. J.*, **344**, 441.

Mathis, J.S., Rumpl, W. and Nordsieck, K.H. (1977) *Astrophys. J.*, **217**, 425.

Mitchell, R.I. (1960) *Astrophys. J.*, **132**, 68.

Mumma, M.J., Weissman, P.R. and Stern, S.A. (1993) in *Protostars and Planets III,* Eds. E.H. Levy, J.I. Lunine, and M.S. Matthews (Tucson: University of Arizona Press).

Murdoch, K.A., Hearnshaw, J.B. and Clark, M. (1993) *Astrophys. J.*, **413**, 349.

Neuhäuser, R., Sterzik, M.F., Schmitt, J.H.M.M., Wichmann, R. and Krautter, J. (1995) *Astron. Astrophys.*, in press.

Poeckert, R. (1982) in *Be Stars,* IAU Symposium No. 98, Eds. M. Jaschek and H. Groth (Dordrecht: D. Reidel), p. 453.

Prosser, C.F. (1992) *Astron. J.*, **103**, 488.

Skrutskie, M.F., Snell, R., Dutkevitch, D., Strom, S.E., Schloerb, F.P. and Dickman, R.L. (1991) *Astron. J.*, **102**, 1749.

Roman, N.G. (1949) *Astrophys. J.*, **110**, 205.

Roman, N.G. and Morgan, W.W. (1950) *Astrophys. J.*, **111**, 426.

Safronov, V.S. (1969) *Evolution of the Protoplanetary Cloud and Formation of the Earth and the Planets,* Translated from Russian (1972), NASA TT F-677.

Sargent, A.I. and Beckwith, S.V.W. (1991) *Astrophys. J. (Letters),* **382**, L31.

Schwan, H. (1990) *Astron. Astrophys.*, **228**, 69.

Seeds, M.A. (1994) *Foundations of Astronomy,* 1994 Edition (Belmont: Wadsworth).

Seuss, Dr. (1965) *I Had Trouble in Getting to Solla Sollew* (New York: Random House).

Shu, F.H., Adams, F.C. and Lizano, S. (1987) *Ann. Rev. Astron. Astrophys.*, **25**, 23.

Singer, S.F. and Stanley, J.E. (1980) in *Solid Particles in the Solar System,* Eds. I. Halliday and B.A. McIntosh (Boston: D. Reidel), p. 329.

Singer, S.F., Stanley, J.E. and Kassel, P. (1984) in *Properties and Interactions of Interplanetary Dust,* Eds. R.H. Giese and P. Lamy (Boston: D. Reidel), p. 117.

Skrutskie, M.F., Snell, R.L., Strom, K.M., Strom, S.E., Edwards, S., Fukui, Y., Mizuno, A., Hayashi, M. and Ohashi, N. (1993) *Astrophys. J.*, **409**, 422.

Skrutskie, M.F., Dutkevitch, D., Strom, S.E., Edwards, S., Strom, K.M., and Shure, M.A. (1990) *Astron. J.*, **99**, 1187.

Smith, B.A. and Terrile, R.J. (1984) *Science,* **226**, 1421.

Smith, B.A. and Terrile, R.J. (1987) *Bull. A.A.S.*, **19**, 829.

Snell, R. (1989) in *Structure and Dynamics of the Interstellar Medium,* Eds. G. Tenorio-Tagle, M. Moles, J. Melnick (Springer-Verlag, Berlin), p. 231.

Stapelfeldt, K.R. *et al.* (1995) *Astrophys. J.*, Aug 20, in press.

Stauffer, J. (1982) *Pub. A.S.P.*, **94**, 678.

Stauffer, J.R. (1984) *Astrophys. J.*, **280**, 189.

Stauffer, J., Hamilton, D., Probst, R., Rieke, G. and Mateo, M. (1989) *Astrophys. J. (Letters),* **344**, L21.

Stauffer, J.R., Hartmann, L.W., Burnham, J.N. and Jones, B.F. (1985) *Astrophys. J.*, **289**, 247.

Stauffer, J.R., Hartmann, L.W. and Jones, B.F. (1989) *Astrophys. J.*, **346**, 160.

Stauffer, J.R., Hartmann, L.W. and Latham, D.W. (1987) *Astrophys. J. (Letters)*, **320**, L51.

Stevenson, D.J. and Lunine, J.I. (1987) *Icarus*, **75**, 146.

Strom, K.M., Strom, S.E., Edwards, S., Cabrit, S., and Skrutskie, M.F. (1989) *Astron. J.*, **97**, 1451.

Struve, O. (1931) *Astrophys. J.*, **73**, 94.

Walter, F.M. (1986) *Astrophys. J.*, **306**, 573.

Walter, F.M. Brown, A., Mathieu, R.D., Myers, P.C. and Vrba, F.J. (1988) *Astron. J.*, **96**, 297.

Weidenschilling, S.J. (1980) *Icarus*, **44**, 172.

Weidenschilling, S.J. (1984) *Icarus*, **60**, 553.

Weinberg, J.L. (Ed.) (1967) *The Zodiacal Light and the Interplanetary Medium*, NASA SP-150.

Wetherill, G.W. (1980a) *Ann. Rev. Astron. Astrophys.*, **18**, 77.

Wetherill, G.W. (1980b) in *The Continental Crust and its Mineralogical Deposits*, Geological Society of Canada Special Paper 20, Ed. D.W. Strangway, p. 3.

Wetherill, G.W. (1989) in *Asteroids II*, Eds. R.P. Binzel, T. Gehrels and M. Shapley. (Tucson: University of Arizona Press), p. 661.

Wetherill, G.W. (1990) *Annu. Rev. Earth Planet. Sci.*, **18**, 205.

Wetherill, G.W. (1992) in *The Search for Other Worlds*, JPL Planetary Science Summer School, August 17-21, 1992. (In-house publication; simply a collection of overheads from the talks.)

Wetherill, G.W. and Stewart, G.R. (1993) *Icarus*, **106**, 190.

Whipple, F.L. (1967) in *The Zodiacal Light and the Interplanetary Medium*, NASA SP-150, Ed. J. Weinberg, p. 409.

Wilking, B.A. (1989) *Pub. A.S.P.*, **101**, 229.

Witteborn, F.C., Bregman, J.D., Lester, D.F. and Rank, D.M. (1982) *Icarus,* **50**, 63.

Wolszczan, A. (1994) *Science,* **264**, 538.

Woolley, R., Epps, E.A., Penston, M.J. and Pocock, S.B. (1970), *A Catalog of Stars within 25 Parsecs of the Sun,* Roy. Obs. Ann., No. 5.

Young, A.T. (1974) in *Methods of Experimental Physics, Vol. 12; Astrophysics, Part A: Optical and Infrared,* Ed. N. Carleton (New York: Academic Press), Section 3.1.